

MODELS AND ALGORITHMS TO DETERMINE CEREBRAL
ACTIVATION USING NEAR INFRARED SPECTROSCOPY

by

MONICA SURESH ALLEN

Presented to the Faculty of the Graduate School of
The University of Texas at Arlington in Partial Fulfillment
of the Requirements
for the Degree of

DOCTOR OF PHILOSOPHY

THE UNIVERSITY OF TEXAS AT ARLINGTON

December 2006

ACKNOWLEDGEMENTS

I would like to express my sincere gratitude to my advisor, Dr. Kambiz Alavi, for his guidance, constant encouragement and support during the period of my research. Working with Dr. Alavi, has provided me with a great opportunity to learn and grow both as a student and a person, for which I am very grateful. I would also like to thank my graduate committee members, Dr. J. Bredow, Dr. T. Black, Dr. C. Corduneanu, Dr. W. Dillon and Dr. B. Svihel for their valuable comments and suggestions.

This thesis is dedicated to my husband, Jeffery and my parents Neela and Suresh Rege. Without their constant love and support, this work never would have been possible. This degree has been a family struggle and I will be indebted to them for sticking with me to help me realize my dreams. I would also like to thank Dr. D. Boas, Dr. T. Odegard and Ted Huppert, for their research guidance that has helped me persevere and succeed in my research endeavors.

Special thanks go out to all my friends and family who have helped me through all the good and bad times, there are too many to name but you know who you are.

November 11, 2005

ABSTRACT

MODELS AND ALGORITHMS TO DETERMINE CEREBRAL ACTIVATION USING NEAR INFRARED SPECTROSCOPY

Publication No. _____

Monica Suresh Allen, PhD

The University of Texas at Arlington, 2005

Supervising Professor: Kambiz Alavi

The specific aims of this dissertation were to develop: (1) Correlations between experimental protocols and oxygenated, deoxygenated, and total hemoglobin concentrations in the brain (2) Mathematical models to associate blood flow and oxygen consumption rate of the activated brain regions with measured hemodynamic changes (3) A phantom that models brain vasculature compliance to validate developed mathematical models in a controlled setup. The primary imaging modality used in the experimentation phase of this research was near infrared spectroscopy. Previously published multimodality measurements were also used to validate the mathematical models.

The single compartment Windkessel model was extended to describe flow-volume dynamics during long duration stimulus and include oxygen transport to tissue. An inductive multi-compartment model was developed which enables the estimation of compartmentalized hemodynamic changes with the modeling of measured oxy- and deoxyhemoglobin changes based on a pseudo-Bayesian framework for multimodality data. In addition, a solution to the single and multi-compartment deductive neurovascular model was also developed. This model defines the relationship between the presented stimulus and the neural activity it elicits which in turn gives rise to the vascular changes. Finally a vascular phantom was developed in the laboratory to validate the flow–volume relationships using compliant vasculature.

TABLE OF CONTENTS

ACKNOWLEDGEMENTS.....	ii
ABSTRACT	iii
LIST OF ILLUSTRATIONS.....	xi
LIST OF TABLES.....	xviii
Chapter	
1. INTRODUCTION.....	1
1.1 Dissertation Outline.....	3
2. BACKGROUND THEORY	6
2.1 Comparison of functional imaging modalities.....	6
2.2 Near infrared spectroscopy (NIRS)	8
2.3 Current status in NIR tomography.....	11
2.4 Instrumentation for NIR tomographic imaging	12
2.5 Forward and inverse reconstruction algorithms for NIRS.....	14
2.5.1 Forward model.....	15
2.5.2 Inverse reconstruction.....	16
2.6 Chapter summary.....	19
3. SINGLE COMPARTMENT WINDKESSEL MODEL	20
3.1 Basic principles of hemodynamic modeling.....	21
3.2 Previously published single compartment flow volume model.....	22

3.2.1 Single compartment Windkessel model.....	22
3.2.2 Assumptions for the Windkessel model.....	23
3.2.3 Solving for the flow- volume relationship.....	25
3.2.4 Calculation of oxygen consumption (CMRO ₂).....	28
3.2.5 Example results with fitting measured NIRS volume.....	29
3.3 Contribution of the current research to the Windkessel model.....	31
3.3.1 Inclusion of multimodality data.....	31
3.3.2 Modeling of long duration data.....	32
3.3.3 Development of oxygen consumption model.....	33
3.4 Combination of multimodality data.....	34
3.4.1 Model parameters and initial conditions.....	35
3.4.2 Results with fitting measured NIRS volume and ASL flow.....	37
3.5 Modeling for long duration stimuli.....	39
3.5.1 Results with fitting measured NIRS volume.....	40
3.6 Oxygen consumption models.....	41
3.6.1 Oxygen extraction temporal function	42
3.6.2 Mitochondrial metabolism model.....	47
3.7 Chapter summary.....	58
4. MULTI-COMPARTMENT WINDKESSEL MODEL.....	60
4.1 Motivation for a multicompartment model.....	61
4.1.1 Three compartment flow-volume model	62
4.1.2 Capillary oxygen extraction model.....	62

4.1.3 Mitochondrial oxygen consumption model	64
4.2 General description of multi-compartment model.....	65
4.3 Vascular model.....	67
4.3.1 Electrical representation	67
4.3.2 Vascular model equations.....	68
4.3.3 Arteriole dilation.....	71
4.3.4 Temporal update	72
4.4 Introduction to oxygen transport models	73
4.4.1 Capillary oxygen extraction model.....	74
4.4.2 Mitochondrial metabolism model.....	80
4.5 Comparison of single and multi compartment model.....	97
4.6 Chapter summary.....	98
5. DEDUCTIVE NEURAL MODEL.....	99
5.1 Previously published neurovascular model.....	101
5.1.1 Hemodynamic model details.....	102
5.1.2 State equations of the neurovascular model.....	103
5.2 Contribution of the current research to the neurovascular model.....	105
5.2.1 Determination of compliance coefficients	106
5.2.2 Three compartment flow-volume model.....	107
5.3 Single compartment neurovascular model.....	109
5.3.1 Analytic solution.....	111
5.3.2 Numerical solution.....	112

5.3.3 Simulations for varied compliance	121
5.3.4 Estimation of system parameters	128
5.3.5 Spatial tomographic images of blood flow and CMRO ₂	130
5.4 Multicompartment neurovascular model.....	132
5.4.1 State equations of the neurovascular model.....	133
5.4.2 Simulations for compartmentalized hemodynamics.....	135
5.4.3 Estimation of system parameters	137
5.5 Future work.....	138
5.6 Chapter summary.....	139
6. DEVELOPMENT OF A VASCULAR PHANTOM.....	140
6.1 Motivation behind a vascular phantom.....	141
6.2 Windkessel theory.....	143
6.2.1 Derivation of the Windkessel model	145
6.3 Materials and methods.....	147
6.3.1 System description.....	148
6.3.2 Experimental methods	154
6.4 Experimental results.....	155
6.4.1 Data fitting procedure.....	155
6.4.2 Optimization results.....	156
6.4.3 Statistical analysis.....	159
6.5 Discussion.....	161
6.6 Future directions.....	162

6.7 Chapter summary.....	163
7. EXPERIMENTAL PROTOCOLS AND RESULTS.....	164
7.1 Protocol: Categorical learning task.....	165
7.1.1 Materials and methods.....	167
7.1.2 Results.....	173
7.1.3 Discussion.....	177
7.1.4 Conclusions.....	178
7.2 Protocol: Verbal fluency and physical exercise.....	178
7.2.1 Materials and methods.....	179
7.2.2 Verbal fluency task results.....	181
7.2.3 Physical exercise results.....	186
7.2.4 Discussion.....	189
7.2.5 Conclusions.....	193
7.3 Invasive rat data (Previously published).....	194
7.3.1 Materials and methods.....	194
7.3.2 Model setup.....	195
7.3.3 Results.....	198
7.3.4 Discussion.....	207
7.3.5 Conclusions.....	208
7.4 Protocol: Neuroeconomic experiment	208
7.4.1 Materials and methods.....	211
7.4.2 Results.....	220

7.4.3 Discussion.....	224
7.4.4 Conclusions.....	225
7.5 Chapter summary.....	226
8. SUMMARY AND FUTURE WORK.....	227
8.1 Theoretical development.....	228
8.1.1 Single compartment Windkessel model	228
8.1.2 Inductive multi-compartment Windkessel model.....	229
8.1.3 Deductive neurovascular model	230
8.2 Experimental development	231
8.2.1 Compliant vascular phantom	231
8.2.2 Experimental protocols and results.....	232
8.3 Future work.....	232
8.3.1 Future theoretical development	232
8.3.2 Future experimental development.....	233
APPENDIX	
A. RESEARCH PUBLICATIONS	235
REFERENCES	238
BIOGRAPHICAL INFORMATION.....	253

LIST OF ILLUSTRATIONS

Figure		Page
2.1	Schematic drawing of the LEDI headband showing the placement of light sources and detectors.....	13
2.2	Probe layout shows channel placement on the subject's head used for the pilot study. Channel 1 is always placed on the subject's upper right temple. The arrows show the position of channels on subject's head, thus giving a reference of spatial distribution.....	14
3.1	Single compartment Windkessel model.....	25
3.2	Results of the single compartment Windkessel model (HbT fit only).....	30
3.3	Framework for including multimodality data	36
3.4	Results of the single compartment Windkessel model (HbT and CBF fit) Duration of task=2 seconds	38
3.5	Results of the single compartment Windkessel model (HbT only) Duration of task=20 seconds.....	40
3.6	Results of the single compartment Windkessel model (All NIRS measurements and CBF fit). Duration of task=2 seconds	45
3.7	Results of the single compartment Windkessel model (All NIRS measurements and CBF fit). Duration of task=20 seconds	47
3.8	Kellman's oxygen extraction curve.....	54
3.9	Results of the single compartment Windkessel model (All NIRS measurements and CBF fit). Duration of task=2 seconds	56
3.10	Results of the single compartment Windkessel model (All NIRS measurements and CBF fit). Duration of task=20 seconds	57
4.1	State space representation of vascular model.....	66

4.2	Electrical circuit analogy for the multi-compartment model	68
4.3	Results of the multicompartment Windkessel model (OE model).....	76
4.4	Multicompartment Windkessel model (individual vascular contributions).....	77
4.5	OE Windkessel model (long duration).....	79
4.6	OE Windkessel model (individual contributions-long duration)	80
4.7	Multicompartment Windkessel model (mitochondrial model).....	93
4.8	Mitochondrial Windkessel model (individual vascular contributions).....	94
4.9	Mitochondrial Windkessel model (long duration)	96
4.10	Mitochondrial Windkessel model (individual contributions-long duration)	97
5.1	Neurovascular model for relating stimulus to blood volume and flow.....	102
5.2	Graph illustrating the Midpoint method. Second order accuracy is obtained by using the initial derivative at each step to find a point halfway across the interval, then using the midpoint derivative across the full width of the interval. In the figure, filled dots represent final function values, while open dots represent function values that are discarded once their derivatives have been calculated and used.....	114
5.3	Step doubling as a means for adaptive step size control in fourth order Runge-Kutta. Points where the derivative is evaluated are shown as filled circles. The open circle represents the same derivative as the filled circle immediately above it, so the total number of evaluations is 11 per two steps. Comparing the accuracy of the big step with the two small steps gives a criterion for adjusting the step size on the next step, or for rejecting the current step as inaccurate	116
5.4	Flow volume simulations for varying values of compliance coefficients (γ), duration of input stimulus=2 seconds	123

5.5	Flow volume simulations for varying values of compliance coefficients (γ), duration of input stimulus=20 seconds	125
5.6	Model fit to experimental NIRS data and predicted temporal evolution of cerebral blood flow, CMRO ₂ and BOLD signals	129
5.7	Spatial tomographic images of the average Δ CBF, Δ CMRO ₂ and Δ BOLD during activation	131
5.8	Results of the multicompartment Windkessel model.....	136
5.9	Model fit to experimental NIRS data and predicted temporal evolution of cerebral blood flow, CMRO ₂ and BOLD signals	138
6.1	Model of the Windkessel concept	145
6.2	Experimental apparatus modeling the Windkessel concept.....	148
6.3	The vascular phantom system	149
6.4	Fluid dispensing system	150
6.5	Data acquisition system.....	151
6.6	KUSB-3100 Economical Multifunction Data Acquisition module	152
6.7	GUI for the Labview Data Acquisition program	153
6.8	Labview Data Acquisition program with all the components.....	153
6.9	Pressure trace and Windkessel fits (Wall thickness 0.093", inner diameter=0.25") Systole fit: $R^2 = 0.9992$, Diastole: $R^2 = 0.9789$	157
6.10	Pressure trace and Windkessel fits (Wall thickness 0.0625", inner diameter=0.25") Systole fit: $R^2 = 0.9996$, Diastole fit: $R^2 = 0.9723$	157
6.11	Pressure trace and Windkessel fits (Wall thickness 0.015", inner diameter=0.25") Systole: $R^2 = 0.9996$, Diastole: $R^2 = 0.9544$	158
6.12	Pressure trace and Windkessel fits (Wall thickness 0.125", inner diameter=0.25") Systole: $R^2 = 0.9995$,	

	Diastole: $R^2 = 0.9753$	158
6.13	Pressure trace and Windkessel fits (Wall thickness 0.469", inner diameter=0.25") Systole: $R^2 = 0.9959$, Diastole: $R^2 = 0.9622$	159
6.14	Resistance vs. Modulus of volume elasticity	160
7.1	Protocol followed for the experiment. A baseline period of rest was followed by a stimulation period where the participant viewed word lists of unrelated words where the central meaning was difficult to extract; then another period of rest was given, again followed by another stimulation period where the participant viewed word lists of related words where the central meaning was easy to extract, and finally a period of rest	168
7.2	Comparison of the Maximum HbO ₂ levels minus baseline activation for block of lists with easily identifiable themes and lists of words with more difficult to identify themes	173
7.3	Maps of maximum $\Delta[\text{HbO}_2]$ and $\Delta[\text{Hb}]$ across the prefrontal cortex from a single representative participant. The left panel represents the graphs of oxyhemoglobin and the right panel represent maps for deoxyhemoglobin. The first row of maps represents the hemoglobin levels at Baseline: period of rest (awake, eyes on fixation point, no stimulation). The second row of maps represents the hemoglobin levels at activation period 1: Presentation of lists of unrelated word where the central meaning was difficult to extract. The third row of maps represents the hemoglobin levels at activation period 2: Presentation of lists of related words where the central meaning was easy to extract.....	175
7.4	Maps of average $\Delta[\text{HbO}_2]$ and $\Delta[\text{Hb}]$ across the prefrontal cortex from a single representative participant. The left panel represents the graphs for oxyhemoglobin and the right panel represent maps for deoxyhemoglobin. The first row of maps represents the hemoglobin levels at Baseline: period of rest (awake, eyes on fixation point, no stimulation). The second row of maps represents the hemoglobin levels at activation period 1: Presentation of lists of unrelated word where the central meaning was difficult to extract. The third row of	

	maps represents the hemoglobin levels at activation period 2: Presentation of lists of related words where the central meaning was easy to extract.....	175
7.5	Block-averaged hemoglobin maps for temporally averaged data for the 10 subjects. Top panels show baseline spatial distribution for oxy hemoglobin changes. Bottom panels show the spatial distribution during the verbal fluency task (stimulation period).....	182
7.6	Block-averaged hemoglobin maps for temporally averaged data for the 10 subjects. Top panels show baseline spatial distribution for deoxy hemoglobin changes. Bottom panels show the spatial distribution during the verbal fluency task (stimulation period).....	183
7.7	Block-averaged hemoglobin maps for temporally averaged data for the 10 subjects. Top panels show baseline spatial distribution for total hemoglobin changes. Bottom panels show the spatial distribution during the verbal fluency task (stimulation period).....	183
7.8	Temporal traces of hemoglobin for averaged data over the region of interest (mid prefrontal cortex) for the 10 subjects. Oxyhemoglobin changes are represented by the red line and deoxy-hemoglobin changes are represented by the blue line and total hemoglobin changes are indicated by the green plots. The periods of baseline (rest) and stimulation are as indicated in the figure	184
7.9	Model fit to experimental NIRS data and predicted temporal evolution of cerebral blood flow, CMRO ₂ and BOLD signals	185
7.10	Spatial tomographic images of the average Δ CBF, Δ CMRO ₂ and Δ BOLD during activation (verbal fluency task)	186
7.11	Block-averaged hemoglobin maps for temporally averaged data for the 10 subjects. Top panels show baseline spatial distribution for oxy hemoglobin changes. Bottom panels show the spatial distribution during the exercise task (stimulation period).....	187
7.12	Block-averaged hemoglobin maps for temporally averaged data for the 10 subjects. Top panels show baseline spatial distribution	

	for deoxy- hemoglobin changes. Bottom panels show the spatial distribution during the exercise task (stimulation period).....	187
7.13	Block-averaged hemoglobin maps for temporally averaged data for the 10 subjects. Top panels show baseline spatial distribution for total hemoglobin changes Bottom panels show the spatial distribution during the exercise task (stimulation period).....	188
7.14	Temporal traces of hemoglobin for averaged data over the region of interest (mid prefrontal cortex) for the 10 subjects. Oxyhemoglobin changes are represented by the red line and deoxyhemoglobin changes are represented by the blue line and total hemoglobin changes are indicated by the green plots. The periods of baseline (rest) and stimulation are as indicated in the figure	188
7.15	Multi-compartment model fit to the experimental data: The experimental data (dots) was fit using the multicompartement model (lines). Here we show representative results from the model fits to stimulus conditions 3, 6, and 9. The error bars show standard error estimated from the seven rats used in this experiment. Each condition was fit independently to generate these plots. The R^2 values for these fits are shown in Table 7.8. Blood flow (black) was measured by laser speckle imaging. Blood flow, volume, oxy- and deoxy-hemoglobin changes are shown in black, green, red, and blue respectively and were measured by optical spectroscopy	199
7.16	Markov Chain Monte Carlo results.....	201
7.17	Single-compartment model fit to the experimental data: The experimental data (dots) was fit using the single compartment model (lines). Here representative results from the model fits to stimulus conditions 3, 6, and 9 are shown. Each condition was fit independently to generate these plots. The R^2 values for these fits are shown in Table 7.8. Blood flow, volume, oxy- and deoxy-hemoglobin changes are shown in black, green, red, and blue respectively. The error bars represented standard errors estimated from the seven rats used in this experiment.....	202
7.18	Compartmental hemodynamic changes: Vascular changes were modeled in the arteriole, capillary, and venous compartments. The time-courses plotted here from the ninth stimulus condition,	

show the representative changes in these three compartments.
The solid lines, show the predicted observation model for either
laser speckle imaging (blood flow) or spectroscopic imaging. The
figures to the right of each plot show an enlargement of the initial
onset times [0-3 seconds] 206

7.19 Branching pathway representation of a two-person neuroeconomic task..... 213

7.20 Step-by-step evolution of a two-person task..... 214

7.21 Step-by-step evolution of a two-person decision task..... 215

7.22 Step-by-step evolution of a one-person decision task..... 216

7.23 Protocol instructions: Welcome screen..... 217

7.24 Protocol instructions: Introduction screen..... 217

7.25 Protocol instructions: Game instructions screen 218

7.26 Temporal evolution of the hemodynamic response measure by NIRS 223

LIST OF TABLES

Table	Page
3.1 Variables used in vascular model.....	28
3.2 Parameters used in single compartment fit	59
5.1 RK5(4)7FM embedded pair (DOPRI5).	121
5.2 Flow volume ratio and dependence on stiffness coefficient, duration of input stimulus=2 seconds	124
5.3 Flow volume ratio and dependence on stiffness coefficient, duration of input stimulus=2 seconds	126
5.4 Comparison of flow volume characteristics using simulation studies and experimental data, duration of input stimulus=2 seconds	127
5.5 Comparison of flow volume characteristics using simulation studies and experimental data, duration of input stimulus=20 seconds	128
6.1 Data statistics (lb) and (ub) represent the lower and upper 95% confidence limits.....	160
7.1 Sample protocol with study blocks	171
7.2 Mean values of maximum $\Delta[\text{HbO}_2]$ for the channels measuring Superior Prefrontal Cortex (n=16)	177
7.3 Mean values of maximum $\Delta[\text{HbO}_2]$ for the channels measuring Inferior Prefrontal Cortex (n=16)* Indicates those contrasts that were significant at an alpha level of $p < .05$)	177
7.4 Summary of results for the oxyhemoglobin and deoxyhemoglobin changes induced during the verbal fluency task. The first column 'S' indicates the subject number. Consecutive columns indicate channel 1 through 16. The '+' sign indicates an increase in levels, '-' sign a decrease in levels and '*' sign indicates a substantial increase in levels, 'C' indicates no change in levels, 'N' indicates	

noise interference. All levels measured are relative to baseline period	190
7.5 Summary of results for the oxyhemoglobin and deoxyhemoglobin changes induced during the physical exercise. The first column ‘S’ indicates the subject number. Consecutive columns indicate channel 1 through 16. The ‘+’ sign indicates an increase in levels, ‘-’ sign a decrease in levels and ‘*’ sign indicates a substantial increase in levels; ‘C’ indicates no change	192
7.6 Comparison of results obtained for both the mental and physical tasks and indicates the changes in oxyhemoglobin and deoxyhemoglobin levels induced for the 10 subjects. The levels of HbO ₂ and Hb were calculated by block averaging over the period of activation and over all 16 channels under examination.....	192
7.7 State estimates: In this table, we present the model estimates from the nine stimulus conditions for the fourteen state variables. For the structural parameters, the mean of the nine conditions is shown. None of the changes in these parameters significantly varied with stimulus condition . In the last column, the values estimated jointly from all nine conditions are shown. The asterisks (*) indicate parameters, that varied significantly (p<0.05) with stimulus condition. The amplitude and time-to-peak of arterial dilation both increased significantly with stimulus condition for the nine independent fits. CMRO ₂ estimated in the independent fits trended to increase, but this was not significant due to variance of the estimates. In contrast, CMRO ₂ significantly increased in the estimates obtained by joint-fits to all nine conditions	200
7.8 Single- and multi-compartment model fits to experimental data: In this table, the R ² values (goodness-of-fit) for the model fits to the nine-stimulus conditions are shown. These R ² values have been adjusted for the degrees-of-freedom. For each condition, the partial R ² value for the flow, volume and oxy-/deoxy-hemoglobin measurements were calculated. This value indicates the explained model variance considering only that component of the measurements. The total R ² indicates the fraction of the total variance accounted for by all measurements. The multi-compartment model significantly improved the fits to the data (p<8x10 ⁻⁵). The most notable improvements were observed in the modeling of deoxyhemoglobin(p<8x10 ⁻⁶)	203
7.9 Spatial and temporal results of a neuroeconomic task	222

CHAPTER 1

INTRODUCTION

Medical imaging is a rapidly developing field with application to structural and functional imaging in the fields of research as well as in hospitals for the clinical diagnosis of disease and monitoring of therapeutic treatment. Measurements of the functional changes in hemodynamic variables, such as blood volume, flow, or hemoglobin oxygenation, have led to important advances in modern neuroscience and have contributed to understanding of the functional physiology of the brain [1]. One of the primary reasons for these advances has been the development and refinement of functional imaging methods over the last several decades. In the activated brain, increased oxygen consumption is typically met with an overcompensating increase in regional blood flow. This results in a net increase in the oxygen content of the activated region of the brain. Hemodynamic measurements quantify these composite changes and are less revealing than direct measures of neuronal or metabolic function [1]. Thus neurovascular models can be invaluable to explore the underlying metabolic and neural responses based on the hemodynamic measurements.

The introduction of vascular descriptions, such as the Balloon [2, 3] and Windkessel models [4, 5] have helped to reveal the brain's metabolic and neuronal functions by providing an interpretation of hemodynamic parameters measured by functional magnetic resonance imaging (fMRI) or optical methods. Such vascular

modeling has been instrumental to progress the understanding of the relationships between blood flow, volume, and oxygenation responses and to neuronal activation [reviewed in [6, 7]]. These models can help elucidate differences between the effects of vascular “plumbing” and the cerebral metabolic rate of oxygen consumption ($CMRO_2$) by separating and identifying the individual contributions of arteriole dilation and oxygen consumption and their relation to the measured hemodynamic response. Such insights could eventually lead to the use of functional imaging tools in clinical applications, since distinguishing these differences could enable quantitative interpretation of hemodynamic signals for the neurosciences and potentially make longitudinal and cross-subject studies more fruitful [1]. As other groups have noted in results from animal models, insight into the underpinnings of the neural-vascular response might have a significant impact in diagnosis and treatment of conditions such as stroke or Alzheimer’s disease [8].

This dissertation focuses on the development and comparison of three different vascular and metabolic models. The specific aims of this dissertation are: (1) To experimentally explore correlations between given motor and cognitive protocols and regional oxygenated hemoglobin (HbO_2), deoxygenated hemoglobin (Hb), and total hemoglobin (HbT) concentrations in the human brain (2) To develop mathematical models that associate cerebral blood flow (CBF) and oxygen consumption rate ($CMRO_2$) of activated brain regions with measured Hb , HbO_2 , and HbT during varied tasks (3) To develop a phantom that models brain vasculature compliance and enables

the analysis of quantified hemodynamic parameters. This will be used to validate the developed mathematical models in a controlled experimental setup.

The combination of noninvasive near infrared (NIR) hemodynamic imaging and modeling is innovative in that it provides heterogeneous maps of hemodynamic parameters (Hb, HbO₂, HbT) related to CBF and CMRO₂ of the human brain. The experiments performed in this dissertation are also novel in that NIRS imaging has not been explored extensively for cognitive protocols. Application of noninvasive functional imaging techniques such as NIRS and the related models to varied protocols can thus be used to further the understanding of the dynamics, mechanisms, and heterogeneity of brain responses to varied tasks.

1.1 Dissertation outline

This dissertation is organized in the following manner.

Chapter 1 - Introduction: gives a general overview of the dissertation and the aims that motivate this work. A short synopsis of the dissertation is included to present a brief summary of the topics covered in each chapter.

Chapter 2 - Background Theory: covers the background theory that underlies the measurements conducted in this dissertation. This chapter starts with the comparison of different imaging modalities used in functional brain imaging and then focuses on the primary imaging modality used in this research, namely NIRS. Instrumentation used in this research, methods for extraction of parameters and finally forward and inverse reconstruction techniques are discussed to conclude the chapter.

Chapter 3 - Single compartment Windkessel model: describes a previously published single compartment flow-volume model. In particular, the model is used as the basis for the inclusion of a model that describes hemodynamic changes during long duration stimulus. An oxygen extraction model and mitochondrial activity model is also developed to describe oxygen consumption dynamics using appropriate temporal basis functions in each case.

Chapter 4 – Multi- compartment Windkessel model: makes three major contributions: (i) description of a new inductive three compartment hemodynamic model which enables the estimation of compartmentalized hemodynamic time-courses from imaging measurements; (ii) development of two novel models to describe mechanisms underlying the changes in measured oxy- and deoxyhemoglobin changes; and finally (iii) a pseudo-Bayesian framework which allows for simultaneous analysis of multimodality data.

Chapter 5 - Deductive Neural model: This chapter is divided into three major parts: (i) simulations to predict measurements based on typical system parameters (ii) calculation of unknown system parameters using measured experimental data (iii) development of a multicompartment input-output nonlinear system consisting of a neural model and vascular model. The simulated results are compared to published data and predicted system parameters are compared to typical values to demonstrate their validity.

Chapter 6 – Compliant Vascular Phantom: presents a summary of the scaled up vascular model developed in the laboratory to validate the flow–volume relationships

using compliant vasculature as described in the single compartment Windkessel model. A program written in LabView is used for data acquisition to collect pressure, volume and flow data. The vascular model is then applied to establish temporal relationships among the measured quantities and the compliance of the vascular tubing being modeled. These relationships are used to validate the hemodynamic mathematical models.

Chapter 7 – Experimental Protocols and Results: outlines the NIRS experiments that were conducted during the course of this research as well as the protocols that were used to collect previously published multimodality data that was used to test the models developed during this research. The basic results without modeling interpretation are presented here.

Chapter 8 – Conclusions and Future Research: summarizes the specific achievements of this research work and provides suggestions for future development and directions for this research.

CHAPTER 2

BACKGROUND THEORY

Neuropsychological data has been used in the past to identify the involvement of brain regions during a given task, but is limited by its inability to distinguish functions performed by specific structures of the brain [9, 10]. This shortcoming has been overcome in recent years by the use of functional brain imaging as a powerful tool to study the relation of human cognition and its neurological basis [11, 12]. Functional brain imaging involves a comparison of hemodynamic responses while performing a particular task versus the measurements taken when the subject is at rest [13, 14]. The difference between images taken while a subject is performing an experimental task and images taken during a control state reveals regions of the brain that are differentially activated by the experimental task.

2.1 Comparison of functional imaging modalities

There are five basic functional imaging modalities: electroencephalography (EEG), positron emission tomography (PET), functional magnetic resonance imaging (fMRI), dynamic infrared imaging (DIRI) and functional near infrared spectroscopy (NIRS) [15]. These imaging modalities can be divided into two categories: first, imaging modalities that image the intrinsic radiation produced by the body and second, modalities that image interactions between probing radiation and the tissues under

examination. EEG and DIRI fall under the first category while MRI, PET and NIRS belong to the second category.

EEG measures electrical activity of the brain by placing electrodes on the scalp. The measurements are synchronized to stimulus events or behavioral responses [16]. PET measures blood flow in the brain with the assumption that neural activity in a region leads to increased blood flow in that region [17]. fMRI tracks activities in the brain by measuring changes in blood oxygenation levels and blood volume. NIRS is based on the principle that all biological tissue is permeable to electromagnetic radiation of varying energy and frequency to different extents. NIRS acquires oxygenated and deoxygenated hemoglobin data as indicators of activation [18, 19] based on their absorption coefficients at the wavelengths of the probing light.

NIRS provides several attractive advantages, including relatively low cost, possible bedside equipment, and no requirement for an exogenous contrast medium to take readings. Additionally, NIRS does not require any radioactive compounds, and therefore the measurements can be repeated without exposing the subject to harmful radiation. Thus NIRS imaging systems are safer, non-ionizing, do not require a shielded room to acquire data (unlike x-ray and MRI methods), and can be performed repeatedly at the bedside. PET and fMRI provide better spatial resolution than EEG or NIRS, but poorer temporal resolution because blood-flow to neurally active areas occurs with a stochastic lag of a few seconds. NIRS provides better spatial resolution than EEG, but lacks the high temporal resolution provided by EEG [15].

The major advantages of unobtrusiveness and portability that NIRS provides could eventually reach the point where it will be possible to take measurements from people as they go about their daily affairs. Detecting abnormalities in the function of tissues could allow earlier intervention than most other imaging modalities which are unable to detect events that do not manifest as a change in tissue structure or composition. Thus NIRS can be used to monitor the progression of conditions and also the response to treatment being administered.

2.2 Near infrared spectroscopy (NIRS)

NIRS instrumentation operates at a frequency range of 700-900 nm, within which tissue has the lowest absorption coefficient [20]. This optical window has optimal penetration depths in tissue and permits the measurement of oxygenated hemoglobin [HbO₂], deoxygenated hemoglobin [Hb] and total hemoglobin [HbT] (proportional to blood volume) [21] through the intact skull. These variables reflect changes in levels of regional cerebral hemoglobin concentration for the region under inspection. A NIRS imaging system can provide maps of the oxygenation state of tissue within a living brain (or other part of the body) and can provide information about the functional and metabolic activity of tissues noninvasively.

Historically, biological chemists and biochemists have utilized Beer-Lambert's law and developed the notation of optical density to express light absorption as a function of hemoglobin concentration [21]

$$\text{Optical Density (OD)} = \log(A_0/A) = \epsilon \quad (1)$$

where A_0 and A are light intensities of the incident and transmitted light, respectively, ϵ is the extinction coefficient of hemoglobin, c is the concentration of hemoglobin, and l is the length of light path through the measured sample. When the measured sample has a mixture of oxygenated and deoxygenated hemoglobin, Equation 1 can be further evolved to [21, 22]

$$OD(\lambda) = \{\epsilon_{Hb}(\lambda)[Hb] + \epsilon_{HbO_2}(\lambda)[HbO_2]\} \cdot l \quad (2)$$

where $OD(\lambda)$ is the optical density at wavelength λ , $\epsilon_{Hb}(\lambda)$ and $\epsilon_{HbO}(\lambda)$ are the extinction coefficients at wavelength λ for molar concentrations of deoxygenated hemoglobin, $[Hb]$, and oxygenated hemoglobin, $[HbO_2]$, respectively, assuming ferrihemoglobin is minimal. By employing two wavelengths, both $[HbO_2]$ and $[Hb]$ can be determined by measuring the OD values at the two specific wavelengths, provided that the values for $\epsilon_{Hb}(\lambda)$ and $\epsilon_{HbO}(\lambda)$ are known:[22, 23]

$$[HbO_2] = \frac{\epsilon_{Hb}(\lambda_2)OD(\lambda_1) - \epsilon_{Hb}(\lambda_1)OD(\lambda_2)}{l[\epsilon_{Hb}(\lambda_2)\epsilon_{HbO}(\lambda_1) - \epsilon_{Hb}(\lambda_1)\epsilon_{HbO}(\lambda_2)]} \quad (3)$$

$$[Hb] = \frac{\epsilon_{HbO}(\lambda_2)OD(\lambda_1) - \epsilon_{HbO}(\lambda_1)OD(\lambda_2)}{l[\epsilon_{Hb}(\lambda_1)\epsilon_{HbO}(\lambda_2) - \epsilon_{Hb}(\lambda_2)\epsilon_{HbO}(\lambda_1)]} \quad (4)$$

It follows that changes in $[Hb]$ and $[HbO_2]$ can be consequently given by Equations 3 and 4 where $\Delta OD(\lambda)$ represents a change in optical density at the specific wavelength, λ , and equals to $\log(A_B/A_T)$. A_B and A_T correspond to light intensities measured under the baseline and transient conditions.

$$\Delta[HbO_2] = \frac{\epsilon_{Hb}(\lambda_2)\Delta OD(\lambda_1) - \epsilon_{Hb}(\lambda_1)\Delta OD(\lambda_2)}{l[\epsilon_{Hb}(\lambda_2)\epsilon_{HbO}(\lambda_1) - \epsilon_{Hb}(\lambda_1)\epsilon_{HbO}(\lambda_2)]} \quad (5)$$

$$\Delta[Hb] = \frac{\varepsilon_{HbO}(\lambda_2)\Delta OD(\lambda_1) - \varepsilon_{HbO}(\lambda_1)\Delta OD(\lambda_2)}{l[\varepsilon_{Hb}(\lambda_1)\varepsilon_{HbO}(\lambda_2) - \varepsilon_{Hb}(\lambda_2)\varepsilon_{HbO}(\lambda_1)]} \quad (6)$$

Note that in principle, l represents the optical path length between the source and detector and whereas d is simply the physical separation between the source and detector through a non-scattering medium. Exact quantification of l for an intact tissue or organ is complex because of light scattering in tissue. Since l is proportional to the separation, d , we can associate l to d as $l = \text{DPF} \cdot d$, where DPF is a differential path length factor to account for light scattering. It has been well accepted that together with DPF, Equation 2 can be treated as modified Beer-Lambert's law; and consequently, Equations 5 and 6 can be correctly used to quantify changes in [Hb] and [HbO₂] in highly scattering media [22, 23] such as in intact tissue or organs. To quantitatively derive relative concentration changes from measurements of light attenuation, the optical path length must be known. Path length can be calculated by multiplying the source-detector separation by a laboratory measured differential path length factor (DPF), which accounts for the increased distance traveled by light due to scattering. Previously published results suggest a slowly varying age dependence of DPF and can be estimated using the following the relation

$$\text{DPF}_{730} = 5.11 + 0.106 \cdot A^{0.723} \quad \text{and} \quad \text{DPF}_{850} = 4.67 + 0.062A^{0.819} \quad (7)$$

where DPF_{730} is the DPF measured at 730 nm, DPF_{850} is the DPF measured at 850 nm and A is age is expressed in years [24]. This theory is to calculate the hemodynamic parameters for the brain regions under examination and applied to derive the model for blood flow and oxygen consumption rate.

2.3 Current status in NIR tomography

Over the last decade, a large number of investigations have been conducted in laboratory and clinical settings using non-invasive, quantitative NIRS to image tissue vasculature oxygenation. Although NIRS imaging is limited by its spatial resolution, it has great potential as a new imaging modality because of its capability to provide functional images with high temporal resolution. NIRS imaging in the brain has been extensively used in previous studies for detection of brain injury/trauma [25], determination of cerebro-vascular hemodynamics and oxygenation [26, 27], and functional brain imaging in response to a variety of neurological activation [21, 28-30]. In recent years, NIR functional brain imaging has been applied to studying hemodynamic response as a function of brain activation using psychological rather than physiological stimuli [31]. NIR techniques produce input optical signals that can non-invasively penetrate the scalp and skull of an adult human and return output signals (scattered light from tissue under examination) that directly relate to changes in the concentration of oxygenated (HbO_2) and deoxygenated hemoglobin (Hb). NIRS can be used to accurately measure relative changes in HbO_2 and Hb, that is, compare readings from an experimental task (activation period) to a control task (baseline period). Thus quantitative changes in total cerebral blood volume proportional to total hemoglobin concentration ($\text{HbT} = \text{HbO}_2 + \text{Hb}$) [31] can be calculated. NIR imaging techniques require application of diffusion theory with complicated boundary conditions [32] to calculate absolute readings of cerebral HbO_2 and Hb concentrations. This analysis can at best provide estimates of absolute values. Therefore, NIRS has been used mainly in

relative experimental studies where meaningful results can be obtained by taking comparative readings from the baseline and activation conditions caused by stimuli [31]. In this way, very accurate boundary conditions for the measurement geometry are not required to produce desired results.

Several research groups have been involved in developing NIR imaging modality through both laboratory and clinical studies. There are three major types of instruments being developed for optical imaging studies: time domain (TD), frequency domain (FD) and continuous wave (CW) [21, 22, 33]. The CW system provides the advantages of simplicity, portability and low-cost when compared to FD and TD imaging systems, and therefore is as the primary tool in this of research.

2.4 Instrumentation for NIR tomographic imaging

A 16-channel (4 sources, 10 detectors) LEDI continuous wave NIRS system (Near Infrared Monitoring Inc., Philadelphia, PA) was used in reflection mode for the research study. The measurements are performed at 730 nm and 850 nm, and the light from the laser diode sources is shone on the tissue under examination. The scattered light is collected through the photodetectors [15, 34]. The placement of the light emitting diode (LED) sources with respect to the detectors on the headband is shown in Figure 2.1. In each experiment the headband is placed across the forehead of the subject of the subject. This placement should cover the regions of the prefrontal cortex as desired for the proposed experiments [35]. The temporal specifications for various parts of the current system affecting the readings are as follows: A/D conversion rate is

60,000 samples/second or A/D conversion every 16.7 microseconds, 250 samples per LED wavelength per detector at 4.2 milliseconds and 2 wavelengths per detector every 12.5 milliseconds. For 16 channels, time required for one whole sample is 200 milliseconds [34]. The readings collected at the detectors are converted to digital format using an A/D converter.

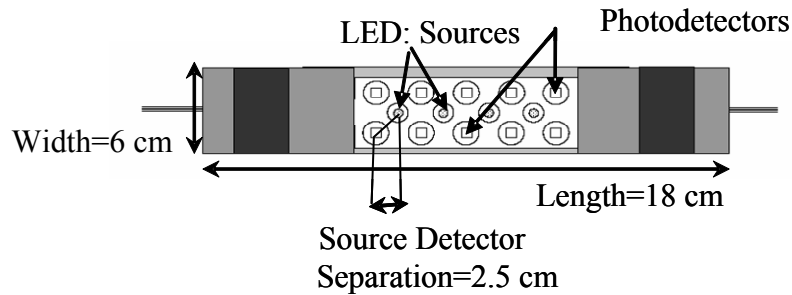


Figure 2.1: Schematic drawing of the LEDI headband showing the placement of light sources and detectors.

The data is analyzed with modified Beer-Lambert's law using optical intensity at the detectors to calculate concentrations of oxygenated and deoxygenated hemoglobin levels with respect to the baseline measurements. Tomographic images are reconstructed using inverse reconstruction as described in detail in Section 2.5.2. The temporal traces are corrected for motion artifacts by examination of all the measured channels for large data aberrations or noise. Such artifacts are filtered out and suppressed during data processing. Further the data is high pass filtered to remove slow drift components and low pass filtered to remove noise caused by physiological components such as heart rate. These components can be separately recorded as auxiliary inputs. The results are then analyzed for temporal and spatial evolution corresponding to the presented stimulus. The data is compared to the type of stimulus

presented and the degree of activation it produces indicated by changes in the hemoglobin levels.

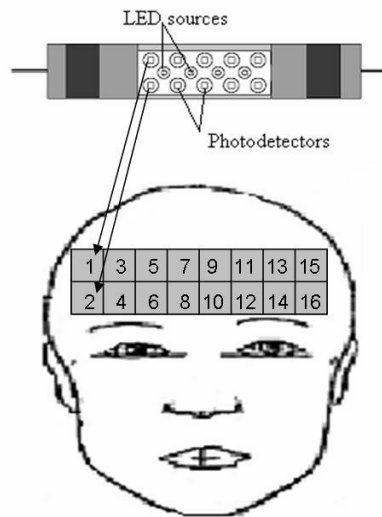


Figure 2.2: Probe layout shows channel placement on the subject's head used for the pilot study. Channel 1 is always placed on the subject's upper right temple. The arrows show the position of channels on subject's head, thus giving a reference of spatial distribution

2.5 Forward and inverse reconstruction algorithms for NIRS

Image reconstruction consists of the forward model and the inverse solution. In the forward model, the area under study is divided into thousands of volume units called voxels. Each voxel is assumed to have predefined absorption and scattering coefficients. Using diffusion theory, the light propagation through the media defining the voxel space is determined. Thus, the forward model defines light propagation through a medium whose properties are known and gives the penetration depth estimation of light in the tissue under examination. In the inverse solution, the voxels are put back together

to produce an image of hemoglobin concentration and oxygen saturation in the area under study based on the data and what is known about light propagation through highly scattering medium. Inverse reconstruction can thus be utilized to determine the concentrations of oxy- and deoxy-hemoglobin in each voxel and helps to calculate unknown hemodynamic properties of the voxel space.

2.5.1 Forward model

In forward computations, the most commonly used theoretical model is diffusion theory [36]. It is a partial differential equation with respect to time and spatial variables that describe photon propagation in tissue, and helps predict measurements at the detectors. Diffusion theory can simulate the transport of photons through tissue [37, 38] but cannot provide accurate analytical solutions for samples that have finite sizes or irregular shapes. Thus, either Finite Difference Method or Finite Element Method (FEM) is utilized in forward model calculations to numerically solve the diffusion equation [39, 40].

The principles given by Hielscher et al. [1] and Pogue et al. have been commonly used to conduct forward calculations. Both temporal and spatial images of the solutions can be calculated using a computational software tool such as Matlab when boundary conditions and input property parameters (i.e., μ_a and μ_s') are entered into the program. Diffusion theory, given in Equation 8, is utilized to calculate the distributions of the photon fluence rate inside tissue.

$$\nabla^2 \Phi + 3\mu_a \mu_s' \Phi = 0 \quad (8)$$

where μ_a and μ_s' are absorption and scattering coefficients in the tissue, respectively, and Φ is photon fluence rate in the tissue. The measure of optical intensity, R , and photon fluence rate are related by $R = |\nabla\Phi|$.

2.5.2 Inverse reconstruction

As summarized by Arridge [36] and Hebden and Hielscher et al. [41], a majority of inverse reconstruction algorithms used for NIR tomographic imaging utilize a perturbation approach that involves inversion of large Jacobian matrixes [39, 40, 42-47]. True and expected spatial distribution of optical properties, $\mu(x, y) = [\mu_a(x, y), \mu_s'(x, y)]$ are assumed to be a small perturbation of an estimated distribution, $\mu_e(x, y)$, where $\mu_a(x, y)$ and $\mu_s'(x, y)$ are two dimensional distributions of the absorption and reduced scattering coefficients, respectively. Measurement values (Φ_c) can be calculated using a forward model with diffusion/transport theory relation (F): $\Phi_c = F[\mu_e(x, y)]$. Maximal or constant fluence values are considered for Φ_m at the boundary (Ω) in time-domain or continuous wave measurements in contrast to frequency-domain measurements where both intensities and phase shifts of photon-density waves are used to calculate Φ_m at locations along the boundary. Based on the assumption that $\mu_e(x, y)$ is a perturbation of $\mu(x, y)$, a Taylor expansion for measured Φ_m is calculated where $\Phi_m = F[\mu(x, y)]$, at $\mu_e(x, y)$

$$\Phi_m = F[\mu(x, y)] = F[\mu_e(x, y)] + \mathbf{J}[\mu_e(x, y)] \Delta\mu(x, y) + \Delta\mu(x, y)^T \mathbf{H}[\mu_e(x, y)] \Delta\mu(x, y) + \dots \quad (9)$$

where F represents the forward model diffusion approximation, $\Delta\mu = \mu(x, y) - \mu_e(x, y)$; $\mathbf{J}[\mu_e(x, y)]$ and $\mathbf{H}[\mu_e(x, y)]$ are the Jacobian and Hessian matrices and are given by the first and second derivatives of F with respect to the optical properties of μ . It follows that the difference between the experimentally measured and predicted values of Φ , i.e., $\Delta\Phi = \Phi_m - \Phi_c$, can be expressed as

$$\Delta\Phi = \mathbf{J}[\mu_e(x, y)] \Delta\mu(x, y) + \Delta\mu(x, y)^T \mathbf{H}[\mu_e(x, y)] \Delta\mu(x, y) + \dots \quad (10)$$

Assuming the second and higher order terms in Equation 10 to be negligible, we obtain $\mu(x, y)$, i.e., $\mu(x, y) = \mu_e(x, y) + \Delta\mu(x, y)$, given below:

$$\mu(x, y) = \mu_e(x, y) + \Delta\mu(x, y) = \mu(x, y) = \mu_e(x, y) + \mathbf{J}[\mu_e(x, y)]^{-1} \Delta\Phi \quad (11)$$

However, the practical approach in solving this inversion problem is an optimization problem because of computational difficulty in the inversion of a large ill-conditioned Jacobian matrix, $\mathbf{J}[\mu_e(x, y)]$. The objective function, Z , is defined as

$$Z[\Delta\mu(x, y)] = \|\Delta\Phi - \mathbf{J}[\mu_e(x, y)] \cdot \Delta\mu(x, y)\| \quad (12)$$

Optimization of Z by iteratively choosing an appropriate set of $\Delta\mu(x, y)$ leads to the final determination of the optical properties of $\mu(x, y)$. Several commonly applied optimization techniques include CGD (Conjugated Gradient Descent), SVG (Singular Value Decomposition) [44, 45], and ART or SART (Simultaneous Algebraic Reconstruction Techniques)[48]. Furthermore, various regularization techniques are often used with the optimization algorithms to make the ill-conditioned Jacobian matrix more diagonally dominant [44]. Thus, optimization techniques along with regularization functions are crucial for inverse reconstruction algorithms in NIR tomographic imaging.

The objective of inverse reconstruction is to find the distribution of properties (i.e. photon fluence rate) to best fit the measured data. This problem can be formulated as a non-linear least square problem as follows: Find the property distribution to minimize $Z = \|\Phi_m - \Phi_c\|$, where Φ_m is the measured data and Φ_c is the model predicted results at measurement points. Constraints are put on the problem to render plausible solutions. The following iterative algorithms can be used to solve the above problem.

1. Given a set of parameter values α (μ_a, μ_s) at a set of specified locations, compute the properties, at each point in the computational grids using the interpolation scheme:

$$\Phi(x, y) = \sum_{i=1}^N \phi_i(x, y) \alpha_i \quad (13)$$

where $\Phi(x, y)$ is the property value at the point (x, y) in the domain and ϕ_i is the i^{th} basis function. If ϕ_i is the Dirac delta function, then each grid point in the computational mesh has independent parameter values. This will lead to an optimization problem with many variables when a fine meshed domain is used to solve the forward problem. The following radial basis function can be used for interpolation [11]

$$\phi_i(x, y) = \left[(x - x_i)^2 + (y - y_i)^2 + h \right]^\beta \quad (14)$$

Note that (x_i, y_i) , $i=1, 2, \dots, N$, are locations for the unknown parameters, h is the shift parameter. When all data are normalized into $[0, 1]$, $h=0.4$, $\beta=0.5$ can be utilized to get good interpolation performance.

2. Solve the forward problem using the distributed parameters obtained in step 1.
3. Evaluate objective function Z and constraint function values, if any.
4. Repeat the above procedures until no further reduction in Z is possible.

Thus, in the inverse solution, the voxels are simply put back together to produce an image of total hemoglobin concentration and oxygen saturation in the area under study.

2.6 Chapter summary

This chapter covers the background theory that underlies the measurements conducted in this dissertation. It starts with the comparison of different imaging modalities used in functional brain imaging and then focuses on the primary imaging modality used in this research namely NIRS. Instrumentation, methods for extraction of parameters and finally forward and inverse reconstruction techniques used in this research are discussed to conclude this chapter.

CHAPTER 3

SINGLE COMPARTMENT WINDKESSEL MODEL

Cerebral hemodynamic response to activation caused by a stimulus input (e.g. finger tapping or verbal fluency task) can be measured by a number of techniques such as NIRS and fMRI. These measurements are composed of the combined effects of oxygen consumption created by metabolic demand and the increased supply of oxygen offered by the dilation of feeding arterioles (reviewed by [49, 50]). During brain activation, increased oxygen demand is met with an overcompensating increase in regional blood flow. This results in a net increase in the oxygen content of the activated brain region [51]. These changes in oxygen content are measured as hemodynamic changes by functional imaging modalities such as fMRI and NIRS.

Blood Oxygenation Level Dependent (BOLD) measurements obtained by fMRI and optical imaging are effective approaches to non-invasively study blood oxygenation changes in tissue. However the interpretation of hemodynamic measurements is complicated by variations in hemoglobin concentrations that depend on incoming blood flow as well as oxygen extraction by tissue [52, 53]. The utility of functional hemodynamic imaging could be improved if it provided a more reliable measure of metabolic function using quantitative models of tissue vasculature [8]. The interpretation of the hemodynamic signal as it relates to neural activity and metabolic demand requires the understanding of the underlying physiological processes that give

rise to measurable changes in hemodynamic response. It is important to understand the mechanisms and processes by which: (i) blood supply increases following activation of the brain by external stimulus, and (ii) how changes in blood flow affect the diffusion of oxygen from the vasculature and hence the changes in concentration of oxygenated, deoxygenated and total hemoglobin in the brain.

3.1 Basic principles of hemodynamic modeling

The purpose of developing hemodynamic models is to quantitatively associate blood flow (CBF) and cerebral metabolic rate of oxygen ($CMRO_2$) with deoxyhemoglobin (Hb), oxyhemoglobin (HbO_2), and total hemoglobin (HbT) measured by NIRS or BOLD signal measured with fMRI techniques. Specifically, in this research a dynamic mathematical model is developed based on the Windkessel model to describe blood oxygenation and transport dynamics to complement previously published flow-volume model. The model is used to characterize the relationship between cerebral blood flow (CBF) and blood volume (which is proportional to HbT) and also to describe the underlying biophysics that dictate blood oxygen saturation and consumption using temporal basis functions.

Since hemodynamic modeling can be applied to blood perfused tissue, a mathematical modeling approach can be taken to study differential brain activation with the assumption that CBF and $CMRO_2$ of the brain are altered during activation by external stimuli. HbO_2 , Hb, and HbT can be related to CBF and $CMRO_2$ directly using mass conservation equations and models of vascular volume changes in response to

pressure changes [54, 55]. This kind of hemodynamic modeling has been applied to NIRS measurements in recent studies that associate the measured dynamic changes of HbO₂ and Hb concentrations to CBF and CMRO₂ of the brain [55].

3.2 Previously published single compartment flow-volume model

A commonly used model to describe the relation between blood flow and oxygen consumption rate of the brain is the Balloon model [2, 3]. The brain can be imagined as a blood filled balloon in a box with incompressible liquid (cerebral spinal fluid) surrounding the tissue [53]. Cerebral blood volume increase is a mechanical consequence of increase in cerebral blood flow. The elastic properties of the vascular bed induce transient mismatches between total hemoglobin concentration (HbT) and cerebral blood flow (CBF) which does not require uncoupling of CBF and CMRO₂ [56]. Typical values for the increase in CMRO₂ are 5-25% and increase in CBF is 20-70%. Oxygen transport is limited and the ratio of coupled relative blood flow and oxygen consumption rate is $\Delta\text{CMRO}_2: \Delta\text{CBF} \sim 1:2$.

3.2.1 Single compartment Windkessel model

The Windkessel formulation [4, 5] can be used to solve the Balloon model. Two algorithms have been published to solve for relative cerebral blood flow: Windkessel model fit described by Boas et al [57] and a power law relation described by Grubb et al [58] given in Equation 15. Equation 15 is a steady state model which was observed in primates by inducing hypercapnia to obtain different increments in $\text{CBF} = F_{\text{in}}$ (blood flow

into the vascular compartment) and $HbT=V_w$ (blood volume in the vascular compartment) and yielded a best fit at $\gamma=0.38$.

$$\frac{V_w(t)}{V_w(0)} = \left(\frac{F_{in}(t)}{F_{in}(0)} \right)^\gamma \quad (15)$$

While this relationship has been used in modeling the hemodynamic response to activation, it was originally measured for global variation in CBF and HbT and has not been validated for transient phenomena or localized changes in hemodynamics. The Windkessel model based on the original Balloon model uses a mechanical model to relate blood flow and blood volume and better models transient responses of the system induced by activation during temporal responses.

3.2.2 Assumptions for the Windkessel model

A constant hematocrit of 1 is assumed in the model. Baseline concentration of total hemoglobin (HbT_{base}) is assumed to be 100 μ M. The baseline concentrations of deoxyhemoglobin (Hb) and oxyhemoglobin (HbO_2) are related to the baseline blood volume and the oxygen saturation (SO_2) of the blood in the region of interest (~ about 65% for the combined venous and capillary compartment represented by the Windkessel chamber).

$$Hb_{base} = HbT_{base} (1 - SO_2) \quad (16)$$

$$HbO_{2,base} = HbT_{base} \cdot SO_2 \quad (17)$$

These baseline parameters are used to calculate normalized hemodynamic parameters that are used in the Windkessel model for the calculation of flow and $CMRO_2$.

$$HbO_{2,norm} = \frac{HbO_{2,meas}}{HbO_{2,base}} \quad (18)$$

$$Hb_{norm} = \frac{Hb_{meas}}{Hb_{base}} \quad (19)$$

$$HbT_{norm} = \frac{HbT_{meas}}{HbT_{base}} \quad (20)$$

$$CBF_{norm} = \frac{CBF_{meas}}{CBF_{base}} \quad (21)$$

Baseline oxygen extraction (E_0) on the venous side is calculated using Equation 22.

$$E_o = 1 - \frac{HbO_{2,base}}{SaO_2 \cdot HbT_{base}} \quad (22)$$

The temporal evolution of oxygen extraction factor is related to the dynamics of blood flow (CBF_{norm}) and is given by

$$E = 1 - (1 - E_0)^{1/CBF_{norm}} \quad (23)$$

The Balloon model was developed for fMRI measurements which are heavily venous weighted. The measured NIRS signal is a mixed compartment signal; therefore the data needs to be converted to a venous contribution signal using a correction factor. Assuming the hemoglobin oxygen saturation on the arterial side is one ($SaO_2=1$), the correction factor related to the dynamic oxygen extraction factor is applied to the concentration of oxy- and deoxyhemoglobin as it travels from the arteriole through the capillary to the venous side. The concentrations of deoxyhemoglobin and oxyhemoglobin as follows:

$$HbO_{2,ven} = HbT \cdot SaO_2 \cdot (1 - E) \quad (24)$$

$$Hb_{base} = HbT - HbO_{2,ven} \quad (25)$$

The venous weighted data can be applied to the Windkessel model to solve for the flow-volume relationship as described in Section 3.2.3.

3.2.3 Solving for the flow-volume relationship

The single compartment Windkessel model consists of a feeding arteriole and a compliant vascular chamber. This vascular model can be represented by an analogous lumped parameter circuit consisting of two resistances and a single capacitance [56]. The model is simple and has been extensively used to describe hemodynamics of the neurovascular system [57]. This electrical analog neglects blood volume in the arteriole compartment and models the resistance (R) and compliance (C) of the Windkessel compartment [59].

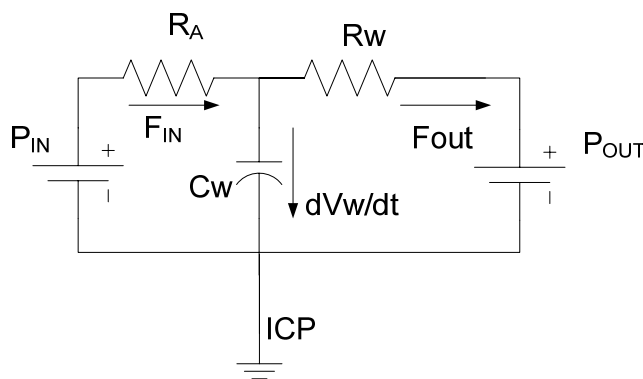


Figure 3.1: Single compartment Windkessel model

The Windkessel model that relates the blood flow and blood volume changes during activation is a mechanical model based on the principle of conservation of mass

to relate changes in CBF and HbT. The model is given by the following equations that describe the physical relationships between blood flow and blood volume [59].

(1) Relation between cerebral blood flow (F), pressure (P) and vascular resistance (R):

$$P(t) = F(t) \cdot R(t) \text{ (Analogous to Ohm's law)} \quad (26)$$

(2) Relation between Windkessel volume (V_w) and pressure (P_w):

$$V_w(t) = AP_w(t)^{1/\beta} \quad (27)$$

(3) Resistance in the Windkessel compartment (R_w) is related to the volume by

$$\frac{R_w(t)}{R_w(0)} = \left(\frac{V_w(0)}{V_w(t)} \right)^\alpha \quad (28)$$

These equations provide a physical model of the vascular response to pressure and resistance changes [59]. From these equations, the Windkessel model can be solved to give coupled differential equations for flow and volume changes resulting from arterial resistance changes [57, 59]

$$\frac{\partial V_w}{\partial t} = F_{in} - F_{out} = F_{in}(t) - \frac{P_w(t)}{R_w(t)} = F_{in}(t) - \frac{V_w(t)^{\alpha+\beta}}{A^\beta R_w(0)V(0)^\alpha} \quad (29)$$

$$F_{in}(t) = P - P_w(t) \quad (30)$$

$$F_{in}(t) = \frac{P - P_w(t)}{R_A(t)} = \frac{P - V_w(t)^\beta / A^\beta}{R_A(t)} \quad (31)$$

$$\frac{\partial V_w}{\partial t} = \frac{P - V_w(t)^\beta / A^\beta}{R_A(t)} - \frac{V_w(t)^{\alpha+\beta}}{A^\beta R_w(0)V(0)^\alpha} \quad (32)$$

A Gaussian temporal basis function is used for the temporal response of arterial resistance during activation described in Equation 33.

$$\mathbf{R}_A(t) = \mathbf{R}_A(0) - (\mathbf{R}_A(0) - \mathbf{R}_{A,\min}) \exp\left(\frac{(t - T_{peak})^2}{\sigma_R^2}\right) \quad (33)$$

The dynamic Windkessel model calculates the blood flow by numerically solving the ordinary differential equation (Equation 32) containing the following parameters: Windkessel vascular reserve (β), Windkessel (vascular) transit time (τ), initial arterial resistance (R_{a0}), minimum arterial resistance ($R_{A,\min}$), time to maximum resistance change (T_{peak}), width of temporal resistance change (σ_R). These parameters are then adjusted and fit to the experimental blood volume and used to predict the values for blood flow [57].

The model is normalized to the range of [0, 1]. Initial conditions are normalized to unity. Initial flow into and out of the tissue is given by $F_{in}(0) = F_{out}(0) = 1$. Since volume is a mechanical consequence of flow, the initial volume can be related to flow by using the mean transit time through the vascular compartment as follows $V_w(0) = F_{in}(0) \cdot \tau$. Initial arterial and Windkessel resistance are normalized as follows: $R_A(0) + R_w(0) = 1$ [57].

Table 3.1 gives a list of the variables used in the flow-volume Windkessel model. The parameters listed are either estimated in the model fits or assumed at unit normalized values through the model. The resistance, capacitance, flow and pressure parameters define the physiological properties of the vascular chamber while the Windkessel parameters define structural parameters of the system. Windkessel vascular reserve parameter (β) relates to the compliance of the vascular compartment and mean

transit time (τ) defines the average time it takes for a bolus to travel through the compartment.

Table 3.1: Variables used in vascular model

Variable Category	Symbol	Description	Value
Resistance	$R_a(t)$	Resistance of the feeding arteriole	Modeled – Dynamic
	$R_w(t)$	Resistance of the Windkessel compartment	Modeled – Dynamic
Capacitance	$C_w(t)$	Capacitance of the Windkessel compartment	Modeled – Dynamic
Flow	$F_{in}(t)$	Flow into system	Modeled – Dynamic
	$F_{out}(t)$	Flow out of system	
Pressure	$P_a(t)$	Pressure of the Windkessel compartment	Modeled – Dynamic
	$P_{in}=MABP$	Mean arterial blood pressure	1 a.u.
	$P_{out}=MVBP$	Mean venous blood pressure	0 a.u.
	ICP	Intracranial Pressure	0 a.u.
Windkessel model	β	Windkessel vascular reserve	Modeled – Static (Structural)
	τ	Windkessel transit time	Modeled – Static (Structural)

3.2.4 Calculation of oxygen consumption ($CMRO_2$)

The cerebral metabolic rate of oxygen is used to describe temporal oxygen dynamics and is defined as the difference between the quantity of oxygen flowing into and out of a region. Oxygen consumption can be calculated by using the measured hemodynamic variables and estimate of flow calculated by the Windkessel or Grubb model using the ratio method as shown in Equation 34. The subscript ‘o’ indicates the

baseline conditions, and $[Hb]_v$ and $[HbT]_v$ indicate deoxyhemoglobin and total hemoglobin concentrations in the localized venous compartment, respectively. The ratio of dynamic $\Delta CMRO_2 / CMRO_{2,0}$ can be calculated [60] using the optimized parameters and the Windkessel model predicted flow $\Delta CBF / CBF_0$ using Equation 35.

$$\left(1 + \frac{\Delta CMRO_2}{CMRO_{2,0}}\right) = \left\{ \left(1 + \frac{\Delta CBF}{CBF_o}\right) \left(1 + \frac{\Delta [HbR]_v}{[HbR]_{v,o}}\right) \left(1 + \frac{\Delta [HbT]_v}{[HbT]_{v,o}}\right)^{-1} \dots \right. \quad (34)$$

$$\left. \dots - \frac{\tau}{F_{in}} \left(\frac{d[HbR]_v}{dt} - \frac{[HbR]_v}{[HbT]_v} \frac{d[HbT]_v}{dt} \right) \right\}$$

Steady state $CMRO_2$ was also calculated using Equation 35 for comparison [57].

$$\left(1 + \frac{\Delta CMRO_2}{CMRO_{2,0}}\right) = \left(1 + \frac{\Delta CBF}{CBF_o}\right) \left(1 + \frac{\Delta [HbR]_v}{[HbR]_{v,o}}\right) \left(1 + \frac{\Delta [HbT]_v}{[HbT]_{v,o}}\right)^{-1} \quad (35)$$

3.2.5 Example results with fitting measured NIRS volume

The data shown in the example results shown in Figure 3.2 is a region-of-interest average for 5 subjects during a 2-second finger tapping task. Details of the protocol and results are provided in Chapter 5. The values for the arterial resistance $R_a(0)$, $R_{a,min}$, T_{peak} and σ_R^2 in addition to the Windkessel volume reserve, β and the vascular transit time, τ , using the multi-compartment Windkessel model are estimated. The model parameters are optimized using a nonlinear χ^2 fit to fit the experimentally measured $\Delta[HbT]$. All the fitting parameters were allowed to vary about typical values obtained from literature. However the vascular reserve parameter, β was set at 1.6 to maintain the

steady state flow-volume exponent $(\alpha+\beta)^{-1}$ within the range of published values of 0.18 to 0.36, where $\alpha=2$ indicates laminar flow within the vessel. The vascular transit time, τ , was allowed to vary as high as 5 seconds in accordance with the observed experimental values (4-5 seconds) from bolus studies.

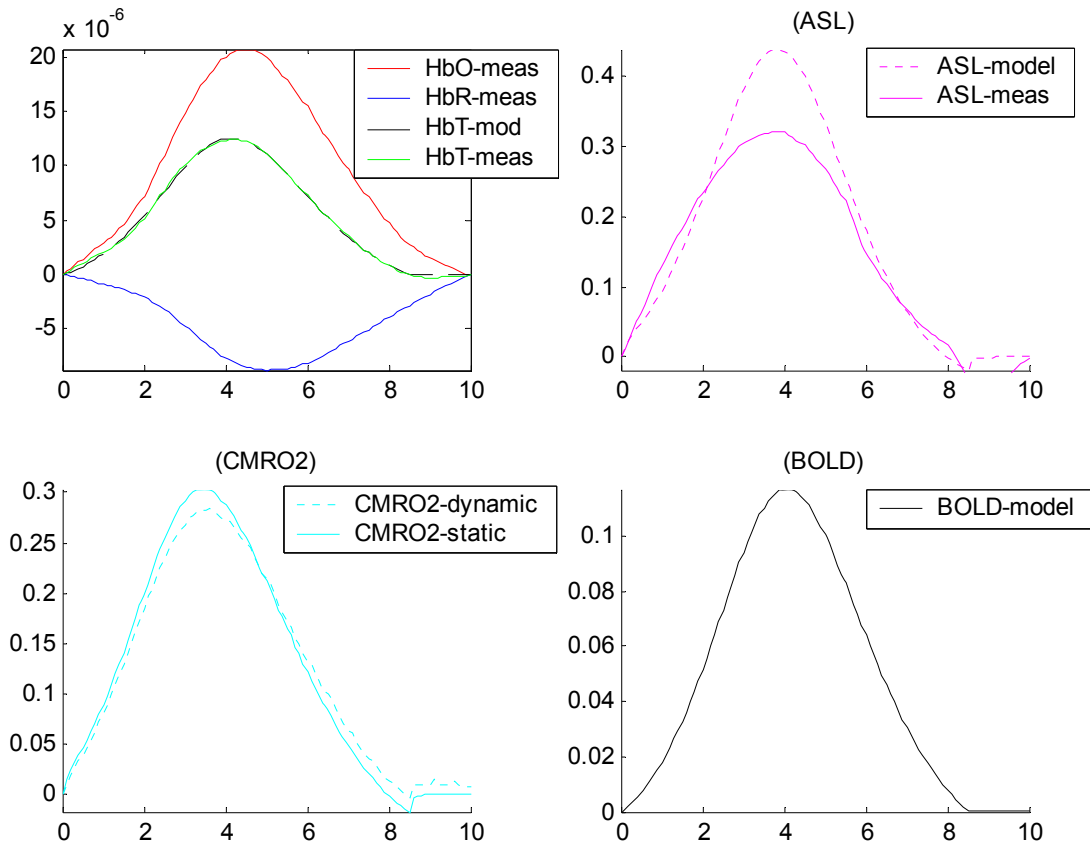


Figure 3.2: Results of the single compartment Windkessel model (HbT fit only)

Figure 3.2 shows temporal plots of cerebral oxygen consumption rate (CMRO₂) and blood flow (BF) labeled in the figure as arterial spin labeling (ASL) data. This fMRI method can be used to measure cerebral blood flow. The data for changes in

deoxyhemoglobin ($\Delta[\text{Hb}]$) and changes in blood volume ($\Delta[\text{HbT}]$) obtained from NIRS were used to predict the BOLD signal ($\Delta\text{BOLD}/\text{BOLD}_0$) using Equation 36 [61].

$$\frac{\Delta\text{BOLD}}{\text{BOLD}_0} = V_0 \left[k_1 \left(1 - \frac{\Delta\text{Hb}}{\text{Hb}_0} \right) + k_2 \left(1 - \frac{\Delta\text{Hb}}{\text{Hb}_0} \cdot \frac{\Delta\text{HbT}}{\text{HbT}_0} \right) + k_3 \left(1 - \frac{\Delta\text{HbT}}{\text{HbT}_0} \right) \right] \quad (36)$$

where $k_1 \approx 7E_0$, $k_2 \approx 2$ and $k_3 \approx 2E_0 - 0.2$ and E_0 is the resting/baseline oxygen extraction fraction for a field strength of 1.5T. These constants that depend on the fMRI user acquisition parameters, such as echo-time, field strength, and imaging echo type and also on features of the subject anatomy such as vascular architecture and the orientation between blood vessels and the imaging fields. Here the BOLD signal is predicted for a 1.5T strength field fMRI measurement.

3.3 Contribution of the current research to the Windkessel model

The published Windkessel model was developed for a short duration stimuli as described in the previous section. Motivation behind the contributions made to the single compartment Windkessel model in this research are described below. This research was carried out with the Photon Migration Institute (MGH) with Dr. D. Boas and T. J. Huppert.

3.3.1 Inclusion of multimodality data

A novel pseudo-Bayesian framework is set up to include multimodality data (NIRS-HbT and ASL-CBF) for a more accurate and unique solution to the flow-volume model parameters based on vessel compliance [62]. This framework can be extended to

also accurately define oxygen transport parameters as described in Section 3.6. In practice, defining a compliance coefficient precisely based on multimodality data is important in studies that explore weakening vessels. The detection of reduced flow-volume ratio could be used in the diagnosis and treatment of conditions such as precursors to aneurysms [63]. In the clinical setting, flow-volume relationship increments from control ratios, could aid in diagnosis of hardening of arteries (atherosclerosis) which lead to conditions such as stroke or monitor the normal aging process [62].

3.3.2 Modeling of long duration data

Convolution of the arterial resistance temporal basis function with the stimulus input function helps to describe arterial resistance changes for long duration stimuli. This allows the application of the Windkessel model to longer duration cognitive studies[15] as were carried out in this research. The previously published Windkessel model was developed for a short duration stimuli as described in Section 3.1. The versatility of the flow-volume mechanical model set-up can be improved by modifying the arterial dilation basis function of the Windkessel model to describe the temporal hemodynamics involved in longer duration stimuli such as verbal fluency tasks, and MMSE (mini mental state examination) that have been used in psychological experiments to diagnose and monitor disease and its progression.

3.3.3 Development of oxygen consumption model

This research adds to existing deductive models by introducing two novel inductive models that include oxygen consumption dynamics. The models are used in conjunction with the existing inductive single compartment Windkessel model that relates the temporal variations of blood flow and blood volume in the brain ($CBF=f(HbT)$). To accurately model these oxygenation changes, two different models are proposed:

(a) Oxygen extraction model: $[Hb, HbO_2] = f(OE)$

(a) Mitochondrial activity $CMRO_2$ model: $[Hb, HbO_2] = f(CMRO_2)$

These models are used to fit NIRS $[Hb]$ and $[HbO_2]$ data in the multimodality fusion framework as described in Section 3.4. This provides a method to describe oxygen transport mechanisms from vascular compartments (vessels) to surrounding parenchymal (extravascular) tissue.

The advantage of defining oxygen transport dynamics inductively is that it helps to determine hidden state variables that define the underlying biophysics of the oxygen extraction process which are not revealed by the cumulative measurements of hemodynamic changes during activation. Such variables are not revealed by deductive modeling which models the effects of the biophysical phenomena rather than provide mathematical descriptions for them. Hence, inductive modeling of oxygen extraction can provide insights into the physiology that cannot be directly measured with the described noninvasive imaging modalities.

Mechanisms that define oxygen transport can help determine (i) the underlying phenomena that result in hemodynamic changes that create functional imaging contrast and define the physiology that helps to translate external/presented stimulus into brain activation and (ii) the metabolic changes observed in the brain under conditions like Alzheimer's disease [33, 64, 65], depression [65], schizophrenia [66] and stroke[67]. Past research efforts have used noninvasive imaging for the diagnosis and treatment monitoring of such conditions. The presented model that defines oxygen transport mechanisms can be used in conjunction with noninvasive imaging to further the understanding of the pathology behind these diseases and eventually help to explore new directions in the early detection as well as treatment alternatives if the effect of these conditions on the physiology is quantified.

This research was carried out with the Photon Migration Institute (MGH) with Dr. D. Boas and T. J. Huppert.

3.4 Combination of multimodality data

Multimodality fusion of simultaneously measured NIRS and fMRI data is novel to the single compartment Windkessel model and is incorporated using an integrated cost minimization routine that accounts for measurement errors of both modalities. Combining imaging modalities can help solve the flow-volume relation uniquely, which is the confounding factor in the calculation of $CMRO_2$ using single modality imaging. This helps to provide a unique solution to define precisely the vascular parameter that describes the compliance of the Windkessel chamber. This set-up can easily be

extended to include oxygen transport dynamics as well as neuronal activation data to further define unknown biophysical parameters.

This research was carried out with the Photon Migration Institute (MGH) with Dr. D. Boas and T. J. Huppert.

3.4.1 Model parameters and initial conditions

The proposed model is based on a bottom-up approach to state estimation. A state vector of unknowns (X) is passed through a set of differential equations describing the vascular and components of the hemodynamic response (refer Figure 3.3). These outputs predict changes in blood flow and volume in the vascular compartment. These predictions are inputs into observation models, which describe measurement process for each measurement modality and are based on the biophysical principles governing each method. Multiple observation models create predictions of multimodality data, which are minimized to the experimental data using a pseudo-Bayesian fusion model, in the form of a weighted least-squares cost function. This advancement in methodology allows fusing of multimodality information from differing measurement sources to directly infer the common physiological states which manifest as functional contrast in each imaging modality.

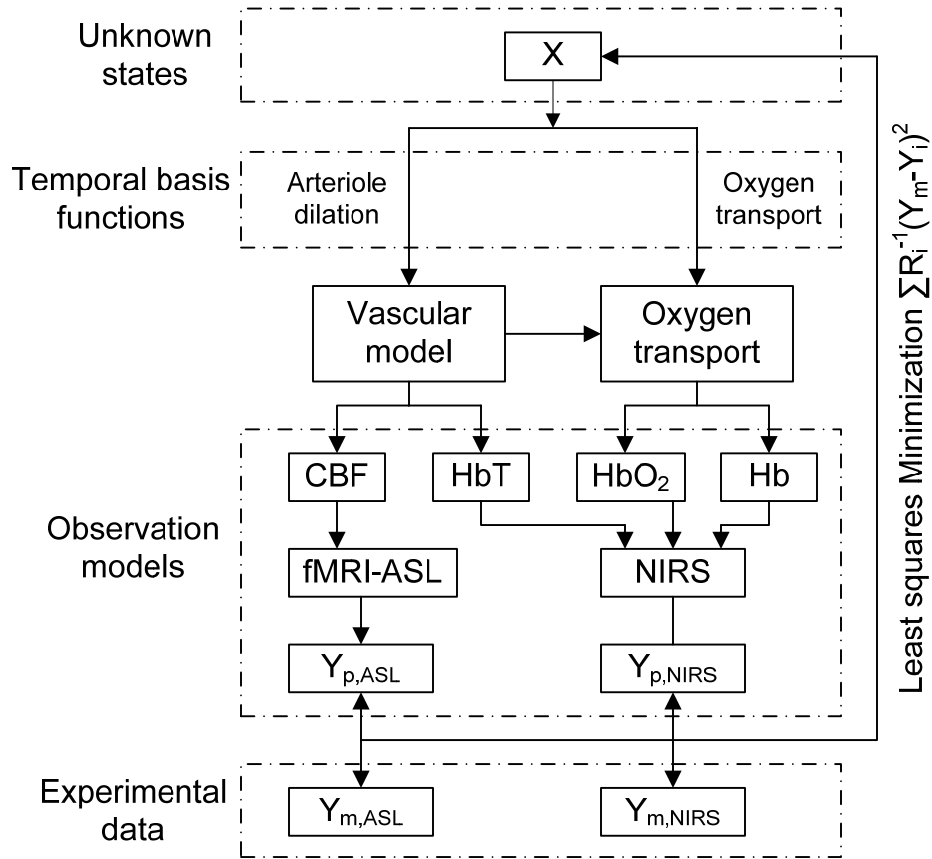


Figure 3.3: Framework for including multimodality data [68]

In order to estimate the states describing the arteriole dilation function, a non-linear, Levenberg-Marquardt algorithm was used and implemented in Matlab [69]. A differential time step of 2 ms was employed for the update of the vascular and oxygen transport models. Smaller time steps were also tested to verify that the time-step did not affect the results. To integrate the multimodality measurements, a weighted least-squares cost function was utilized, with the weights given by the inverse of the measurement variances for each modality. These weights are estimated from the variance in the estimate of the hemodynamic responses across the subjects.

In the previous section, the vascular volume reserve (β) was defined to be ~ 1.6 as given in previously published literature values; however a large range of values can be used for β to achieve a model fit of the blood volume alone. Thus results include a wide range of values for the magnitude of flow, which directly depends on the initial guess for the vascular volume reserve parameter (β). To better constrain β , we simultaneously perform a χ^2 nonlinear fit to changes measured in cerebral blood flow (ΔCBF) along with the changes measured in cerebral blood volume (ΔHbT). Flow and volume data predicted from the Windkessel model (Equations 29-32) are used in a nonlinear fit to measured data. The physiological range of values for each of the parameters was used to impose a constraint on the upper and lower range of fitting values. The fitting routine was iterated until a defined convergence criterion was met (10^{-6} times the variance of the measurement error). It was also verified that the final estimate was independent of the choice of the initial guess for each state and the same initial guess.

3.4.2 Results with fitting measured NIRS volume and ASL flow

Oxyhemoglobin (HbO_2) and deoxyhemoglobin (Hb) changes in the adult human brain were measured using simultaneous near-infrared spectroscopy (NIRS) and ASL (arterial spin labeling)-based fMRI during motor activation using a finger-tapping paradigm. The data used in the volume fit alone is used again in this section. Details of the protocol and results are provided in [60].

The total flow into the model (F_{in}) was fit to experimentally measured blood flow and blood volume respectively. As expected, the estimated values for the arterial

resistance $R_a(0)$, $R_{a,min}$, T_{peak} and σ_R^2 did not vary much from those predicted using the volume fit alone. However a consistent value of Windkessel volume reserve, β (~ 1.5) and vascular transit time, τ (~ 4 seconds), is obtained using the simultaneous fits of flow and volume which is independent of the initial guess of the values. Plots of the volumes and flow in the Windkessel compartment are shown in Figure 3.4. The steady state and dynamic $\Delta CMRO_2/ CMRO_{2,0}$ and flow ($\Delta CBF/ CBF_0$) were also calculated with the optimized parameters and plotted for completeness.

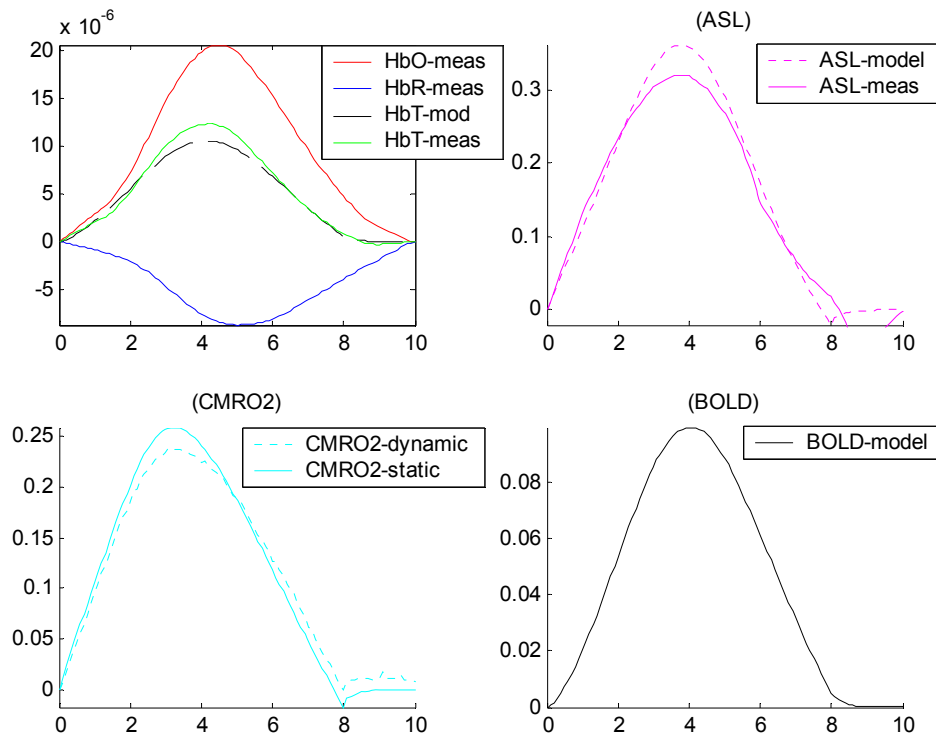


Figure 3.4: Results of the single compartment Windkessel model (HbT and CBF fit)
Duration of task=2 seconds

3.5 Modeling for long duration stimuli

The arterial resistance model which was described by a temporal Gaussian function was convolved with a neural input function (stimulus) to describe the relationship between flow and volume in longer stimuli (>2 seconds).

$$\mathbf{R}_A(t) = \left\{ \mathbf{R}_A(0) - (\mathbf{R}_A(0) - \mathbf{R}_{A,\min}) \exp\left(\frac{(t - \mathbf{T}_{peak})^2}{\sigma_R^2}\right) \right\} \otimes \mathbf{N}(t) \quad (37)$$

Based on the theory used in describing similar responses in deductive modeling [49], a simple inhibitory feedback system is used, in which the neural response $N(t)$ is treated as the difference between an excitatory input $s(t)$ and an inhibitory input $I(t)$. The stimulus input $s(t) = 1$ when $0 \leq t \leq t_0$ where $0 \leq t \leq t_0$ is the duration of the stimulus and the function $u(t) = 0$ otherwise. The inhibitory response is driven by the neural response with a gain factor of κ and a time constant of τ_1 .

$$\mathbf{N}(t) = \mathbf{s}(t) - \mathbf{I}(t) \quad (38)$$

$$\frac{d\mathbf{I}}{dt} = \frac{\kappa\mathbf{N}(t) - \mathbf{I}(t)}{\tau_1} \quad (39)$$

Such convolution has also been previously described to relate the neural activity to the measured hemodynamic signal [70, 71] where κ represents the efficacy with which the neural response determines changes in the blood flow.

3.5.1 Results with fitting measured NIRS volume

The data shown in Figure 3.5 are example results using region-of-interest average measurements for 5 subjects during a 20-second finger-walking task. Only NIRS measurements were available for the task and flow and BOLD signal are predicted from these measurements. Plots of the volumes and flow in the Windkessel compartment are shown in Figure 3.5. The ratio of steady state and dynamic $\Delta\text{CMRO}_2/\text{CMRO}_{2,0}$ and flow ($\Delta\text{CBF}/\text{CBF}_0$) were also calculated with the optimized parameters and plotted for completeness.

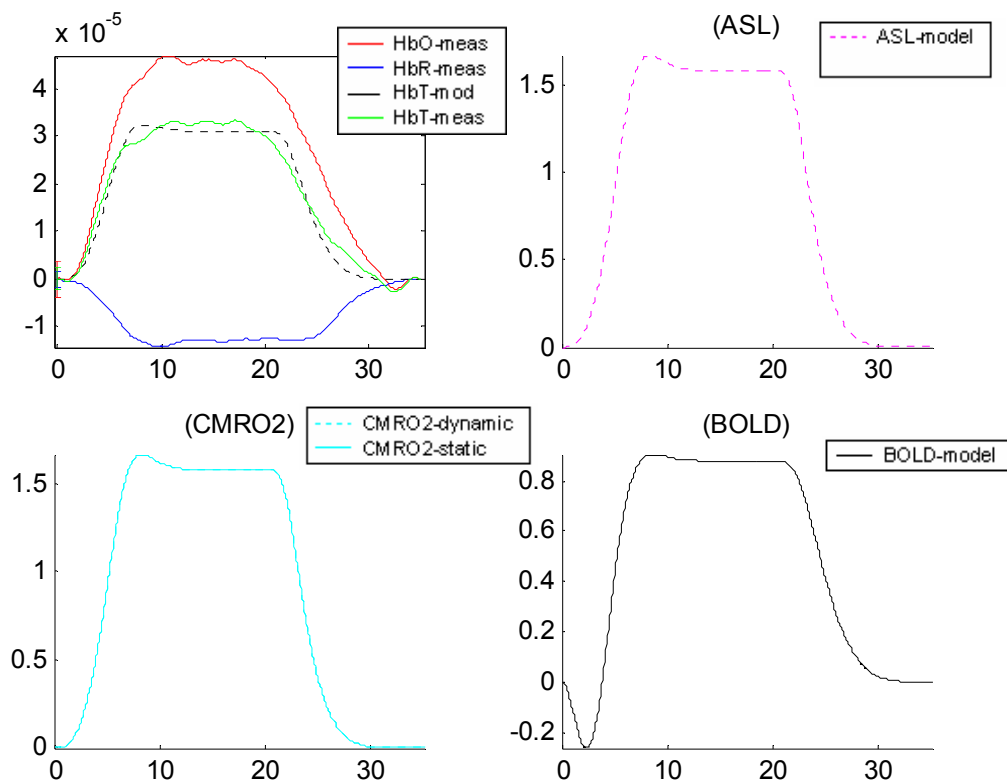


Figure 3.5: Results of the single compartment Windkessel model (HbT only). Duration of task=20 seconds

3.6 Oxygen consumption models

In the previous sections, calculations of the dynamic and steady state cerebral metabolic rate of oxygen consumption (CMRO₂) were performed using Equations 34 and 35. The values of deoxyhemoglobin $\Delta[\text{Hb}]$ used for the CMRO₂ calculation were the experimentally measured. Previously published deductive models have described oxygen consumption dynamics to calculate the total deoxyhemoglobin in the tissue element [49, 72]. The entry rate of oxygen into the venous compartment is $F_{in} * E * C_a$, where E is the net oxygen extraction from the blood as it passes through the capillary bed. The clearance rate of deoxyhemoglobin from the tissue is $F_{out} * C_v$ (average venous concentration = Hb/HbT). After normalization these phenomena can be used to define the temporal changes in deoxyhemoglobin as follows:

$$\frac{d[\text{Hb}]}{dt} = \frac{1}{\tau_0} \left(F_{in} \frac{E}{E_0} - F_{out} \frac{\text{Hb}}{\text{HbT}} \right) \quad (40)$$

where τ_0 is the mean transit time through the venous compartment and E can be empirically defined as $E = 1 - (1 - E_0)^{1/F}$ to approximate a wide range of transport conditions [49, 72].

Two novel inductive models are developed to include descriptions of oxygen consumption dynamics. This alternative approach of inductive modeling had several advantages over deductive modeling as described in Section 3.3.3. These models are used to fit NIRS data of ($[\text{Hb}]$ and $[\text{HbO}_2]$) and fMRI data (CBF measured using ASL) in the multimodality fusion framework (as detailed in Section 3.4) to describe oxygen

transport mechanisms from vascular compartments (vessels) to surrounding parenchymal (extravascular) tissue in conjunction with flow-volume relationships.

3.6.1 Oxygen extraction temporal function

In this model, it is assumed that the changes in oxygen extraction (OE) occur in the Windkessel compartment, and that these changes are negligible in the feeding arteriole. A Gaussian function is assumed to approximate changes in the oxygen consumption in the Windkessel compartment (refer Equation 41). This function is similar to the arterial dilation basis function. A Gaussian function is chosen for both the OE changes (Equation 41) and arterial dilation changes because both these changes are brought forth by cerebral activation. Increased oxygen demand in the brain and arterial dilation are results of the same neural response, thus similar temporal basis functions are assumed for modeling both the vascular as well as metabolic functions.

$$OE(t) = OE_{\max}(0) - (OE_{\max} - OE(0)) \exp\left(-\frac{(t - T_{peak})^2}{\sigma_c^2}\right) \quad (41)$$

$OE(0)$ represents the baseline OE and OE_{\max} represents the maximum change of OE from its baseline value in the Windkessel compartment. The baseline OE in the Windkessel compartment is calculated as a function of the flow into the compartment (F), oxygen saturation of the blood coming into the compartment ($SO_{2,in}$) and oxygen saturation of the blood going out of the compartment ($SO_{2,out}$). At baseline oxygen extraction is described by,

$$OE(0) = \frac{1}{2}(F_{in}(0) + F_{out}(0))(SO_{2,in}(0) - SO_{2,w}(0)) \quad (42)$$

Changes in OE in the feeding arteriole are assumed to be negligible during activation and thus OE is kept constant at the baseline value (Equation 42) in the feeding arteriole over the entire time period of the experiment. The temporal changes in oxygen saturation of the Windkessel compartment are described by the following differential equation (Equation 43).

$$V_w \left(\frac{d(SO_{2,in})}{dt} - \frac{d(SO_{2,w})}{dt} \right) = \frac{1}{2}(F_{in} + F_{out})(SO_{2,in} - SO_{2,w}) - OE \quad (43)$$

where OE represents the oxygen extraction in the vascular compartment and is related to the CMRO₂ in the compartment, V_w represents the blood volume in the Windkessel compartment and SO_{2,in} and SO_{2,w} represents the oxygen saturation of the blood entering and leaving the vascular compartment respectively.

$$V_w \left(\frac{d(SO_{2,in})}{dt} - \frac{d(SO_{2,w})}{dt} \right) = \left\{ \begin{array}{l} \frac{1}{2}(F_{in} + F_{out}) \left(SO_{2,in}(t-1) + \frac{d(SO_{2,in})}{dt} \cdot dt \right. \\ \left. - SO_{2,w} - \frac{d(SO_{2,w})}{dt} \cdot dt \right) - OE \end{array} \right. \quad (44)$$

$$\frac{d(SO_{2,w})}{dt} \left[\frac{1}{2}(F_{in} + F_{out}) - V_w \right] = \left\{ \begin{array}{l} SO_{2,in}(t-1) \left[\frac{1}{2}(F_{in} + F_{out}) \right] \dots \\ + \frac{d(SO_{2,in})}{dt} \cdot dt \cdot \left[\frac{1}{2}(F_{in} + F_{out}) - V_w \right] \dots \\ - SO_{2,w} \left[\frac{1}{2}(F_{in} + F_{out}) \right] - OE \end{array} \right. \quad (45)$$

We can thus obtain the oxygen saturation at the present time instant by adding the update as follows

$$SO_{2,w}(t) = SO_{2,w}(t-1) + \frac{d(SO_{2,w}(t))}{dt} \cdot dt \quad (46)$$

The changes in concentrations of oxyhemoglobin and deoxyhemoglobin were calculated next,

$$\Delta[HbO_2] = HbT \cdot SO_{2,w} \quad (47)$$

$$\Delta[Hb] = HbT \cdot (1 - SO_{2,w}) \quad (48)$$

where $SO_{2,w}$ is the oxygen saturation and HbT is the blood volume in the Windkessel compartment.

3.6.1.1 Results with fitting measured multimodality data (short duration)

A χ^2 nonlinear fit of flow, volume as well as the changes in the concentration of deoxyhemoglobin and oxyhemoglobin to the experimentally measured values of $\Delta[HbO_2]$ and $\Delta[Hb]$ was performed. This helped predict parameters that were previously fixed while fitting only flow and volume experimental values. In this section, we fit for the baseline oxygen saturation and volume fraction in every compartment and $OE(0)$, OE_{min} , T_{peak} and σ_c^2 to define the oxygen consumption in the Windkessel compartment in addition to the flow and volume parameters defined in the previous sections. The predicted OE function was compared to the $CMRO_2$ function calculated from the empirical formulae given by (Equations 34 and 35) using predicted values of $\Delta[HbO_2]$, $\Delta[Hb]$, $\Delta[HbT]$ and ΔCBF using the proposed oxygen extraction model. The data shown in the example results is a region-of-interest average for 5 subjects during a 2-second finger tapping task. This data is the same as that presented in previous sections

and is used again here to explore the development of the model and facilitate easy comparison to results calculated with other models.

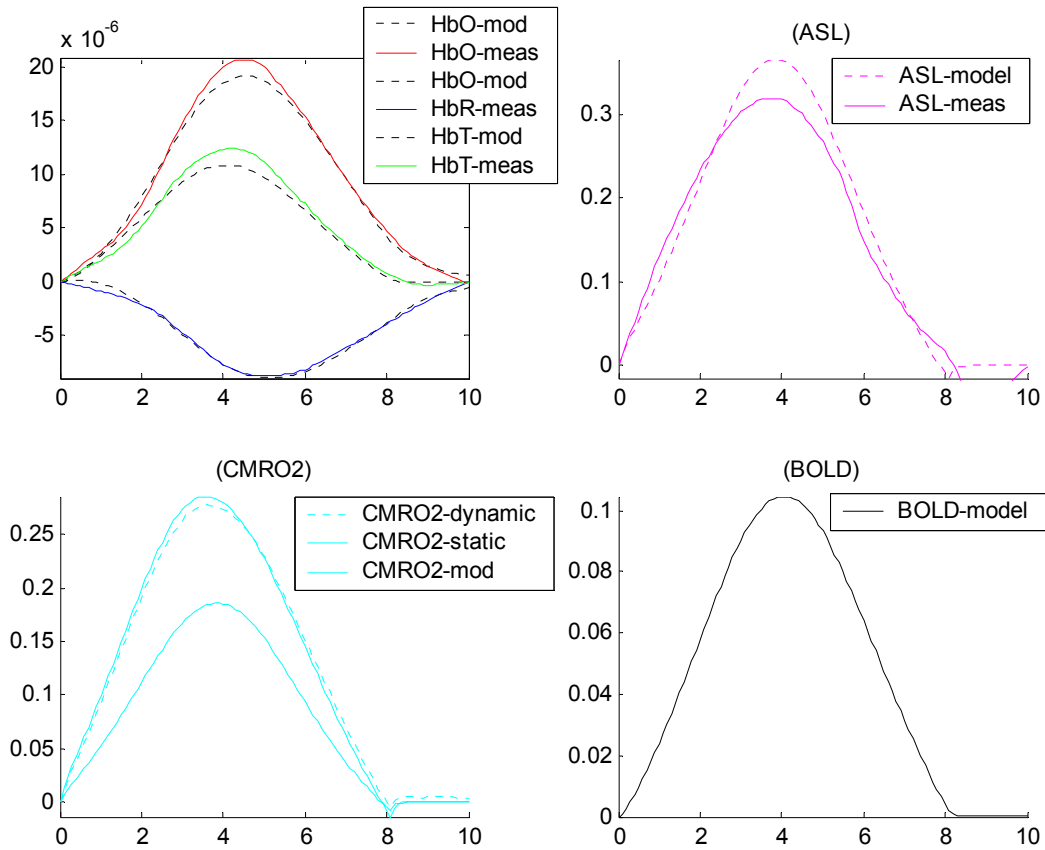


Figure 3.6: Results of the single compartment Windkessel model (All NIRS measurements and CBF fit). Duration of task=2 seconds

3.6.1.2 Results with fitting measured multimodality data (long duration)

Similar to the flow-volume model set-up described in Equation 37, the oxygen extraction basis function was also modified to describe the temporal hemodynamics

involved in longer duration stimuli. Both the arterial resistance and oxygen extraction functions model were convolved with the input stimulus (Equation 37 and 49).

$$OE(t) = OE_{\max} + (OE_{\max} - OE(0)) \exp\left(\frac{(t - T_{peak})^2}{\sigma_c^2}\right) \otimes N(t) \quad (49)$$

where $N(t)$ represents the neural activity (Equations 38 and 39). Plots of the volume and flow in the Windkessel compartment are shown in Figure 3.7. The ratio of dynamic $\Delta CMRO_2 / CMRO_{2,o}$ and flow ($\Delta CBF / CBF_o$) were calculated with the optimized parameters. Steady $\Delta CMRO_2 / CMRO_{2,o}$ was plotted for comparison. The data is a region-of-interest average for 5 subjects during a 20-second finger-walking task. Only NIRS measurements were available for the task and the flow and BOLD signal are predicted and plotted for completeness.

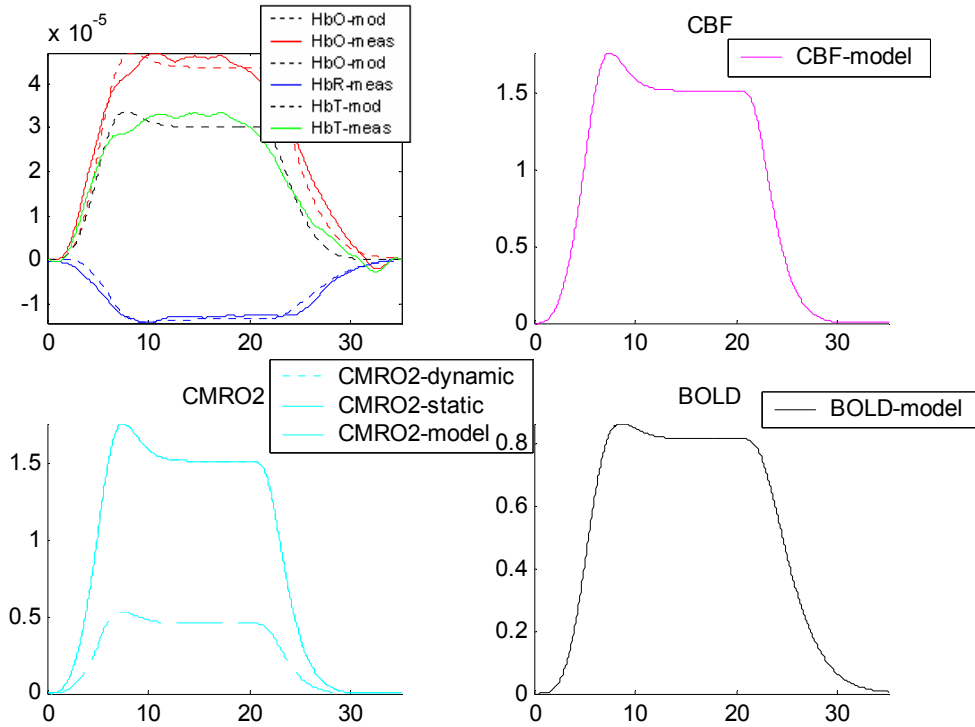


Figure 3.7: Results of the single compartment Windkessel model (All NIRS measurements and CBF fit). Duration of task=20 seconds

3.6.2 Mitochondrial metabolism model

This model is based on the recent finding that increased neuronal activity results in a localized increase in the mitochondrial function and thus changes in oxygen extraction results from this underlying mitochondrial function which gives rise to varying degrees of oxygen extraction in the vascular compartment [50]. The system is based on the principle that oxygen diffusion is caused by the gradient of partial pressure of oxygen. The oxygen content is the amount of oxygen carried within the blood and is the sum of the oxygen bound to hemoglobin and oxygen dissolved in the blood plasma [73].

$$c_n O_2(t) = \alpha_n \cdot p_n O_2(t) + H_n \cdot HGB \cdot S_n O_2 \quad (50)$$

The Hüfner number (H_n) is the amount of oxygen bound per gram of hemoglobin ($H_n=1.39$ ml O₂/gm Hb[73]). The hemoglobin content of blood (HGB) is assumed to be 16 gm Hb/dL of blood [73]. Finally, α_p is the solubility of oxygen in blood plasma ($\alpha_p = 0.0039$ ml O₂/mmHg/dL [73, 74]). Under normal physiological conditions, the amount of plasma-dissolved oxygen in the blood offers a negligible contribution (~2-3%) and is neglected in the fits used for this model. In the extra-vascular tissue, oxygen solubility is greater than in the plasma ($\alpha_t = 0.0118$ ml O₂/mmHg/dL [74]) and oxygen content depends only on oxygen partial pressure (i.e. $c_t O_2(t) = \alpha_t \cdot p_t O_2(t)$).

3.6.2.1 Mitochondrial temporal basis function

A Gaussian function is assumed to describe the changes in the oxygen consumption which is caused to mitochondrial activity as outlined in Equation 14, and this function is similar to the arterial dilation function.

$$CMRO_{2,mit}(t) = CMRO_{2,mit,max}(0) - (CMRO_{2,mit,max} - CMRO_{2,mit}(0)) \exp\left(-\frac{(t - T_{peak})^2}{\sigma_c^2}\right) \quad (51)$$

where $CMRO_{2,mit}(0)$ represents the baseline $CMRO_2$ in the mitochondria and $CMRO_{2,mit,max}$ represents the maximum change of $CMRO_{2,mit}$ from its baseline value. The model presented links the cerebral metabolic rate of oxygen ($CMRO_2$) to cerebral blood flow (CBF) using the diffusivity for oxygen (kO_2) of the vascular compartment.

3.6.2.2 Initial conditions

The diffusivity for oxygen (kO_2) in the vascular compartment is related to the initial conditions where V_w represents the volume of the Windkessel compartment, F_{in} and F_{out} represents the flow coming into and out of the vascular compartment, and $C_{in}O_2$ and $C_{out}O_2$ represent the partial pressure of oxygen of the blood coming into and leaving the vascular compartment and $C_T O_2$ represents oxygen tension in the tissue.

$$kO_2 = \frac{F_{in}(0)c_{in}O_2(0) - F_{out}c_{out}O_2(0)}{V_w(0) \left[\frac{1}{2}(c_{in}O_2(0) + c_{out}O_2(0)) - c_T O_2(0) \right]} \quad (52)$$

The baseline $CMRO_2$ in every compartment is calculated as a function of the pressure and the oxygen diffusivity of the vascular compartment.

$$CMRO_2(0) = kO_2 \left\{ \frac{1}{2} [(c_{in}(0) + c_{out}(0)) - c_t(0)] \right\} \quad (53)$$

3.6.2.3 Temporal update for cO_2

To define oxygen transport between the vascular segments and the surrounding tissue, a system of differential equations is derived which is dependent on (i) the flow changes described by the vascular component of the model and (ii) changes in mitochondrial metabolism, which result in changes in oxygen consumption in the extra-vascular tissue compartment [71, 74].

The changes in the oxygenation of each vascular compartment are functions of the amount of oxygen flowing into and out of the compartment and are governed by the

blood flow and the oxygen extracted from the compartment to the surrounding extra-vascular tissue. Oxygen extraction is driven by the differences in the oxygen content between the vascular compartments and the surrounding tissue [7, 71],

$$\frac{dC_n O_2(t)}{dt} = -kO_2 [C_n O_2(t) - C_t O_2(t)] \quad (54)$$

In Equation 54, kO_2 is the intrinsic rate constant for this process and can be defined from the baseline relationships between SO_2 , blood flow, and the O_2 levels of the compartment and extra-vascular tissue [75, 76].

In order to derive the equations for oxygen transport, the vascular compartment is assumed to obey the principles of mass balance of the amount of O_2 (N_{O_2}).

$$\frac{dN_{O_2}}{dt} = \left(\frac{dN_{O_2}}{dt} \right)_{Flow_in} - \left(\frac{dN_{O_2}}{dt} \right)_{Flow_out} - \left(\frac{dN_{O_2}}{dt} \right)_{Extracted} \quad (55)$$

Using the relationship between the amount of oxygen carried in each compartment and the oxygen concentration ($N_{O_2}(t) = C_n O_2(t) \cdot V_n(t)$), a set of differential equations is set up to describe the delivery of oxygen into the vascular compartment [68]. The mean oxygen content of a vascular segment has been defined as the average of the concentration (content) of either end (i.e. $C_n O_2(t) = \frac{1}{2} [C_{In} O_2(t) + C_{OUT} O_2(t)]$). In the extra-vascular compartment, the change in the amount of oxygen is the difference between oxygen delivered to the tissue and oxygen consumed,

$$\frac{dN_{tissue} O_2(t)}{dt} = kO_2 \left\{ \frac{1}{2} [C_{In} O_2(t) - C_{OUT} O_2(t)] - C_t O_2(t) \right\} - CMRO_2(t) \quad (56)$$

The system of equations (Equations 54 and 55) can be solved using a discrete update.

$$\frac{d(V_w(t)c_w O_2(t))}{dt} = \left\{ \begin{array}{l} F_{in}(t)c_{in} O_2(t) - F_{out}(t)c_w O_2(t) \\ -kO_2 \left[\frac{1}{2}(c_{in} O_2(t) + c_w O_2(t)) - c_t O_2(t) \right] V_w(t) \end{array} \right\} \quad (57)$$

$$\left. \begin{array}{l} V_w(t) \cdot \frac{d(c_w O_2(t))}{dt} \\ + c_w O_2(t) \cdot \frac{d(V_w(t))}{dt} \end{array} \right\} = \left\{ \begin{array}{l} F_{in}(t)c_{in} O_2(t) - F_{out}(t)c_w O_2(t) \dots \\ -kO_2 \left[\frac{1}{2}(c_{in} O_2(t) + c_w O_2(t)) - c_t O_2(t) \right] V_w(t) \end{array} \right\} \quad (58)$$

$$\left. \begin{array}{l} V_w(t) \cdot \frac{d(c_w O_2(t))}{dt} \end{array} \right\} = \left\{ \begin{array}{l} F_{in}(t)c_{in} O_2(t) - F_{out}(t)c_w O_2(t) \dots \\ -kO_2 \left[\frac{1}{2}(c_{in} O_2(t) + c_w O_2(t)) - c_t O_2(t) \right] V_w(t) \dots \\ -c_w O_2(t) \cdot \frac{d(V_w(t))}{dt} \end{array} \right\} \quad (59)$$

$$\frac{d(c_w O_2(t))}{dt} \left\} = \left\{ \begin{array}{l} \frac{F_{in}(t)}{V_w(t)} c_{in} O_2(t) - \frac{F_{out}(t)}{V_w(t)} c_w O_2(t) \dots \\ -kO_2 \left[\frac{1}{2}(c_{in} O_2(t) + c_w O_2(t)) - c_t O_2(t) \right] - \frac{c_w O_2(t)}{V_w(t)} \cdot \frac{d(V_w(t))}{dt} \end{array} \right\} \quad (60)$$

$$\frac{d(c_w O_2(t))}{dt} \left\} = \left\{ \begin{array}{l} \frac{F_{in}(t)}{V_w(t)} c_{in} O_2(t) - \frac{F_{out}(t)}{V_w(t)} \left(c_w O_2(t-1) + \frac{d(c_w O_2(t))}{dt} \right) \dots \\ -kO_2 \left[\frac{1}{2} \left\{ c_{in} O_2(t) + \left(c_w O_2(t-1) + \frac{d(c_w O_2(t))}{dt} \right) \right\} \right] \dots \\ - \left(c_t O_2(t-1) + \frac{d(c_t O_2(t))}{dt} \right) \left[\frac{c_w O_2(t-1) + \frac{d(c_w O_2(t))}{dt}}{V_w(t)} \right] \cdot \frac{d(V_w(t))}{dt} \end{array} \right\} \quad (61)$$

$$\left. \begin{array}{l} \frac{d(c_w O_2(t))}{dt} \\ \left[1 + \frac{F_{out}(t)}{V_w(t)} + \frac{kO_2}{2} + \frac{1}{V_w(t)} \cdot \frac{d(V_w(t))}{dt} \right] \\ + \frac{d(c_t O_2(t))}{dt} [-kO_2] \end{array} \right\} = \left\{ \begin{array}{l} c_{in} O_2(t) \left[\frac{F_{in}(t)}{V_w(t)} - \frac{kO_2}{2} \right] \dots \\ + (c_w O_2(t-1)) \cdot \left[-\frac{F_{out}(t)}{V_w(t)} - \frac{kO_2}{2} \right] \\ - \frac{1}{V_w(t)} \cdot \frac{d(V_w(t))}{dt} + (c_t O_2(t-1)) [kO_2] \end{array} \right\} \quad (62)$$

The oxygen content in the extravascular tissue compartment is described to evolve in time according to Equation 63.

$$\frac{dc_t O_2}{dk} = kO_2 \left\{ \frac{1}{2} [(c_{in}(t) + c_w(t)) - c_t(t)] \right\} - CMRO_2(t) \quad (63)$$

The increments calculated in Equation 63 are added to the values of oxygen content at the previous time points to get the values of partial pressure at the present time point.

$$\frac{dc_t O_2}{dk} = \left\{ kO_2 \left[\frac{1}{2} \left[\left(c_{in}(t) + c_w(t-1) + \frac{d(c_w O_2(t))}{dt} \right) - \left(c_t(t-1) + \frac{d(c_t O_2(t))}{dt} \right) \right] \right] \right\} - CMRO_2(t) \quad (64)$$

$$\left. \begin{aligned} & \frac{d(c_w O_2(t))}{dt} \left[-\frac{kO_2}{2} \right] \\ & + \frac{dc_t O_2}{dk} [1 + kO_2] \end{aligned} \right\} = \left\{ \begin{aligned} & c_{in}(t) \left[\frac{kO_2}{2} \right] + c_w(t-1) \left[\frac{kO_2}{2} \right] + c_t(t-1) [-kO_2] \\ & - CMRO_2(t) \end{aligned} \right. \quad (65)$$

Combining both the vascular oxygen transport and tissue to mitochondria oxygen consumption equations into matrix form we get

$$\begin{aligned}
& \begin{bmatrix} 1 & 0 & 0 \\ 0 & 1 + \frac{F_{out}(t)}{V_w(t)} + \frac{kO_2}{2} + \frac{1}{V_w(t)} \cdot \frac{d(V_w(t))}{dt} & -kO_2 \\ 0 & -\frac{kO_2}{2} & 1 + kO_2 \end{bmatrix} \cdot \begin{bmatrix} \frac{d(c_{in}O_2(t))}{dt} \\ \frac{d(c_wO_2(t))}{dt} \\ \frac{d(c_tO_2(t))}{dt} \end{bmatrix} \\
& = \left\{ \begin{bmatrix} 0 & 0 & 0 \\ \frac{F_{in}(t)}{V_w(t)} - \frac{kO_2}{2} & -\frac{F_{out}(t)}{V_w(t)} - \frac{kO_2}{2} - \frac{1}{V_w(t)} \cdot \frac{d(V_w(t))}{dt} & kO_2 \\ \frac{kO_2}{2} & \frac{kO_2}{2} & -kO_2 \end{bmatrix} \cdot \begin{bmatrix} c_{in}O_2(t) \\ c_wO_2(t) \\ c_tO_2(t) \end{bmatrix} \right. \\
& \quad \left. - \begin{bmatrix} 0 \\ 0 \\ CMRO_2(t) \end{bmatrix} \right\} \quad (66)
\end{aligned}$$

We can obtain the oxygen content at the present time instant by adding the update,

$$c_nO_2(t) = c_nO_2(t-1) + \frac{d(c_nO_2(t))}{dt} \cdot dt \quad (67)$$

where $n \in \{w, t\}$ and 'w' represents the oxygen content of the blood in the Windkessel vascular compartment and 't' represents the oxygen content in the tissue.

After solving for the oxygen content in each compartment, the oxygen saturation of hemoglobin and the partial pressure of oxygen dissolved in the plasma can be recovered with the Equation 50. The saturation of hemoglobin is also related to the partial pressure of oxygen by the hemoglobin dissociation curve described using Kelman's equation (described in the next section) and can be used to derive temporal changes in the oxy- and deoxyhemoglobin content in each compartment. Changes in concentrations of oxyhemoglobin and deoxyhemoglobin are calculated as follows,

$$Hb = HbT(1 - SO_2) \quad (68)$$

$$HbO_2 = HbT \cdot SO_2 \quad (69)$$

where SO_2 is the oxygen saturation and HbT is the total hemoglobin content.

3.6.2.4 Calculation of partial pressure of oxygen

The oxygen saturation in the vascular compartment can be used to calculate the partial pressures in that vascular compartment. This is done using the oxyhemoglobin dissociation curve which describes the relation between the partial pressure of oxygen and the related oxygen saturation. This curve shows that the affinity of hemoglobin for oxygen increases as more molecules of oxygen bind to it till it reaches a maximum after which the hemoglobin becomes saturated with oxygen. This behavior causes the dissociation curve to have a sigmodal shape which can be described using Kellman's equation [77].

$$SO_2 = \left(\frac{-8532.2289 \cdot pO_2 + 2121.4010 \cdot pO_2^2 - 67.073989 \cdot pO_2^3 + pO_2^4}{935960.87 + 31346.258 \cdot pO_2 + 2396.1674 \cdot pO_2^2 - 67.104406 \cdot pO_2^3 + pO_2^4} \right) \quad (70)$$

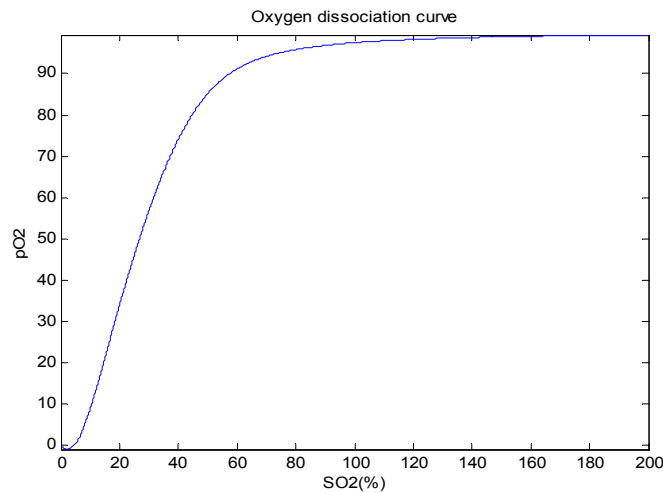


Figure 3.8: Kellman's oxygen extraction curve

3.6.2.5 Results with fitting measured multimodality data

A χ^2 nonlinear fit of flow, volume as well as the changes in the concentration of deoxyhemoglobin and oxyhemoglobin to the experimentally measured values of $\Delta[\text{HbO}_2]$ and $\Delta[\text{Hb}]$ was performed. This helped to predict parameters that were previously fixed while fitting only flow and volume experimental values. In this section in addition to the flow and volume parameters, we fit for the baseline oxygen saturation, volume fraction as well as parameters such as $\text{CMRO}_2(0)$, $\text{CMRO}_{2, \text{min}}$, T_{peak} and σ_c^2 that define the oxygen consumption caused by mitochondria. The predicted CMRO_2 function in the mitochondria was compared to the calculated CMRO_2 functions (Equations 34 and 35) using values of $\Delta[\text{HbO}_2]$, $\Delta[\text{Hb}]$, $\Delta[\text{HbT}]$ and ΔCBF using the single compartment model.

The changes in deoxy- $\Delta[\text{Hb}]$ and total hemoglobin $\Delta[\text{HbT}]$ were used to predict the BOLD signal ($\Delta\text{BOLD}/\text{BOLD}_0$) using Equation 36. By assuming a function for CMRO_2 caused by mitochondrial activity, several degrees of freedom were added to this model. The oxygen diffusivity for the vascular compartment was calculated to fit for oxyhemoglobin, $\Delta[\text{HbO}_2]$ and deoxyhemoglobin, $\Delta[\text{Hb}]$ along with the flow and volume. The data used is the same 2-second finger tapping data described in previous sections.

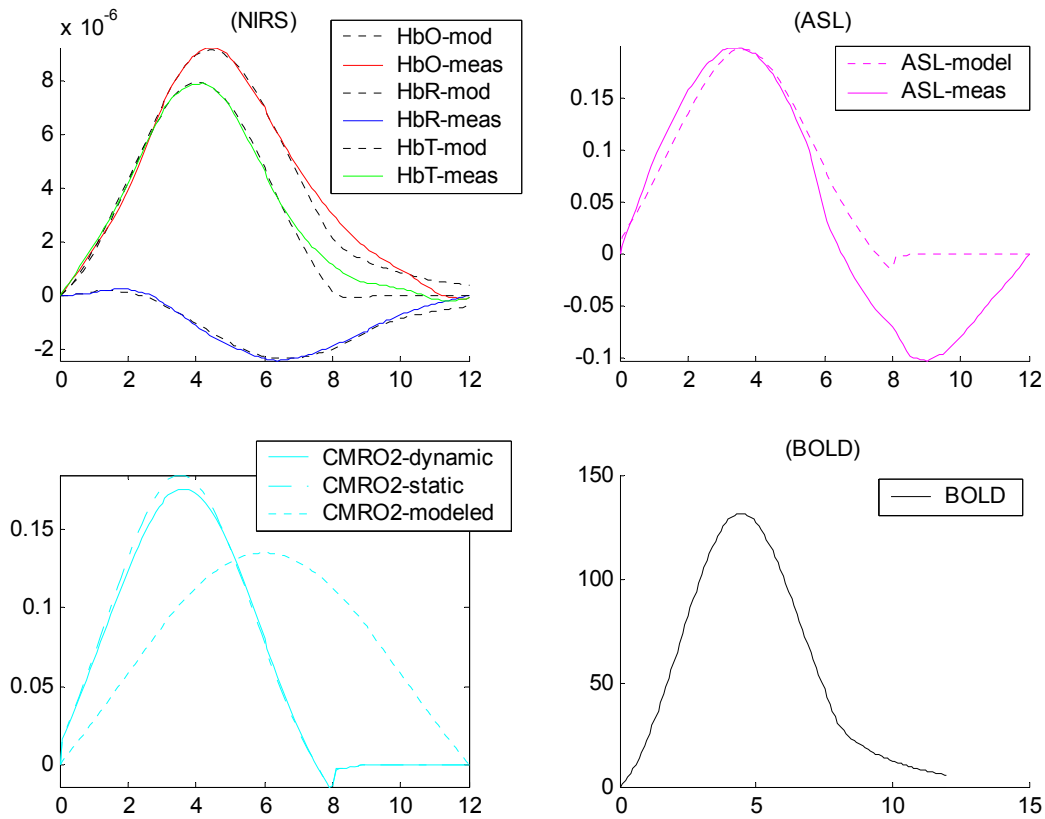


Figure 3.9: Results of the single compartment Windkessel model (All NIRS measurements and CBF fit). Duration of task=2 seconds

3.6.2.6 Modeling long duration stimuli

Similar to the oxygen extraction and flow-volume model setup, the mitochondrial activity basis function was also modified to describe the temporal hemodynamics involved in longer duration stimuli. Both the arterial resistance and oxygen extraction functions model were convolved with the input stimulus (Equation 37 and 69) where temporal evolution of $N(t)$ is described by Equations 38 and 39.

$$CMRO_{2,mit}(t) = \begin{cases} CMRO_{2,mit,max} + (CMRO_{2,mit,max} - CMRO_{2,mit}(0)) \exp\left(\frac{(t - T_{peak})^2}{\sigma_c^2}\right) \\ \otimes N(t) \end{cases} \quad (71)$$

Plots of the volumes and flow in the Windkessel compartment are shown in Figure 3.10.

The data used is the same 20-second finger walking data described in previous sections for long duration stimuli.

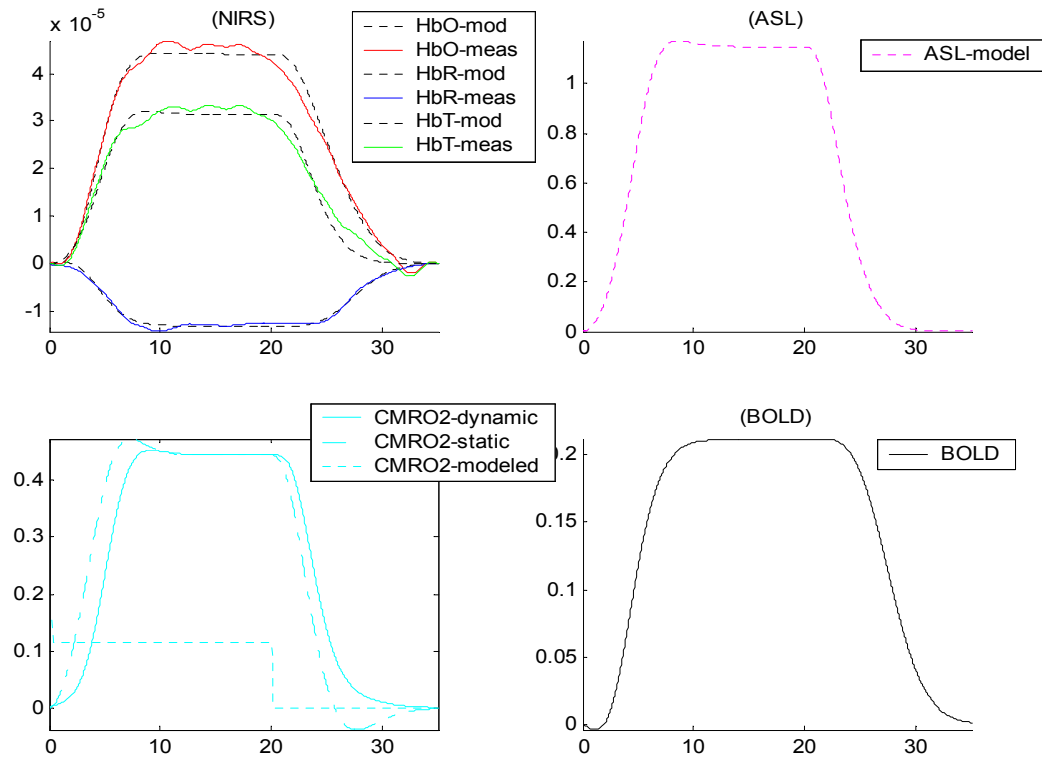


Figure 3.10: Results of the single compartment Windkessel model (All NIRS measurements and CBF fit). Duration of task=20 seconds

3.7 Chapter summary

Summarizing this chapter, three novel contributions were made to the single compartment model: (i) The inductive flow-volume model was extended to describe the dynamics during long duration stimulus; (ii) Oxygen extraction model was added to describe the oxygen consumption dynamics; and (iii) Mitochondrial activity model developed a physiologically more accurate description of the oxygen consumption dynamics by adding the extravascular tissue compartment with the oxygen consumption basis function described at the mitochondrial level.

Table 3.2 gives a list of the variables that are used in all the described models with physiological ranges listed for each parameter. Dynamic parameters are expected to vary with stimulus amplitude while structural/static parameters are expected to be conserved (Refer Chapter 6 where this hypothesis is tested)

Table 3.2: Parameters used in single compartment fit

		Symbol	Description	Physiological range
Dynamic	Arteriole dilation temporal basis	ΔR_a	Change arterial resistance	[0-10]%
		$R_{a,min}$	Minimum arterial resistance	-
		T_{peak}	Time to maximum resistance change	[1-6] s
		σ_a	Width of temporal resistance change	[1-4] s
	Oxygen extraction temporal basis	ΔOE	Change oxygen extraction	[0-10]%
		OE_{max}	Maximum oxygen extraction	-
		T_{peak}	Time to maximum oxygen extraction	[1-6] s
		σ_a	Width of temporal oxygen extraction change	[0-4]
	CMRO ₂ temporal basis	$\Delta CMRO_2$	Change CMRO ₂	[0-10]%
		$CMRO_{2max}$	Maximum CMRO ₂	-
		T_{peak}	Time to maximum CMRO ₂	[0-4] s
		σ_a	Width of temporal CMRO ₂ change	[0-4]
	Neural basis function	κ	Gain factor inhibitory response	[0-2]
		τ_1	Time constant inhibitory response	[1-3] s
Structural	Initial arterial resistance	$R_a(0)$	Initial arterial resistance	[0.1-0.8]
	Windkessel parameters	β	Windkessel vascular reserve	[1-5]
	Baseline arteriole saturation	SO_2	Baseline oxygen saturation	0.65

CHAPTER 4

MULTI-COMPARTMENT WINDKESSEL MODEL

Hemodynamic changes provide an indirect estimate of the brain's neuronal activity which evokes changes in metabolism. These metabolic changes are reflected by variations in the local concentration of oxy- and deoxy-hemoglobin. Regional blood flow and oxygen supply to tissue also increase through dilatory effects on feeding arterioles caused by the actions of vaso-active agents. Therefore, measurements such as blood oxygen level dependent fMRI (BOLD-fMRI) or near-infrared spectroscopy (NIRS) have an ambiguous relationship with underlying electrical and metabolic neuronal activity [49]. The separation of the neuro-vascular and neuro-metabolic influences on functional hemodynamic measurements is imperative for understanding the interplay of these phenomena.

The neurovascular and neurometabolic mechanisms represent two external driving forces that control hemodynamic changes in blood flow, volume, and oxygenation. The vascular and oxygen transport components of the vascular network can be represented by a series of connected compliant pipes with passive diffusion of oxygen across permeable blood vessel walls into the surrounding tissue [78]. Such a model can be characterized by non-linear differential equations, which depend on the physiological and structural properties of the brain that are static in time. Thus parameter estimation techniques can be used to calculate system component values

from experimental data with changes in arterial dilation and $CMRO_2$ estimated by dynamically changing functions during brain function.

4.1 Motivation for a multicompartment model

In recent years, the development of invasive optical imaging experiments in animal models have enabled the measurement of hemodynamic changes at a higher temporal and spatial resolution than has been previously possible with fMRI methods in human models [7, 79-82]. Such experiments can provide segmentation of cerebral vasculature into arteriolar, capillary and venous compartments based on diameter, and spatial location of vessels. The detailed information from these experiments has been invaluable in examining the effectiveness of assumptions made in earlier vascular models. Discrepancies are being noted between comprehensive experimental results from animal models and the assumptions of the earlier single-compartment vascular models [7]. In order to reconcile these differences, the use of multi-compartment models of the vascular network which describe hemodynamic changes in three vascular compartments, namely the arterial, capillary, and venous compartments has been recently suggested [7, 83].

This research was carried out with the Photon Migration Institute (MGH) with Dr. D. Boas and T. J. Huppert.

4.1.1 Three compartment flow-volume model

In this chapter, a novel inductive multi-compartment model of the vascular and oxygen transport changes to model the composite hemodynamic response is presented. Several improvements that extend from previously described single compartment flow-volume model [9-11] are introduced. In particular, a capillary compliance model motivated by experimental observations [6] of microvascular (or parenchymal) volume changes indicative of increased capillary perfusion is developed. The three compartment vascular model includes flow volume dynamics observed by introducing capillary compliance to describe volume changes indicative of increased capillary perfusion [82].

This model helps to define the individual contribution and temporal evolution of cerebral blood volume and blood flow in each vascular compartment and provides quantification of compartmentalized hemodynamics based on realistic representation of cerebrovascular structures and their physiological role and contribution to measured cerebral hemodynamics.

4.1.2 Capillary oxygen extraction model

An inductive three compartment capillary oxygen extraction model is developed in this research which distinguishes itself from the previously published deductive model [7] by providing description of the underlying biophysics of the measurements using temporal basis functions described by the oxygen extraction driving function. The parameters of the basis functions are determined by fitting the predicted hemodynamics

to measured data thus revealing hidden states that are not previously defined. Description of oxygen extraction is assumed to result from the capillary compartment alone which has the highest contribution to tissue oxygenation [84, 85] with the assumption that arteriole and venial contribution to oxygen dynamics is negligible. This model is a first step to a physiologically relevant description of metabolic activity.

Description of metabolic activity and oxygen transport dynamics as they relate to flow-volume dynamics is the focus of many research efforts [61, 75, 84]. Such modeling has been instrumental in the diagnosis and treatment monitoring of diseases such as depression [86] and Alzheimer's disease [87] which cause changes in localized metabolism in the brain. In past research efforts, metabolic activity has been imaged using positron emission tomography (PET) [88]. PET provides direct estimates of the cerebral metabolic rate of oxygen or oxygen consumption dynamics. These methods involve the introduction of radioactive compounds into the subject. Therefore, the repeated measurements required to provide meaningful results in longitudinal studies are difficult due to radiation exposure concerns. Noninvasive functional imaging techniques such as fMRI and NIRS can be repeated in a "within subject" design without significant health risks. The utility of such imaging techniques can be improved if they provide a direct estimate of metabolic rate as it relates to neural activity, and neurovascular modeling is a means of quantitatively predicting such changes from measured hemodynamics.

4.1.3 Mitochondrial oxygen consumption model

While the capillary extraction model provides a good first step to include three compartment flow-volume mechanisms in an oxygen transport model, the assumption that oxygen diffusion through arterioles and venules is negligible has been disputed, especially in animal models [6]. Although, defining oxygen extraction simply as removal of oxygen from the vascular network can help fit hemodynamic data, it does not provide the physiological basis for the complicated process of oxygen consumption.

Neuronal activity is believed to affect hemodynamic function through two major mechanisms. Blood oxygenation is determined by (i) the balance of oxygen supplied from the blood vessels and (ii) oxygen consumed by glycolysis to support baseline and functional levels of cellular function. Increased neuronal activity is accompanied by an increase in cerebral oxygen consumption caused by the energy demand to replenish synaptic neural-transmitter states, membrane potentials, or other indirect effects mechanisms [89]. The increase in oxygen demand is compensated for with an increase in the regional blood supply to the brain. Studies of cerebral metabolism have implied that oxygen transport originates at the cellular level (in the mitochondria) and follows a path of oxygen transport from the blood vessels to the parenchymal tissue and then the mitochondrial structures where it is consumed to support increased energy demand created by activation. Defining this pathway with the temporal basis function at the cellular level, as is presented in this model, provides a description consistent with physiological observations of the oxygen consumption mechanism. Such a model can thus help accurately determine parameters that define this underlying process that is a

direct result of activation and can provide a true measure of brain function from the hemodynamic measurements obtained using current imaging techniques [68].

The capillary oxygen transport model is modified to include oxygen transport dynamics caused by oxygen extracted from the arteriolar and venial compartments in the mitochondrial oxygen consumption model and to allow potential changes in the oxygen tension within the extra-vascular parenchymal tissue. The role of oxygen transport from the arterioles and venules has been motivated by recent experimental results [75, 76] and theoretical descriptions [74, 83]. The model provides a more realistic physiological model of cerebrovascular and metabolic changes and allows potential changes in the oxygen tension within the extra-vascular parenchyma tissue. The model is based on the effect of mitochondrial oxygen consumption which is elevated in localized regions of the brain during stimuli driven activation [11, 12]. This research was carried out with the Photon Migration Institute (MGH) with Dr. D. Boas and T. J. Huppert.

4.2 General description of multi-compartment model

In contrast to previous models, the multi-compartment model presented in this research is built using an inductive or bottom-up approach [90] (Refer Figure 4.1). This inductive modeling approach is similar to the procedure described in Chapter 3 Section 3.4 [57], but represents a significant deviation from the deductive approaches used in most other vascular descriptions. Error in the model is minimized by the simultaneous comparison of the predicted data to experimental multimodality measurements to

estimate $CMRO_2$ and arteriole dilation defined by hidden state. This multi-compartment model provides a direct estimate of the vascular and metabolic changes from the multimodal measurements of blood flow, volume, and oxygenation. The imaging measurements are combined within a pseudo-Bayesian statistical framework to provide a more robust estimation of the state variables by accounting for the differing sources of noise and measurement errors associated with individual instrumentation.

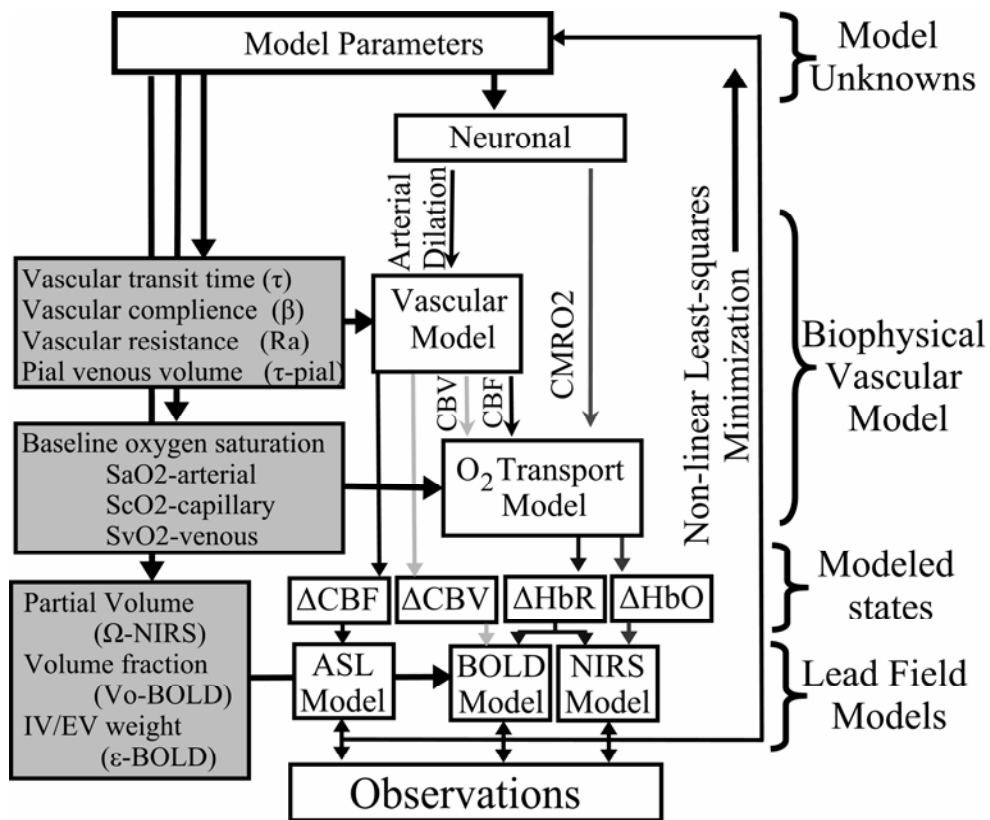


Figure 4.1: State space representation of vascular model [68]

4.3 Vascular model

The vascular component of the model is described by a set of physical relationships that depict three connected, compliant, vascular compartments (namely the arterial, capillary, and venous compartments). The model of vascular changes described in this work is built around the relationships between blood flow and volume changes originally proposed in the Balloon model [2, 3, 6, 7] and later extended to include an empirical description of vascular compliance in the Windkessel model [4, 5].

4.3.1 Electrical representation

The vascular compartments can be represented by an analogous network of resistor and capacitor (electrical) elements as depicted in Figure 4.2. The resulting differential equations that govern changes in blood flow and volume are driven by the active dilation of the arterioles which decreases the input vascular resistance. The pressure gradient between compartments (equivalent to electrical potential difference) drives the flow of blood (analogous to electrical current) between compartments. As the pressure increases, the vascular compartment expands causing blood volume to increase. The increase in blood volume in a compartment is equivalent to the build-up of charge on a non-linear capacitor whose capacitance decreases as the compartment expands against the pressure of the surrounding brain leading to a saturating blood volume expansion function. Finally, the heart and systemic circulation create a constant pressure drop across the entire system and are modeled as a single constant DC voltage source. Cerebral blood volume is equivalent to electrical charge. The flow of charge

(i.e. current) models blood flow changes and is proportional to the blood pressure drop across compartments and inversely proportional to vascular resistance. Non-linear capacitor elements model the vascular compliance of each compartment.

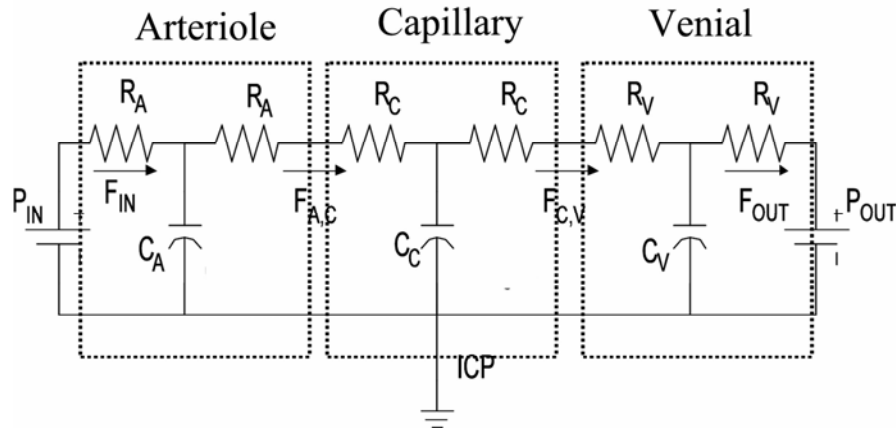


Figure 4.2: Electrical circuit analogy for the multi-compartment model [68]

4.3.2 Vascular model equations

The correspondence of this model with an electrical circuit readily allows the derivation of the differential equations to model the physical flow and volume changes based on Kirchoff's relationships and summarized by the following physical principles. The flow between each compartment is calculated using the Ohm's law analogy ($V=IR$), where I , V and R are analogous to the blood flow, blood pressure and vascular resistance, respectively. The pressure (P) drop across vascular compartments ($n \rightarrow n+1$) is the product of the flow (F) from the n^{th} into the $(n+1)^{\text{th}}$ compartment and the vascular resistance (R) between the compartments,

$$P_n(t) - P_{n+1}(t) = F_{n,n+1}(t) \cdot [R_n(t) + R_{n+1}(t)] \quad (72)$$

This leads to the set of differential equations that describe the differential volume changes in each compartment based on flow mismatch,

$$\frac{dV_n}{dt} = F_{n-1,n}(t) - F_{n,n+1}(t) \quad (73)$$

$$\frac{dV_n}{dt} = \frac{P_{n-1}(t) - P_n(t)}{R_{n-1}(t) + R_n(t)} - \frac{P_n(t) - P_{n+1}(t)}{R_n(t) + R_{n+1}(t)} \quad (74)$$

These equations can be elaborated to describe the three-compartment vascular formulation. The volume changes in every compartment is related to the pressure and resistance of the compartment and hence related to the changes in flow in the compartment. Equations 75, 76 and 77 describe the differential equations that relate the volume to flow changes in individual compartments namely arteriolar, capillary and venous compartments [68].

Arteriolar compartment:

$$\frac{dV_a}{dt} = \frac{P_{in}(t) - P_a(t)}{R_a(t)} - \frac{P_a(t) - P_c(t)}{R_a(t) + R_c(t)} = F_{in} - F_{ac} \quad (75)$$

Capillary compartment:

$$\frac{dV_c}{dt} = \frac{P_a(t) - P_c(t)}{R_a(t) + R_c(t)} - \frac{P_c(t) - P_v(t)}{R_c(t) + R_v(t)} = F_{ac} - F_{cv} \quad (76)$$

Venous compartment:

$$\frac{dV_v}{dt} = \frac{P_c(t) - P_v(t)}{R_c(t) + R_v(t)} - \frac{P_v(t) - P_{out}(t)}{R_v(t)} = F_{cv} - F_{out} \quad (77)$$

In this model, the capillary and venous compartments are modeled compliant vessels. The capacitance (C_n) describes the vascular compliance and hence the limit for

volume changes in these compartments. In the electrical circuit analogy, charge build-up on these capacitors models blood volume changes. In the vascular network, compliance modeled by capacitance is a non-linear function of the pressure (P_n) between the vascular compartment and the intra-cranial pressure (ICP) and varies according to an inverse power law relation of Windkessel volume reserve (β) as described in the single compartment Windkessel model [5]

$$C_n(t) = A_n \cdot [P_n(t)]^{\left(\frac{1}{\beta_n}\right)^{-1}} \quad n \in \{\text{Capillary, Venous}\} \quad (78)$$

In this model, β_n is the Windkessel vascular reserve of the n^{th} compartment. We assume the vascular reserve to have the same value for both the capillary and venous compartments. A_n is a scaling constant determined by the initial conditions and can be removed with normalization,

$$A_n = \frac{V_n(0)}{\left[F_{n-1,n}(0) \cdot (R_{n-1}(0) + R_n(0))\right]^{\frac{1}{\beta_n}}} \quad (79)$$

Combining Equations 73, 78 and 79, the flow in the capillary and venous compartments is a function of the pressure, volume and the resistance of the compartments and is described by

$$F_{n-1,n} = \frac{P_{n-1}(t) - V_n(t)^{\beta_n} / A^{\beta_n}}{R_{n-1}(t) + R_n(t)} \quad (80)$$

$$F_{n,n+1} = \frac{V_n(t)^{\alpha+\beta_n}}{A^{\beta_n} \cdot V_n(0)^\alpha \cdot (R_n(0) + R_{n+1}(0))} \quad (81)$$

where $\alpha = 2$ and represents laminar flow in the compartments [5].

Volume expansion of the arterials is caused by the active dilation of these vessels. The changes in arterial volume (ΔV_a) are determined by the change in the diameter of the compartment (ΔD_a).

$$\frac{V_a(t)}{V_a(0)} = \left(\frac{D_a(t)}{D_a(0)} \right)^2 \quad (82)$$

The arterial resistance (R_a) is proportional to the vessel's length (l_a) and inversely proportional to the fourth power of its diameter (D_a) according to Poiseuille's Law [91]. η represents the viscosity of blood and is removed with normalization.

$$R_a(t) = \frac{128 \cdot \eta}{\pi} \cdot \frac{l_a}{D_a(t)^4} \quad (83)$$

4.3.3 Arteriole dilation

The arteriolar dilation variations that drive the flow and volume changes in the vascular network are defined in the state vector (X) and are estimated as part of the minimization of the residual model error in the hemodynamic measurements. A temporal Gaussian function is used to describe the response of arteriolar resistance during cerebral activation [57],

$$R_A(t) = R_A(0) - (R_A(0) - R_{A,\min}) \exp\left(-\frac{(t - T_{peak})^2}{\sigma_R^2}\right) \quad (84)$$

This function is defined by the baseline resistance ($R_A(0)$), the functional percent change in resistance (ΔR_A), the time-to-peak (τ_{peak}), and the temporal width (σ_R) of the response. These parameters are estimated in the model as part of the state vector by the fitting procedure. The temporal basis function reduces the degrees of freedom of the

arteriolar resistance by estimating a subset of state variables instead of the full dynamic variation. The basis function assumption is similar to the use of temporal basis functions in the generalized linear model [92] as seen in fMRI studies. As a future extension, an explicit model of the effect of vaso-reactive signaling molecules could be included to model the response to measured neuronal stimulation [90, 92].

4.3.4 Temporal update

A differential temporal update is sequentially applied to the arterial, capillary and finally the venous compartment to calculate the blood flow and volume changes for each of the vascular compartments. This update is driven by changes in the arteriolar resistance, which is an input to the system and is described by variables estimated within the state vector. The value of the hydrostatic pressure of the subsequent compartment (i.e. capillary) at the previous time instance, and the vascular resistance and inflow to the present (i.e. arterial) compartment at the current time instant are used to calculate the differential update in the system (including vascular resistance, capacitance, and out-flow from arterioles). This differential change is used to update the set of states that describe physiological changes (blood flow and volume) for the arterial compartment at the current time instant. Next, the same procedure is repeated to update the capillary and the venous compartments.

The differential equations (defined by Equations 73-82) can be formulated with variables of flow and resistance represented as unit-normalized quantities. Thus, the model naturally estimates relative changes in the hemodynamic parameters. At baseline,

the relationship between the Windkessel volume and the incoming blood flow is given by the vascular transit time ($V_w(0) = F_{in}(0) \cdot \tau$), where the Windkessel volume is equal to the sum of the volumes of the three vascular compartments (arterial, capillary and venous). Initial volume fractions of 25%, 15%, and 60% for the arterial, capillary and venous compartments are assumed [7, 93]. The sum of the initial total resistance in the three compartments is set at unity. The baseline arterial resistance ($R_a(0)$) is estimated by the state vector and the remaining resistance is equally distributed between the capillary and venous compartments [57].

4.4 Introduction to oxygen transport models

The multiple-compartment model [94] assumes that the region of interest consists of three compartments in the optical absorption perspective: the arterial (inflow) compartment, the venous (outflow) compartment, and the metabolic (consumption) compartment. In addition to vascular changes, increased neuronal activity results in a localized increase in the mitochondrial function [95]. This increase results in elevated oxygen consumption, which increases the extraction of oxygen from the vascular network, while increased blood flow competes to lower the oxygen extraction fraction. The second element of this multicompartment model, describes the process of oxygen extraction from the vascular compartments.

The dynamic and steady state cerebral metabolic rate of oxygen consumption ($CMRO_2$) were calculated using Equations 34 and 35 along with volume and flow values that were predicted in the multi-compartment model. The values for

deoxyhemoglobin $\Delta[\text{Hb}]$ used for the CMRO_2 calculation are the experimentally measured values for deoxyhemoglobin. This $\Delta[\text{Hb}]$ value measured by NIRS is an average across all three compartments, the arterial, capillary and venous. To accurately model these changes and their distribution across the three vascular compartments, two different models are presented (i) the capillary oxygen extraction model and (ii) the mitochondrial metabolism CMRO_2 model.

4.4.1 Capillary oxygen extraction model

It is expected that the greatest changes in oxygen consumption occur in the capillary compartment where the metabolic activity is the greatest. In the capillary oxygen extraction model, it is assumed that the changes in oxygen extraction (OE) occur primarily in the capillary compartment, and that oxygenation changes are negligible in the arterial and venous compartments. A Gaussian function is assumed for change in the oxygen consumption in the capillary compartment as outlined in Equation 85 and this function is similar to the arterial dilation function. A Gaussian function is chosen for both the OE changes and arterial dilation changes because both these changes are brought forth by cerebral activation and increased oxygen demand in the brain and hence similar functions are chosen for both functions.

$$OE(t) = OE_{\max}(0) - (OE_{\max} - OE(0)) \exp\left(-\frac{(t - T_{peak})^2}{\sigma_c^2}\right) \quad (85)$$

where $OE(0)$ represents the baseline OE and OE_{\max} represents the maximum change of OE from its baseline value in the capillary compartment. The baseline OE in every

compartment is calculated as a function of the flow into the compartment (F_{in}), oxygen saturation of the present ($SO_{2,in}$) and next compartment ($SO_{2,out}$), at baseline.

$$OE(0) = \frac{1}{2} (F_{in}(0) + F_{out}(0)) (SO_{2,in}(0) - SO_{2,w}(0)) \quad (86)$$

Changes in OE in the arterial and venous compartment are assumed to be negligible during activation and thus OE is kept constant at the baseline value (Equation 86) in these compartments to model the entire time period of the experiment. The changes in oxygen saturation over time are described by the following differential equation.

$$V_w \left(\frac{d(SO_{2,in})}{dt} - \frac{d(SO_{2,w})}{dt} \right) = \frac{1}{2} (F_{in} + F_{out}) (SO_{2,in} - SO_{2,w}) - OE \quad (87)$$

where OE represents the oxygen extraction in a compartment and is related to the $CMRO_2$ in the compartment, V_w represents the blood volume in the compartment and $SO_{2,in}$ and $SO_{2,w}$ represents the oxygen saturation of the blood entering and leaving the vascular compartment respectively. Temporal updates are performed in the same fashion as described in Chapter 3. Changes in concentrations of oxyhemoglobin and deoxyhemoglobin were calculated as follows,

$$\Delta[HbO_2] = HbT \cdot SO_2 \quad (88)$$

$$\Delta[Hb] = HbT \cdot (1 - SO_2) \quad (89)$$

where SO_2 is the oxygen saturation and HbT is the blood volume in the compartment.

4.4.1.1. Results of the capillary oxygen extraction model

A χ^2 nonlinear fit of flow, volume as well as the changes in the concentration of deoxyhemoglobin and oxyhemoglobin to the experimentally measured values of $\Delta[\text{HbO}_2]$ and $\Delta[\text{Hb}]$ was performed (Refer Figure 4.3). In this section, the baseline oxygen saturation and volume fraction in every compartment and $\text{CMRO}_2(0)$, CMRO_2 , T_{peak} , T_{peak} and σ_c^2 are estimated to define the oxygen consumption in the capillary compartment in addition to the flow and volume parameters. The predicted OE function is compared to the calculated CMRO_2 function using predicted values of $\Delta[\text{HbO}_2]$, $\Delta[\text{Hb}]$, $\Delta[\text{HbT}]$ and ΔCBF using the multi-compartment model. The data that the model predicted for changes in deoxyhemoglobin ($\Delta[\text{Hb}]$) and changes in blood volume ($\Delta[\text{HbT}]$) were used to predict the BOLD signal using Equation 36.

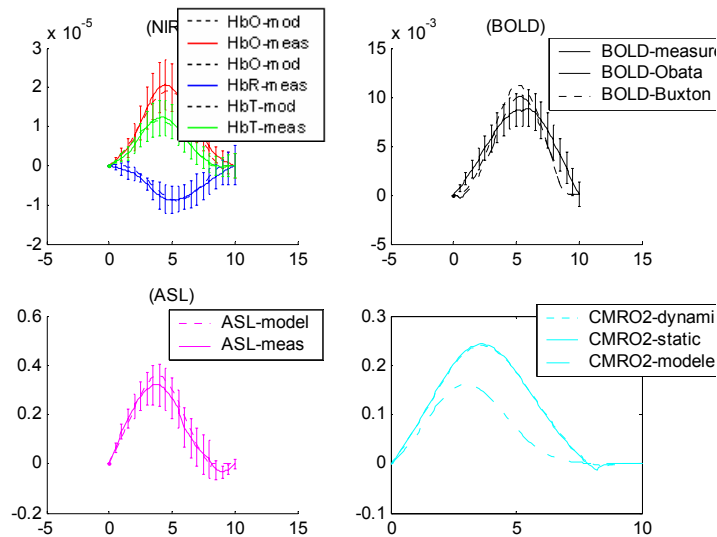


Figure 4.3: Results of the multicompartment Windkessel model (OE model)

Vascular changes were modeled in the arteriole, capillary, and venous compartments. The time-courses plotted show the representative changes in these three compartments. The predicted response curves for each of the vascular compartments, shown in Figure 4.4. The largest magnitude of blood volume changes originated from the venous compartment. However, the arteriole compartment had the largest fractional volume changes. Blood volume changes in the arterioles initiated and peaked slightly before the volume changes in the capillaries or venules. In the blood flow response, the magnitude of the change in all three compartments was nearly identical. The blood flow response was slightly lagged from the arteriole to venous compartments. This result is consistent with deductive model presented in Zheng et al [7].

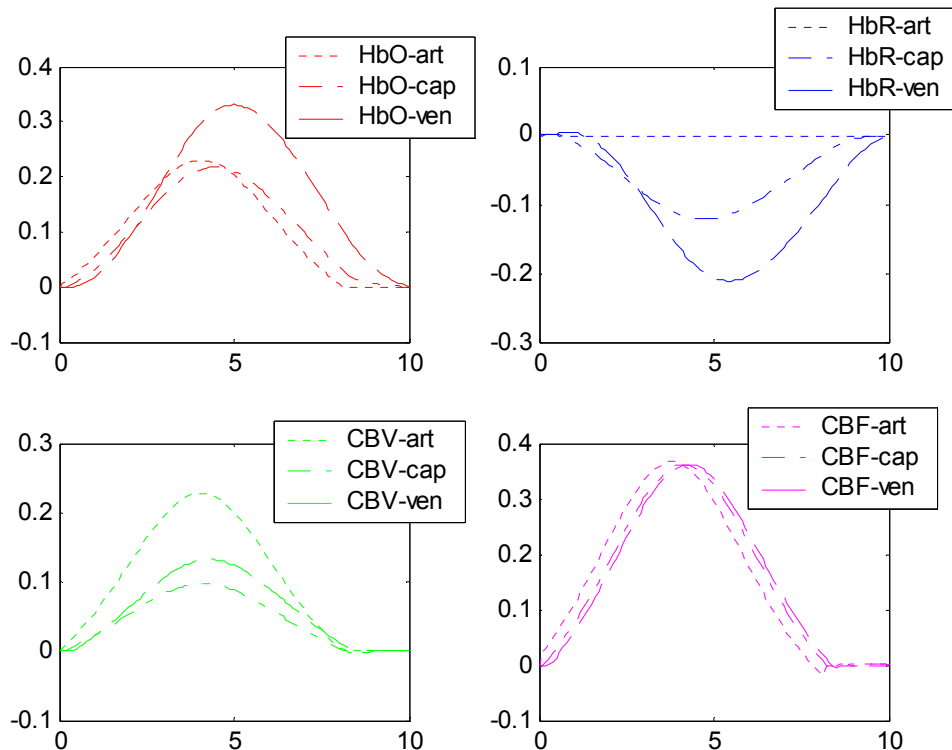


Figure 4.4: Multicompartment Windkessel model (individual vascular contributions)

Similar to the flow-volume model set-up described in Chapter 3, the oxygen extraction basis function was also modified to describe the temporal hemodynamics involved in longer duration stimuli. Both the arterial resistance and oxygen extraction functions model were convolved with input stimulus function (Equation 91 and 92).

$$OE(t) = OE_{\max} + (OE_{\max} - OE(0)) \exp\left(\frac{(t - T_{peak})^2}{\sigma_c^2}\right) \otimes N(t) \quad (90)$$

Based on the theory used in describing similar responses in deductive modeling [49], a simple inhibitory feedback system is used, in which the neural response $N(t)$ is treated as the difference between an excitatory input $s(t)$ and an inhibitory input $I(t)$.

$$N(t) = s(t) - I(t) \quad (91)$$

$$\frac{dI}{dt} = \frac{\kappa N(t) - I(t)}{\tau_1} \quad (92)$$

The stimulus input $s(t) = 1$ when $0 \leq t \leq t_0$ where $0 \leq t \leq t_0$ is the duration of the stimulus and the function $s(t) = 0$ otherwise. The inhibitory response is driven by the neural response with a gain of κ and a constant of τ_1 . Results are shown in Figure 4.5.

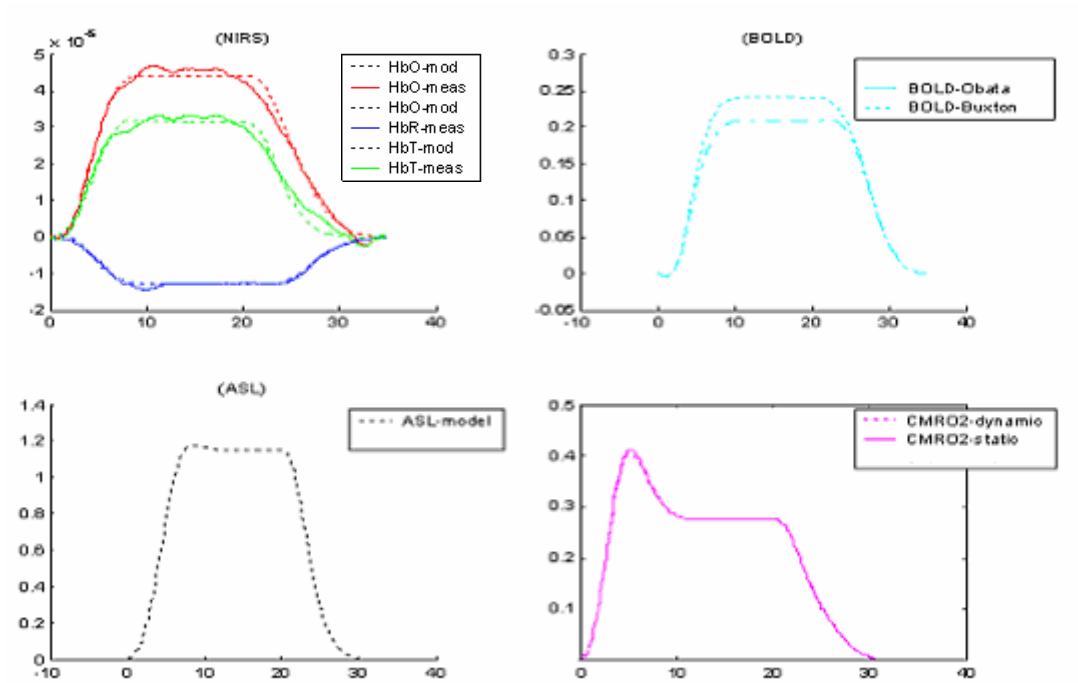


Figure 4.5: OE Windkessel model (long duration)

Vascular changes were modeled in the arteriole, capillary, and venous compartments. The time-courses plotted show the representative changes in these three compartments. The predicted response curves for each of the vascular compartments, shown in Figure 4.6, are in qualitative agreement with previously published experimental findings [82].

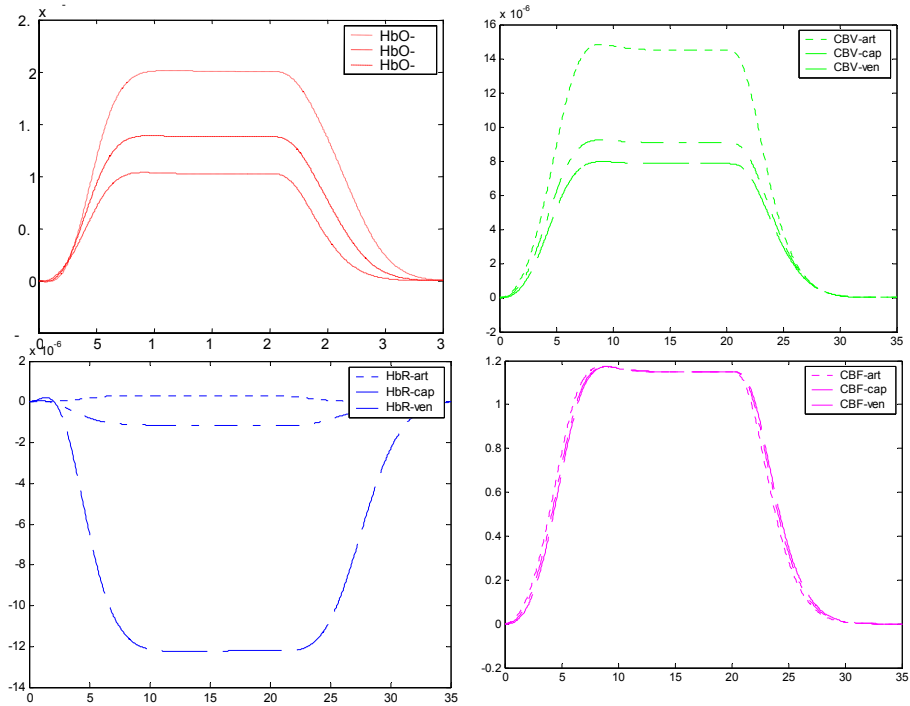


Figure 4.6: OE Windkessel model (individual contributions-long duration)

4.4.2 Mitochondrial metabolism model

A model of the oxygen transport dynamics between the arteriole, capillary, and venial compartments and the extra-vascular parenchyma tissue, which considers the differing permeability of these vessels is introduced. The oxygen extraction from all three compartments is based on recent experimental observations [75, 76, 96]. The system is built on the principle of oxygen diffusion caused by the gradient partial pressure of oxygen between the arteriole, capillary, and venial compartments and the extra-vascular tissue [71, 74].

To define oxygen transport between the vascular segments and the surrounding tissue a system of differential equations are derived which are dependent on (i) the flow changes described by the vascular component of the model which supply oxygen to the activated regions and (ii) changes in mitochondrial metabolism which result in changes in oxygen consumption in the extra-vascular tissue compartment [71, 74]. In this model it is assumed that the changes in oxygen extraction result primarily from an underlying mitochondrial function which gives rise to varying degrees of oxygen extraction in the three vascular compartments. A Gaussian function similar to the arterial dilation function is assumed for changes in the oxygen consumption which is caused by mitochondrial activity as outlined in Equation 93.

$$CMRO_{2,mit}(t) = CMRO_{2,mit,max}(0) - (CMRO_{2,mit,max} - CMRO_{2,mit}(0)) \exp\left(-\frac{(t - T_{peak})^2}{\sigma_c^2}\right) \quad (93)$$

where $CMRO_{2,mit}(0)$ represents the baseline $CMRO_2$ in the mitochondria and $CMRO_{2,mit,max}$ represents the maximum change of $CMRO_{2,mit}$ from its baseline value.

The intrinsic rate constant (k_{O_2}) for the oxygen extraction process and can be defined from the baseline relationships between oxygen saturation (SO_2), blood flow, and the oxygen content of the blood (c_nO_2) for the compartment and extra-vascular tissue. The effect of oxygen diffusion across both the arteriole and venial walls suggested by experiential findings [75, 76] is included in this model. Oxygen delivery in each vascular compartment is assumed to be caused by the gradient of the partial pressure of oxygen in the compartment and is proportional to the oxygen content of the blood in the vasculature. The model presented links the cerebral metabolic rate of

oxygen (CMRO₂) to cerebral blood flow (CBF) using the diffusivity for oxygen (kO₂) of the vascular compartment and is developed as an extension of the single compartment mitochondrial oxygen consumption model described in Chapter 3, Section 3.6. It is expected that the kO₂ of the capillary bed will be the highest and lower in the arterial and venous vascular compartment and range of these parameters is set accordingly[68]. The initial conditions can be expressed in matrix form using two matrices Y_1 and Y_2 .

$$Y_1 = \begin{bmatrix} F_{in} \cdot c_{in}o_2(0) - F_{ac} \cdot c_a o_2(0) \\ F_{ac} \cdot c_a o_2(0) - F_{cv} \cdot c_c o_2(0) \\ F_{cv} \cdot c_c o_2(0) - F_{out} \cdot c_v o_2(0) \end{bmatrix} \quad (94)$$

$$Y_2 = \begin{bmatrix} V_a \left\{ \begin{array}{l} \frac{1}{2}(c_{in}O_2(0) + c_a O_2(0)) \\ -c_t O_2(0) \end{array} \right\} & 0 & 0 \\ 0 & V_c \left\{ \begin{array}{l} \frac{1}{2}(c_a O_2(0) + c_c O_2(0)) \\ -c_t O_2(0) \end{array} \right\} & 0 \\ 0 & 0 & V_v \left\{ \begin{array}{l} \frac{1}{2}(c_c O_2(0) + c_v O_2(0)) \\ -c_t O_2(0) \end{array} \right\} \end{bmatrix} \quad (95)$$

The diffusivity for oxygen (kO₂) in the vascular compartments is related to the initial conditions and is represented by the array (Equation 96) where the first element kO₂ (1) represents the oxygen diffusivity of the arterial compartment, the second element kO₂ (2) represents the oxygen diffusivity of the capillary compartment, and third element kO₂ (3) represents the oxygen diffusivity of the venous compartment,

$$kO_2 = (Y_2)^{-1}Y_1 \quad (96)$$

The baseline $CMRO_2$ in every compartment is calculated as a function of the flow into the compartment (F), and the partial pressure of oxygen in the vascular compartments.

$$CMRO_2(0) = \left\{ \begin{aligned} & kO_{2,a} \left\{ \frac{1}{2} [c_{in}(0) + c_a(0)] - c_t(0) \right\} + kO_{2,c} \left\{ \frac{1}{2} [c_a(0) + c_c(0)] - c_t(0) \right\} \\ & + kO_{2,v} \left\{ \frac{1}{2} [c_c(0) + c_v(0)] - c_t(0) \right\} \end{aligned} \right\} \quad (97)$$

The temporal update is set up similar to Equation 57 (Chapter 3, Section 3.6). This model provides a set of four differential equations based on mass-balance which govern the flow of O_2 in the system.

Arterial compartment:

$$\frac{d(V_a(t).c_a O_2(t))}{dt} = \left\{ \begin{aligned} & F_{in}(t)c_{in} O_2(t) - F_{ac}(t)c_a O_2(t) \\ & - kO_{2,a} \left[\frac{1}{2} (c_{in} O_2(t) + c_a O_2(t)) - c_t O_2(t) \right] V_a(t) \end{aligned} \right\} \quad (98)$$

Capillary compartment:

$$\frac{d(V_c(t).c_c O_2(t))}{dt} = \left\{ \begin{aligned} & F_{ac}(t)c_c O_2(t) - F_{cv}(t)c_c O_2(t) \\ & - kO_{2,c} \left[\frac{1}{2} (c_a O_2(t) + c_c O_2(t)) - c_t O_2(t) \right] V_c(t) \end{aligned} \right\} \quad (99)$$

Venous compartment:

$$\frac{d(V_v(t).c_v O_2(t))}{dt} = \left\{ \begin{aligned} & F_{cv}(t)c_v O_2(t) - F_{out}(t)c_v O_2(t) \\ & - kO_{2,v} \left[\frac{1}{2} (c_c O_2(t) + c_v O_2(t)) - c_t O_2(t) \right] V_v(t) \end{aligned} \right\} \quad (100)$$

Extra-vascular tissue compartment:

$$\frac{dc_t O_2}{dk} = \begin{cases} kO_{2,a} \left\{ \frac{1}{2} [(c_{in}(t) + c_a(t)) - c_t(t)] \right\} + kO_{2,c} \left\{ \frac{1}{2} [(c_a(t) + c_c(t))cP_t(t)] \right\} \dots \\ + kO_{2,v} \left\{ \frac{1}{2} [(c_c(t) + c_v(t)) - c_t(t)] \right\} - CMRO_2(t) \end{cases} \quad (101)$$

Using a discrete time step integral, we can simultaneously solve for the temporal update on $c_N O_2$ in each of these four compartments, namely the three vascular compartments ($n \in$ arterial, capillary and venous) and the extra-vascular tissue compartment driven by the changes in flow, volume, and $CMRO_2$.

$$\frac{d(V_a(t) \cdot c_a O_2(t))}{dt} = \begin{cases} F_{in}(t)c_{in} O_2(t) - F_{ac}(t)c_a O_2(t) \\ -kO_{2,a} \left[\frac{1}{2} (c_{in} O_2(t) + c_a O_2(t)) - c_t O_2(t) \right] V_a(t) \end{cases} \quad (102)$$

$$V_a(t) \cdot \frac{d(c_a O_2(t))}{dt} + c_a O_2(t) \cdot \frac{d(V_a(t))}{dt} = \begin{cases} F_{in}(t)c_{in} O_2(t) - F_{ac}(t)c_a O_2(t) \dots \\ -kO_{2,a} \left[\frac{1}{2} (c_{in} O_2(t) + c_a O_2(t)) - c_t O_2(t) \right] V_a(t) \end{cases} \quad (103)$$

$$V_a(t) \cdot \frac{d(c_a O_2(t))}{dt} = \begin{cases} F_{in}(t)c_{in} O_2(t) - F_{ac}(t)c_w O_2(t) \dots \\ -kO_2 \left[\frac{1}{2} (c_{in} O_2(t) + c_c O_2(t)) - c_t O_2(t) \right] V_a(t) - c_a O_2(t) \cdot \frac{d(V_a(t))}{dt} \end{cases} \quad (104)$$

$$\frac{d(c_a O_2(t))}{dt} = \begin{cases} \frac{F_{in}(t)}{V_a(t)} c_{in} O_2(t) - \frac{F_{ac}(t)}{V_a(t)} c_a O_2(t) \dots \\ -kO_{2,a} \left[\frac{1}{2} (c_{in} O_2(t) + c_a O_2(t)) - c_t O_2(t) \right] - \frac{c_a O_2(t)}{V_a(t)} \cdot \frac{d(V_a(t))}{dt} \end{cases} \quad (105)$$

$$\frac{d(c_a O_2(t))}{dt} = \left\{ \begin{array}{l} \frac{F_{in}(t)}{V_a(t)} c_{in} O_2(t) - \frac{F_{ac}(t)}{V_a(t)} \left(c_a O_2(t-1) + \frac{d(c_a O_2(t))}{dt} \right) \dots \\ - k O_{2,a} \left[\frac{1}{2} \left(c_{in} O_2(t) + \left(c_a O_2(t-1) + \frac{d(c_a O_2(t))}{dt} \right) \right) \right] \dots \\ - \left(c_t O_2(t-1) + \frac{d(c_t O_2(t))}{dt} \right) \left[\frac{c_a O_2(t-1) + \frac{d(c_a O_2(t))}{dt}}{V_a(t)} \right] \cdot \frac{d(V_a(t))}{dt} \end{array} \right. \quad (106)$$

$$\left[\begin{array}{l} \frac{d(c_a O_2(t))}{dt} \\ \left[1 + \frac{F_{ac}(t)}{V_a(t)} + \frac{k O_{2,a}}{2} + \frac{1}{V_a(t)} \cdot \frac{d(V_a(t))}{dt} \right] \\ \frac{d(c_t O_2(t))}{dt} [-k O_{2,a}] \end{array} \right] = \left\{ \begin{array}{l} c_{in} O_2(t) \left[\frac{F_{in}(t)}{V_w(t)} - \frac{k O_{2,a}}{2} \right] \\ + (c_a O_2(t-1)) \\ \left[-\frac{F_{ac}(t)}{V_a(t)} - \frac{k O_{2,a}}{2} - \frac{1}{V_a(t)} \cdot \frac{d(V_a(t))}{dt} \right] \\ + (c_t O_2(t-1)) [k O_{2,a}] \end{array} \right. \quad (107)$$

Similarly we can get expressions for the capillary and venous compartment. Additional terms are obtained in the temporal updates of these compartments because the pressure of the blood coming into the compartment depends on the temporal evolution of blood flow in the vasculature and hence is a function of time that needs to be updated as well.

$$\frac{d(c_c(t) \cdot p_c O_2(t))}{dt} = \left\{ \begin{array}{l} F_{ac}(t) c_a O_2(t) - F_{cv}(t) c_c O_2(t) \\ - k O_{2,c} \left[\frac{1}{2} (c_a O_2(t) + c_c O_2(t)) - c_t O_2(t) \right] V_c(t) \end{array} \right. \quad (108)$$

$$V_c(t) \cdot \frac{d(c_c O_2(t))}{dt} + p_c O_2(t) \cdot \frac{d(c_c(t))}{dt} = \left\{ \begin{array}{l} F_{ac}(t) c_a O_2(t) - F_{cv}(t) c_c O_2(t) \dots \\ - k O_{2,c} \left[\frac{1}{2} (c_a O_2(t) + c_c O_2(t)) - c_t O_2(t) \right] V_c(t) \end{array} \right. \quad (109)$$

$$V_c(t) \cdot \frac{d(p_c O_2(t))}{dt} \Bigg\} = \left\{ \begin{array}{l} F_{ac}(t)c_a O_2(t) - F_{cv}(t)c_c O_2(t) \dots \\ -kO_{2,c} \left[\frac{1}{2}(c_a O_2(t) + c_c O_2(t)) - c_t O_2(t) \right] V_c(t) - c_c O_2(t) \cdot \frac{d(V_c(t))}{dt} \end{array} \right. \quad (110)$$

$$\frac{d(c_c O_2(t))}{dt} \Bigg\} = \left\{ \begin{array}{l} \frac{F_{ac}(t)}{V_c(t)} c_a O_2(t) - \frac{F_{cv}(t)}{V_c(t)} c_c O_2(t) \dots \\ -kO_{2,c} \left[\frac{1}{2}(c_a O_2(t) + c_c O_2(t)) - c_t O_2(t) \right] - \frac{c_c O_2(t)}{V_c(t)} \cdot \frac{d(V_c(t))}{dt} \end{array} \right. \quad (111)$$

$$\frac{d(c_c O_2(t))}{dt} \Bigg\} = \left\{ \begin{array}{l} \frac{F_{ac}(t)}{V_c(t)} \left(c_a O_2(t-1) + \frac{d(c_a O_2(t))}{dt} \right) - \frac{F_{cv}(t)}{V_c(t)} \left(c_c O_2(t-1) + \frac{d(c_c O_2(t))}{dt} \right) \dots \\ -kO_{2,c} \left[\frac{1}{2} \left\{ \left(c_a O_2(t-1) + \frac{d(c_a O_2(t))}{dt} \right) + \left(c_c O_2(t-1) + \frac{d(c_c O_2(t))}{dt} \right) \right\} \dots \right. \\ \left. - \left(c_t O_2(t-1) + \frac{d(c_t O_2(t))}{dt} \right) \right] - \frac{\left(c_c O_2(t-1) + \frac{d(c_c O_2(t))}{dt} \right)}{V_c(t)} \cdot \frac{d(V_c(t))}{dt} \end{array} \right. \quad (112)$$

$$\left. \begin{array}{l} \frac{d(c_a O_2(t))}{dt} \left[-\frac{F_{ac}(t)}{V_c(t)} + \frac{kO_{2,c}}{2} \right] \\ + \frac{d(c_c O_2(t))}{dt} \left[1 + \frac{F_{cv}(t)}{V_c(t)} + \frac{kO_{2,c}}{2} + \frac{1}{V_c(t)} \cdot \frac{d(V_c(t))}{dt} \right] \\ + \frac{d(c_t O_2(t))}{dt} [-kO_{2,c}] \end{array} \right\} = \left\{ \begin{array}{l} c_a O_2(t-1) \left[\frac{F_{ac}(t)}{V_c(t)} - \frac{kO_{2,c}}{2} \right] \\ + (c_c O_2(t-1)) \\ \left[-\frac{F_{cv}(t)}{V_c(t)} - \frac{kO_{2,c}}{2} - \frac{1}{V_c(t)} \cdot \frac{d(V_c(t))}{dt} \right] \\ + (c_t O_2(t-1)) [kO_{2,c}] \end{array} \right. \quad (113)$$

Similarly in the venous compartment we get the temporal update

$$\left. \begin{aligned} & \frac{d(c_c O_2(t))}{dt} \left[-\frac{F_{cv}(t)}{V_v(t)} + \frac{kO_{2,v}}{2} \right] \\ & + \frac{d(c_v O_2(t))}{dt} \left[1 + \frac{F_{out}(t)}{V_v(t)} + \frac{kO_{2,v}}{2} + \frac{1}{V_v(t)} \cdot \frac{d(V_v(t))}{dt} \right] \\ & + \frac{d(c_t O_2(t))}{dt} [-kO_{2,v}] \end{aligned} \right\} = \left\{ \begin{aligned} & c_c O_2(t-1) \left[\frac{F_{cv}(t)}{V_v(t)} - \frac{kO_{2,v}}{2} \right] \\ & + (c_v O_2(t-1)) \\ & \left[-\frac{F_{out}(t)}{V_v(t)} - \frac{kO_{2,v}}{2} - \frac{1}{V_v(t)} \cdot \frac{d(V_v(t))}{dt} \right] \\ & + (c_t O_2(t-1)) [kO_{2,v}] \end{aligned} \right\} \quad (114)$$

The oxygen content in the extra-vascular tissue compartment is described to evolve in time according to Equation 115,

$$\frac{dc_t O_2}{dk} = \left\{ \begin{aligned} & kO_{2,a} \left\{ \frac{1}{2} [(c_{in}(t) + c_a(t)) - c_t(t)] \right\} + kO_{2,c} \left\{ \frac{1}{2} [(c_a(t) + c_c(t)) - c_t(t)] \right\} \\ & + kO_{2,v} \left\{ \frac{1}{2} [(c_c(t) + c_v(t)) - c_t(t)] \right\} - CMRO_2(t) \end{aligned} \right\} \quad (115)$$

The increments calculated in Equation 115 are added to the values of oxygen content at the previous time points to get the values of oxygen content at the present time point.

$$\frac{dc_t O_2}{dk} = \left\{ \begin{aligned} & kO_{2,a} \left\{ \frac{1}{2} \left[\left(c_{in}(t) + c_a(t-1) + \frac{d(c_a O_2(t))}{dt} \right) - \left(c_t(t-1) + \frac{d(c_t O_2(t))}{dt} \right) \right] \right\} \\ & + kO_{2,c} \left\{ \frac{1}{2} \left[\left(c_a(t-1) + \frac{d(c_a O_2(t))}{dt} \right) + \left(c_c(t-1) + \frac{d(c_c O_2(t))}{dt} \right) \right] \right. \\ & \quad \left. - \left(c_t(t-1) + \frac{d(c_t O_2(t))}{dt} \right) \right\} \\ & + kO_{2,v} \left\{ \frac{1}{2} \left[\left(c_c(t-1) + \frac{d(c_c O_2(t))}{dt} \right) + \left(c_v(t-1) + \frac{d(c_v O_2(t))}{dt} \right) \right] \right. \\ & \quad \left. - \left(c_t(t-1) + \frac{d(c_t O_2(t))}{dt} \right) \right\} \\ & - CMRO_2(t) \end{aligned} \right\} \quad (116)$$

$$\left. \begin{aligned}
& \frac{d(c_a O_2(t))}{dt} \left[-\frac{kO_{2,a}}{2} - \frac{kO_{2,c}}{2} \right] \\
& + \frac{d(c_c O_2(t))}{dt} \left[-\frac{kO_{2,c}}{2} - \frac{kO_{2,v}}{2} \right] \\
& + \frac{d(c_v O_2(t))}{dt} \left[-\frac{kO_{2,v}}{2} \right] \\
& + \frac{dc_t O_2}{dk} [1 + kO_{2,a} + kO_{2,c} + kO_{2,v}]
\end{aligned} \right\} = \begin{cases}
c_{in}(t) \left[\frac{kO_{2,a}}{2} \right] \\
+ c_a(t-1) \left[\frac{kO_{2,a}}{2} + \frac{kO_{2,c}}{2} \right] \\
+ c_c(t-1) \left[\frac{kO_{2,c}}{2} + \frac{kO_{2,v}}{2} \right] \\
+ c_v(t-1) \left[\frac{kO_{2,v}}{2} \right] \\
+ c_t(t-1) [-kO_{2,a} - kO_{2,c} - kO_{2,v}] \\
- CMRO_2(t)
\end{cases} \quad (117)$$

This yields the set of temporal update equations expressed in matrix form as follows,

$$\begin{bmatrix} \frac{dc_{in} O_2}{dt} \\ \frac{dc_a O_2}{dt} \\ \frac{dc_c O_2}{dt} \\ \frac{dc_v O_2}{dt} \\ \frac{dc_t O_2}{dt} \end{bmatrix} = (A)^{-1} Y \quad (118)$$

where

$$A(t) = \begin{bmatrix}
1 & \begin{pmatrix} 0 \\ 1 + \frac{F_{ac}(t)}{V_a(t)} \dots \\ \dots + \frac{kO_{2,a}}{2} \\ \dots - \frac{1}{V_a(t)} \\ \dots \frac{d(V_a(t))}{dt} \end{pmatrix} & 0 & 0 & 0 & 0 \\
0 & \begin{pmatrix} -\frac{F_{ac}(t)}{V_c(t)} \dots \\ \dots + \frac{kO_{2,c}}{2} \\ \dots + \frac{1}{V_c(t)} \\ \dots \frac{d(V_c(t))}{dt} \end{pmatrix} & \begin{pmatrix} 1 + \frac{F_{cv}(t)}{V_c(t)} \\ \dots + \frac{kO_{2,c}}{2} \\ \dots + \frac{1}{V_c(t)} \\ \dots \frac{d(V_c(t))}{dt} \end{pmatrix} & 0 & 0 & -kO_{2,c} \\
0 & 0 & \begin{pmatrix} -\frac{F_{cv}(t)}{V_v(t)} \dots \\ \dots + \frac{kO_{2,v}}{2} \\ \dots + \frac{1}{V_v(t)} \\ \dots \frac{d(V_v(t))}{dt} \end{pmatrix} & \begin{pmatrix} 1 + \frac{F_{out}(t)}{V_v(t)} \dots \\ \dots + \frac{kO_{2,v}}{2} \\ \dots + \frac{1}{V_v(t)} \\ \dots \frac{d(V_v(t))}{dt} \end{pmatrix} & 0 & -kO_{2,v} \\
0 & \begin{pmatrix} -\frac{kO_{2,a}}{2} \dots \\ \dots - \frac{kO_{2,c}}{2} \end{pmatrix} & \begin{pmatrix} -\frac{kO_{2,c}}{2} \dots \\ \dots - \frac{kO_{2,v}}{2} \end{pmatrix} & \begin{pmatrix} -\frac{kO_{2,v}}{2} \end{pmatrix} & \begin{pmatrix} 1 + kO_{2,a} \dots \\ \dots + kO_{2,c} \\ \dots + kO_{2,v} \end{pmatrix} & 0
\end{bmatrix} \tag{119}$$

and

$$Y(t) = \begin{bmatrix} 1 & 0 & 0 & 0 & 0 \\ 0 & \begin{pmatrix} \frac{F_{in}(t)}{V_w(t)} \dots \\ \frac{kO_{2,a}}{2} \end{pmatrix} & \begin{pmatrix} \frac{F_{ac}(t)}{V_a(t)} \dots \\ \frac{kO_{2,a}}{2} \\ \frac{1}{V_a(t)} \frac{d(V_a(t))}{dt} \end{pmatrix} & 0 & 0 \\ 0 & \begin{pmatrix} \frac{F_{ac}(t)}{V_c(t)} \dots \\ \frac{kO_{2,c}}{2} \end{pmatrix} & \begin{pmatrix} \frac{F_{cv}(t)}{V_c(t)} \dots \\ \frac{kO_{2,c}}{2} \\ \frac{1}{V_c(t)} \frac{d(V_c(t))}{dt} \end{pmatrix} & 0 & 0 \\ 0 & 0 & \begin{pmatrix} \frac{F_{cv}(t)}{V_v(t)} \dots \\ \frac{kO_{2,v}}{2} \end{pmatrix} & \begin{pmatrix} \frac{F_{out}(t)}{V_v(t)} \dots \\ \frac{kO_{2,v}}{2} \\ \frac{1}{V_v(t)} \frac{d(V_v(t))}{dt} \end{pmatrix} & 0 \\ \frac{kO_{2,a}}{2} & \begin{pmatrix} \frac{kO_{2,a}}{2} \dots \\ \frac{kO_{2,c}}{2} \end{pmatrix} & \begin{pmatrix} \frac{kO_{2,c}}{2} \dots \\ \frac{kO_{2,v}}{2} \end{pmatrix} & \begin{pmatrix} \frac{kO_{2,v}}{2} \end{pmatrix} & \begin{pmatrix} -kO_{2,a} \dots \\ -kO_{2,c} \\ -kO_{2,v} \end{pmatrix} \end{bmatrix} \quad (120)$$

The differential increments calculated in Equation 118 are added to the values of oxygen content at the previous time points to get the values of oxygen content at the present time point.

$$c_n O_2(t) = c_n O_2(t-1) + \frac{d(c_n O_2(t))}{dt} \cdot dt \quad (121)$$

where $n \in \{w, t\}$ and 'w' represents the oxygen content of the blood in the vascular compartment and the subscript 't' represents the oxygen content in the tissue. $dc_N O_2/dt$ represents an array of oxygen content increases in the vascular compartments as they relate to the hemodynamic changes created by activation and increased metabolic activity. The first element of the array dc_{in}/dt is the incoming oxygen content which is assumed to be constant, the second element of the array dc_a/dt , represents the change in the oxygen content in the arterial compartment, the third element of the array, dc_c/dt , represents the change in the oxygen content in the capillary compartment, the fourth element of the array, dc_v/dt , represents the change in the oxygen content in the venous compartment, and the fifth element of the array, dc_t/dt , represents the change in the oxygen content in the tissue surrounding the vasculature under consideration. In the extra-vascular compartment, the change in the amount of oxygen is the difference between oxygen delivered to the tissue and oxygen consumed[68].

The mean arterial blood pressure represents the input pressure to the model (P_{in}) is assumed to be constant at 112 mm of Hg through the whole experiment. The oxygen content in each compartment is used to calculate the saturation and partial pressure of oxygen in that compartment. This is done using the dissociation curve described in Chapter 3. Changes in concentrations of oxyhemoglobin and deoxyhemoglobin are,

$$\Delta[HbO_2] = HbT \cdot SO_2 \quad (122)$$

$$\Delta[Hb] = HbT \cdot (1 - SO_2) \quad (123)$$

where SO_2 is the oxygen saturation and HbT is the blood volume in the compartment.

4.4.2.1. Results of the mitochondrial metabolism model

A χ^2 nonlinear fit of flow, volume as well as the changes in the concentration of deoxyhemoglobin and oxyhemoglobin to the experimentally measured values of $\Delta[\text{HbO}_2]$ and $\Delta[\text{Hb}]$ was performed. The baseline oxygen saturation and volume fraction in every compartment and $\text{CMRO}_2(0)$, $\text{CMRO}_{2, \text{min}}$, T_{peak} and σ_c^2 are estimated to define the oxygen consumption caused by mitochondria in addition to the flow and volume parameters defined in the previous sections. The predicted CMRO_2 function in the mitochondria was compared to the calculated CMRO_2 function using calculated values of $\Delta[\text{HbO}_2]$, $\Delta[\text{Hb}]$, $\Delta[\text{HbT}]$ and ΔCBF which were predicted using the multi-compartment model.

The data that the model predicted for changes in deoxyhemoglobin ($\Delta[\text{Hb}]$) and changes in blood volume ($\Delta[\text{HbT}]$) was used to predict the BOLD signal using Equation 36. Thus in this model several degrees of freedom were added to the model by assuming a function for CMRO_2 caused by mitochondrial activity. Oxygen diffusivity for every compartment was calculated allowing us to for oxyhemoglobin, $\Delta[\text{HbO}_2]$ and deoxyhemoglobin, $\Delta[\text{Hb}]$ along with the flow and volume as described in the preceding sections.

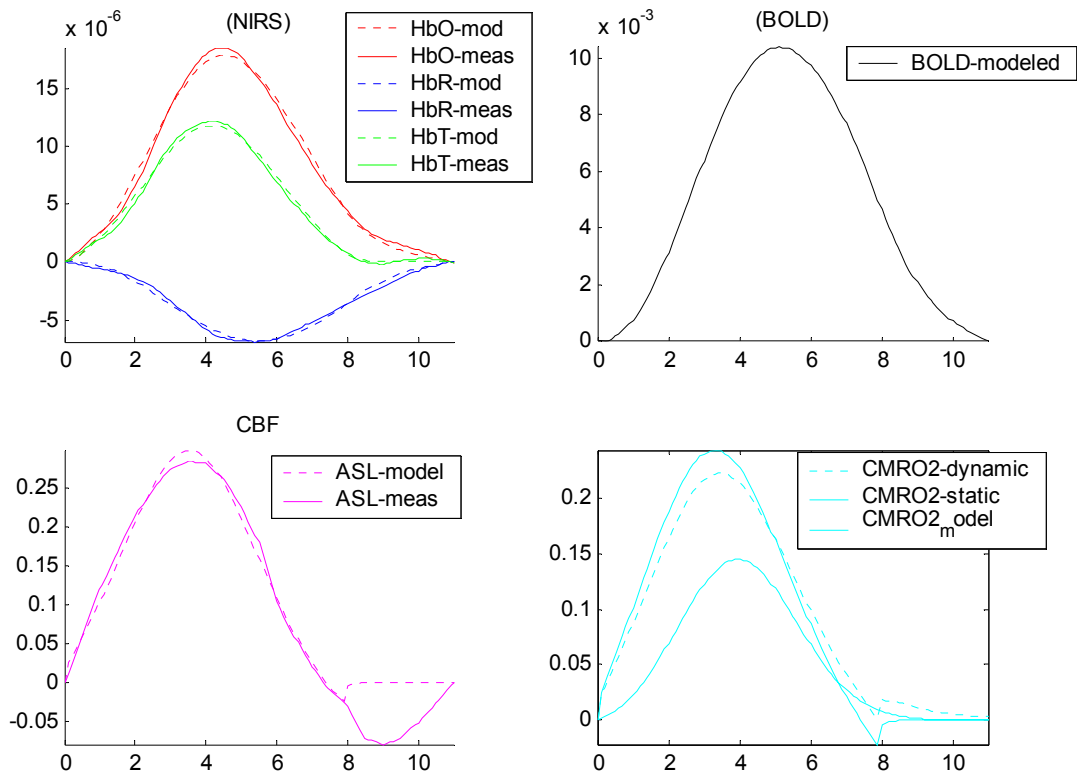


Figure 4.7: Multicompartment Windkessel model (mitochondrial model)

4.4.2.2 Compartmentalized changes in hemodynamics

It was observed that the majority of the contrast of oxy- and deoxy-hemoglobin changes arose from the venous structures. These large changes are the result of the large wash-out effects in this compartment, which has the lowest initial SO_2 . From the model, venous oxygen saturation was assumed to be around 62-66%. This low saturation allows large changes in the blood oxygenation of the venous compartment in response to the same magnitude of increased blood flow and similar volume changes as

the other compartments. In comparison, the oxygen saturation of the arteriole compartment (95%) is very close to that of the feeding (artery) blood (98.7%). Thus in the arteriole compartment, changes in oxy- and deoxy-hemoglobin arise from blood volume changes with little direct influence of increased flow. This result can be explained by the direct contribution of blood flow changes, which wash-out the baseline deoxy-hemoglobin concentration.

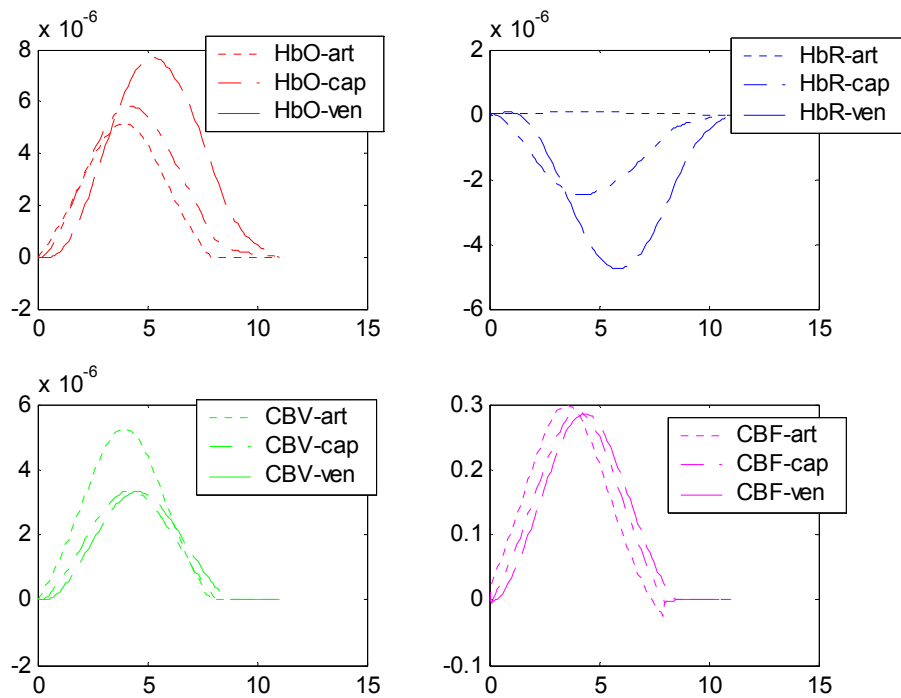


Figure 4.8: Mitochondrial Windkessel model (individual vascular contributions)

Similar to the oxygen extraction and flow-volume model set-up, the mitochondrial activity basis function was also modified to describe the temporal hemodynamics involved in longer duration stimuli. Both the arterial resistance and

oxygen extraction functions model were convolved with the input stimulus function (Equation 124).

$$CMRO_{2,mit}(t) = \left\{ \begin{array}{l} CMRO_{2,mit,max} + (CMRO_{2,mit,max} - CMRO_{2,mit}(0)) \exp\left(\frac{(t - T_{peak})^2}{\sigma_c^2}\right) \\ \otimes N(t) \end{array} \right. \quad (124)$$

Based on the theory used to describe similar responses in deductive modeling [49], a simple inhibitory feedback system is used, in which the neural response $N(t)$ is treated as the difference between an excitatory input $s(t)$ and an inhibitory input $I(t)$ (refer Equation 91 and 92). Plots of the volumes and flow in the Windkessel compartment are shown in Figure 4.9. The ratio of dynamic $\Delta CMRO_2 / CMRO_{2,0}$ were also calculated with the optimized parameters.

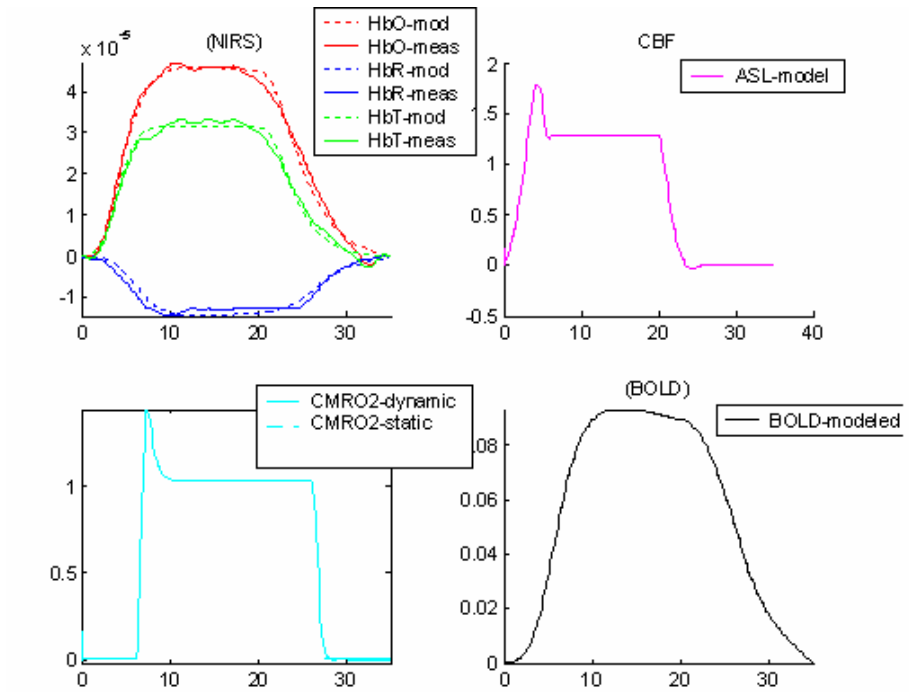


Figure 4.9: Mitochondrial Windkessel model (long duration)

Vascular changes were modeled in the arteriole, capillary, and venous compartments. The time-courses plotted in Figure 4.10 show the changes in these three compartments.

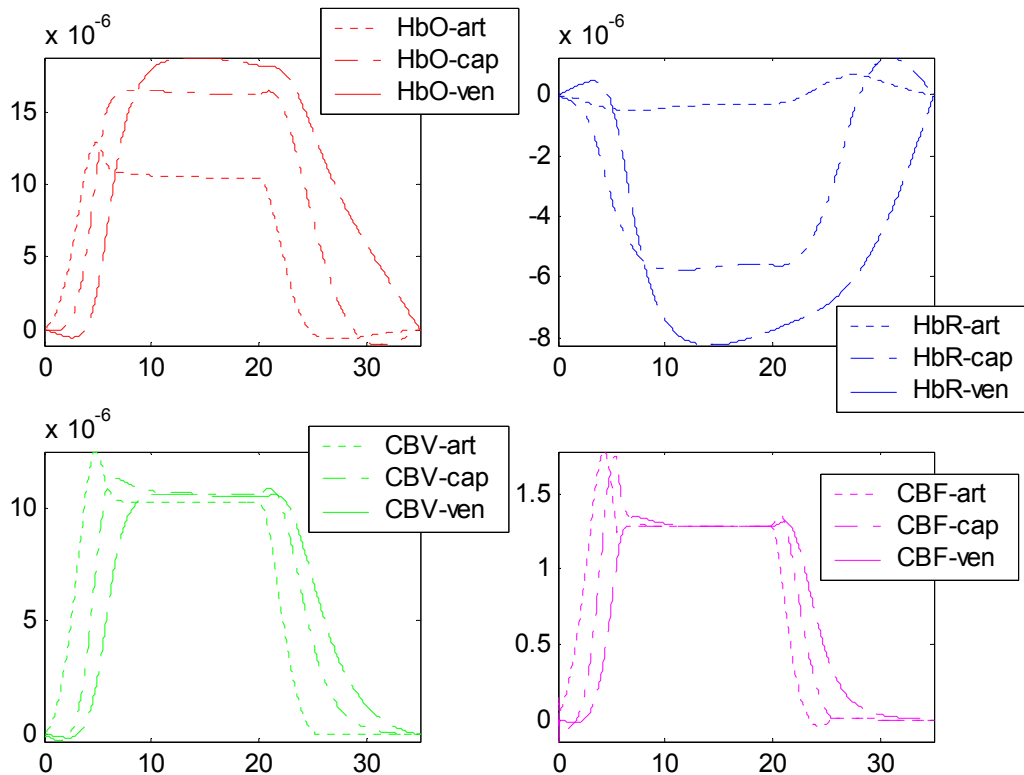


Figure 4.10: Mitochondrial Windkessel model (individual contributions-long duration)

4.5 Comparison of single and multi compartment model

To further examine the validity of the proposed multicompartment model, results were compared to the previously described single-compartment Windkessel models [5, 57] (results in Chapter 7). The single-compartment Windkessel model fits to the experimental data demonstrated shortcomings of this model for estimating the oxygenation component of the hemodynamic response. This result is in agreement with the similar findings by Zheng et al in a deductive multi-compartment model [7].

Although simpler, single-compartment models have been previously demonstrated to model fMRI data [3, 5, 6], the higher temporal resolution and spectroscopic information of optical imaging requires a more detailed model. In agreement with previous work [7], the multi-compartment model performed better than the single-compartment formulation, even after the additional degrees-of-freedom for the more complicated model were accounted for. Comparison of this previously published single compartment model and the presented multiple-compartment Windkessel model revealed that both models accurately reproduced the relationship between flow and volume. In contrast, the multi-compartment model performed significantly better at modeling oxy- and deoxy-hemoglobin measurements, as well as the overall data set (detailed results in Chapter 7).

4.6 Chapter summary

The proposed multi-compartment model makes three significant contributions: (i) The multi-compartment model shows significant improvements in the modeling of measured oxy- and deoxy-hemoglobin changes with the inclusion of oxygen transport in the arterial, capillary, venous and tissue compartment; (ii) The model allows the estimation of compartmentalized hemodynamic time-courses from imaging measurements; and (iii) The bottom-up framework of this model allows for inclusion of multimodality data in a Bayesian model, which improves the accuracy of the estimated states and compensates for uneven measurement of noise across modalities.

CHAPTER 5

DEDUCTIVE NEURAL MODEL

The aim of noninvasive imaging such as near infrared imaging and functional magnetic resonance imaging is to investigate the neural correlates of specific cognitive processes, their temporal and spatial evolution, and their relationship to measured hemodynamics. The standard approach used in hemodynamic modeling is to relate imaging measurements to underlying neural processes that give rise to the measured response. Deductive models with black box formulations involve linear convolution that relate experimentally designed inputs through a hemodynamic response function, to observed oxygenation dependent signals. However, such models are blind to the causal mechanisms that underlie observed hemodynamic responses. Measured changes in cerebral blood flow, volume, and oxygenation have a nonlinear indirect relationship with evoked neuronal activity and electrophysiological changes. Moreover, these hemodynamic changes reflect the consequences of these underlying phenomena of the neuro-metabolic (oxygen metabolism) and neuro-vascular (vaso-dilatory) coupling. The ability to measure hemodynamic responses with imaging methods like functional T_2^* -weighted (BOLD) MRI has been invaluable in functional organization mapping of the brain. However, these measurements are dependent on both vascular and metabolic function and thus have an ambiguous and non-linear relationship with underlying electrical and metabolic responses[6]. The physiological interpretation of hemodynamic

changes is complicated by the differences in mechanical properties of the vasculature and baseline physiological values, such as basal blood volume, flow, and oxygen extraction of individual subjects. Intra- and inter-subject variations in baseline physiology result in significant variations in the evoked hemodynamic responses [51, 97, 98]. The utility and repeatability of hemodynamic based imaging methods can be improved if they provide direct information about neuronal function, such as changes in the cerebral metabolic rate of oxygen ($CMRO_2$) which is less susceptible to baseline variability.

Recent developments have focused on how hemodynamic responses are generated and include biophysical input-output state models of the neurovascular coupling with neural and hemodynamic state equations. Forward models with parameters at the neural level are used to model the whole causal chain from external stimuli, via induced neural dynamics, to observed responses. The aim of the two models presented in this chapter is to explore the relation between hemodynamic responses, input stimulus and the mechanisms that translate local neural dynamics into observed hemodynamic oxygenation signals. The multicompartiment model presented in this research is unique since it provides a direct relationship between input stimulus (described by a simple step function that depends on experimental timing) and the evoked hemodynamic response. It provides the missing link between neural response and the measured hemodynamic response. This biophysical neurovascular model is extensively explored in the context of vessel compliance and stimulus duration. The described deductive model has the inherent advantage of reduced number of model

parameters as compared to inductive models. This manifests as computational efficiency and removes interdependencies of parameter definitions that hinder accurate and unique solutions to the system.

5.1 Previously published neurovascular model

The Balloon and Windkessel model described in previous chapters provide the foundation for detailed biophysical models of neurovascular coupling. These models predict how increases in regional blood flow dilate a venous balloon which leads to increased blood volume and decrease deoxyhemoglobin content with an overcompensating supply of oxygenated blood which surpasses consumption created by activation. The assumptions of these models and their impact have been explored in Chapter 3. The vascular model was first extended by Friston et al. [12, 13] to include the effects of external inputs, on an autoregulated vasodilatory signal, assuming that the relationship between evoked neural activity and blood flow is linear.

This linear relationship had been demonstrated directly in animal studies by combining optical imaging, laser Doppler flowmetry and multielectrode recordings [14, 15], and indirectly in perfusion studies of the human brain [16]. As detailed in Figure 5.1, the extended input-state-output model of Friston [13] comprises four hemodynamic state variables, combined into a vector x , whose interactions are described by differential equations with five hemodynamic parameters. These parameters have an explicit biophysical meaning. At the beginning of the hemodynamic cascade, a flow-inducing signal is triggered by neural responses to experimental inputs, which are

weighted by different efficacies which represent the neural parameters of the model. The flow inducing signal results in measurable changes in cerebral hemodynamics namely blood volume, blood flow, oxy- and deoxyhemoglobin.

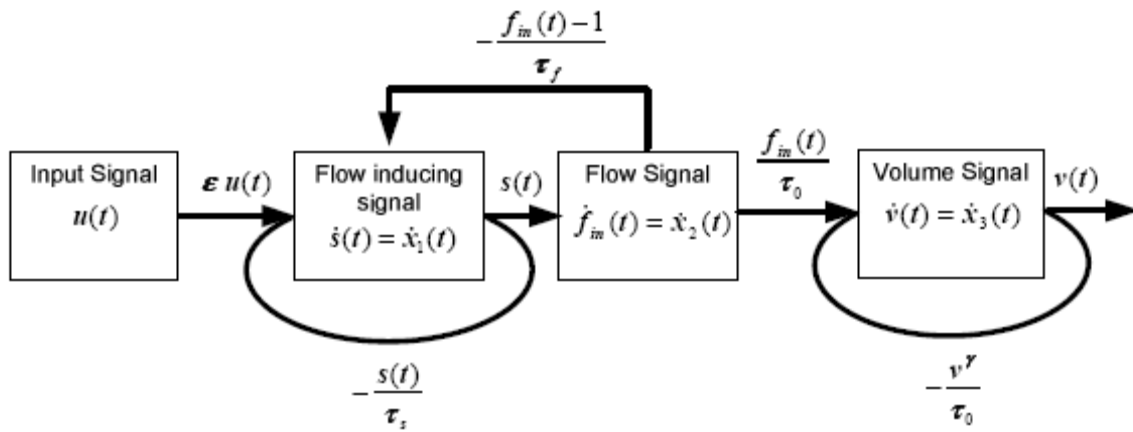


Figure 5.1: Neurovascular model for relating stimulus to blood volume and flow [70]

5.1.1 Hemodynamic model details

The single compartment neurovascular model published initially by Friston et al combines the Balloon/Windkessel model with a simple dynamic model of changes in cerebral blood flow caused by neural activity [70]. The model is a single input single output (SISO) system with a stimulus function as input. This stimulus has a time evolution that is experimentally designed and elicits a neural signal which induces increased flow into the locally activated regions of the brain and results in changes in the blood volume which is an output of the system. Changes in blood volume can be measured using various imaging techniques as described in previous chapters. The model has five primary parameters and three state variables each with its corresponding differential equation.

The system of coupled differential equations expresses how each state variable changes over time and its relation to other variables in the system. The system of nonlinear differential equations reveals interdependencies and physiological relationships between neurovascular variables. The state equations and the output nonlinearly define a static nonlinear function of the state variables that give the output and specify the form of the model. The parameters determine a specific realization of the model and can be determined by minimization of error between model predicted response variables and hemodynamic data measured using imaging modalities such as NIRS or fMRI. The output (blood volume) is a nonlinear function of the intermediate state variables and parameters that define its temporal evolution and spatial extent.

5.1.2 State equations of the neurovascular model

The dynamic system that links the synaptic activity with the cerebral blood flow is linear and can be described by the following equation

$$\dot{f}_{in} = s \quad (125)$$

where f_{in} is the blood flow entering the vascular compartment and s is a result of the neural signal and is a flow inducing signal. The signal is assumed to be a result of neuronal responses to the input, which is the experimentally designed stimulus function, $u(t)$.

$$\dot{s} = \epsilon u(t) - \frac{s}{\tau_s} - \frac{f_{in} - 1}{\tau_f} \quad (126)$$

ϵ , τ_s , and τ_f are parameters that represent the efficacy of the neuronal response and represent the effectiveness with which the stimulus input causes an increase in the neural signal, the rate constant for signal decay or elimination, and the rate constant for autoregulatory feedback from blood flow respectively. The existence of the feedback term can be inferred from: (i) poststimulus undershoots in rCBF [99] and (ii) the well-characterized vasomotor signal in optical imaging [100]. Both support the notion of local closed-loop feedback mechanisms as modeled in Equations 126 and 127. These equations represent the neural activity that governs the arterial dilation caused by the action of vasoactive agents. These agents are believed to be released from the astrocytic processes [101, 102] in contact with cerebral arteries and directly influence changes in blood flow and volume during cerebral activation.

The next equation is the Balloon model vascular component of the neurovascular model. Blood flow coming into and leaving the vascular compartment along with the blood vessel compliance determine the rate of change of blood volume in the local cerebral vasculature.

$$\tau_0 \dot{v} = f_{in} - f_{out} = f_{in} - v^\gamma \quad (127)$$

Equation 127 represents the normalized change in blood volume and reflects the difference between inflow, f_{in} and outflow, f_{out} of blood from the vascular compartment with a time constant (mean transit time), τ_0 . Outflow is a function of volume that models the balloon-like capacity of the vascular compartment which can expel blood at a

greater rate when distended. Compliance can be modeled with a single parameter that describes the elasticity coefficient which determines the expansion of the blood vessel against the surrounding tissue and intracranial pressure.

5.2 Contribution of the current research to the neurovascular model

The published neurovascular model described in the previous section was developed for hemodynamic experimental data measured using functional magnetic resonance imaging. There are three contributions made by this research to this model (i) exploration of the effect of vascular compliance on flow-volume ratio and the importance of quantitatively defining this compliance coefficient for diagnosis of disease in clinical settings; (ii) development of novel tomographic images of CBF and CMRO₂ using measured NIRS data and (iii) development of a multi-compartment model to describe the entire chain of cascading effects from the presentation of stimulus to translation onto neural activity which reflects as changes in the measurable hemodynamic signals. The multi-compartment model presents a biophysical model of the cerebral neurovascular system in the context of a physiologically relevant model that defines the compartmentalized hemodynamics in the arterioles, capillaries and veins. Specific motivations behind the contributions made in this research are described below.

5.2.1 Determination of compliance coefficients

The first contribution of this research is the setting up a new framework to include multimodality data (NIRS-HbT and ASL-CBF) for a more accurate and unique solution to the neurovascular model parameters based on vessel compliance [62]. This framework can be extended in future work to also include neural activity parameters by adding intermediate states using experimental data which can be measured by either noninvasively by electroencephalography (EEG) and magneto encephalography (MEG), or invasively in animal models using electrode recording techniques.

In practice, defining compliance coefficient precisely based on multimodality data is important in studies that explore weakening vessels (leading to reduced flow-volume ratio) that can be used in the diagnosis and treatment of conditions such as aneurysms [63]. In the clinical setting, flow-volume relationship which show increments from control/normal ratio values measured in healthy subjects, could aid in diagnosis of hardening of arteries (e.g. conditions such as atherosclerosis) which lead to diseases such as stroke. Such data describing detailed response of vessel compliance its relationship to blood flow and blood volume could also be used to provide insight into the normal aging process [62].

The compliance parameter has been determined as a state variable in previous chapters of this research using single and multiple compartment inductive models. The aim here is to explore the functional parameters that govern arterial dilation caused by the action of vasoactive agents. While this presents an effective approach to defining the underlying phenomena of cerebral activation, temporal basis functions add several

degrees of freedom to describe the biophysical underpinnings of each imaging modality and its corresponding measurements. This can lead to non-unique solutions of parameters and temporal basis functions which may not necessarily have direct physical implications on the monitoring of disease and health. Another disadvantage of using inductive modeling is the coupling of parameters which creates interdependencies that are very difficult to resolve as the number of minimization parameters exceeds the number of unique data sets (flow, volume and oxygenation) available for fitting routines.

The two biophysical neurovascular models presented in this chapter are extensively explored to include multimodality data in the context of determining vessel compliance and the effect of stimulus duration. It is important to note that this model has only five optimization parameters compared to the temporal basis model which has over ten parameters to describe the flow volume relationship. In comparison to the previously presented single and multi compartment inductive models, there is a large reduction in the number of optimization parameters. This manifests as computational efficiency and also results in the removal of interdependencies of parameter definitions that can prevent accurate and unique solutions of the system under consideration.

5.2.2 Three compartment flow-volume model

The advancement of fMRI noninvasive methods and optical imaging experiments in human and animal models have enabled the measurement of hemodynamic changes at a higher temporal and spatial resolution than has been

previously possible [7, 79-82]. Invasive experiments can provide segmentation of cerebral vasculature into arteriolar, capillary and venous compartments based on diameter, and spatial location of vessels and thus warrant the use of multi-compartment models of the vascular network which describe hemodynamic changes in three vascular compartments, namely the arterial, capillary, and venous compartments [7, 83].

In this chapter, a multi-compartment model of the vascular flow and volume changes to model the composite hemodynamic response is presented. The three compartment vascular model includes flow volume dynamics observed by introducing compliant capillary and venous compartments that respond to changes in increased blood flow based on the compliance of the vessels they describe [82]. Further, the individual contribution and temporal evolution of cerebral blood volume and blood flow in each vascular compartment is examined and compared to the results obtained using the multicompartment inductive model presented in Chapter 4. This provides cross-validation of the assumptions made in the model such as baseline (steady state) conditions and results obtained using the newly defined system of equations. The most significant contribution made by the deductive flow-volume model is the definition of neurovascular response from presentation of stimulus to measured hemodynamics in terms of a simplified model that reduces the number of system parameters used during optimization.

5.3 Single compartment neurovascular model

The Balloon model has been extended by Friston et al. [12, 13] to include the effects of external inputs on an autoregulated vasodilatory signal assuming that the relationship between evoked neural activity and blood flow is linear. The extended input-output state model discussed by Friston et al [13] comprises four hemodynamic state variables, combined into a vector x , whose interactions are described by differential equations with five hemodynamic parameters. Consider the hemodynamic model equations described by the differential equations:

$$\dot{x} = A(t)x(t) + B(t)u(t) \quad (128)$$

$$y(t) = x_3(t) \quad (129)$$

where $x(t)$ is a 3x1 vector, $u(t)$ and $y(t)$ are scalars, and

$$A(t) = \begin{bmatrix} -\frac{1}{\tau_s} & -\frac{1}{\tau_f} & 0 \\ 1 & 0 & 0 \\ 0 & \frac{1}{\tau_0} & -\frac{1}{\tau_0} \end{bmatrix} \quad (130)$$

$$B(t) = \begin{bmatrix} -\frac{1}{\tau_f} + \varepsilon u(t) \\ 0 \\ x_3^\gamma(t) \end{bmatrix} \quad (131)$$

Where $x(t) = \begin{bmatrix} s(t) \\ f_{in}(t) \\ v(t) \end{bmatrix}$, $x(0) = \begin{bmatrix} 0 \\ 1 \\ 1 \end{bmatrix}$ and the differential equation has a converging

solution for all $t \geq 0$. Matrix A is a constant with respect to time and the matrix B

describes the relationship with the input signal and also contains the nonlinear relationship of flow and volume. The problem is set up using a variation of parameters approach. Each element of \mathbf{A} and \mathbf{B} describes a physical parameter that models the link between blood flow and volume in the human brain.

A linear model is assumed to link synaptic activity ($u(t)$: input signal to the hemodynamic system) and the neural response ($x_1(t) = s(t)$ which represents is a flow inducing signal). The input signal is a step function over time and describes an activity that creates changes in brain response. This activity can be as simple as motor response caused by finger tapping to a more complex cognitive task such as a verbal fluency examination (protocol described in detail in Chapter 7). The blood flow is defined as the input flow to the brain region under consideration ($x_2(t) = f_{in}(t)$). The efficacy of synaptic activity (ϵ) represents the increase in neural response that is caused by the input stimulus and in turn results in an increase in blood flow. The parameter (τ_s) represents the signal decay constant for the neural signal which determines the time the system takes to return to baseline or equilibrium state. The time-constant for autoregulatory feedback (τ_f) for blood flow creates the oscillatory dynamics that are characteristic of the hemodynamic system. The mean transit time of the blood (τ_0) represents the time taken for blood to traverse through the region of interest in the brain modeled by the Windkessel compartment in the vascular component of the model. The most important parameter examined is the stiffness parameter (γ) which determines the nonlinear relationship between flow and volume when laminar flow is assumed [59]. The stiffness parameter (γ) describes the compliance of the Windkessel compartment

and determines the stiffness of the capillaries and veins and describes blood volume changes in the system with respect to increased blood flow. In previously published literature, this value has been estimated at between 2.5 and 3.03 [58, 103]. In this research, simulation studies are presented for values of γ between 1 and 5. The stiffness coefficient value is inferred from the simulations to give the steady state flow-volume ratio observed in empirical studies.

5.3.1 Analytic solution

The system of equations that define the neurovascular model are integrated using the variation of constants method to solve the presented set of equations.

$$x(t) = e^{A(t)}x(0) + \int_0^t e^{-A(t-s)}B(s)ds \quad (132)$$

Solving for $e^{A(t-s)} = I + At + \frac{A^2t^2}{2!} + \dots$

$$e^{A(t-s)} = \begin{bmatrix} 1 & 0 & 0 \\ 0 & 1 & 0 \\ 0 & 0 & 1 \end{bmatrix} + \begin{bmatrix} -\frac{1}{\tau_s} & -\frac{1}{\tau_f} & 0 \\ 1 & 0 & 0 \\ 0 & \frac{1}{\tau_0} & 0 \end{bmatrix} (t-s) + \begin{bmatrix} -\frac{1}{\tau_s} & -\frac{1}{\tau_f} & 0 \\ 1 & 0 & 0 \\ 0 & \frac{1}{\tau_0} & 0 \end{bmatrix}^2 \frac{(t-s)^2}{2!} + \dots \quad (133)$$

$$e^{A(t-s)} = \begin{bmatrix} 1 - \frac{(t-s)}{\tau_s} - \frac{(\tau_s^2 - \tau_f)(t-s)^2}{2\tau_f\tau_s^2} & -\frac{(t-s)}{\tau_f} + \frac{(t-s)^2}{2\tau_f\tau_s} & 0 \\ (t-s) - \frac{(t-s)^2}{2\tau_s} & 1 - \frac{(t-s)^2}{2\tau_s} & 0 \\ -\frac{(t-s)^2}{2\tau_0} & \frac{(t-s)}{\tau_0} & 1 \end{bmatrix} \quad (134)$$

Substituting in Equation 132 we get

$$x_1 = -\frac{t}{\tau_f} + \frac{t^2}{2\tau_f\tau_s} + \int_0^t \left\{ [\varepsilon u(t-s) + 1/\tau_f] \cdot \left[1 - \frac{(t-s)}{\tau_s} - \frac{(t-s)^2(\tau_s^2 - \tau_f)}{2\tau_f\tau_s^2} \right] \right\} ds \quad (135)$$

$$x_2 = 1 - \frac{t^2}{2\tau_f} + \int_0^t \left\{ [\varepsilon u(t-s) + 1/\tau_f] \cdot \left[(t-s) - \frac{(t-s)^2}{2\tau_0} \right] \right\} ds \quad (136)$$

$$x_3 = 1 + \frac{t}{\tau_0} + \int_0^t \left\{ [\varepsilon u(t-s) + 1/\tau_f] \cdot \left[\frac{(t-s)^2}{2\tau_0} \right] + x_3^\gamma \right\} ds \quad (137)$$

These equations can be integrated and solved simultaneously using a numerical integration technique. The technique adopted in this paper is an adaptive step Runge-Kutta (4,5) method. Details are discussed in the next section.

5.3.2 Numerical solution

The system used to describe the localized changes in hemodynamics can be framed as a canonical initial value problem where the behavior of the system is described by a system of ordinary differential equation (ODE) of the form $dx/dt = f(x,t)$ where f is a known function, x is the state of the system, and dx/dt is the time derivative of x . The variables x and dx/dt are vectors. As the name suggests, in an initial value problem x at time=0 is known and the goal is to follow x over time thereafter[104].

The standard differential equation solver is the fourth-order Runge-Kutta method. It has more precision than the Euler's algorithm from which it is derived and offers several attractive features such as ease of programming and mathematical simplicity. With the addition of an adaptive or self-adjusting step size, the fourth-order Runge-Kutta method is both robust and capable of providing solutions to complex problems. Next, a basic derivation of the Runge-Kutta method is provided in addition to background theory and underlying equations [105].

The approximate solution for a given point in space using the Euler method is $y_{n+1} = y_n + hf(x_n, y_n)$ which advances a solution from x_n to $x_{n+1} = x_n + h$. It advances the solution through an interval h , and uses the derivative at the beginning of that interval to avoid discontinuities at the boundaries. This implies that the error in a single step is limited to only one power of h smaller than the correction [106]. Euler's method is not very accurate, when compared to more complicated methods using an equivalent step size and can also be unstable. Thus a more complex method, namely the Runge-Kutta solver, is adopted for this development. The Runge-Kutta solver uses the following method to find the solutions to a given system of differential equations. A trial step to the midpoint of the interval is taken. Then the values of both x and y at that midpoint are used to compute the "real" step across the whole interval [106]. This is illustrated below in Figure 5.2.

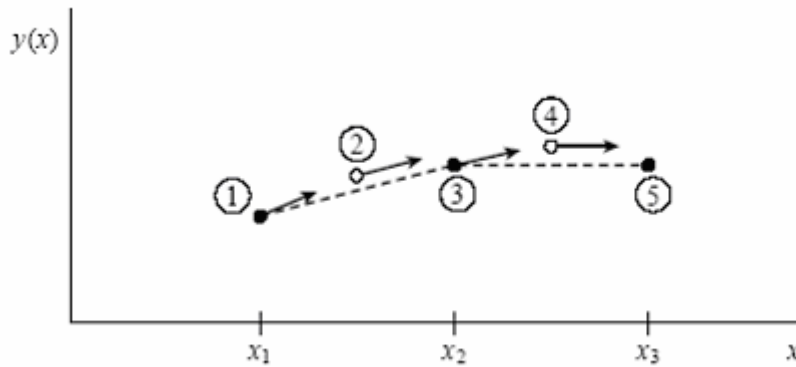


Figure 5.2 Graph illustrating the Midpoint method. Second order accuracy is obtained by using the initial derivative at each step to find a point halfway across the interval, then using the midpoint derivative across the full width of the interval. In the figure, filled dots represent final function values, while open dots represent function values that are discarded once their derivatives have been calculated and used [106]

Putting this idea in the form of equations,

$$\begin{aligned}
 k_1 &= hf(x_n, y_n) \\
 k_2 &= hf\left(x_n + \frac{1}{2}h, y_n + \frac{1}{2}k_1\right) \\
 y_{n+1} &= y_n + k_2 + O(h^3)
 \end{aligned}
 \tag{138}$$

Symmetrization cancels out the first order term (which is shown in the error term) and makes the method a second order solver. A method is conventionally called n th order if its error term is $O(h^{n+1})$. In fact, Equation 138 above describes the second-order Runge-Kutta or midpoint method. There are many ways to evaluate the right-hand side $f(x, y)$ that have different coefficients of higher-order error terms but lead to solutions that agree with those derived using a first order method. By choosing the optimal combination of right hand side terms, error terms can be systematically eliminated order by order. This is the basic idea of the Runge-Kutta method. The most

commonly employed method for numerical solutions is the fourth order Runge-Kutta formula because of its elegant organization that renders it easy to implement [106].

$$\begin{aligned}
 k_1 &= hf(x_n, y_n) \\
 k_2 &= hf\left(x_n + \frac{h}{2}, y_n + \frac{k_1}{2}\right) \\
 k_3 &= hf\left(x_n + \frac{h}{2}, y_n + \frac{k_2}{2}\right) \\
 k_4 &= hf(x_n + h, y_n + k_3) \\
 y_{n+1} &= y_n + \frac{k_1}{6} + \frac{k_2}{3} + \frac{k_3}{3} + \frac{k_4}{6} + O(h^5)
 \end{aligned}
 \tag{139}$$

The fourth-order Runge-Kutta method requires four evaluations of the right hand side per step h . This is almost always superior to the midpoint method. In fact, this method proves to be very effective when combined with an adaptive step size algorithm. Each step in a sequence of steps is treated identically in a Runge-Kutta method [106]. Prior behavior of a solution is not used in its propagation and this is justified mathematically since any point along the trajectory of an ordinary differential equation can serve as an initial point. This approach does not minimize computer time, and can fail for problems whose nature requires a variable/adaptive step size. Adaptive step size control helps minimize computing time and is discussed in detail in the next section [106].

5.3.2.1 Adaptive step size

Adaptive step size control is used to give better accuracy to a solution while minimizing computational effort. The basic idea is to take small steps in areas of rapid change and larger steps where the rate of change is slower [106]. This usually results in

gains of efficiency that are ten to a hundred or more times faster than without adaptive step size control. Implementation of adaptive step size control requires that the stepping algorithm signal information about its performance, and most important, an estimate of its truncation error. In a fourth-order Runge-Kutta method, a technique called step doubling is often used. Each step is taken twice, once as a full step, then, independently, as two half steps (refer Figure 5.3).

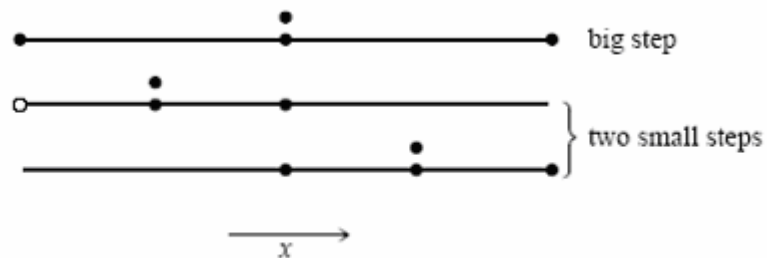


Figure 5.3 Step doubling as a means for adaptive step size control in fourth order Runge-Kutta. Points where the derivative is evaluated are shown as filled circles. The open circle represents the same derivative as the filled circle immediately above it, so the total number of evaluations is 11 per two steps. Comparing the accuracy of the big step with the two small steps gives a criterion for adjusting the step size on the next step, or for rejecting the current step as inaccurate

Each of the three separate steps in the procedure requires 4 evaluations, however the single and double sequences share a starting point and thus the total number of evaluations required is 11. This should not be compared to 4, but rather to 8 evaluations (due to the two half-steps), since the accuracy of the half step size is achieved. The overhead cost is therefore a factor 1.375 [106].

To illustrate the advantage of this method, let us denote the exact solution for an advance from x to $x + 2h$ by $y(x + 2h)$ and the two approximate solutions by y_1 (one step $2h$) and y_2 (2 steps each of size h)[104]. Since the basic method is fourth order, the true solution and the two numerical approximations are related by

$$\begin{aligned} y(x + 2h) &= y_1 + (2h)^5 \phi + O(h^6) + \dots \\ y(x + 2h) &= y_2 + 2(h^5)\phi + O(h^6) + \dots \end{aligned} \quad (140)$$

where, to order h^5 , the value ϕ remains constant over the step. In a Taylor series expansion, ϕ represents a number whose order of magnitude is $(y^{(5)}(x)/5!)$. The first expression in Equation 140 involves $(2h)^5$ since the step size is $2h$, while the second expression involves $2(h^5)$ since the error on each step is $h^5\phi$ [106]. The difference between the two numerical estimates gives the truncation error

$$\Delta \equiv y_2 - y_1 \quad (141)$$

The method aims to keep the truncation error to a desired degree of accuracy which is neither too large nor too small. This is realized by adjusting the step size, h [106]. Equation 142 can be solved by ignoring terms of order h^6 and higher, to improve our numerical estimate of the true solution $y(x + 2h)$, namely,

$$y(x + 2h) \equiv y_2 + \frac{\Delta}{15} + O(h^6) \quad (142)$$

This estimate is accurate to the fifth order, one order higher than the original Runge-Kutta steps. Although the estimate is accurate to the fifth-order, the truncation error is not known at this stage. Therefore, Δ is used as the error estimate. Such a procedure is called “local extrapolation” [106].

An alternative step size adjustment algorithm is based on the embedded Runge-Kutta formula, originally invented by Fehlberg. An interesting fact about Runge-Kutta formula is that for orders, M , higher than four, more than M function evaluations (though never more than $M + 2$) are required [106]. Thus the fourth-order method is often the first choice in numerical analysis problems. Fehlberg discovered a fifth-order method with six function evaluations where another combination of the six functions gives a fourth-order method. The difference between the two estimates of $y(x + h)$ is used as an estimate of the truncation error to adjust the step size. Accordingly, embedded Runge-Kutta formulas, which are roughly a factor of two more efficient, have superseded algorithms based on step-doubling. The general form of a fifth-order Runge-Kutta formula is [106]

$$\begin{aligned}
k_1 &= hf(x_n, y_n) \\
k_2 &= hf(x_n + a_2h, y_n + b_{21}k_1) \\
&\dots \\
k_6 &= hf(x_n + a_6h, y_n + b_{61}k_1 + \dots + b_{65}k_5) \\
y_{n+1} &= y_n + c_1k_1 + c_2k_2 + c_3k_3 + c_4k_4 + c_5k_5 + c_6k_6 + O(h^6)
\end{aligned} \tag{143}$$

The embedded fourth-order formula and its corresponding error estimate are as follows

$$y_{n+1}^* = y_n + c_1^*k_1 + c_2^*k_2 + c_3^*k_3 + c_4^*k_4 + c_5^*k_5 + c_6^*k_6 + O(h^5) \tag{144}$$

$$\Delta \equiv y_{n+1} - y_{n+1}^* = \sum_{i=1}^6 (c_i - c_i^*)k_i \tag{145}$$

At this step, the approximate error is known and the next step is to keep the error within desired bounds. The error, Δ , is proportional to the fifth power of the step

size ($\sim h^5$). If we take a step, h_l , and produce an error, Δ_l , then the step h_0 that would have given some other value Δ_0 is readily estimated as [106]

$$h_0 = h_l \left| \frac{\Delta_0}{\Delta_l} \right|^{0.2} \quad (146)$$

Let Δ_0 denote the desired accuracy. Equation 146 is used in two ways: If Δ_l is larger than Δ_0 in magnitude, the equation indicates how much to decrease the step size when the present (failed) step is retried. On the other hand, if Δ_l is smaller than Δ_0 , then the equation can be used to determine the increment of the step size for the next step. Local extrapolation consists in accepting the fifth order value y_{n+1} , even though the error estimate actually applies to the fourth order value y^*_{n+1} . The desired accuracy, Δ_0 , is a vector, one for each equation in the set of ODEs. In general, all equations are assumed to be within their respective allowed errors. In other words, we will rescale the step size according to the needs of the equation with the worst error [106].

The next step is to relate the desired accuracy, Δ_0 , to some user defined error bounds. When dealing with a set of equations whose dependent variables differ enormously in magnitude, fractional errors are utilized (For example, $\Delta_0 = \epsilon y$, where ϵ is the number like 10^{-6}). When dealing with oscillatory functions that pass through zero but are bounded by some maximum values, Δ_0 is set equal to ϵ times the maximum values [106].

A well-known method for adjusting step size selection to the event functions is to include their first time derivative in the array of integrating variables. The extended system of differential equations can be written as

$$\frac{d}{dt} \left[\frac{y}{g} \right] = \left[\frac{f(y,t)}{g(y,t)} \right] \quad (147)$$

where y represents the state variables of the system, and g is an array collecting all active event functions. However, this measure alone does not suffice to warrant reliable event detection, because in a high order of the interpolation polynomials of the integrator, an even number of roots can occur within the integrator steps that remain undetected when simple sign checks are used [106].

Reliable event detection can be obtained by exploiting polynomials generated by the integrator for event functions in the extended system concurrently with a polynomial root finding algorithm to predict the number of roots contained in a single integration step [105]. However, standard interpolation polynomials of numerical integration codes often have the disadvantage of discontinuities at mesh points. Continuous extension interpolation polynomials that follow dense output formulas of [107] are employed in the Matlab routine (ode45) [108, 109] used in this research, to ensure continuity at the endpoints of an interval. The basic form of dense-output Runge-Kutta scheme is as follows

$$\begin{aligned} y_{n+1} &= y_n + h \sum_{i=1}^s b_i f_i \\ f_1 &= f(y_n, t_n) \\ f_i &= f(y_n + h \sum_{j=1}^{i-1} a_{ij} f_j, t_n + c_i h), i = 2, \dots, s \end{aligned} \quad (148)$$

A continuous extension can be computed using the same function evaluations, f_i , with

$$y_{n+1}^*(\sigma) = y_n + \sigma h \sum_{i=1}^s b_i^*(\sigma) f_i \quad , \quad 0 \leq \sigma \leq 1, \quad (149)$$

where $b_i^*(\sigma)$ are given polynomials of the interpolation parameter $0 \leq \sigma \leq 1$ (see Table 5.1). The DOPRI5 scheme [110, 111] is a 7-stage explicit Runge-Kutta formula of fifth order with an embedded fourth order step for step size control. The fourth order continuous extension is used for the interpolation polynomials.

Table 5.1 RK5(4)7FM embedded pair (DOPRI5) [112]

c_i	a_{ij}						\hat{b}_i	b_i	b_i^*
0	-	-	-	-	-	-	$\frac{35}{384}$	$\frac{5179}{57600}$	$\frac{435\sigma^3 - 1184\sigma^2 + 1098\sigma - 384}{384}$
$\frac{1}{5}$	$\frac{1}{5}$	-	-	-	-	-	0	0	0
$\frac{3}{10}$	$\frac{3}{40}$	$\frac{9}{40}$	-	-	-	-	$\frac{500}{1113}$	$\frac{7571}{16695}$	$\frac{500\sigma(6\sigma^2 - 14\sigma + 9)}{1113}$
$\frac{4}{5}$	$\frac{44}{45}$	$-\frac{56}{15}$	$\frac{32}{9}$	-	-	-	$\frac{125}{192}$	$\frac{393}{940}$	$-\frac{125\sigma(9\sigma^2 - 16\sigma + 6)}{1113}$
$\frac{8}{9}$	$\frac{19372}{6561}$	$-\frac{25360}{2187}$	$\frac{64448}{6561}$	$-\frac{212}{729}$	-	-	$-\frac{2187}{6784}$	$-\frac{92097}{339200}$	$\frac{729\sigma(35\sigma^2 - 64\sigma + 26)}{1113}$
1	$\frac{9017}{3168}$	$-\frac{355}{33}$	$\frac{46732}{5247}$	$\frac{49}{176}$	$-\frac{5103}{18656}$		$\frac{11}{84}$	$\frac{187}{2100}$	$\frac{11\sigma(3\sigma - 2)(5\sigma - 6)}{84}$
1	$\frac{35}{384}$	0	$\frac{500}{1113}$	$\frac{125}{192}$	$-\frac{2187}{6784}$	$\frac{11}{84}$	0	$\frac{1}{40}$	$\frac{\sigma(\sigma - 1)(5\sigma - 3)}{2}$

5.3.3 Simulations for varied compliance

An input-output nonlinear system consisting of a neural model and the Windkessel/Balloon model is presented. In this investigation, the input-output state model was used to explore hemodynamic responses to short (2 second) and long (20 second) stimuli with different compliance coefficients. The simulated results are

compared to published data and the system parameters predicted are compared to typical values to demonstrate their validity. A series of simulation studies is presented to explore the effect of the temporal length of input stimulus and compliance of the blood vessels on the hemodynamic output response functions produced. The model used in the input-output state system is a combination of the neural response model [70] and the Windkessel/Balloon model [113]. The neural response model specifies the relationship between input stimulus and the synaptic activity, while the Windkessel model describes the relationship between neural activity and evoked hemodynamic changes.

The objective is to compare the effect of varying compliance on the relationship of blood flow with blood volume. To achieve this end, graphs of blood flow and blood volume with a constant stimulus input of 2 seconds, with fixed time constants and neuronal efficacy are presented. The following typical values are used in the simulation: $\varepsilon=0.54$, $\tau_s=0.86$ seconds, $\tau_f=0.41$ seconds and $\tau_0=1$ second. Next, the time traces for $\gamma=1, 2, 3, 4$ and 5 are plotted to compare the change induced in the blood volume graphs by varying compliance.

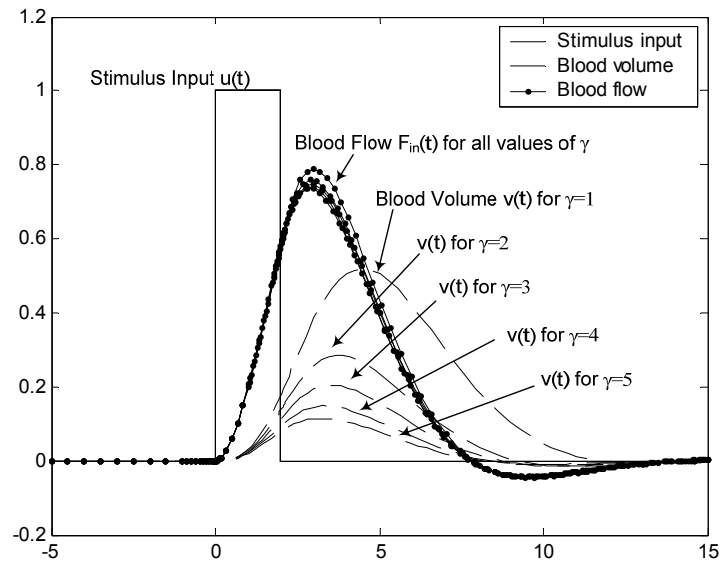


Figure 5.4: Flow volume simulations for varying values of compliance coefficients (γ), duration of input stimulus=2 seconds

As seen in Figure 5.4, changing compliance does not change the magnitude of flow to a large extent and the curves almost overlap each other. This is expected since blood flow depends only on the neural activity and the input stimulus can thus be thought of as an input function to the vascular component of the model which is unaffected by the system parameters. Blood volume exhibits large changes with varying compliance. This also follows the predicted physical behavior of a Windkessel chamber which can be imagined as an expandable tube whose properties are defined by the system parameters of the vascular model. As the tube becomes more compliant ($1/\gamma$ increases), the blood volume shows larger increases due to decreased resistance. To further quantify the results, the ratio of maximum flow to maximum volume for each value of γ is calculated. The results are presented in Table 5.2. These results are

compared to previously published data, which predict a flow to volume ratio of ~ 3.5 . It is concluded that for the human brain, a stiffness coefficient $\gamma \sim 3$ is appropriate. These results concur with previously published results [58] which predict $\gamma \sim 3.03$.

Table 5.2: Flow volume ratio and dependence on stiffness coefficient, duration of input stimulus=2 seconds

Stiffness coefficient (γ)	Flow volume ratio
1	1.439562
2	2.577324
3	3.851490
4	5.111237
5	6.398648

To validate the model for longer duration input, we repeat calculations of blood flow and blood volume using the same system with a constant stimulus input of 20 seconds and fixed time constants and neuronal efficacy. We use the following typical values for our simulation: $\varepsilon=0.3$, $\tau_s=0.86$ seconds, $\tau_f=0.41$ seconds and $\tau_0=1$ second. Next the time traces for $\gamma=1, 2, 3, 4$ and 5 are plotted to compare the change induced in the volume graphs by varying compliance (Refer Figure 5.5). Similar to the results obtained with a 2 second input we observe that changing compliance does not change the flow graph much while blood volume exhibits large changes with varying compliance.

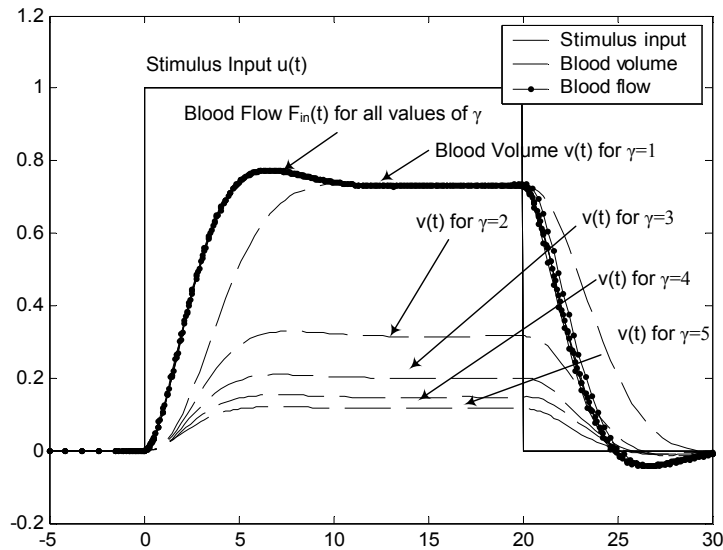


Figure 5.5: Flow volume simulations for varying values of compliance coefficients (γ), duration of input stimulus=20 seconds

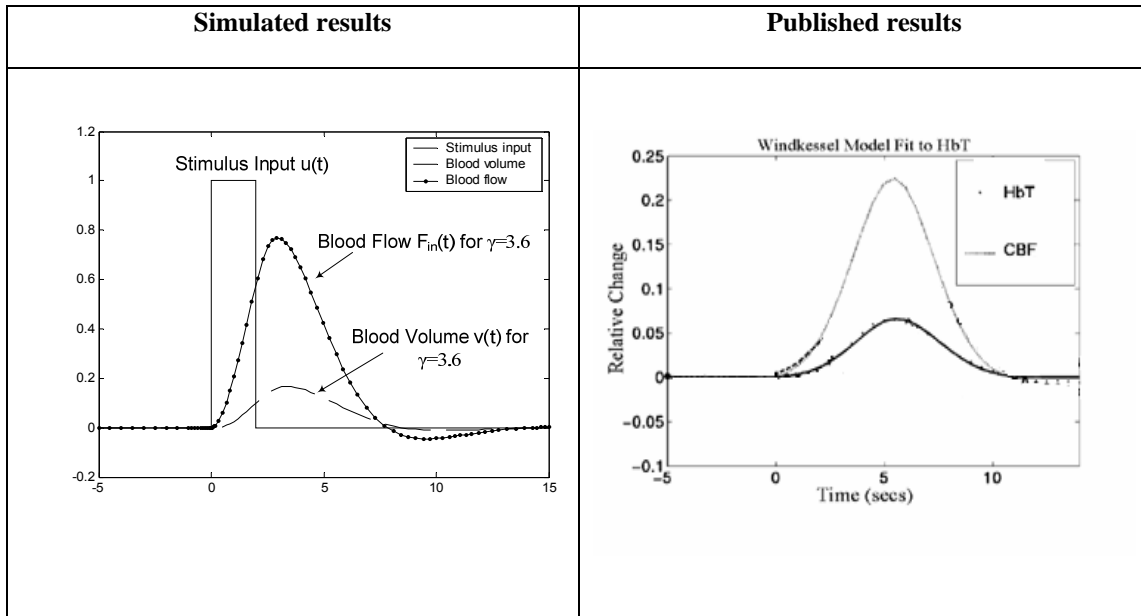
The flow to volume ratio for each value of γ is calculated again. The results are presented in Table 5.3. Since there is very little data published with simultaneous measurements of blood flow and blood volume at long duration input stimuli, it is surmised that the flow-volume ratio should remain the same with varying input. This is a reasonable assumption, since flow-volume ratio depends only the changes in the compliance parameter of the system and should therefore not be affected by the change in duration of the input stimulus. Again it is observed that a stiffness coefficient $\gamma \sim 3$ is appropriate which gives a flow to volume ratio of 3.68.

Table 5.3: Flow volume ratio and dependence on stiffness coefficient, duration of input stimulus=2 seconds

Stiffness coefficient (γ)	Flow volume ratio
1	1.052535
2	2.351108
3	3.685428
4	5.025735
5	6.362376

Table 5.4 shows results simulated with a 2 second input stimulus. These results are compared to previously published results measured during a 2 second finger tapping task using near infrared spectroscopy on the motor cortex of human subjects. The stimulus is started at time=0 seconds in the published results. In the measured data, the stiffness parameter, γ , is optimized to be 3.6 to give a flow-volume ratio of 4.5. The flow and volume curves are simulated using the same stiffness parameter (= 3.6) and the results yield a flow-volume ratio of 4.6 which is comparable to the published data.

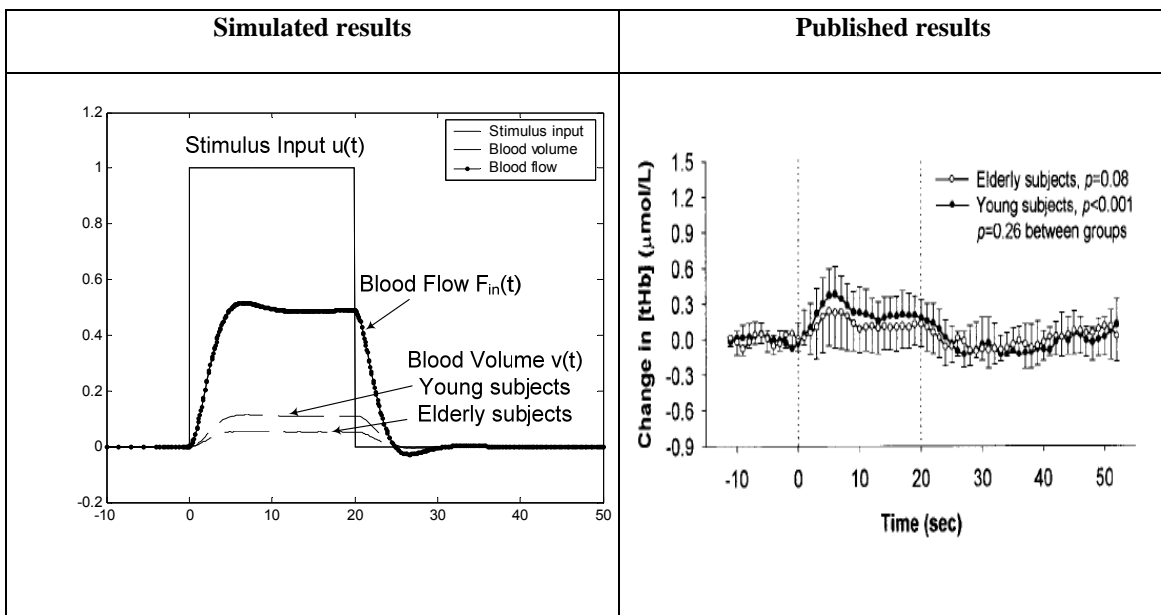
Table 5.4: Comparison of flow volume characteristics using simulation studies and experimental data, duration of input stimulus=2 seconds



Next, the simulated results for longer duration stimuli are compared to previously published data. Table 5.5 shows results simulated with a 20 second input stimulus. The published data was measured during a 20 second finger tapping task using near infrared spectroscopy and the region of interest was the motor cortex of human subjects. The stimulus is started at time=0 second in the published results. The published results contain a comparison of younger and older subjects and the blood volume changes induced by the same task across the two age groups. This is an interesting result to compare our simulations, since arteries and capillaries harden and lose compliance with advanced age [62]. This condition is called atherosclerosis. Thus the research compares the changes of varying compliance on blood volume keeping all other parameters that relate to stimulus constant. A qualitative comparison of the

simulated results with the published results is presented in Table 5.5. A compliance coefficient of $\gamma=3.8$ is assumed for young subjects which yields a flow-volume ratio of 4.5 and a $\gamma=7.6$ for elderly subjects which yields a flow-volume ratio of 9. It can be seen that the flow-volume ratio almost doubles which concurs with qualitatively with published results.

Table 5.5: Comparison of flow volume characteristics using simulation studies and experimental data, duration of input stimulus=20 seconds



5.3.4 Estimation of system parameters

Experimental data can be fit using the state space single compartment neurovascular model. The stimulus input which contains the activation timing for the experiment is used to determine the blood volume in the vascular compartments [where $\text{HbT}=v(t)$] as a function of time. The system parameters that define the neuronal

changes as well as vascular changes are calculated by minimizing the difference between the predicted model blood volume and measured blood volume.

The fitting parameters (efficacy of synaptic activity (ϵ), signal decay constant (τ_s) time-constant for autoregulatory feedback (τ_f), mean transit time of the blood (τ_0) and stiffness parameter (γ)) are optimized in a nonlinear χ^2 fit to the experimentally measured $\Delta[\text{HbT}]$ while flow and CMRO_2 are empirically determined. Figure 5.6 shows the time courses for $[\text{Hb}]$, $[\text{HbO}_2]$ and $[\text{HbT}]$ for the verbal fluency task averaged across ten subjects. Details are provided in Chapter 7. Only the activation period of the data is used for each optimization to avoid issues with the post stimulus shoots in the data.

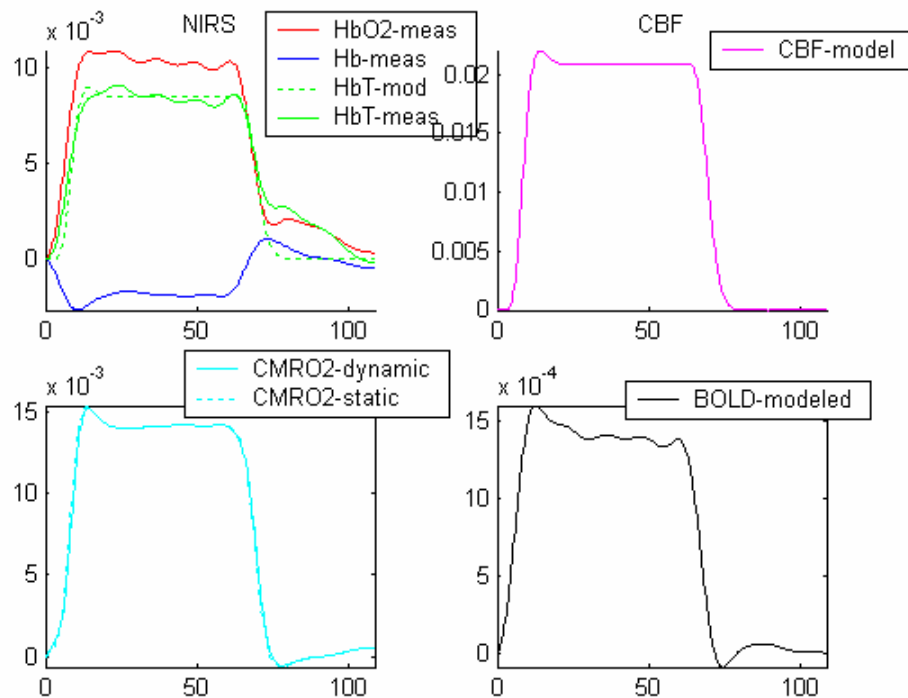


Figure 5.6: Model fit to experimental NIRS data and predicted temporal evolution of cerebral blood flow, CMRO_2 and BOLD signals

5.3.5 Spatial tomographic images of blood flow and CMRO₂

Hemodynamic spatial profiles were collected and analyzed through the NIRS measurements in order to reveal brain activation in the participants. Entire time courses of individual parameters (i.e., [HbO₂] and [Hb]) were measured during the entire period of stimulation. The time epochs of cerebral activation were separated from baseline/rest period with markers. For spatial maps, the mean hemoglobin levels for each channel were calculated for the blocked period of activation and then averaged for the ten subjects. Thus, spatial maps of the temporal average over activation blocks were constructed and compared to the average readings taken during baseline. This helped identify which areas of the prefrontal cortex under observation showed the largest changes in [Hb] and [HbO₂] over time.

Similar to the spatial maps of the measured hemodynamics, maps of predicted measures of cerebral blood flow, CMRO₂ and BOLD signals were constructed. The following procedure was used to construct tomographic maps of cerebral activation. The NIRS readings for each channel were used to calculate changes in total blood volume over time. This data was used in conjunction with the model predicted temporal dynamics to determine temporal changes in blood flow, CMRO₂, and BOLD. These time traces were determined by fitting data for each channel across the prefrontal cortex. The averages of the time traces during periods of activation were calculated for each channel. Inverse reconstruction techniques similar to [Hb] and [HbO₂] were used to construct maps of blood flow, CMRO₂, and BOLD (shown in Figure 5.7) to reveal true cerebral activation patterns.

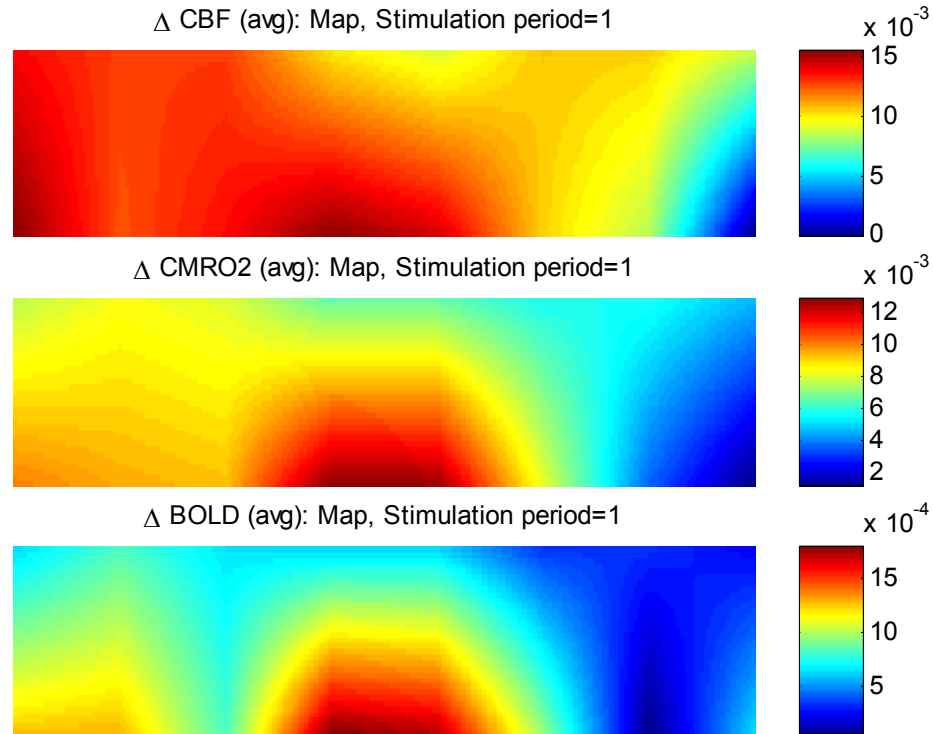


Figure 5.7: Spatial tomographic images of the average Δ CBF, Δ CMRO₂ and Δ BOLD during activation

It should be noted that while Δ CBF shows large activation in the entire prefrontal cortex, but as hypothesized Δ CMRO₂ and Δ BOLD reveal more specific areas of activation namely the inferior median prefrontal cortex. This indicates that stimulus response in the cerebral cortex is spatially more specific if the true measures of cerebral activation such as metabolic activity are used. Further such tomographic reconstructions of BOLD signals predicted from NIRS signals can be used to validate the spatial activation revealed by NIRS thus suggesting the use of NIRS as a precursory diagnostic tool before fMRI studies are conducted.

5.4 Multicompartment neurovascular model

Several groups have introduced physiological models to depict the biophysics of the cerebral vascular response that can be used to estimate relative CMRO₂ changes from measurements of the changes in cerebral blood flow, volume, and oxygenation (i.e. BOLD) [3, 49, 71, 85, 114]. Simplified models of the vascular unit have been developed based on the hydrodynamics of compliant Windkessel volume (derived from the German word meaning “air chamber”) [4]. These models describe the relationship between a flow inducing response caused by vaso-active agents and the measurable hemodynamic changes such as blood flow and volume. The single compartment model equations (described in previous sections) are drawn from basic principles of fluid dynamics and are characterized by a limited number of unknown model parameters that define the lumped mechanical properties of the vascular network [4, 6, 113]. These parameters are determined using measurements of blood flow and volume changes and then applied to estimate evoked changes in oxygen metabolism [4, 115, 116].

The vascular multicompartment is defined by three connected compliant, vascular compartments (arterial, capillary, and venial). Changes in blood flow and volume are driven by the active dilation of the arteries. Arterial dilation is the result of neuro-vascular coupling and is caused by the release of vaso-active agents which actively dilate or contract [117] the smooth-muscle arterial blood vessels. These vaso-active agents are believed to be released from the astrocytic processes which are in contact with cerebral arteries [118]. Active arterial dilation decreases the input vascular resistance and creates a pressure gradient which leads to increased blood flow into the

system. The increased hydrostatic pressure also causes blood volume to increase by the expansion of the vascular compartment against the surrounding tissue which resists compression thus giving rise to a saturating volume function. A system of differential equations can be used to describe the effects of arterial dilation on vascular hemodynamics.

5.4.1 State equations of the neurovascular model

As described in Section 5.1, the dynamical system that links the synaptic activity with the cerebral blood flow is linear and can be described by Equation 125. The synaptic signal is linked to neuronal responses and the experimentally designed stimulus function, $u(t)$ (refer Equation 126). These equations represent the neural activity that governs the arterial dilation caused by the action of vasoactive agents. These agents are believed to be released from the astrocytic processes[101, 102] in contact with cerebral arteries and directly influence changes in blood flow and volume during cerebral activation.

The next equations describe the balloon model vascular component of the neurovascular model. Blood flow coming into and leaving the vascular compartment along with the blood vessel compliance determine the rate of blood volume change in the local cerebral vasculature. The normalized change in blood volume reflects the difference between inflow, f_{in} and outflow, f_{out} of blood from the individual vascular compartments. Outflow is a function of volume that models the balloon-like capacity of the vascular compartment which can expel blood at a greater rate when distended.

Compliance can be modeled with three distinct parameters that describe the elasticity coefficients of each vascular compartment. The compliance coefficient determines the expansion of the blood vessel against the surrounding tissue and intracranial pressure. The balloon model component of the neurovascular model is modified to include the capillary and venous compartments. Blood flow coming to and leaving the vascular along with the blood vessel compliance determine the rate of blood volume change in the local cerebral vasculature. In order to calculate the blood flow and volume changes for each of the vascular compartments, a differential temporal update is sequentially applied to the arteriole, capillary and finally venial compartment. This update is driven by changes in the stimulus which creates downstream changes in neural activity and flow inducing signals. The stimulus function, as described earlier, is an input to the system and is described by variables estimated within the state vector. The instantaneous value of the flow in the subsequent compartment (i.e. capillary) at the previous time instance, and the inflow to the current (i.e. arteriole) compartment at the current time instance are used to calculate the differential update in the system (including vascular compliance and out-flow from arterioles). This differential change is used to update the set of physiological changes (blood flow and volume) for the arteriole compartment at the current instance. Following the update of the arteriole compartment, the same procedure is used to update the capillary and the venial compartments. The differential equations (defined by equations 150-152) can be formulated with variables of flow and volume represented as unit-normalized quantities.

The blood flow and volume in the vascular compartments is described by the following equations:

$$\text{Arterial compartment} \quad \tau_0 \dot{v} = f_{in} - f_{ac} = f_{in} - v_a^{\gamma_a} \quad (150)$$

$$\text{Capillary compartment} \quad \tau_0 \dot{v} = f_{ac} - f_{cv} = v_a^{\gamma_a} - v_c^{\gamma_c} \quad (151)$$

$$\text{Venous compartment} \quad \tau_0 \dot{v} = f_{cv} - f_{out} = v_c^{\gamma_c} - v_v^{\gamma_v} \quad (152)$$

At baseline, the relationship between the Windkessel volume and the incoming blood flow is given by the vascular transit time ($V_w(0) = F_{in}(0) \cdot \tau$), where the Windkessel volume is equal to the sum of the volumes in the three vascular compartments (arteriole, capillary and venial). It is assumed initial volume fractions of 25%, 15%, and 60% for the arteriole, capillary and venial compartments [7, 93]. The sum of the initial total flow in the three compartments is set at unity.

5.4.2 Simulations for compartmentalized hemodynamics

As observed in the inductive models, the arteriole compartment had the largest fractional volume changes. Also, volume changes in the arterioles peaked before the capillaries and venules. Blood flow change in all three compartments was nearly identical but temporally lagged from the arteriole to venous compartments. The time constants of the arteriole, capillary and venous compartments have a ratio 0.25:0.60:0.15 to reflect the baseline volume fractions of each compartment since normalized flow is obtained. The predicted response curves for each of the vascular compartments, shown in Figure 5.8, are in qualitative agreement with previously

published experimental findings [82]. The largest magnitude of blood volume change originated from the venous compartment. However, the arteriole compartment had the largest fractional volume change. Blood volume changes in the arterioles initiated and peaked slightly before the volume changes in the capillaries or venials. In the blood flow response, it was found that the magnitude of the change in all three compartments was nearly identical. The blood flow response was slightly lagged from the arteriole to venous compartments.

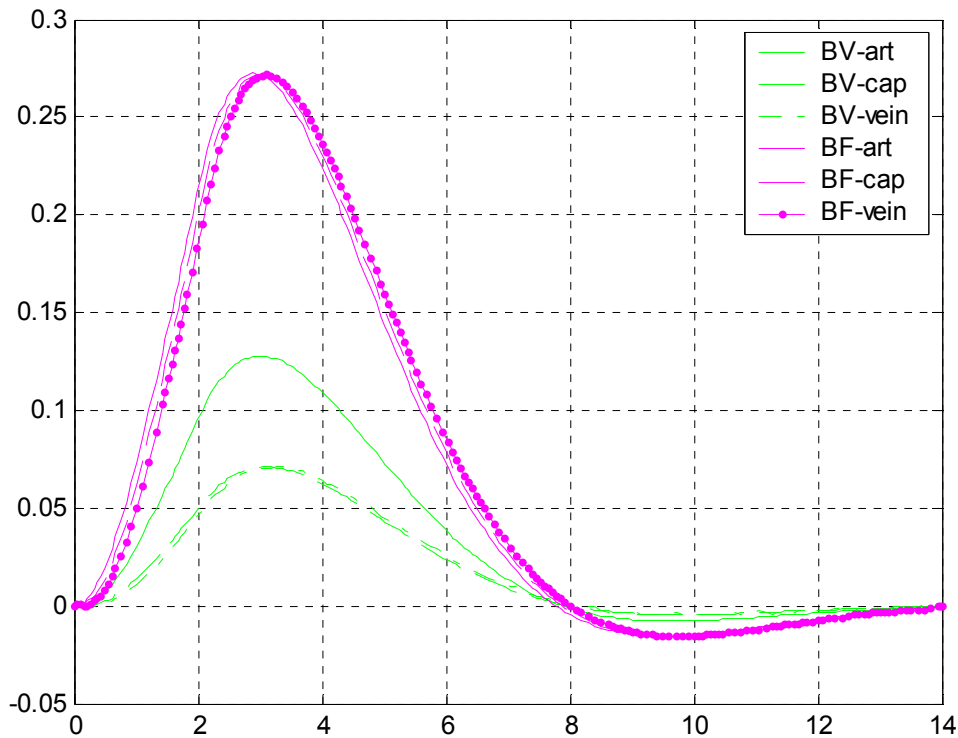


Figure 5.8: Results of the multicompartment Windkessel model

5.4.3 Estimation of system parameters

Experimental data can be fit using the state space multicompartment neurovascular model similar to the single compartment model. The stimulus input contains the timing information for the experiment and is used to determine the blood volume in the vascular compartments as a function of time. The system parameters that define the neuronal changes as well as vascular changes are calculated by minimizing the difference between the predicted model blood volume and measured blood volume.

The fitting parameters (efficacy of synaptic activity (ϵ), signal decay constant (τ_s) time-constant for autoregulatory feedback (τ_f), mean transit time of the blood (τ_0) and stiffness parameter (γ)) are optimized in a nonlinear χ^2 fit to the experimentally measured $\Delta[\text{HbT}]$ and the sum of the volume changes in the three vascular compartments. Blood flow and CMRO_2 are calculated using the neurovascular estimate of $\Delta\text{CBF}/\text{CBF}_0$.

Figure 5.9 shows the time courses for $[\text{Hb}]$, $[\text{HbO}_2]$ and $[\text{HbT}]$ during a 2-second finger tapping task averaged across five subjects. All the hemodynamic changes measured with NIRS exhibit similar behavior and slowly return to baseline after cessation of stimulus. Details are provided in Chapter 7. Only the activation period of the data is used for each optimization routine to avoid issues with the post stimulus over and under shoots in the experimentally measured hemodynamic data

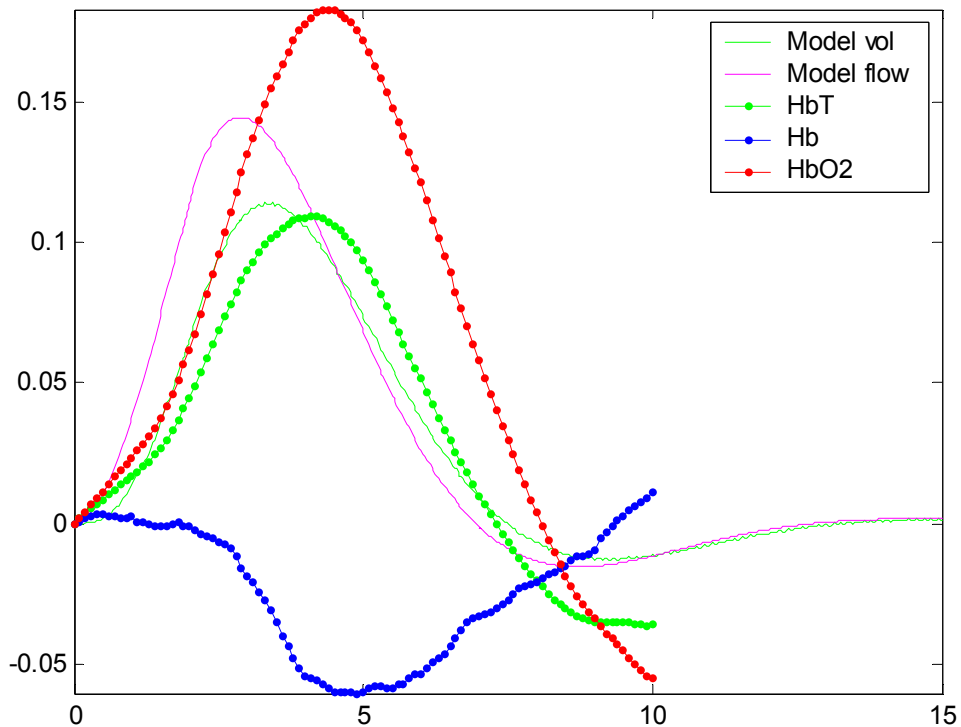


Figure 5.9: Model fit to experimental NIRS data and predicted temporal evolution of cerebral blood flow, $CMRO_2$ and BOLD signals

5.5 Future work

Much of the discussion above is preoccupied with nonlinear models that predict cerebral hemodynamics. Interactions at the neuronal level are relevant and motivate the extensive use of factorial designs in neuroimaging that look explicitly for such interactions as the causes of neuronal responses. These interaction terms can be further explored using multimodality imaging data and are accommodated in the current framework presented here by forming additional inputs that enter into the model. In the models described above, it is assumed that a stimulus function elicits a flow-inducing

signal and that can be described by a single parameter since neuronal activity mediates between the stimulus and flow-inducing signal. However neuronal dynamics can differ in form over different stimuli induced by different trials and experiments. For example, some stimuli may engage high level processing (such as those experiment involving complex psychological phenomena such as language processing tasks). The current models can be extended to include neuronal activity and a distinction between early or transient and late or enduring responses. A suggested extension for the model is to include further state variables that represent the transient and neuronal activity in the region of interest.

5.6 Chapter summary

This chapter was divided into three major parts: (i) simulations to predict measurements based on typical system parameters; (ii) calculation of unknown system parameters using measured experimental data; and (iii) development of a multicompartment input-output nonlinear system consisting of a neural and vascular model. The simulated results are compared to published data and predicted system parameters are compared to typical values demonstrating their validity.

CHAPTER 6

DEVELOPMENT OF A VASCULAR PHANTOM

Blood vessel compliance and resistance are important physical characteristics of the neurovascular system. However both parameters cannot be measured by conventional noninvasive imaging methods. The compliance of the neurovascular system together with peripheral resistance dictates the blood pressure, flow and volume characteristics. The compliance of an individual vascular segment governs the pulse wave velocity along the vessel, and has a major influence on the nature of the flow characteristics within the vessel [119, 120].

Over the last few decades, there has been a plethora of work with physical models of the vascular system. Models have been used in a range of applications from verification of the mathematical theories of blood flow [121] to studying the response of hemodynamic fMRI and NIRS measurements [122, 123]. Hemodynamic biomechanical models have also been used as predictive tools to study sections of the circulatory system [124, 125] and the effects of system parameters such as peripheral resistance, pressure and vascular compliance on the measurements of pressure, flow and volume. However, little quantitative work has been performed to replicate the mechanical behavior of arterial vessels in a controlled laboratory setup. The mechanical properties of the arterial wall have a significant effect on the blood flow and volume

characteristics of the circulation, and should therefore be mimicked in any model of blood circulation.

The similarity of the arterial circulation to the system used in the original fire engine and in pipe organs has been often used to create simplified analogous models of the vascular system. Such systems provide a steady flow through an outlet despite intermittent pumping through an inlet. Stephen Hales (1773) was one of the first people to suggest that this principle could be used to describe the behavior of the systemic arterial system. Otto Frank (1899) applied Hales' idea and this came to be known as the "Windkessel" theory (Windkessel is the German word for air-chamber). A description of an early Windkessel model was given by the German physiologist Otto Frank in an article published in 1899 [126]. The model compared the heart and systemic arterial system to a closed hydraulic circuit comprised of a water pump connected to a chamber.

6.1 Motivation behind a vascular phantom

Physiological changes occur in the vascular system as a result of degeneration due to advancement in age or due to disease such as atherosclerosis. This chapter aims to study the relationship between the compliance of a vessel and its peripheral resistance and their effect on flow-volume waveforms. The single compartment Windkessel model of vascular flow and volume is used in the study. The parameter that defines arterial compliance is known as the modulus of volumetric elasticity (E'). It is expected that an increase in modulus of volumetric elasticity of vascular segments correlates to an increase in peripheral resistance (R_s). Lower volumetric elasticity

indicates a more compliant vessel, while a more rigid vessel has a higher E' . Increased resistance to flow in blood vessels can be detrimental to health as in the case with arteriosclerosis, a general term for the thickening and hardening of arteries. Arteries that lead to the brain may cause a stroke if they become narrow and hard.

In aged human subjects, arteries gradually stiffen due to the progressive degeneration of the vascular wall, a process independent of the disease, atherosclerosis. The content of collagen increases and the elastic fibers of the media become fragmented causing a rise in the collagen to elastin ratio. As a result, the compliance of the blood vessels decreases by more than a factor of 2 between the ages of 20 and 60 years [127]. The characteristic impedance of blood vessels is affected by the decrease in compliance and consequent increase in peripheral resistance caused by thickening of the vessel walls. Blood volume supplied to the organs (in this case the cerebral cortex) also declines with age [62]. The declining volume is attributed to the greater load imposed by the increase in peripheral resistance putting older patients at a higher risk for stroke.

Atherosclerosis is a type of arteriosclerosis. The name comes from the Greek words athero (meaning gruel or paste) and sclerosis (hardness). It describes the process of fatty substances, cholesterol, cellular waste products, calcium and fibrin (a clotting material in the blood) building up in the inner lining of an artery. If the wall is thickened sufficiently, the diameter of the blood vessel is reduced and less blood volume will be supplied to the organ thus decreasing the oxygen supply. If the oxygen supply to the brain is reduced enough, a stroke can occur.

The primary aim of the work described here was to characterize elastic vessels which approximate the mechanical behavior of human blood vessels through physical models of vascular circulation that are more representative of the hemodynamic situation observed *in vivo*. Furthermore, vessels of different wall thicknesses and elasticity were characterized to explore the degree to which vascular volume and peripheral resistance are affected by the hardening of blood vessels caused by changes in the pathology resulting from aging and disease.

6.2 Windkessel theory

Mathematical models have been used in the past to study the hemodynamics of various vascular beds. Previously published models have explored the single lumped parameter representation of the blood vessel of interest where nonlinear capacitance changes are used to describe the elasticity (Windkessel compliance) of the vascular bed. In the past, Windkessel chambers have been modeled in laboratories as reservoirs of air where the compliance is regulated by the pressure and volume of the air within the chamber. It likens the heart and systemic arterial system to a closed hydraulic circuit comprised of a water pump connected to a chamber. The circuit is filled with water except for a pocket of air in the chamber [128]. As water is pumped into the chamber, the water both compresses the air in the pocket and pushes water out of the chamber, back to the pump. The compressibility of the air in the pocket simulates the elasticity and extensibility of the major artery, as blood is pumped into it by the heart ventricle. This effect is commonly referred to as arterial compliance. The resistance water

encounters while leaving the Windkessel and flowing back to the pump, simulates the resistance to flow encountered by the blood as it flows through the arterial tree from the major arteries, to minor arteries, to arterioles, and to capillaries, caused by the decreasing vessel diameter. This resistance to flow is commonly referred to as peripheral resistance [128]. Although these systems allow the gross characteristics of the arterial system to be studied, wave propagation characteristics such as pulse wave velocity and reflection are not accounted for. A more accurate and physiologically relevant phantom of the vascular system would thus involve the pumping of fluid through expandable vessels akin to actual blood circulation through the vascular bed.

The Windkessel theory models the vascular bed as a system of interconnected tubes with fluid storage capacity (refer Figure 6.1). The length of artery can thus be roughly approximated to operate as a reservoir, which receives blood in an intermittent fashion through ventricular ejection while outflow issues blood in a different time dependent fashion at the distal end. Peripheral resistance is approximated to be constant and following a Poiseuillean dynamic. The property of the system enabling it to store blood is defined by its modulus of volume elasticity E' as $E' = dp/dV$ where p represents pressure and V represents volume [129]. Compliance can be defined as the inverse of the volume modulus of elasticity, $C=1/E'$.

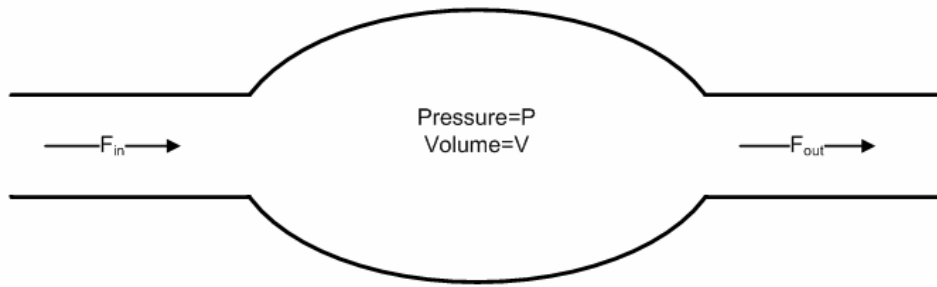


Figure 6.1: Model of the Windkessel concept.

6.2.1 Derivation of the Windkessel model

All pressure changes in the vascular system are considered to be simultaneous, that is an infinite wave velocity is assumed. In such a scheme, ventricular ejection flow which is the flow entering the vascular system (F_{in}) and pressure can be related to each other by equating the difference between inflow and outflow to the rate of storage which is the volume change in the vascular compartment. The following mathematical model (Equation 153) relates flow rate, pressure, resistance, and the elastic properties of the artery as defined in the Windkessel concept.

$$F_{in}(t) - F_{out}(t) = \frac{dV}{dt} \quad (153)$$

The relationship between pressure and volume in terms of elasticity can be expressed in terms of Equation 154 where the change in volume of the blood vessel can be determined as a product of a material property in the Windkessel chamber and the pressure derivative, which is an observable quantity.

$$\frac{dV}{dt} = \frac{dV}{dp} \cdot \frac{dp}{dt} = (1/E') \frac{dp}{dt} \quad (154)$$

Considering that the drop in pressure across the capillary bed is negligible compared to the systemic pressure,

$$F_{in}(t) - p / R_s = (1 / E') \frac{dp}{dt} \quad (155)$$

$$E'(F_{in}(t) - p / R_s) = \frac{dp}{dt} \quad (156)$$

$$E' F_{in}(t) = \frac{dp}{dt} + E' \frac{p}{R_s} \quad (157)$$

$$\frac{dP}{F_{in}(t) - p / R_s} = E' dt \quad (158)$$

$$\ln(F_{in}(t) - p / R_s) = E' t + c \quad (159)$$

$$F_{in}(t) - p / R_s = c_1 e^{-E't} \quad (160)$$

In this equation, the outflow is described by pressure divided by the peripheral resistance, R_s , neglecting venous pressure. It is assumed that inflow during systole is constant and equal to $F_{in,0}$.

$$c_1 = F_{in,0} - \frac{p_o}{R_s} \quad (161)$$

$$F_{in}(t) - p / R_s = \left(F_{in,0} - \frac{p_o}{R_s} \right) e^{-E't} \quad (162)$$

Rearranging the equation, the expression for systolic pressure, when $0 \leq t \leq t_s$, where t_s is the duration of systole and p_o is the pressure at the onset of systole.

$$p(t) = R_s F_{in,0} - \left(R_s F_{in,0} - p_o \right) e^{-E't / R_s} \quad (163)$$

During the diastole, when $F_{in}=0$, for $t_s \leq t \leq T$, where T is the duration of the cycle and p_T is the arterial pressure at the end of diastole.

$$p(t) = p_T e^{(E'/R_s)(T-t)} \quad (164)$$

The general form with the stroke volume (V_s) can be expressed as,

$$V_s = \int_0^{t_s} F_{in}(t) dt = \int_0^T F_{in}(t) dt = \frac{1}{R_s} \int_0^T p(t) dt \quad (165)$$

The total peripheral resistance can be calculated if the stroke volume V_s and the pressure data from 0 to T are known.

$$R_s = \frac{1}{V_s} \int_0^T p(t) dt \quad (166)$$

The estimation of the integral for the pressure curve can be easily achieved but R_s is unknown. It is difficult to directly obtain peripheral vessel resistance *in vivo* using conventional imaging techniques. However optimization techniques can be used to derive this quantity indirectly using observable quantities such as blood pressure and volume.

6.3 Materials and methods

Pressure traces were collected for 5 tubes of different compliance. While a bolus injection of 50 ml of water was made into a tube, a pressure transducer recorded the pressure data. Using the equations above, values for R_s and E' were calculated for each tube. Peripheral resistance, R_s , is determined by integrating over the duration of the pressure trace and dividing by the stroke volume (Equation 166).

6.3.1 System description

The system consists of 3 subsystems: (1) Vascular phantom; (2) Fluid dispensing system; and (3) Data acquisition system (refer Figure 6.2). The vascular phantom consists of a fluid reservoir and the compliant tube to mimic the expandable Windkessel chamber. The fluid dispensing subsystem consists of a syringe pump to model the cerebral activation which causes an increase in blood flow. Finally the data acquisition subsystem consists of a pressure transducer, voltage amplifier and data acquisition card connected to a computer to collect pressure data from the input of the vascular phantom. Each subsystem is discussed in detail in the next few sections.

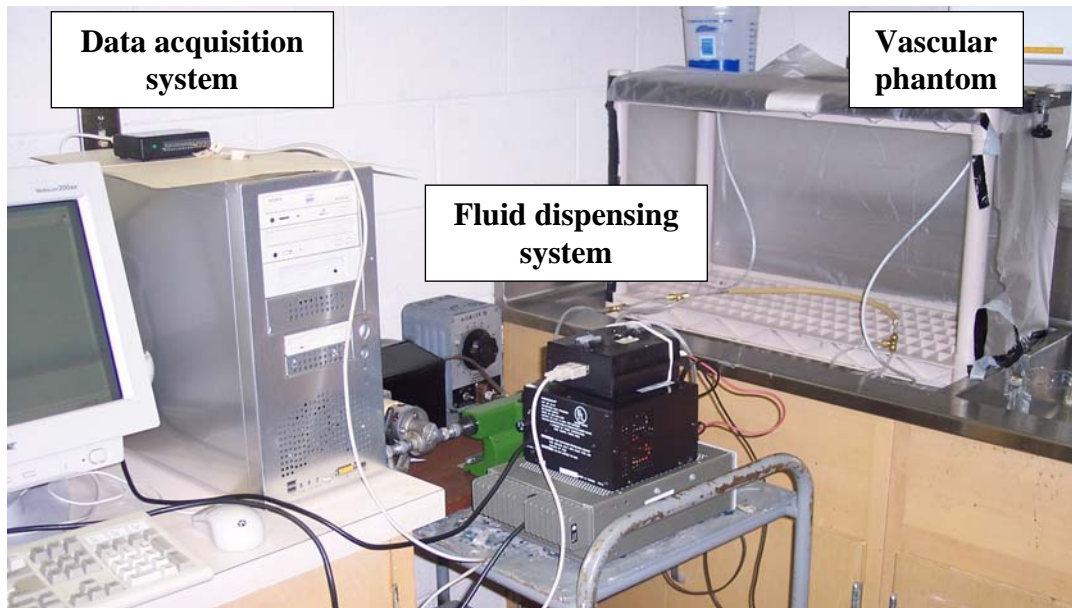


Figure 6.2: Experimental apparatus modeling the Windkessel concept

6.3.1.1 Vascular phantom

The vascular phantom consists of rigid tubing that represents the arteries and veins and compliant latex tubing that represent the capillary or Windkessel chamber (refer Figure 6.3). A reservoir containing water is used to provide the systemic flow and gravity is utilized to establish equilibrium conditions. The rigid tube that represents the arterial compartment was connected into a brass T-connector. The three arms of the T-connector were connected to (1) the fluid dispensing system, (2) the fluid reservoir and (3) a second T-connector that connects to the compliant tubing and pressure transducer. The other end of the compliant tubing is connected to a control valve that regulates the flow of fluid leaving the system.

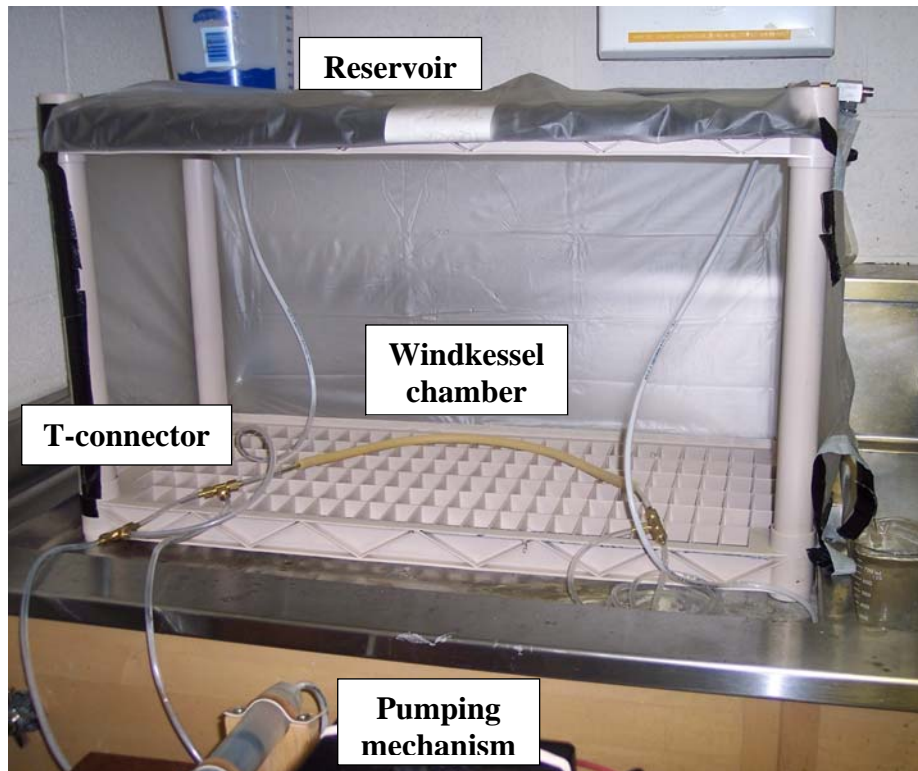


Figure 6.3: The vascular phantom system

6.3.1.2 Fluid dispensing system

The fluid dispensing system consists of a syringe pump. The syringe pump utilizes a high voltage (170 VDC) DC power supply connected to a universal motor that controls the motion of a linear motion stage which is connected to a 60 cc syringe that dispenses fluid (refer Figure 6.4). The 60cc syringe is joined to the brass T-connector with a small piece of rigid tubing that fits securely around both the opening of the syringe and the connector. The high voltage power supply was constructed using a variac, full wave rectifier, and 16mF capacitor. The variac was adjusted to control the speed of the motor.

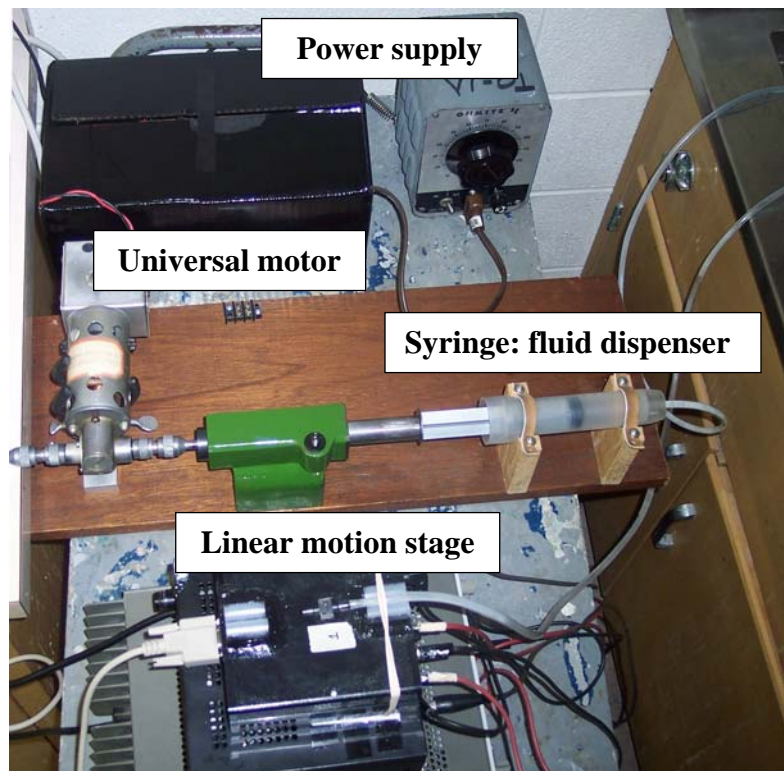


Figure 6.4: Fluid dispensing system

6.3.1.3 Data acquisition system

The pressure transducer used in this research was an Omega PX26 wet/wet differential pressure sensor. This pressure sensor requires a 10V DC power supply and 16.7 mV of voltage output corresponds to 1 psi of pressure difference. Since the output of the transducer is outside the input range of the data acquisition card, it was amplified by a factor of 100 using a non-inverting operational amplifier. The output of this voltage amplifier was input to the DAQ card (Refer Figure 6.5).

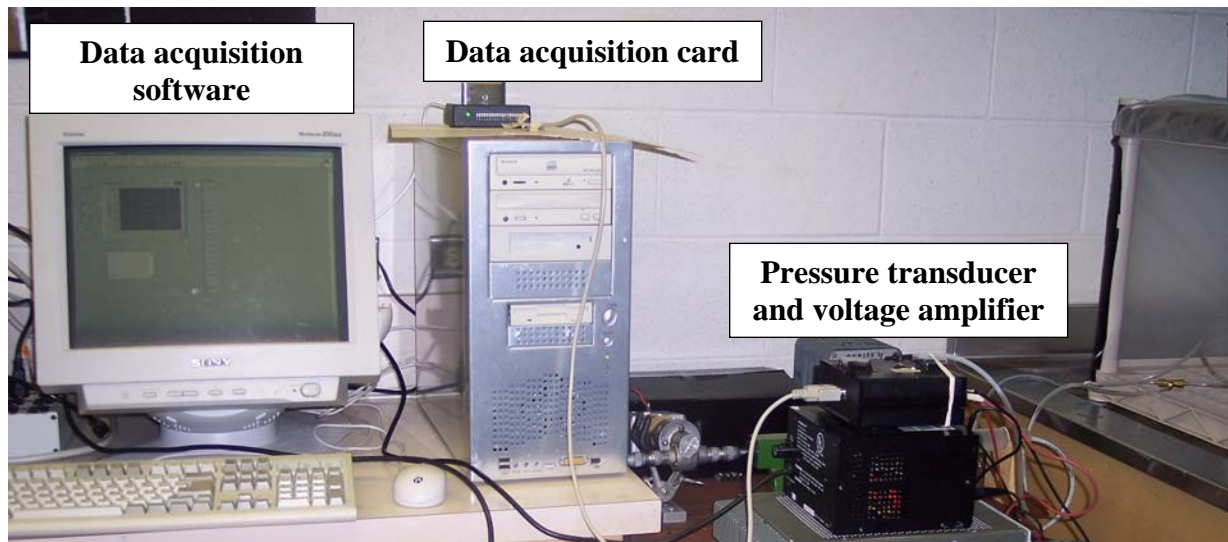


Figure 6.5: Data acquisition system

The DAQ card used was a Keithley KUSB-3100 plug-and-play data acquisition system using Universal Serial Bus (USB). The Model KUSB-3100 module, our economical solution, provides 8 single-ended inputs with 12-bit resolution, up to 50kS/s throughput, two 12-bit $\pm 10V$ analog outputs, 16 digital I/O lines, and 1 counter/timer and can be run under Windows® 2000 and XP platforms[130].



Figure 6.6: KUSB-3100 Economical Multifunction Data Acquisition module [130]

A Labview program is used to control the DAQ card and acquire pressure data from the sensor. The front panel is shown in Figure 6.7. The program has the following functionality

- a. Data source: User chooses to either acquire data from the DAQ card or from a previously ran experiment where the data was saved in a file.
- b. Channel: User chooses which one of the 16 I/O lines (0-15) to acquire data from. In this experiment, channel 0 was used.
- c. High and low limit: User sets the expected input range of the data thus setting the gain of the DAQ card.
- d. Stop: User can choose to stop data acquisition using this control.
- e. Waveform: The selected data set is displayed on the waveform plot. The x-axis shows time in seconds and the y-axis displays the pressure data. Pressure data is displayed in volts as acquired by the pressure transducer and can be converted to psi using a linear pressure-voltage relationship.

6.3.2 Experimental methods

The vascular phantom was filled with water to bring the system to steady state/equilibrium. This was done by pumping water through the system removing all air bubbles. This puts the system into steady state that resembles the vascular system in the human body which has a constant baseline flow. The increase in cerebral blood flow is seen as a change over baseline/resting blood flow.

Next the syringe was filled with 30 cc of water and aligned with the linear stage arm. The valve from the reservoir to the artery was closed to prevent any back flow into the reservoir. In the human body, a pressure differential prevents backflow to the heart through the arteries. Closing the valve creates an analogous situation and prevents backflow in the reservoir. The variac was set at 170V to drive the motor. This caused the motor to push 35 cc in 3.5 seconds.

Using the system shown above, ten trials were conducted for each type of tubing. LabVIEW was configured to take 100 points per second with each experiment lasting 8-10 seconds. The program was set to 'Run' and the bolus injection was sent through the tubing and collected in the beaker at the other end. The same procedure was repeated for each trial. In the experimental set-up five tubes of varying compliance were used as part of the Windkessel model. The tubes were selected to provide a broad range of compliance. Water pumped into the Windkessel chamber (modeled by the compliant tube) caused the chamber to expand. Water was then expelled from the system at a constant rate regulated by a valve at the distal/venous end. The valve on the

output was kept at the same setting through the entire experiment with a magnitude of flow smaller than the elevated flow created by the fluid dispensing system.

The vascular chamber's elasticity simulates the distensible nature of a blood vessel as fluid is pumped into it. This effect is referred to as vessel compliance. The resistance water encounters while traversing the system simulates resistance to flow encountered by blood as it flows through the vascular system. This resistance to flow is called peripheral resistance [128]. The blood vessel of interest can be represented mathematically by a single lumped parameter representation of the vessel elasticity, or a 'Windkessel' compliance, with a tube representing the vessel dimensions. The two important parameters examined in this experiment, are peripheral resistance and vessel compliance.

6.4 Experimental results

This section presents the optimization/fitting procedure used to analyze the pressure data along with results for each tube. Statistical analysis for the predicted compliance coefficient and peripheral resistance values are also presented.

6.4.1 Data fitting procedure

Ten sets of pressure vs. time data were collected for each tube. Also, the peripheral resistance (R_s) for each tube was calculated using Equation 166. First the diastole of the pressure curve was fit using Equation 164 to predict values for compliance coefficient (E'). The diastole represents the time from the end of the syringe

stroke when incoming flow into the system is zero to the end of the experiment (pressure returns to baseline). The beginning of diastole was identified by locating the peak of the pressure trace which marks the end of the systole. Next the systole was fit using Equation 163, to cross validate the values obtained from fitting the diastole. The systole represents the time from the start to the end of the syringe stroke (pressure goes from baseline to peak). Fitting the systole provides two values, E' and $F_{in,0}$. Now E' can be cross validated with the value obtained from the diastole and $F_{in,0}$ can be compared to the know constant inflow into the system provided by the syringe. The goodness-of-fit estimates are calculated for each optimization procedure using R-squared values.

6.4.2 Optimization results

The resulting exponential fit was compared to Equation 163 and 164 and values for E' and F_{in} were computed. Figures 6.9-6.13 show representative pressure traces for each of the five tubes.

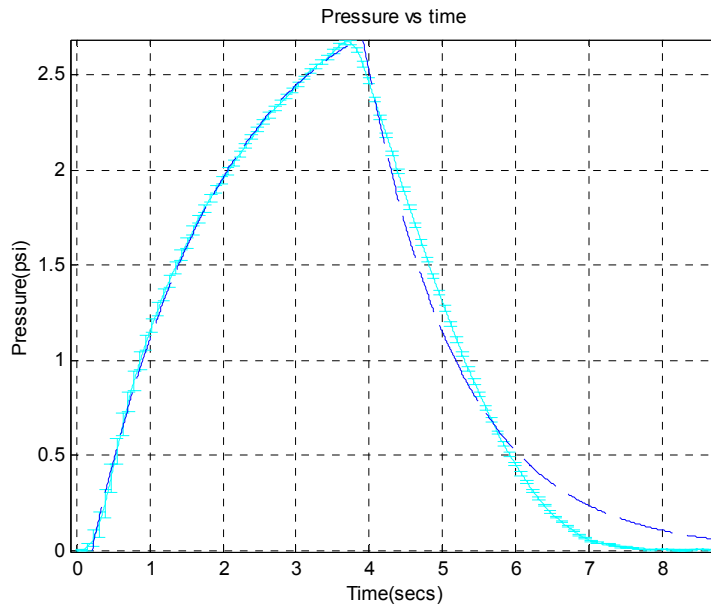


Figure 6.9: Pressure trace and Windkessel fits (Wall thickness 0.093", inner diameter=0.25") Systole fit: $R^2 = 0.9992$, Diastole: $R^2 = 0.9789$

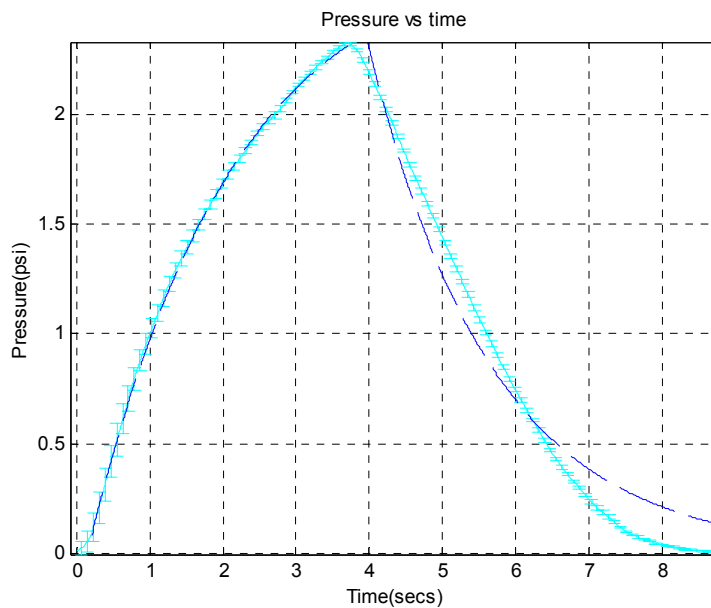


Figure 6.10: Pressure trace and Windkessel fits (Wall thickness 0.0625", inner diameter=0.25") Systole fit: $R^2 = 0.9996$, Diastole fit: $R^2 = 0.9723$

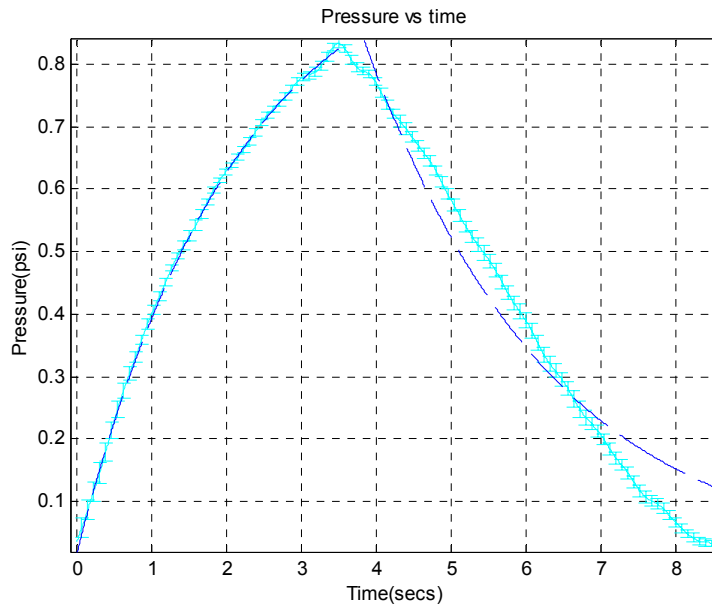


Figure 6.11: Pressure trace and Windkessel fits (Wall thickness 0.015", inner diameter=0.25") Systole: $R^2 = 0.9996$, Diastole: $R^2 = 0.9544$

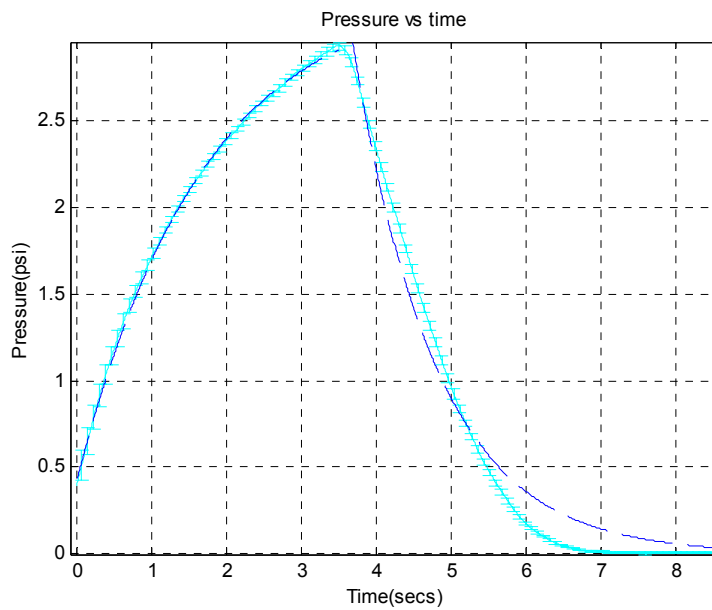


Figure 6.12: Pressure trace and Windkessel fits (Wall thickness 0.125", inner diameter=0.25") Systole: $R^2 = 0.9995$, Diastole: $R^2 = 0.9753$

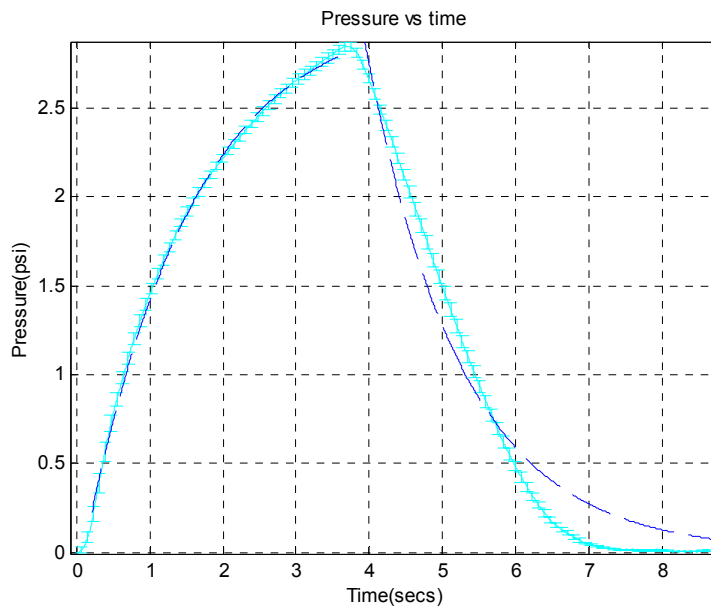


Figure 6.13: Pressure trace and Windkessel fits (Wall thickness 0.469", inner diameter=0.25") Systole: $R^2 = 0.9959$, Diastole: $R^2 = 0.9622$

6.4.3 Statistical analysis

The ten trials for the five tubes are consistent within their respective sets of data with small standard deviations. Ten trials were performed for each type of tube. In Figure 6.14, the scatter plot of peripheral resistance and modulus of volumetric elasticity is shown. The Windkessel model predicts that peripheral resistance increases as compliance decreases (that is modulus of volume elasticity increases). This trend is observed in the graph where resistance linearly increases with increase in modulus of volume elasticity. The correlation coefficient in the two quantities is also very high (~97%) further illustrating the strong codependence.

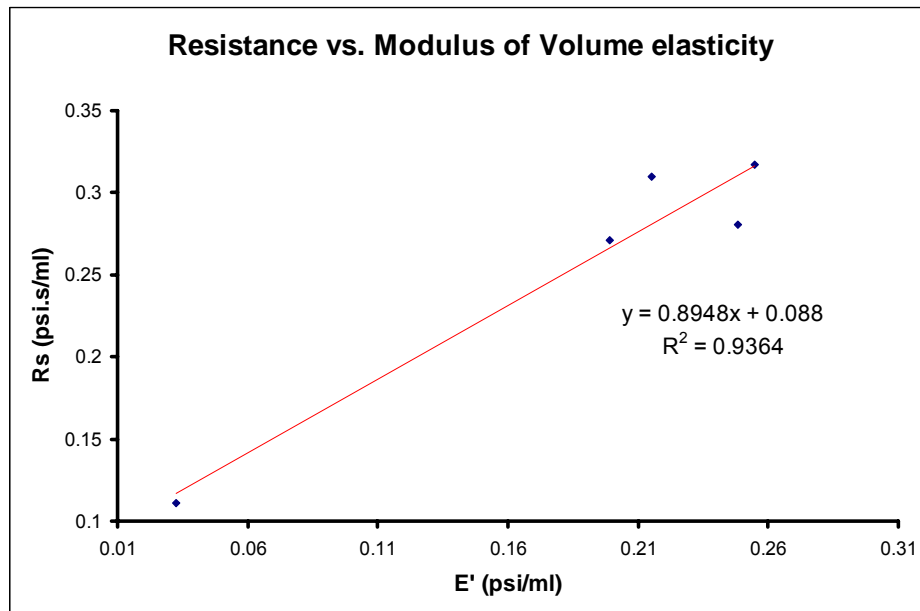


Figure 6.14: Resistance vs. Modulus of volume elasticity

In addition the 95% confidence limits for E' , F_{in} and R_s were determined. The known value of F_{in} was compared to the value of F_{in} obtained using the fitting routine on the systole. The results of this statistical analysis are displayed in Tables 6.1 below.

Table 6.1: Data statistics (lb) and (ub) represent the lower and upper 95% confidence limits.

Vascular Phantom data statistics								
Wall width inch	R_s psi.s/ml	$R_s(lb)$ psi.s/ml	$R_s(ub)$ psi.s/ml	E psi/ml	$E(lb)$ psi/ml	E' (ub) psi/ml	$F_{in}(lb)$ ml	Known F_{in} ml
0.015	0.111	0.111	0.111	0.042	0.042	0.042	32.817	35
0.062	0.271	0.271	0.271	0.124	0.122	0.126	37.096	35
0.093	0.281	0.281	0.281	0.260	0.236	0.284	40.114	35
0.125	0.309	0.309	0.309	0.233	0.231	0.234	37.054	35
0.469	0.317	0.317	0.317	0.230	0.229	0.231	34.125	35

6.5 Discussion

During experimentation there was only a small radial expansion seen in the vascular tubing segment following the bolus injection. This means the experiment was confined to a Hooke's law linear regime consistent with Windkessel theory. The expanding tube acted like a capacitor and started discharging water when the peak pressure was reached at the end of injection (i.e. end of systole) followed by an exponential fall of pressure as the liquid was discharged from the tube till the pressure inside the tube returned to atmospheric pressure (i.e. end of diastole). The diastole region of the pressure traces obtained from the tubes with different compliance follows the exponential behavior predicted by the Windkessel model. As can be seen in Figures 6.7-6.11, the diastolic regions for the tubes differed significantly in pressure as the compliance of the tubes changed.

The measurements made on the five tubes of different compliance show good agreement with the mathematical predictions made using the Windkessel model as indicated by the high R^2 values. The compliance of the latex vessels has been shown to affect the mean arterial resistance provided to flow through them. High values of compliance tend to decrease the peripheral resistance within the vessel, with the more rigid vessels impeding the flow. The vessels are made of latex and are permeable to oxygen and hold great promise for use in models of the vascular system.

6.6 Future directions

A potential variation on the phantom could include doing multiple, periodic pulses to model repeated stimuli. Another possible experiment could involve putting tubes of varying compliance in series with pressure and flow measurements made at the entry point into each vessel segment. Such a vascular model could be used to validate the flow volume dynamics in a multi-compartment Windkessel model. Furthermore, physiologically realistic structures could be made by placing several tubes together using y-connections to model the complicated capillary bed. Further work is also required to completely characterize the vessels and to compare their dynamic properties (such as pulse velocity and spatial flow profiles) with those of a natural artery. The use of these compliant artificial vessels will allow the construction of more physiologically accurate flow systems with the possibility of making comparative measurements between a vascular model, normal subjects and a patient group with arteriosclerosis.

Finally, the vascular phantom could be significantly modified to model oxygen transport dynamics. A Doppler flow meter can be used to measure the blood flow at different locations. Rabbit/rat blood mixed with heparin can be used in the vascular phantom. A co-oximeter can be used to measure Hb, HbO₂, HbT concentrations, and hemoglobin oxygen saturation (SO₂) of the blood before being added in the solution. Two frequently used methods to deoxygenate a blood solution can be combined to model vascular oxygen dynamics: the first is to bubble a non-oxygen gas through the blood mixture, and the second is to add yeast to the mixture. The yeast will consume the oxygen in the blood mimicking tissue oxygen consumption. The measurement can be

taken over several oxygenating-deoxygenating cycles using NIRS source and detector pair to quantify Hb, HbO₂, and HbT of the phantom solution. These hemodynamic concentrations can be calculated by applying the Beer-Lambert's law using the absorption coefficients at different wavelengths and the diffusion theory. The O₂ molecules in the circulated blood will penetrate through the capillary bed and be consumed by the yeast in the surrounding liquid. The rate of O₂ consumption depends on the concentrations of the yeast, blood flow, and the HbO₂ concentration. The deoxygenated blood can be re-oxygenated in the oxygenation chamber and circulated back into the system. Thus, this hemodynamic phantom can simulate the physiological hemodynamic process with controlled parameters of CBF and CMRO₂ by controlling the pumping rate and concentrations of the yeast in the tissue-simulating liquid. For dynamic measurements, the NIR source/detector fibers can be placed either in reflectance or in transmittance geometry along the circumference of the container.

6.7 Chapter summary

A technique has been described to provide a reliable method to characterize compliant vessels for use in arterial models. In addition, the described vascular phantom proves the hypothesis that compliance directly affects the volume and resistance of a blood vessel when flow is constant. The phantom provides a method to validate the flow-volume relationship described by the Windkessel model and can be modified to include oxygen transport dynamics as well as transient phenomena like pulse velocity.

CHAPTER 7

EXPERIMENTAL PROTOCOLS AND RESULTS

The development of near infrared spectroscopy (NIRS) as a viable brain imaging technique has primarily centered on measuring hemodynamic values that are associated with the performance of perceptual or motor tasks. For example, previous researchers have utilized NIRS to measure hemodynamic values while participants opened and closed their hands at a constant rate. While research using NIRS to measure brain function associated with such tasks furthers the current understanding of the instrumentation, far less research has attempted to validate NIRS as a viable means of measuring neurological correlates of cognitive activity.

As such, the primary goal of the experiments conducted during the course of the present research was to demonstrate the feasibility of NIRS when used in conjunction with cognitive designs to identify brain regions preferentially activated by a stimulus task. This chapter outlines the NIRS experiments that were conducted during this research as well as the results from previously published multimodality data that was used to test the models developed during this research. The models are also cross validated against each other.

7.1 Protocol: Categorical learning task

Little work has attempted to validate NIRS as a viable means of measuring neurological correlates of cognitive activity in the brain using appropriate controls. The goal of this research was to use near infrared spectroscopy (NIRS) and mapping (NIRM) to identify regions of the brain that are preferentially activated by a task. Such an endeavor seemed particularly timely, because to date, much of the research conducted using NIRS has centered on the comparison of blocks of activation evoked using an activation task to a resting baseline period. During the baseline period, participants sit quietly and clear their minds while staring at a fixation point. The comparison of hemodynamic values measured while participants perform a task of interest to a resting baseline period can be informative when participants are performing simple behavioral or perceptual tasks. However, a simple comparison to baseline is far less informative when participants are required to perform complex higher order cognitive tasks. Unlike a simple task that requires participants to look at a grid pattern for example, a cognitive task, such as word recognition, requires the orchestration of numerous basic cognitive processes. As such, one of the keys to studying cognitive processes is the selection of appropriate activation and control tasks. These tasks are typically selected such that they differ only in one key cognitive process. If a researcher has successfully chosen two tasks that only differ in one cognitive process, it logically follows that any difference in the observed level of activation is induced by the cognitive process of interest. A baseline period, during which time a person stares at a

fixation point, does not typically meet this criterion, because the task of interest will vary from a resting baseline along multiple cognitive domains.

To this end, we implemented a blocked design experiment in an attempt to better isolate brain activation associated with the extraction of the underlying meaning of a list of words. For a blocked design the same types of events are grouped together to produce a presentation block of like items. The block design stands in contrast to an event-related design, in which different types of items are intermixed amongst one another. The block design is particularly advantageous given the physiological characteristics of the hemodynamic response allowing for a better signal to noise ratio. The blocking of like items provides a means of evoking activation that can be imaged but the selection of an appropriate control task is paramount for obtaining meaningful, easily interpretable results.

The present investigation focused on identifying areas of the prefrontal cortex involved in processing the gist (i.e., central meaning) of a list of semantically related words. To accomplish this, we used a standard blocked presentation design and NIRS equipment in conjunction with a commonly used word learning paradigm. In addition, we selected two tasks that varied only in the degree to which participants would be able to extract gist from a list of words. Both tasks involved the exact same procedures and processes with the exception that one of the tasks incorporated study lists that were easier to process for a central meaning or gist.

7.1.1 Materials and methods

Participants ($N = 16$, 11 females, mean age 21, range 18–34 years) were recruited from the participant pool of the Department of Psychology at the University of Texas at Arlington. The subjects completed the research as partial fulfillment of a course research requirement. All participants were native speakers of English with normal or corrected-to-normal vision and reported no history of significant neurological problems. Participants provided informed consent in accordance with the guidelines set forth by the Office of Research Compliance at the University of Texas at Arlington. This research was carried in conjunction with Dr. H. Liu and Dr. Timothy Odegard at the Department of Psychology (UTA).

7.1.1.1 Protocol details

Twelve word lists served as stimuli. Each list consisted of 10 words that were all related to a critical central word; this central word represented the underlying meaning or gist of the list. For example, the words: *water*, *stream*, *lake* are all related to the central word *river*. Of the 12 lists presented to participants, 6 were easy gist lists, each composed of 10 words that were all highly related to a central gist. In addition, 6 of the lists were difficult gist lists, each consisting of 10 words that were more difficult to process for their central meaning.

Prior to the start of the experiment, all participants were informed that they would be presented with two blocks of word lists. They were instructed to attend closely to the relationship among the words presented in each of the study lists (e.g.,

glass, pane, shade, ledge, sill, house, open, curtain, frame, shutter), and were further instructed to attempt to identify the one word that tied them all together (e.g., *window*). The participants were informed that they would be given a memory test for the words after studying all of the word lists. Two blocks of word lists were then presented to each participant.

Prior to the start of each study block, the participants completed a period of baseline measurement, during which time they were instructed to clear their minds and to fixate on an asterisk mark displayed on a computer screen for 60 seconds. After the baseline period, the first block of study lists began. During a study block, words were displayed one at a time for approximately 2.31 seconds each in the center of a computer screen. When a word appeared on the screen, a recording of a female voice saying the word was also played over a pair of speakers. After all six lists had been presented during the first study block; the participants completed a second 60-second baseline period. After this second baseline period, the participants viewed a second block of six study lists.



Figure 7.1: Protocol followed for the experiment. A baseline period of rest was followed by a stimulation period where the participant viewed word lists of unrelated words where the central meaning was difficult to extract; then another period of rest was given, again followed by another stimulation period where the participant viewed word lists of related words where the central meaning was easy to extract, and finally a period of rest

Whether or not the participants first studied a block of easy or difficult gist lists was counterbalanced across participants, such that half of the participants were first presented with an easy gist block and the remaining half of the participants were first presented with a difficult gist block. The entire experimental protocol is shown schematically in Figure 7.1. After viewing both study blocks, participants completed another baseline period, followed by a recognition memory test for the words presented during the study blocks.

7.1.1.2 Protocol details

Noninvasive near infrared spectroscopy was used to acquire cerebral hemodynamic changes while participants encoded lists of thematically related words. NIRS uses the wavelength range of 700-900 nm, within which tissue has the least absorption coefficient. For this experiment, we used a LEDI system (Near Infrared Monitoring, Inc., Philadelphia, PA). The NIR light from four light emitting diodes (LEDs) was shone on the tissue under examination, and each of the LEDs provided the two selected wavelengths to be turned on in temporal sequence. The headband was placed across the forehead of the participant with detector 1 on the top right temple of the participant. This placement of the headband enabled the NIR light to interrogate the area of the brain behind the forehead (i.e., the prefrontal cortex) (for details refer Chapter 2). A reliable optical signal was measured with minimum noise interference by implementing proper controls during experimentation. Ambient light was kept at a minimum level during the course of the experiment, and errors introduced by loss of

light due to hair were reduced by clearing the probe of such interference.

The values for oxygenated hemoglobin [HbO_2], deoxygenated hemoglobin [Hb] and total hemoglobin [HbT] were calculated using the measured optical intensities. Markers were added to the data during the course of the experiment to distinguish temporal periods of baseline (rest) and periods of neurological activation for each participant. Baseline values of [HbO_2] were quantified as zero or near zero, and all subsequent measurements were relative to the baseline. Hemodynamic spatial profiles were collected and analyzed through the NIRS measurements in order to reveal brain activities of the participants. Entire time courses of individual parameters (i.e., [HbO_2] and [Hb]) were measured during the entire period of stimulation (i.e., during both blocks of lists for easy and difficult gist).

For spatial maps, the hemoglobin levels for each channel were averaged over each blocked period of activation. The stimulation period was divided into two distinct activation blocks: one with the lists where the central theme was easy to derive and the other one with the lists where the gist was harder to derive. Thus, spatial maps of the temporal average over activation blocks were constructed and compared to the average of readings taken during baseline (no stimulation: fixation point presented). This helped identify which areas of the prefrontal cortex under observation showed the largest changes in [Hb] and [HbO_2] over time.

Table 7.1: Sample protocol with study blocks

Block no.	Event Type	Screen Display	Duration (sec)
Baseline	Fixation point	*	60
Stim. Block 1	Indicator	UNRELATED	2.64
		BOUNCE, FIGHT, BLAZE, TOBACCO, SILL, CIGAR, FUR, SUBWAY, OPEN, BILLOWS	Total=13.2 (1.32 per word)
		UNRELATED	2.64
		TIRE, CAPITALGLOVES, HATE, CURTAIN, FRAME, FURY, BALL, POLLUTION, COUNTRY	Total=13.2
		UNRELATED	2.64
		TEMPER, SOLES, SHADE, LOUD, TOUCH, ELASTIC, MAD, ASHES, GALOSHES, METROPOLIS	Total=13.2
		UNRELATED	2.64
		FEATHER, SPRINGY, TOWN, STREETS, FEAR, NEW YORK, LEDGE, PILLOW, VILLAGE, FLUFFY	Total=13.2
		UNRELATED	2.64
		HOUSE, HARD, PANE, PUFF, RAGE, CROWDED, FIRE, COTTON, CHIMNEY, LIGHT	Total=13.2
		UNRELATED	2.64
		PLUSH, HATRED, GLASS, WRATH, DOOR, FOAM, HAPPY, CIGARETTE, ERASER, STATE	Total=13.2
Baseline	Fixation point	*	60
Stim. Block 1	Indicator	RELATED	2.64
		WATER, STREAM, LAKE, MISSISSIPPI, BOAT, TIDE, SWIM, FLOW, RUN, BARGE	Total=13.2
		RELATED	2.64
		HILL, VALLEY, CLIMB, SUMMIT, TOP, MOLEHILL, PEAK, PLAIN, GLACIER, GOAT	Total=13.2
		RELATED	2.64
		GARBAGE, WASTE, CAN, REFUSE, SEWAGE, BAG, JUNK, RUBBISH, SWEEP, SCRAPS	Total=13.2
		RELATED	2.64
		STEAL, ROBBER, CROOK, BURGLAR, MONEY, COP, BAD, ROB, JAIL, GUN	Total=13.2
		RELATED	2.64
		LOW, CLOUDS, UP, TALL, TOWER, JUMP, ABOVE, BUILDING, NOON, CLIFF	Total=13.2
		RELATED	2.64
		TABLE, SIT, LEGS, SEAT, COUCH, DESK, RECLINER, SOFA, WOOD, CUSHION	Total=13.2
Baseline	Fixation point	*	60

7.1.1.3 Statistical analysis

All inferential statistical analyses were performed on the maximum [HbO₂] values measured during a study block with respect to the baseline maximum [HbO₂] values. The data was baseline corrected to remove the effects of baseline drift. A simple subtractive method was used to correct all the values in the data set before the maximum baseline [HbO₂] levels were calculated. A 60-second baseline period preceded each of the study blocks. The maximum [HbO₂] value from the baseline period that immediately preceded a study block was subtracted from the maximum [HbO₂] value during the study block. This was done for each participant's maximum [HbO₂] values and for each of the study blocks with easy or hard gist lists. The corresponding corrected maximum [HbO₂] values are provided in Table 7.2 and 7.3 with standard errors provided in parentheses (n=16).

Planned comparisons were performed on these values comparing the amount of activation measured at a given channel when participants encoded a block of easy gist list compared to hard gist lists. While statistical analyses were conducted for [Hb], [HbO₂] and [HbT], significant differences between the two phases of study were found to occur predominantly for [HbO₂], and thus only [HbO₂] results are presented in this paper. This is consistent with previous studies conducted with similar protocols using NIRS to measure effects of cognitive stimulation on the prefrontal cortex. We observed increased levels of HbO₂ in the medial inferior and right inferior regions of the prefrontal cortex when participants were presented with lists of words that were more difficult to process for a central meaning than when presented with lists of words that

had an easily identifiable central meaning (see Figure 7.2 refer to odd numbered channels). When presented with a more difficult set of lists to process for a central theme, additional resources were recruited from specific prefrontal regions, and these differences were successfully measured using NIRS technology.

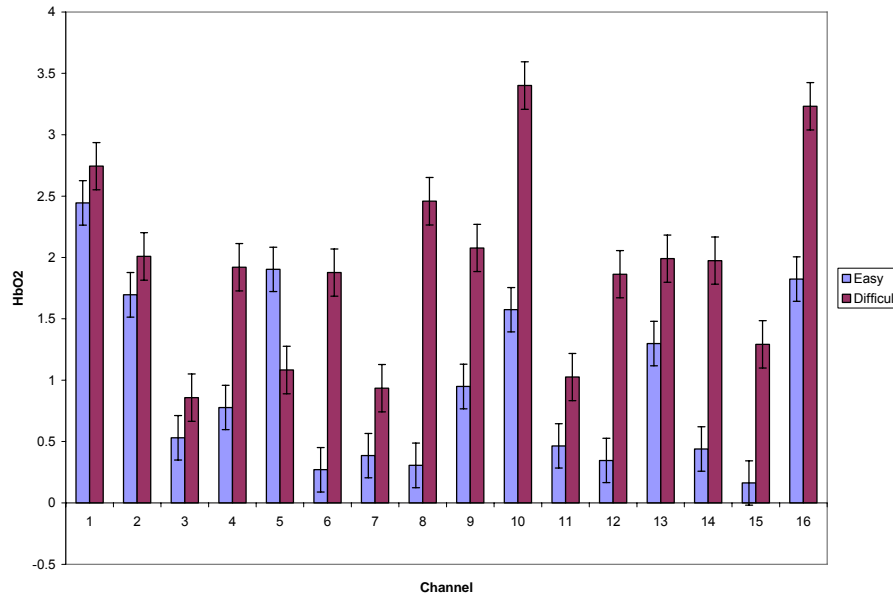


Figure 7.2: Comparison of the Maximum HbO₂ levels minus baseline activation for block of lists with easily identifiable themes and lists of words with more difficult to identify themes.

7.1.2 Results

The LEDI equipment was used to measure changes in [HbO₂] and [Hb] from regions of interest. These readings were used to generate spatial maps of Δ [HbO₂] and Δ [Hb] during baseline and activation periods to illustrate the differences in hemodynamic variables between blocks of activation. Baseline periods corresponded to the NIRS readings taken when the participants were in a resting state (awake with eyes

open but no stimulation), while activation periods were associated with the readings when the participants were performing the experimental task (see Fig. 7.1). Specifically, the results of the data were gathered over 16 channels during the course of measurement.

The focus of the study was on the spatial distribution of changes in Δ [HbO₂] and Δ [Hb] during activation periods and to investigate the differences in hemodynamic variables between blocks of activation. Thus, spatial maps of maximum levels of Δ [HbO₂] measured from the 16 channels taken during baseline and the two blocks of cognitive tasks from a single participant are provided in Figure 7.3, as an example. The spatial maps of the block-averaged responses of Δ [HbO₂] and Δ [Hb] measured on the same participant are shown in Figure 7.4. Figure 7.4 plots each channel's average hemoglobin concentration level ([Hb] or [HbO₂]) over the entire period of activation measured from the region of interest, allowing for the identification of areas in the prefrontal cortex that exhibited the largest changes in [HbO₂] over time and are hence inferred to be preferentially activated by the presented task. Each map in Figures 7.3 and 7.4 is a low pass filtered graphical representation of the areas of the forehead along which the measurements were taken. Spatially, the NIR readings indicate regions from the right to the left of the subject's forehead extending from the left to the right on the plotted maps.

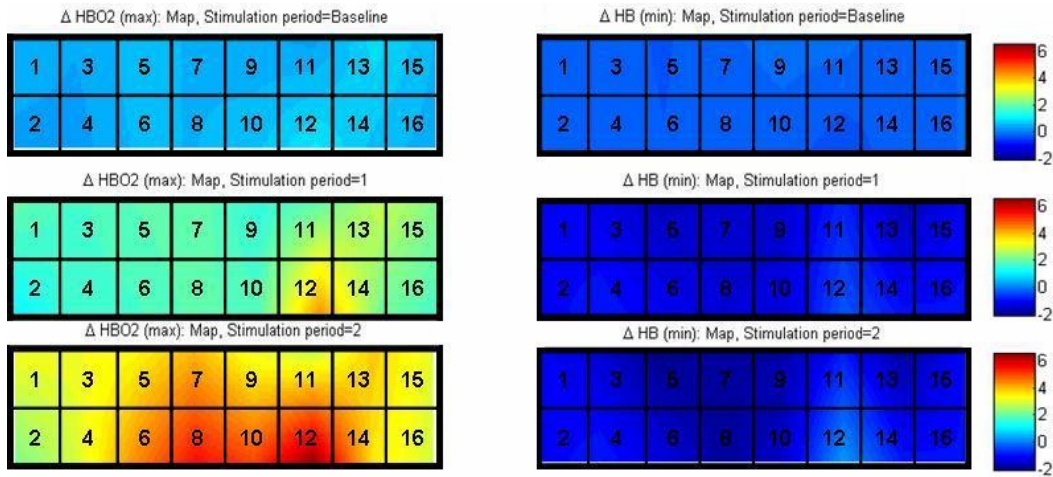


Figure 7.3: Maps of maximum $\Delta[\text{HbO}_2]$ and $\Delta[\text{Hb}]$ across the prefrontal cortex from a representative participant. The first row of maps represents the hemoglobin levels at Baseline: period of rest (eyes on fixation point, no stimulation). The second row of maps represents the hemoglobin levels at activation period 1: Presentation of lists of unrelated word where the central meaning was difficult to extract. The third row of maps represents the hemoglobin levels at activation period 2: Presentation of lists of related words where the central meaning was easy to extract

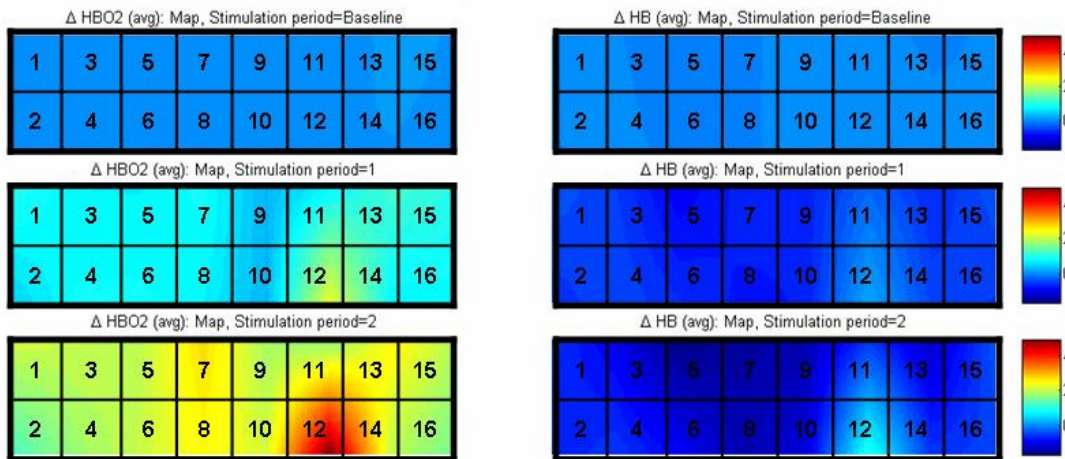


Figure 7.4: Maps of average $\Delta[\text{HbO}_2]$ and $\Delta[\text{Hb}]$ across the prefrontal cortex from a representative participant. The first row of maps represents the hemoglobin levels at Baseline: period of rest (eyes on fixation point, no stimulation). The second row of maps represents the hemoglobin levels at activation period 1: Presentation of lists of unrelated word where the central meaning was difficult to extract. The third row of maps represents the hemoglobin levels at activation period 2: Presentation of lists of related words where the central meaning was easy to extract

Planned comparisons between the easy and difficult gist blocks revealed increased activation in medial inferior regions of the prefrontal cortex when participants encoded the easy lists compared to the hard lists. Based on Figure 7.3, we observe that significantly greater levels of maximum $\Delta[\text{HbO}_2]$ were shown in several channels (e.g., channels 6, 8, 10 and 12) when participants encoded a block of easy lists in comparison to a block of hard lists, $F(1, 15) = 7.05$; $F(1, 15) = 4.27$; $MSE = 3.84$.

To further identify the extent to which increased levels of activation were concentrated in the medial inferior prefrontal cortex, maximum $\Delta[\text{HbO}_2]$ values were averaged across channels 6, 8, 10 and 12 (i.e., the channels measuring the medial inferior prefrontal cortex) and compared to maximum $\Delta[\text{HbO}_2]$ values averaged across channels 5, 7, 9, 11 (i.e., the channels likely to interrogate the medial superior prefrontal cortex). There was no significant difference between the inferior ($M = .90$) and superior ($M = .65$) regions when the participants encoded blocks of hard gist lists, $F < 1$. There was, however, a significant difference between the maximum $\Delta[\text{HbO}_2]$ values measured in the medial inferior and medial superior prefrontal cortex, based on the NIR readings from the same channels as those used above, when participants encoded easy lists (inferior $M = 2.05$; superior $M = .68$), $F(1, 15) = 3.91$. Thus the results provide suggestive evidence that the medial inferior prefrontal cortex is involved in processing the gist of study materials.

Table 7.2 Mean values of maximum $\Delta[\text{HbO}_2]$ for the channels measuring Superior Prefrontal Cortex (n=16)

Channel numbers	1	3	5	7	9	11	13	15
Easy Block	0.78 (0.21)	0.60 (0.24)	0.70 (0.23)	0.63 (0.19)	0.71 (0.22)	0.67 (0.26)	1.08 (0.39)	1.32 (0.40)
Hard Block	0.72 (0.28)	0.61 (0.29)	0.72 (0.31)	0.64 (0.27)	0.58 (0.23)	0.65 (0.26)	0.85 (0.29)	0.78 (0.28)
F(1, 15)	<1	<1	<1	<1	<1	<1	<1	<1

Table 7.3 Mean values of maximum $\Delta[\text{HbO}_2]$ for the channels measuring Inferior Prefrontal Cortex (n=16)* Indicates those contrasts that were significant at an alpha level of $p < .05$

Channel numbers	2	4	6	8	10	12	14	16
Easy Block	1.58 (0.46)	1.69 (0.65)	2.10 (1.21)	1.90 (0.96)	1.90 (0.66)	2.29 (0.85)	2.10 (0.55)	2.14 (0.56)
Hard Block	1.04 (0.40)	0.71 (0.35)	0.26 (0.70)	0.80 (0.76)	1.70 (0.72)	0.86 (0.55)	1.35 (0.42)	1.34 (0.44)
F (1, 15)	<1	2.03*	7.05*	2.54*	<1	4.27*	1.15	1.35

7.1.3 Discussion

Comparisons of the oxygenated hemoglobin data were carried out for each block to reveal regions of the brain that were preferentially activated by the presented task. The data was compared using the type of task presented to illustrate the differences in activation produced by individual tasks. The experimental results indicate increased activation in medial inferior regions of the prefrontal cortex when the participants encoded lists with a central meaning that was easier to process when compared to lists with a central meaning that was more difficult to process. This is an important observation, documenting the brain regions that vary from baseline and are activated during the presented word learning task. More importantly, the results identify brain

regions that varied when participants performed two cognitive tasks that only differed in the ease by which individuals could process the underlying meaning of lists of words.

7.1.4 Conclusions

In conclusion, we have reported a novel application of near infrared spectroscopy to cognitive studies. We observed increased levels of changes in [HbO₂] in the medial inferior prefrontal cortex when the participants were presented with lists of words that were easier to process for a central meaning in comparison to lists of words that were more difficult to process for a central meaning. These results suggest that the medial inferior prefrontal cortex is involved in the extraction of gist. This study supports previously published fMRI [131] results by application of a less cumbersome and unobtrusive imaging method. We believe that NIRS can be extended as a convenient brain imaging tool with a wide range of possible applications to the study of cognitive neuroscience, such as for developmental studies involving children.

7.2 Protocol: Verbal fluency and physical exercise

Early diagnosis of diseases such as Alzheimer's disease (AD), schizophrenia, etc. is crucial because symptoms respond best to available treatments in the initial stages of the disease. Studies have shown that there are marked changes in brain oxygenation during mental and physical tasks that can be detected with noninvasive functional brain imaging. The goal of our study is to explore the possibility of using near infrared spectroscopy (NIRS) and mapping (NIRM) as a diagnostic tool for

diseases such as AD before the onset of significant morphological changes in the brain.

This study focuses on the changes in oxygenation levels of the prefrontal cortex during mental and physical activation. Areas of the brain that control memory, namely the prefrontal cortex and the hippocampus, are most affected in the first stage which usually lasts two to three years [132]. It is critical to diagnose the disease in its initial stage, because this is the time when symptoms respond best to available treatments [133].

7.2.1 Materials and methods

Healthy subjects with no history of psychiatric or neurological disorders were recruited for each study. For the verbal fluency task, ten subjects were recruited (ages 22-35; mean age 26; four female; six males). For the physical exercise task, ten subjects were recruited (ages 22-35; mean age 25; three female; seven males). Participants provided informed consent in accordance with the guidelines set forth by the Office of Research Compliance at the University of Texas at Arlington. This research was carried in conjunction with Dr. H. Liu.

7.2.1.1 Protocol details

The two experiments conducted were physical and mental exercise protocols and their effects on regional cerebral hemoglobin levels were determined. The task given to the subjects for the mental exercise was a verbal fluency task. Subjects sat in a convenient position at rest throughout the duration of the examination that included a

period of rest (1 minute), a period of cognitive stimulation (1 minute, subjects had to perform a letter fluency task) followed by a period of rest (1 minute). For the verbal fluency task the subjects were asked to think of as many words as they could think of beginning with the letters A, F and M in the 1-minute cognitive period. The second task given to the subjects was a physical exercise. Subjects sat on an exercise bicycle during the experiment that consisted of a period of rest (1 minute), a period of cycling with no grade or resistance added (3 minutes), and finally another period of rest (2 minutes). Neuroimaging studies suggest that neural activation associated with a particular stimulus returns to baseline (rest) levels after the cessation of that task and thus differential activation of the brain regions by a given protocol can be measured.

7.2.1.2 Data acquisition

Noninvasive near infrared spectroscopy (NIRS) was used to acquire cerebral oxygenation level data in both the experiments. We use the LEDI system (Near Infrared Monitoring Inc.) in reflection mode. The measurements were performed at 730 nm and 850 nm. Brain volume measured by optical spectroscopy corresponds to a banana shaped figure under the light source and the detector capturing the light on the surface of the body under examination with the infrared radiation penetrating a few centimeters deep into the brain (for further details refer Chapter 2)

The values for oxygenated hemoglobin [HbO_2], deoxygenated hemoglobin [Hb] and total hemoglobin [HbT] are recorded. Markers are added to distinguish period of baseline (rest), period of activation and time to return to baseline reading (second period

of rest) from each other. It should be reiterated at this point that the baseline values are not exactly quantified and all subsequent measurements are relative to the baseline and therefore are not exact values of actual oxygenation levels in the brain.

A reliable optical signal with minimal noise interference was recorded in response to brain activation during the measurements performed on the 10 subjects. NIRS has been used in this study because meaningful results can be obtained by taking comparative readings from the baseline and activation conditions caused by stimuli. Results of the data gathered during the course of this research are summarized below. First the verbal fluency task results are presented followed by the results of the physical exercise task.

7.2.2 Verbal fluency task results

The mental exercise experiment was performed with the optodes placed externally to cover the prefrontal cortex of a subject. This area of the brain is known to carry out complex functions involving learning and memory. The data was analyzed using block averages of oxyhemoglobin and deoxyhemoglobin concentration changes induced by the verbal fluency test. A simultaneous increase in HbO₂ and a decrease in Hb were observed and are considered to be indicative of a hemoglobin response to brain activation. A significant hemoglobin response to brain activation was obtained in 8 out of 10 subjects.

The spatial maps of the block averaged oxy-, deoxy- and total hemoglobin responses measured on the ten subjects are shown in Figure 7.5, 7.6 and 7.7

respectively. The spatial maps plot each channel's average oxyhemoglobin level over the entire period of activation as compared to the baseline readings. This helps identify areas of the prefrontal cortex that show the largest changes in oxy-hemoglobin over time. Baseline indicates readings taken when the subject is in resting state (awake, eyes open but no stimulation). Activation indicates readings taken when the subject is performing the verbal fluency test. During verbal fluency task there is an increase in HbO₂ and decrease in Hb in the prefrontal cortex. Figure 7.8 shows the temporal traces of oxyhemoglobin and deoxyhemoglobin of averaged traces of region-of-interest channels indicating the maximal change in oxyhemoglobin.

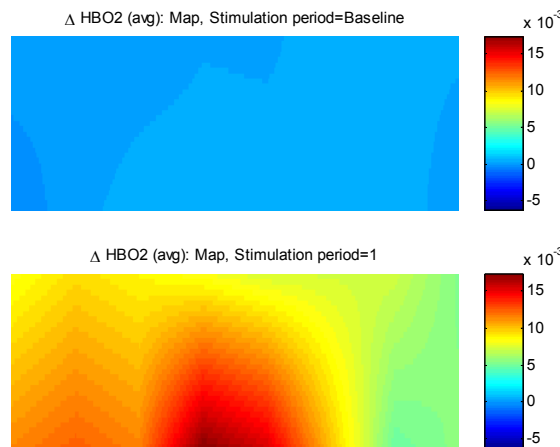


Figure 7.5: Block-averaged hemoglobin maps for temporally averaged data for the 10 subjects. Top panels show baseline spatial distribution for oxy hemoglobin changes Bottom panels show the spatial distribution during the verbal fluency task (stimulation period).

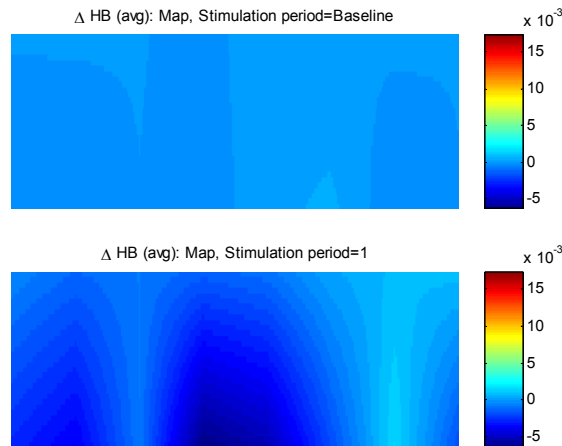


Figure 7.6: Block-averaged hemoglobin maps for temporally averaged data for the 10 subjects. Top panels show baseline spatial distribution for deoxyhemoglobin changes Bottom panels show the spatial distribution during the verbal fluency task (stimulation period).

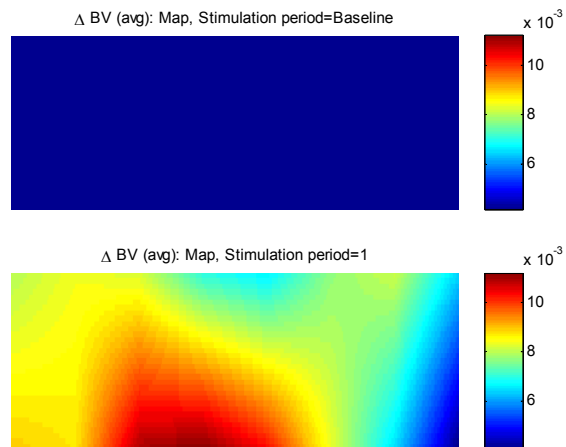


Figure 7.7: Block-averaged hemoglobin maps for temporally averaged data for the 10 subjects. Top panels show baseline spatial distribution for total hemoglobin changes Bottom panels show the spatial distribution during the verbal fluency task (stimulation period).

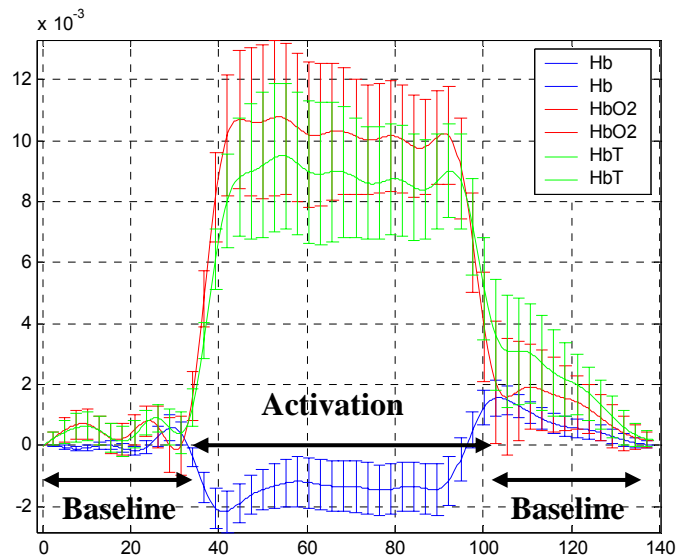


Figure 7.8: Temporal traces of hemoglobin for averaged data over the region of interest (mid prefrontal cortex) for the 10 subjects. Oxy hemoglobin changes are represented by the red line and deoxy-hemoglobin changes are represented by the blue line and total hemoglobin changes are indicated by the green plots. The periods of baseline (rest) and stimulation are as indicated in the figure.

Figure 7.9 shows the time courses for $[Hb]$, $[HbO_2]$ and $[HbT]$ for the verbal fluency task averaged across ten subjects. The response is characterized by an increase in $[HbO_2]$ and a decrease in relative concentration of $[Hb]$. All the hemodynamic changes measured with NIRS exhibit similar behavior and slowly return to baseline after cessation of stimulus. The data is modeled using the single compartment Windkessel model. Only the activation period of the data is used for each optimization routine to avoid issues with the post stimulus over and under shoots in the hemodynamic responses measured in the experimental data.

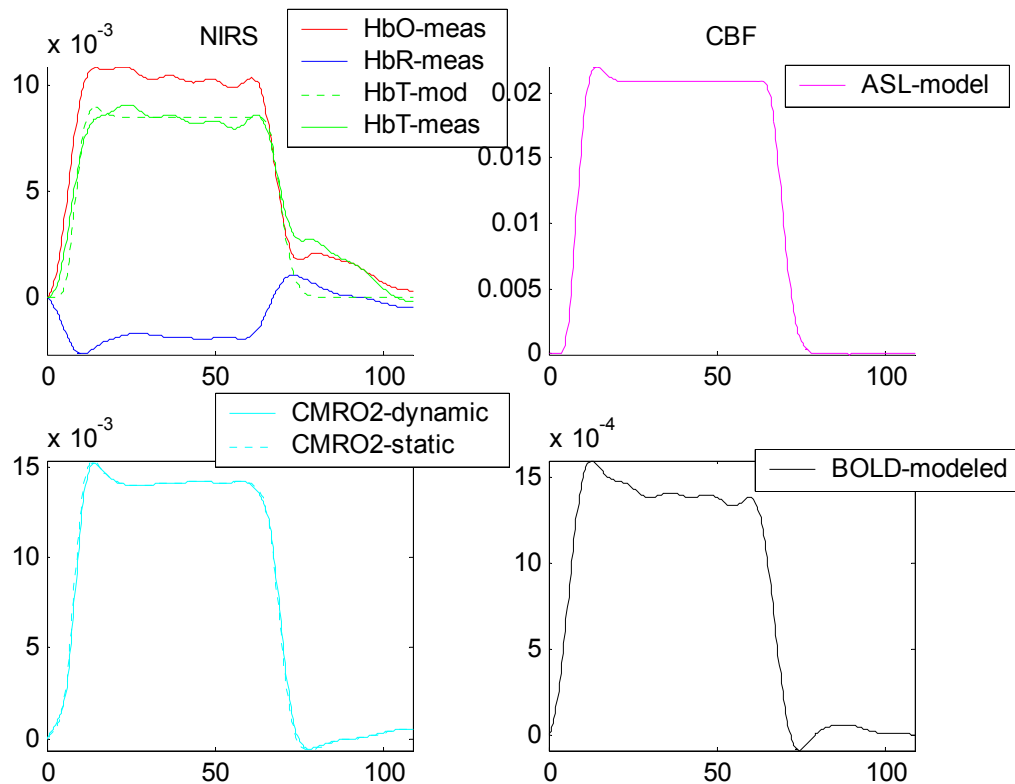


Figure 7.9: Model fit to experimental NIRS data and predicted temporal evolution of cerebral blood flow, CMRO₂ and BOLD signals

7.2.2.1 Spatial tomographic images of blood flow and CMRO₂

Similar to the spatial maps of the measured hemodynamics, maps of predicted measures of cerebral blood flow, CMRO₂ and BOLD signals were constructed (Figure 7.10). The following procedure was used to construct tomographic maps of cerebral activation. The NIRS readings for each channel were used to calculate changes in total blood volume over time. This data was used in conjunction with the model predicted temporal dynamics to determine temporal changes in blood flow, CMRO₂, and BOLD. These time traces were determined by fitting data for each channel across the prefrontal

cortex. The averages of the time traces during periods of activation were calculated for each channel. Inverse reconstruction techniques similar to [Hb] and [HbO₂] were used to construct maps of blood flow, CMRO₂, and BOLD to reveal cerebral activation.

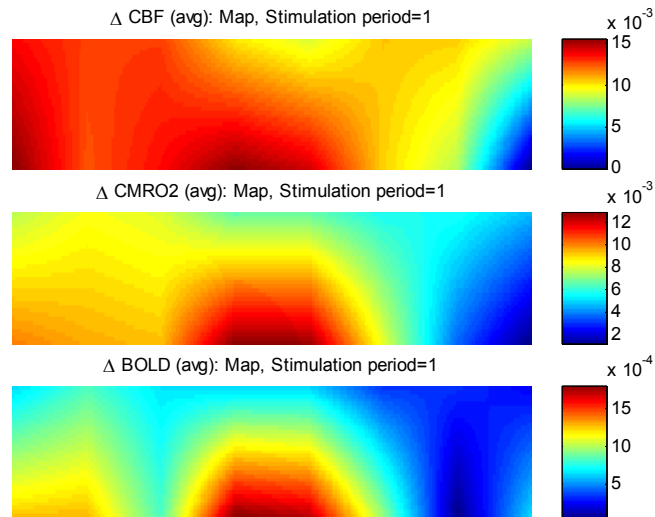


Figure 7.10: Spatial tomographic images of the average Δ CBF, Δ CMRO₂ and Δ BOLD during activation (verbal fluency task)

7.2.3 Physical exercise results

The optodes were placed in the same location as in the mental exercise. This helps to compare the [HbO₂] and [Hb] trends observed over the course of both experiments. Spatial and temporal plots of oxy-, deoxy- and total hemoglobin levels are shown in Figures 7.11, 7.12 and 7.13 respectively. During the physical exercise task there is an increase in HbO₂ and only a slight decrease in Hb in the prefrontal cortex. Figure 7.14 shows the temporal traces of oxyhemoglobin and deoxyhemoglobin in the individual channels indicating the maximal change in oxyhemoglobin.

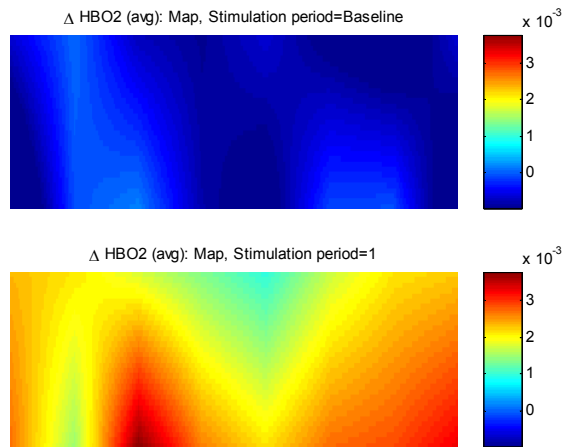


Figure 7.11: Block-averaged hemoglobin maps for temporally averaged data for 10 subjects. Top panels show baseline spatial distribution for oxyhemoglobin changes
Bottom panels show the spatial distribution during the exercise task.

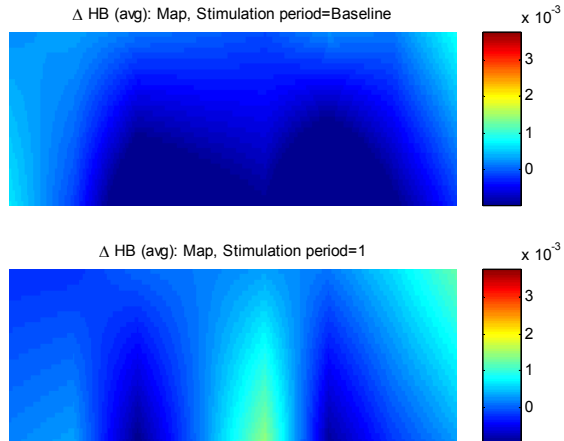


Figure 7.12: Block-averaged hemoglobin maps for temporally averaged data for the 10 subjects. Top panels show baseline spatial distribution for deoxy- hemoglobin changes
Bottom panels show the spatial distribution during the exercise task.

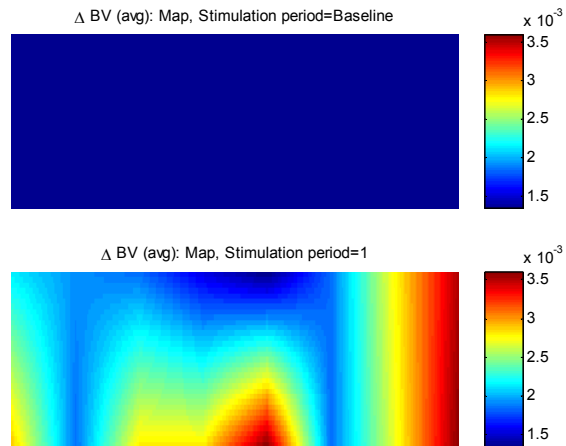


Figure 7.13: Block-averaged hemoglobin maps for temporally averaged data for the 10 subjects. Top panels show baseline spatial distribution for total hemoglobin changes. Bottom panels show the spatial distribution during the exercise task.

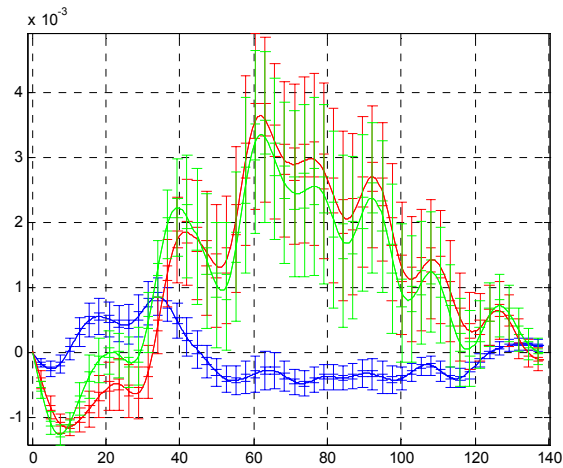


Figure 7.14: Temporal traces of hemoglobin for averaged data over the region of interest (mid prefrontal cortex) for the 10 subjects. Oxy hemoglobin changes are represented by the red line and deoxy-hemoglobin changes are represented by the blue line and total hemoglobin changes are indicated by the green plots. The periods of baseline (rest) and stimulation are as indicated in the figure.

7.2.4 Discussion

The first test carried out during this study was a verbal fluency test. Previous research using functional MRI suggests that the prefrontal cortex is activated during verbal fluency tasks [134]. These tasks require the retrieval of semantically associated words from long-term memory storage. The test performed by the subjects in the present study invokes such activity in the brain [135]. However it is clear that the involvement of these neural networks causes changes in the activity observed in the frontal lobe. In the early stages of Alzheimer's disease, patients who exhibit little or no frontal pathology related to the disease, still experience difficulty while performing verbal fluency tasks. This research explores changes in the oxygenation levels in the prefrontal cortex of the brain created by verbal fluency tasks in healthy subjects. This region was chosen for this study because the prefrontal cortex is involved in maintenance of material in correct order, control of cognitive activities, memory and language, and manipulation of knowledge. It was observed that the cognitive task administered in this study caused a rise in the oxygenated hemoglobin [HbO_2] coupled with a fall in deoxygenated hemoglobin [Hb] in the region. Most subjects returned to baseline values after the experiment was finished.

As expected there was a rise in the oxygenated hemoglobin in the prefrontal cortex of the brain during the verbal fluency task in healthy subjects. One would expect these results to vary in patients with AD [136]. Optical properties of the degenerating brain as in AD patients would vary from that of healthy adults [137]. This change in absorption and scattering coefficients can be attributed to several factors. These factors

include altered blood flow, reduced brain volume, neuronal atrophy and changes in white to gray matter ratio. If this is assumed to be true, then NIRS measurement of the affected brain during the performance may reveal critical information regarding brain atrophy in AD patients far before it can be seen as structural changes [138, 139].

Table 7.4: Summary of results for the oxyhemoglobin and deoxyhemoglobin changes induced during the verbal fluency task. The first column ‘S’ indicates the subject number. Consecutive columns indicate channel 1 through 16. The ‘+’ sign indicates an increase in levels, ‘-’ sign a decrease in levels and ‘*’ sign indicates a substantial increase in levels, ‘C’ indicates no change in levels, ‘N’ indicates noise interference. All levels measured are relative to baseline period.

S	Oxygenated Hemoglobin [HbO ₂]																Deoxygenated Hemoglobin [Hb]															
	1	2	3	4	5	6	7	8	9	10	11	12	13	14	15	16	1	2	3	4	5	6	7	8	9	10	11	12	13	14	15	16
1	*	*	*	*	+	+	*	*	+	*	+	+	+	+	+	+	-	-	-	-	-	-	-	-	-	-	-	-	-	-	-	
2	+	+	+	+	+	*	+	*	+	*	*	+	+	+	+	+	-	-	-	-	-	-	-	-	-	-	-	-	-	-	-	
3	+	+	+	+	*	*	*	*	+	+	+	+	+	+	+	+	C	C	C	C	-	-	-	-	-	C	C	C	C	-	-	-
4	+	+	+	+	C	*	C	+	C	*	C	*	+	C	C	C	-	-	-	-	C	C	C	C	C	C	C	C	-	-	-	
5	+	+	+	*	C	*	+	*	+	*	+	+	+	+	+	+	-	-	-	-	C	C	C	C	+	+	+	+	+	+	+	
6	*	+	*	+	+	+	C	+	-	+	+	+	*	+	*	+	C	C	C	C	C	C	C	C	+	+	+	+	+	+	+	
7	+	*	+	*	+	*	C	*	C	*	+	*	+	C	+	C	C	C	C	C	C	C	C	C	C	C	C	C	C	C	C	
8	+	C	+	+	+	*	+	*	*	*	+	+	+	+	+	+	-	-	-	-	-	-	-	-	C	C	C	C	C	C	C	
9	N	+	+	+	*	+	*	+	+	*	+	*	+	+	+	+	N	C	C	C	+	+	+	+	-	-	-	-	-	-	-	-
10	+	*	*	+	+	+	+	+	+	*	+	+	+	+	+	+	C	C	C	C	-	-	-	-	C	C	C	C	-	-	-	-

The second test performed as part of this study was a physical exercise task. The importance of regular physical exercise to maintain a healthy physiological as well as psychological life is widely accepted. Studies have indicated that AD patients affected by dementia demonstrate a significant improvement in scores on psychological tests such as verbal span tests and attention span matrix tests after undergoing exercise-training programs for a few months or more. Previous studies also suggest that AD

patients have a lower blood flow to the brain that can be improved by physical exercise[140]. Physical exercise is related to serotonin levels in the brain that have been linked to several brain functions like appetite control, thermoregulation, and attention span and also play an important role in pathophysiology of mood, depression and Alzheimer's disease [18, 141].

It was observed in this study that exercise was related to a rise in HbO₂ and a concurrent small decrease in Hb in the prefrontal cortex (refer Table 7.5 and 7.6). It is expected that in AD patients these levels will show a relatively slower recovery to baseline conditions after cessation of stimulus, when compared to healthy controls. It is also expected that the time to recover to baseline values would gradually decrease if the AD subjects were given a fitness-training program and the NIRS variables recorded before and after the program would show observable differences for the same. This fall in recovery time may also be accompanied by a rise in the oxygenated hemoglobin to the brain after the exercise program. These levels may improve dramatically over months of physical training routines [141]. It is suggested that physical exercise is not a very strong indicator of the onset of AD and may not help in the early detection of the disease. However when used in conjunction with the mental examination described in the previous section, it can be used to determine the effectiveness of an administered treatment for AD.

Table 7.5: Summary of results for the oxyhemoglobin and deoxyhemoglobin changes induced during the physical exercise. The first column ‘S’ indicates the subject number. Consecutive columns indicate channel 1 through 16. The ‘+’ sign indicates an increase in levels, ‘-’ sign a decrease in levels and ‘*’ sign indicates a substantial increase in levels; ‘C’ indicates no change.

S	Oxygenated Hemoglobin [HbO ₂]																Deoxygenated Hemoglobin [Hb]															
	1	2	3	4	5	6	7	8	9	10	11	12	13	14	15	16	1	2	3	4	5	6	7	8	9	10	11	12	13	14	15	16
1	+	*	C	*	+	-	+	-	C	C	+	+	+	*	+	+	C	C	C	C	C	C	C	C	C	C	C	C	C	C		
2	+	+	+	*	+	+	+	+	+	+	+	*	+	*	+	+	C	C	C	C	C	C	C	C	C	C	C	C	C	C		
3	+	*	+	+	+	*	+	*	+	*	+	+	+	+	+	+	C	C	C	C	C	C	C	C	C	C	C	C	C	C		
4	-	-	-	-	C	C	C	C	-	C	-	C	-	C	-	-	C	C	C	C	C	C	C	C	C	C	C	C	C	C		
5	-	-	-	-	C	C	C	C	C	C	C	C	C	C	C	-	C	C	C	C	C	C	C	C	C	C	C	C	C	C		
6	*	+	+	C	+	*	*	*	C	C	C	C	C	+	*	*	*	*	*	*	*	*	*	*	*	*	*	*	*	*	*	
7	C	C	C	*	C	*	C	*	C	*	C	C	C	C	C	C	C	C	C	C	C	C	C	C	C	C	C	C	C	C		
8	+	+	+	+	+	+	+	+	+	+	+	+	+	*	*	*	*	*	*	*	*	*	*	*	*	*	*	*	*	*	*	
9	C	C	C	+	C	*	-	C	-	+	+	+	+	C	C	C	C	C	C	C	C	C	C	C	C	C	C	C	C	C		
10	+	+	+	+	+	C	*	*	*	+	+	+	+	+	+	+	C	C	C	C	C	C	C	C	C	C	C	C	C	C		

Table 7.6: Comparison of results obtained for both the mental and physical tasks and indicates the changes in oxyhemoglobin and deoxyhemoglobin levels induced for the 10 subjects. The levels of HbO₂ and Hb were calculated by block averaging over the period of activation and over all 16 channels under examination.

S	Verbal Fluency Task		Physical Exercise Task	
	HbO ₂	Hb	HbO ₂	Hb
1	+	-	+	-
2	+	-	+	-
3	+	-	+	-
4	+	-	-	+
5	+	-	-	-
6	+	-	+	-
7	+	-	+	-
8	+	-	+	-
9	+	-	+	-
10	+	-	+	-

Since the entire study has been carried out using near-infrared spectroscopy, it is pertinent to present the advantages and shortcomings of the technique. NIRS has the advantage of high temporal resolution of 300 milliseconds or less [33]. The method is completely non-invasive with minimal restriction on the examinee. NIRS systems are usually inexpensive, portable and can be coupled with other imaging tools such as EEG, fMRI and PET to enhance the results [142].

7.2.5 Conclusions

In conclusion, this study demonstrated that the prefrontal cortex is activated by verbal fluency task causing a marked increase in the regional cerebral oxygenated hemoglobin level coupled with a fall in deoxygenated hemoglobin levels. In addition, the physical exercise caused a rise in oxygenated hemoglobin level with a smaller decrease in deoxygenated hemoglobin level. Whether these findings can be used to detect prefrontal cortex damage in Alzheimer's patients can be the subject of further investigation. This study adds to previously published studies by comparing both physical and mental exercise effects on the prefrontal cortex. Furthermore, the instrument used in this study is a 16-channel NIRS system that covers the entire breadth of the prefrontal cortex over both the left and right hemispheres which has not been explored extensively to date. NIRS systems can be integrated with PET and fMRI systems to give both structural and functional brain damage assessment in AD patients.

7.3 Invasive rat data (Previously published)

This section presents previously published multimodality data that was not collected during the course of this research [80, 143] but was used to test the models developed during this research. The protocol is presented here for completeness and the results have been published previously by Dunn et al [80].

7.3.1 Materials and methods

Male Sprague-Dawley rats (250-350g, n=7) were anesthetized with 2% halothane and prepared as previously described [143]. A whisker deflection stimulus was used for stimulus [144]. The stimulus consisted of a single whisker deflection of varying amplitude (from 1 to 9) and 20ms duration. Stimuli were presented using a rapid, randomized event-related paradigm.

Multi-wavelength spectroscopic imaging of total hemoglobin concentration and oxygenation were performed using the instrument and methods described in previously published literature [143]. Briefly, the cortex was illuminated by a filtered mercury xenon arc lamp (10-nm bandpass filters centered at wavelengths of 560, 570, 580, 590, 600, and 610nm). Images were acquired onto a cooled 12-bit CCD camera at an effective frame rate of 18Hz. The modified Beer-Lambert law was used to convert these spectral images into images of oxy- and deoxy-hemoglobin concentration changes. Differential path-length factors that accounted for the different optical path-lengths of each wavelength were used as described in Kohl *et al* [145].

Blood flow was imaged using laser speckle contrast [80, 143]. Images of CBF changes were determined by calculating the changes in the speckle contrast in a series of laser speckle images [146]. Speckle contrast images were averaged across trials and the averaged set was converted to relative blood flow ($1 + \Delta\text{CBF}/\text{CBF}_0$) by converting each speckle contrast value to an intensity autocorrelation decay time [146] and dividing by baseline [80]. Both laser speckle and spectroscopic results were deconvolved using the stimulus presentation timing to determine the blood flow and hemoglobin responses. The group average of the seven rats was calculated after normalizing to the amplitude of the 9th condition.

7.3.2 Model setup

A module measurement model function was used to describe the biophysics by which the auxiliary states (HbO_2 , Hb , HbT , and CBF) are measured by one or more imaging modalities. Separating the measurement model from the rest of the system, allows this work to be easily extended to multimodality imaging measurements [90]. The measurement models are assumed to have uniform sensitivity to each compartment and these measurements represent the sum or the average of the contributions from all the vascular compartments [68] ($n \in \{\text{Arteriole}, \text{Capillary}, \text{Venial}\}$),

$$Y_{\text{spectral}, \text{HbX}}(t) = \sum_n \Delta\text{HbX}_n(t) \quad (167)$$

$$Y_{\text{speckle}}(t) = \sum_n \Delta\text{CBF}_n(t) / \sum_n \Delta\text{CBF}_0(t) \quad (168)$$

The framework of this model allows the incorporation of true measurement sensitivity profiles, such as those obtained from the consideration of the optical photon transport process or fMRI measurement models. This could be extended to the fusion of multimodality data into image reconstructions of hemodynamic and metabolic changes.

7.3.2.1 Model parameters and initial conditions

A non-linear Levenberg-Marquardt algorithm implemented in Matlab was used to estimate the states describing the $CMRO_2$ and arteriole dilation functions [69]. A differential time step of 2 ms was used for the update of the vascular and oxygen transport models. Smaller time steps were also tested to verify that the time-step did not affect the results. To integrate the multimodality measurements, a weighted least-squares cost function was employed, with the weights given by the inverse of the measurement variances for each modality. These weights are estimated from the variance in the estimate of the hemodynamic responses across the seven rats. The physiological range of values for each of the parameters was used to impose a constraint on the upper and lower range of fitting values. The fitting routine was iterated until a defined convergence criterion was met (10^{-6} times the variance of the measurement error). Each of the nine stimulus conditions was fit independently and the process took approximately 120 minutes per condition (Pentium(R) 4; 3.0 GHz). It was verified that the final estimate was independent of the choice of the initial guess for each state and the same initial guess was used for each of the nine conditions [68].

In order to estimate the confidence-bounds for each of the states, a Markov Chain Monte Carlo sampling of the state-space was performed [147]. The change in χ^2 value at each sample step was used to approximate “energy cost” for determining the probability of the acceptance of each step using the equation,

$$P(k | \{j < k\}) = \begin{cases} 1 & \text{if } \Delta\chi^2 \leq 1 \\ e^{-\Delta\chi^2} & \text{else} \end{cases}, \quad (169)$$

where k defines the index current iteration and $\{j < k\}$ is the set of all previous steps. The density of samplings approximates the n^{th} -dimensional probability density function where n is the number of degrees-of-freedom in the state-vector. This defines the confidence bounds on each of the state estimates.

7.3.2.2 Single-compartment Windkessel model

In addition to fitting experimental data with the multi-compartment vascular model, the results are compared to the single-compartment version of the Windkessel model [5, 57] using a similar fitting procedure. Temporal basis functions were used to describe the arteriole dilation and CMRO_2 time-courses while performing a non-linear minimization to estimate the unknown states. This inductive modeling approach is similar to fitting of arteriole dilation described in Boas et al [57], but represents a significant deviation from the deductive approaches used in most other similar model descriptions. This allows the inference of arteriole dilation and CMRO_2 from the joint set of measurements within the same pseudo-Bayesian framework used in the multi-compartment model and the ability to make direct comparisons of the results obtained

in both cases. The single-compartment model had eleven degrees-of-freedom. The capillary and venial oxygen saturations were reduced to a single compartment. The bounded ranges for all parameters were the same as the multi-compartment model, which is in agreement with previous literature [57]. Baseline vascular fractions were assumed to be 20% and 80% for the arteriole and Windkessel compartments [57].

7.3.3 Results

Using the multi-compartment model to fit the region-of-interest averaged response of the seven rats, we are able to estimate the unknown state parameters. Initially the response curves from each of the nine conditions were fit independently. The state estimates for each of these nine stimulus amplitudes are provided in Table 7.7 and the model fits to the experimental data are shown in Figure 7.15 for (representative) conditions 3, 6, and 9. The resulting multi-compartment fits modeled nearly all the variance of the response for all hemodynamic parameters and yielded highly significant R^2 fits to each of the nine conditions, as summarized in Table 7.8. The partial R^2 values (adjusted for the model degrees-of-freedom) were calculated from the variance of the individual hemodynamic measurements (HbO₂, Hb, HbT, and/or CBF) using the model results to examine the goodness-of-fit for each of the multimodal observations. This calculation demonstrated nearly equally distributed variances across each of these measurements and showed that the model equally incorporated each of the measured components.

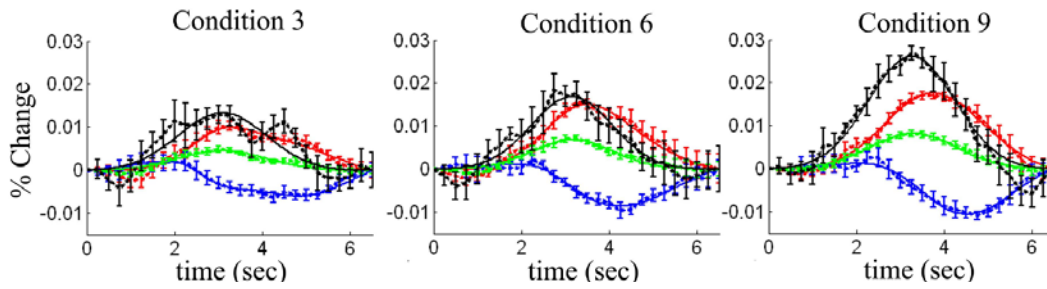


Figure 7.15: Multi-compartment model fit to the experimental data: The experimental data (dots) was fit using the multi-compartment model (lines). Here we show representative results from the model fits to stimulus conditions 3, 6, and 9. The error bars show standard error estimated from the seven rats used in this experiment. Each condition was fit independently to generate these plots. The R^2 values for these fits are shown in Table 7.8. Blood flow (black) was measured by laser speckle imaging. Blood flow, volume, oxy- and deoxy-hemoglobin changes are shown in black, green, red, and blue respectively and were measured by optical spectroscopy [68].

The state parameters estimated by this model consist of both structural and functional properties of the system. The parameters characterizing the functional response ($CMRO_2$ and arteriole dilation) are expected to differ between the stimulus conditions, whereas, the structural estimates are expected to be conserved. To test this hypothesis, the results of conditions 1-3, 4-6, and 7-9 were grouped and a one-way ANOVA test was performed between groups. As expected, the estimates of the functional states varied significantly ($p < 0.05$) across the three groups, as indicated with an asterisk in Table 7.7. The magnitude and time-to-peak of the estimated arteriole dilation and $CMRO_2$ responses increased with stimulus condition. In contrast to the functional parameters, the estimate for the structural parameters did not vary significantly across the three groups. For these parameters, the mean of the nine conditions is shown in table 7.7. The Windkessel vascular reserve (β) was estimated in the range of 1.1–2.9 (mean 1.8) for the nine conditions. Similarly, the estimate of the

vascular transit time (τ) was also conserved across the three groups of conditions with a range of 0.61-1.31sec (mean 0.70sec). In addition, we estimated baseline total-hemoglobin to be 88-133 μ M (mean 113 μ M).

Table 7.7: State estimates: In this table, we present the model estimates from the nine stimulus conditions for the fourteen state variables. For the structural parameters, the mean of the nine conditions is shown. None of the changes in these parameters significantly varied with stimulus condition. In the last column, the values estimated jointly from all nine conditions are shown. The asterisks (*) indicate parameters, that varied significantly ($p < 0.05$) with stimulus condition. The amplitude and time-to-peak of arterial dilation both increased significantly with stimulus condition for the nine independent fits. $CMRO_2$ estimated in the independent fits trended to increase, but this was not significant due to variance of the estimates. In contrast, $CMRO_2$ significantly increased in the estimates obtained by joint-fits to all nine conditions [68].

		Variable	Stimulus Condition									Mean	Fit Together
			1	2	3	4	5	6	7	8	9		
Dynamic	Arteriole dilation temporal basis	ΔR_A	0.94	1.05	1.41	1.72	1.69	1.84	2.57	2.65	3.00	*	--
		τ_{peak}	3.00	3.11	2.96	3.12	3.11	3.03	3.32	3.26	3.22	*	--
		σ_A	2.38	1.97	1.35	1.15	1.48	1.32	1.55	1.56	1.36		--
	$CMRO_2$ temporal basis	$\Delta CMRO_2$	0.53	0.24	0.34	0.35	0.22	0.27	1.28	0.36	0.28		--
		τ_{peak}	1.49	1.86	1.68	1.49	1.71	1.91	1.32	1.37	1.27		--
		σ_c	1.77	1.15	1.11	1.72	1.61	1.54	2.12	1.84	1.08		--
Structural		$R_A(0)$	0.73	0.77	0.74	0.73	0.76	0.77	0.66	0.68	0.76	0.73	0.79
	Windkessel parameters	β	1.32	1.33	2.27	2.79	1.21	1.14	2.94	1.52	1.19	1.75	1.45
		τ	0.79	0.68	0.65	1.31	0.70	0.66	0.75	0.62	0.61	0.75	0.60
		τ_{pial}	1.27	0.77	0.75	1.09	0.59	0.71	1.40	0.80	0.63	0.89	0.96
		$[HbT]_o$	113.8	118.7	114.3	133.4	112.9	110.7	133.4	92.4	87.7	113.04	102.5
		S_aO_2	0.940	0.940	0.950	0.972	0.947	0.943	0.973	0.939	0.938	0.95	0.938
		S_cO_2	0.709	0.704	0.731	0.749	0.740	0.712	0.732	0.730	0.747	0.73	0.694
	S_vO_2	0.635	0.631	0.656	0.687	0.667	0.635	0.655	0.656	0.673	0.66	0.616	

7.3.3.1 Model uniqueness

To examine the uniqueness of the model fits, the results using Markov chain Monte Carlo simulations were examined to determine the variance in each of the

estimate [147]. A low correlation was observed between most of the individual state estimates, which indicates that these states were fairly independent. The state estimates of the Windkessel vascular reserve (β), transit time (τ), and baseline total hemoglobin ($[HbT_o]$) were also examined. Analysis along the axis of each degree-of-freedom yields the confidence bounds for each of the states (refer Figure 7.16).

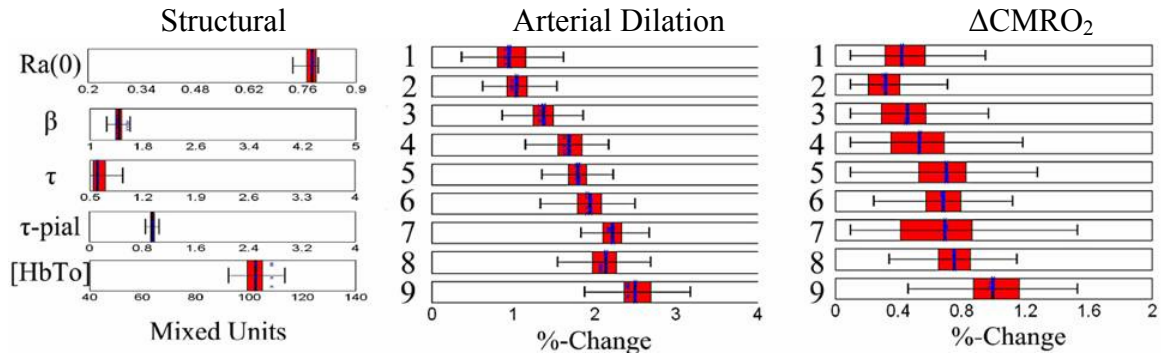


Figure 7.16: Markov Chain Monte Carlo results[68]

To further investigate the behavior of the model, the dependence of our final state estimates on the initial guess of the minimization routine was inspected. Although the Levenberg-Marquardt algorithm was chosen for its robustness to initial guess [69], it is important to verify this in the experimental fits. A Monte Carlo sampling of the initial guess value for several of the stimulus condition data sets was examined and the final fits were found to be independent of this starting point.

7.3.3.2 Comparison to the single compartment Windkessel model

To further examine the validity of the proposed multiple compartment model, the results were compared to the previously single-compartment Windkessel models [5, 57]. The single-compartment Windkessel model fits to the experimental data (shown in

figure 7.17) demonstrated shortcomings of this model for estimating the oxygenation component of the hemodynamic response. This result is in agreement with the similar findings by Zheng et al, of a multi-compartment model [7]. The degree-of-freedom adjusted R-squared and partial R-squared values for both the multi-compartment and single Windkessel-compartment model fits are shown in Table 7.8.

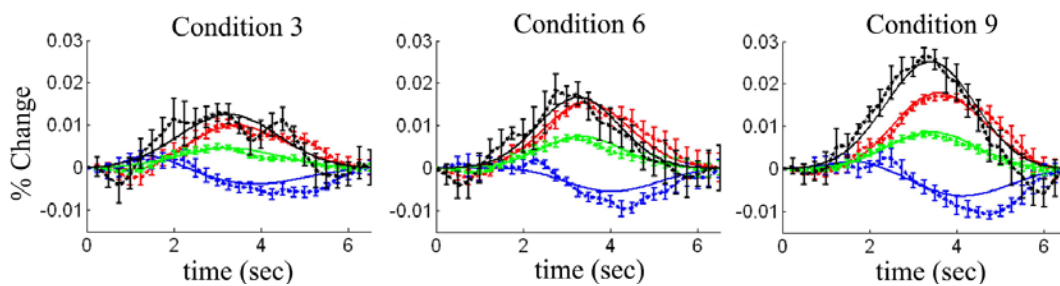


Figure 7.17: Single-compartment model fit to the experimental data: The experimental data (dots) was fit using the single-compartment model (lines). Here representative results from the model fits to stimulus conditions 3, 6, and 9 are shown. Each condition was fit independently to generate these plots. The R^2 values for these fits are shown in table 7.8. Blood flow, volume, oxy- and deoxy-hemoglobin changes are shown in black, green, red, and blue respectively. The error bars represented standard errors estimated from the seven rats used in this experiment [68].

Both models were able to reproduce the blood flow and volume changes as well as oxy-hemoglobin changes in the measured data. Using a Z-transform, a paired T-test of these fits [148] was performed. The single Windkessel-compartment model did not fit the deoxy-hemoglobin ($p < 8 \times 10^{-6}$) and oxy-hemoglobin ($p < 2 \times 10^{-4}$) time-courses as well as the multicompart model. The blood flow and volume estimates were also significantly better in the multi-compartment model by this test ($p < 6 \times 10^{-3}$ and $p < 2 \times 10^{-3}$).

3). The overall model fit to all observations was also significantly better for the multi-compartment model ($p < 8 \times 10^{-5}$).

Table 7.8: Single- and multi-compartment model fits to experimental data: In this table, the R-squared values (goodness-of-fit) for the model fits to the nine-stimulus conditions are shown. These R-squared values have been adjusted for the degrees-of-freedom in each model. For each condition, the partial R^2 value for the flow, volume and oxy-/deoxy-hemoglobin measurements were calculated. This value indicates the explained model variance considering only that component of the measurements. The total R-squared indicates the fraction of the total variance accounted for by all measurements. The multi-compartment model significantly improved the fits to the data ($p < 8 \times 10^{-5}$). The most notable improvements were observed in the modeling of deoxy-hemoglobin ($p < 8 \times 10^{-6}$) [68].

	Stimulus Condition								
	1	2	3	4	5	6	7	8	9
Multi-compartment									
R^2_{adj} -HbO ₂	0.94	0.98	0.97	0.90	0.99	0.98	0.98	0.99	0.99
HbR	0.81	0.98	0.98	0.95	0.96	0.98	0.97	0.99	0.98
HbT	0.94	0.96	0.93	0.87	0.99	0.97	0.98	0.99	0.99
CBF	0.92	0.73	0.86	0.92	0.99	0.96	0.98	0.92	0.97
Total	0.91	0.95	0.95	0.89	0.98	0.98	0.98	0.98	0.99
Single-compartment									
R^2_{adj} -HbO ₂	0.94	0.96	0.93	0.85	0.98	0.97	0.95	0.98	0.98
HbR	0.62	0.81	0.66	0.68	0.81	0.79	0.76	0.81	0.74
HbT	0.94	0.95	0.90	0.87	0.98	0.95	0.97	0.98	0.98
CBF	0.93	0.63	0.85	0.92	0.97	0.93	0.98	0.88	0.95
Total	0.89	0.88	0.87	0.87	0.95	0.93	0.94	0.95	0.95

Although simpler, single-compartment models have been previously demonstrated to model fMRI data [3, 5, 6], the higher temporal resolution and spectroscopic information of optical imaging requires a more detailed model. In agreement with previous work [7], we found that the multi-compartment model performed better than the single-compartment formulation, even after the additional

degrees-of-freedom for the more complicated model were accounted for ($p < 8 \times 10^{-5}$). Comparison of this previously published single compartment model and our multiple-compartment Windkessel model revealed that both models accurately reproduced the relationship between flow and volume, as indicated by the goodness-of-fit of blood flow and volume measurements by both models (Table 7.8). The differences in these two models were significant in the fitting of oxy- and deoxyhemoglobin, but not significant if only blood flow and volume were fit. This finding is consistent with the previous report, which found that both a single and three-compartment model could nearly equally model flow and volume changes [7]. The estimates of arteriole dilation were significantly higher in the single-compartment model ($p < 2 \times 10^{-6}$). Both models predicted a linear relationship with stimulus condition ($R^2 = 0.98$ [single] and $R^2 = 0.96$ [multi]).

In contrast, the multi-compartment model performed significantly better at modeling oxy- and deoxy-hemoglobin measurements, as well as the overall data set. The single-compartment model had significantly lower R^2 values for all nine conditions of model fits to oxy- and deoxy-hemoglobin data than the multi-compartment model. The discrepancy between measured and predicted oxygenation changes affected the estimates of $CMRO_2$ changes with the single-compartment model. The $CMRO_2$ changes predicted by the multi-compartment model were significantly better correlated with stimulus condition than those of the single-compartment model ($R^2 = 0.08$ [single] and $R^2 = 0.87$ [multi]). Due to the large variance in the estimate of $CMRO_2$ changes in

the single-compartment model, the difference in the two estimates was not statistically different (paired T-test).

7.3.3.3 Flow-volume and flow-consumption ratios

From the functional responses, we found that the ratio of maximum flow to maximum volume changes was 2.84 [range 2.83-2.85]. This estimate was extremely well conserved between the nine conditions. This trend tested significant in the grouped ANOVA test ($p < 0.006$). The ratio of maximum flow to maximum $CMRO_2$ change was 2.5 +/- 0.3. This also did not vary significantly with stimulus condition (one-way ANOVA). The estimates of these values were more conserved in the joint fitting results.

7.3.3.4 Compartmentalized changes in hemodynamics

Figure 7.18 shows the predicted hemodynamic changes in each of the vascular compartments for stimulus condition 9. The time courses of blood flow and oxy-, deoxy-, and total-hemoglobin changes are shown for the three vascular compartments and the modeled observation (i.e. the sum or mean of the three compartment changes). The neighboring plots show the time-course of the initial response from 0-3 seconds post stimulus. Similar dynamic behavior was observed with the model fits to the other eight experimental conditions. No differences were noted between the independent and the joint estimates for the nine conditions.

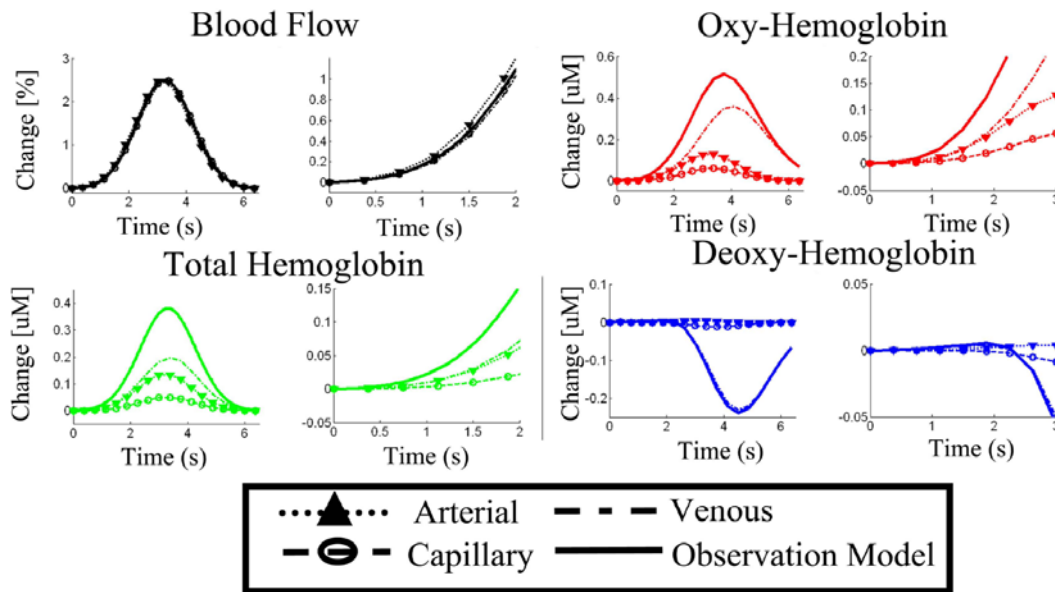


Figure 7.18: Compartmental hemodynamic changes: Vascular changes were modeled in the arteriole, capillary, and venous compartments. The time-courses plotted here from the ninth stimulus condition, show the representative changes in these three compartments. The solid lines show the predicted observation model for either laser speckle imaging (blood flow) or spectroscopic imaging. The figures to the right of each plot show an enlargement of the initial onset times [0-3 seconds] [68].

The predicted response curves for each of the vascular compartments, shown in Figure 7.18 are in qualitative agreement with previously published experimental findings [82]. The largest magnitude of blood volume changes originated from the venous compartment. However, the arteriole compartment had the largest fractional volume changes. Blood volume changes in the arterioles initiated and peaked slightly before the volume changes in the capillaries or venials. In the blood flow response, the magnitude of the change in all three compartments was nearly identical. The blood flow response was slightly lagged from the arteriole to venous compartments. This result is consistent with previously published results [7].

In addition, the majority of the contrast of oxy- and deoxy-hemoglobin changes arose from the venous structures. These large changes are the result of the large wash-out effects in this compartment, which has the lowest initial SO_2 , around 62-66%. This low saturation allows large changes in the blood oxygenation of the venous compartment in response to the same magnitude of increased blood flow and similar volume changes as the other compartments. In comparison, the oxygen saturation of the arteriole compartment (95%) is very close to that of the feeding (artery) blood (98.7%). Thus in the arteriole compartment, changes in oxy- and deoxy-hemoglobin arise from blood volume changes with little direct influence of increased flow. In all nine conditions, larger and more latent oxy-hemoglobin changes were observed than total-hemoglobin. This result can only be explained by the direct contribution of blood flow changes, which wash-out the baseline deoxy-hemoglobin concentration.

7.3.4 Discussion

The multicompartment model was able to reproduce the majority of the measured hemodynamic responses, as noted by the large R^2 values for the model fits to each condition shown in Table 7.8. In the model fits to the parametric whisker stimulus, the estimates of the change in $CMRO_2$ and arteriole dilation increased linearly with stimulus amplitude ($R^2=0.87$ and 0.96 respectively). Because of the framework of the model, these changes could be estimated independently for the nine conditions or by jointly estimating these changes using the complete parametric data and assuming common values for baseline properties for the nine conditions. Consistent estimates

were found with both approaches, while the variance in the estimates decreased for the joint estimation as expected.

Using Monte Carlo methods, the state estimates were seen to be independent of the initial guess given to the minimization routine. The model consistently estimated the state variables representing structural and baseline properties. The finding that the model estimated values independent of the stimulus condition is further supporting evidence of the utility of the model to infer details of the vascular anatomy.

7.3.5 Conclusions

The multicompartment model makes three significant contributions: (i) the multicompartment model shows significant improvements in the modeling of measured oxy- and deoxy-hemoglobin changes; (ii) the model allows the estimation of baseline hemodynamic and metabolic parameters from the time-courses of dynamic hemodynamic measurements; and (iii) the bottom-up framework of this model allows for inclusion of multimodality data in a Bayesian model, which improves the accuracy of the estimated states and compensates for uneven measurement noise across modalities. This framework can be readily extended to the analysis of human functional neuroimaging measurements [68].

7.4 Protocol: Neuroeconomic experiment

Classical economic theory supports the model of constrained utility maximization based on deliberation, where a decision is based on careful balancing of

the rewards and losses [149]. Although this phenomenon plays an important role in decision making, contributions of “automatic” processes (over which an individual has little or no deliberate control) and emotion are ignored in this theory [10, 150]. The above described processes are essential for daily functioning and gain additional importance when deliberative systems are impaired by chemical or physiological imbalances such as brain damage, disease, stress, or impulse [89, 151, 152]. Neuroeconomics focuses on incorporating the effects of neuropsychology and social cognition on classical economic theory to better model individual behavior [9, 16, 34]. Social cognition is the ability of a person to explain and predict behavior of one’s self and others around him/her using tools like interpretation of body language. This contributes to the fostering of feelings like cooperation, deception and empathy [150, 153, 154]. This capacity is also known as “theory of mind” or ”mentalizing” and is an automatic, high level brain function [155]. Classical economic theory assumes that individuals make inferences from the actions of others to their underlying preferences and beliefs and that such inferences are not any more or less difficult than any other types of inferences [149, 156]. However, “mentalizing” is a special ability differing over a heterogenous population and only a small portion can be attributed to general logical reasoning [154, 156]. Neuroeconomics aims to bridge the gap between classical economics and psychology to explain individual behavior and decisions.

Although neuropsychology data can identify the involvement of brain regions in a given task, it is limited by its inability to distinguish functions performed by specific structures of the brain [9, 10]. This shortcoming has been overcome in recent years by

the use of functional brain imaging as a powerful tool to study the relation of human cognition and its neurological basis [11, 12]. Functional brain imaging involves a comparison of people performing different tasks [13, 14]. The difference between images taken while a subject is performing an experimental task and images taken during a control state reveals regions of the brain that are differentially activated by the experimental task. In one of the first imaging studies conducted by economists, McCabe et al. [157] theorized that certain areas of the brain were important in games involving trust and cooperation. They found that players who were more trusting and cooperative showed more brain activity in Brodmann area 10 and the limbic system. These results were obtained by using functional MRI studies in two person cooperative games [13, 157, 158]. This research aims to extend this work to further enhance the understanding of neural circuits involved in cognitive neuroeconomic tasks.

The combination of noninvasive NIR hemodynamic imaging and modeling is innovative in that it provides heterogeneous maps of hemodynamic parameters (Hb, HbO₂, HbT) related to HbT and CMRO₂ of the human brain. Furthermore, the presented experiments are also novel in that NIRS imaging has not been explored for cognitive decision making tasks using neuroeconomic protocols. This functional imaging technique and the related model enhance the understanding of the dynamics, mechanisms, and heterogeneity of brain responses of individuals with diverse history and traditional backgrounds when faced with varied decision-making tasks.

7.4.1 Materials and methods

The protocol involved neuroeconomic trust games with two-person interaction. The games were designed to help the cooperation between individuals over mutual gains and make cooperative choices that realize these gains. Previous research suggests that mental state attribution involves the use of prefrontal cortex in integrating theory-of-mind processing with cooperative actions [157]. Subjects played a standard two-person “trust and reciprocity” game with human counterparts for cash rewards. The imaging modality used was fNIRS, and the region of interest was the prefrontal cortex of the brain, especially Brodmann area 10.

Healthy subjects with no history of psychiatric or neurological disorders were recruited for each study from the George Mason university undergraduate population. Ten subjects were recruited (ages 20-32; mean age 24; three female; seven males). All participants were native speakers of English. Participants provided informed consent in accordance with the guidelines set forth by the Office of Research Compliance at the University of Texas at Arlington and the Institutional review board guidelines at George Mason University. This research was carried in conjunction with the Neuroeconomics research group headed by Dr. K. McCabe at George Mason University and Dr. H. Liu.

7.4.1.1 Protocol description

Experiments were conducted using various neuroeconomic behavioral protocols. In order to simulate a real-life financial decision scenario, subjects responded to cash-payoffs presented by different decisions made between visually presented choices.

Keyboard buttons were programmed to be response buttons to help a subject present his/her decision (for example moving left or right on a decision tree). Some protocols involved games played between two subjects or a human and computer, where each participant played the role of the first or second decision maker in each game [157]. The subjects are informed of their counterpart type in the experiments before each game. Such experiments help show differences in the levels of brain activation and the regions they activate when behaviors like cooperation and competitiveness play a role in the decision being made. Experiments were conducted to study the results of such financial games as trust games, punish games and mutual advantage games. Analyses of the spatial distribution of hemodynamic parameters over the duration of different games were analyzed to compare the responses elicited by each game. Further analysis of data using blood flow and oxygenation levels were also carried out as described.

Subjects respond to cash-payoff salient features of a visually presented two-person binary game tree by pressing response buttons with their right (move right) or left hand (move left). The subjects played the role of either first decision maker or second decision maker in each game. Second decision maker sees the first decision makers' choice before making their decision. Subjects were matched with either a human or computer counterpart and were informed of their counterpart's type before seeing the game tree. When the subjects played the computer they were told the fixed probabilistic strategy it used. The task was administered in several runs. In each run the games are randomly presented with different payoffs with counterbalanced roles and counterparts.

7.4.1.2 Protocol presentation

The experimental protocol was called the “Incentives and Decision Making-Two-Person Economic Decision-Making Experiment”. The decision tasks consisted of branching pathways with payoffs as seen in Figure 7.19. DM stands for Decision-Maker. The number 1 or 2 indicates first or second player, respectively. Therefore, X1 means DM1 chooses the pathway, and X2 means DM2 chooses the pathway. At the end of each path earnings are listed in cents for each Decision-Maker as follows: (DM1’s Earnings, DM2’s Earnings). For example in Figure 7.19, if DM1 moves left, then DM1 and DM2 receive 15¢. In Figure 7.20, if DM1 moves left and then DM2 moves right, then DM1 receives 25¢ and DM2 receives 40¢.

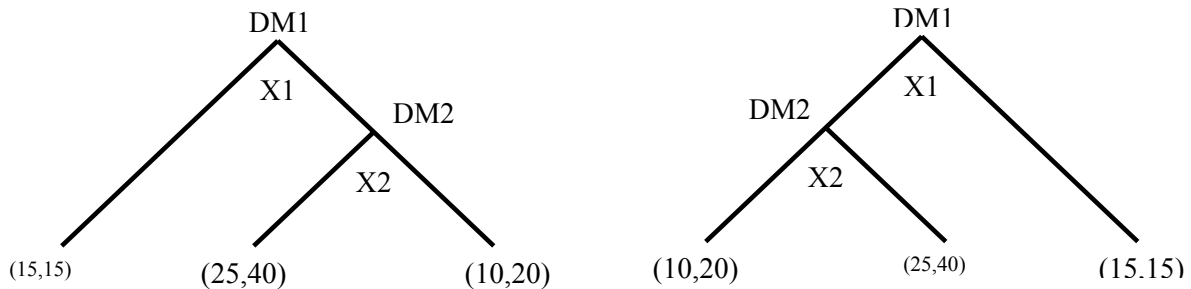


Figure 7.19: Branching pathway representation of a two-person neuroeconomic task

Each experimental trial consisted of four different parts. Figure 7.21 shows what DM1 (top row of pictures) and DM2 (bottom row of pictures) will see in each stage. Note that photographs of the participants will be used during the actual experiment. The subject’s picture indicates which Decision-Maker the person plays (either DM1 or DM2). These roles may change with each trial. DM1 always moves first by choosing

left or right. As shown in the bottom row (second panel) of Figure 7.20, DM2 will see nothing during this period. After seeing DM1's decision, DM2 moves left or right. DM1 will see nothing during this period (see third panel top row). The results of DM1's and DM2's decisions are displayed for both to see. Both Decision-Makers received the earnings from the task.

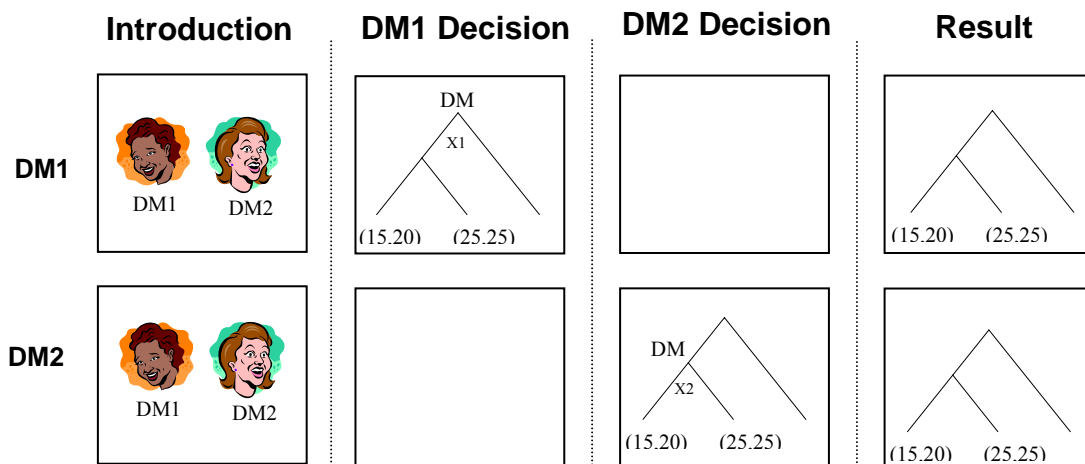


Figure 7.20: Step-by-step evolution of a two-person task

There are two different types of conditions in the experiment: Two-Person Decision condition and One-Person Decision condition. In the Two-Person Decision condition, both Decision-Makers participate, and depending on their decisions they will receive the earnings (refer Figure 7.21).

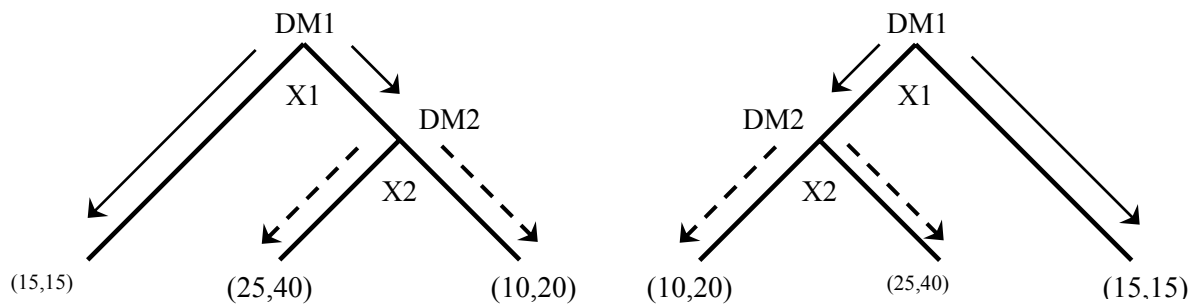


Figure 7.21: Step-by-step evolution of a two-person decision task

DM1 chooses first which way to go, either ending the task by going left or continuing it by going right (Figure 7.21 left panel). Note that in Figure 7.21 (right panel), going right ends the task, but going left continues the task). After seeing DM1's decision, DM2 chooses the path by moving left or right. After both Decision-Makers have chosen the paths, their decisions are compiled and both participants will receive their earnings from that task. For example, if you are DM1 in Figure 7.22 you decide first. By moving right, you will end the game and DM2 cannot make any further decision. DM1 and DM2 receive 15¢. If you move left, you let DM2 make the final decision. If DM2 moves right, DM1 earns 25¢ and DM2 earns 40¢; but if DM2 moves left, DM1 earns 10¢ and DM2 earns 20¢. In the One-Person Decision condition tasks only one individual makes a decision as follows (Figure 7.22). DM2's decision does not depend on DM1's decision.

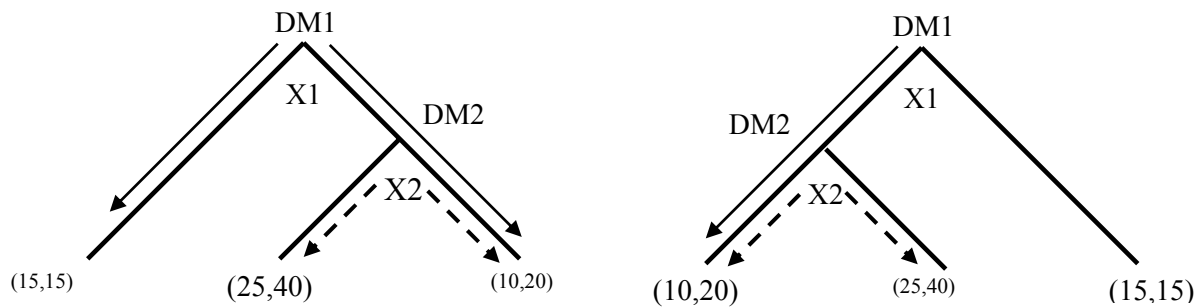


Figure 7.22: Step-by-step evolution of a one-person decision task

DM1 chooses first which way to go, either by going left or right. Afterwards, DM2 chooses which way to go, either by moving left or right. After both Decision-Makers have chosen the paths, their decisions are compiled and each Decision-Maker will receive the selected earning. For example, as DM1 in Figure 7.22 you can choose to move left or right to get to the desired earnings. If you go left, you earn 15¢, but if you move right, you receive 10¢. Afterwards, DM2 can choose to move left or right to get to the desired earnings. By moving left, DM2 earns 40¢ or by moving right DM2 earns 20¢.

7.4.1.3 Protocol instructions

The following figures show the actual protocol instructions that the participants in the experiment will see. Refer Figures 7.23-7.25.

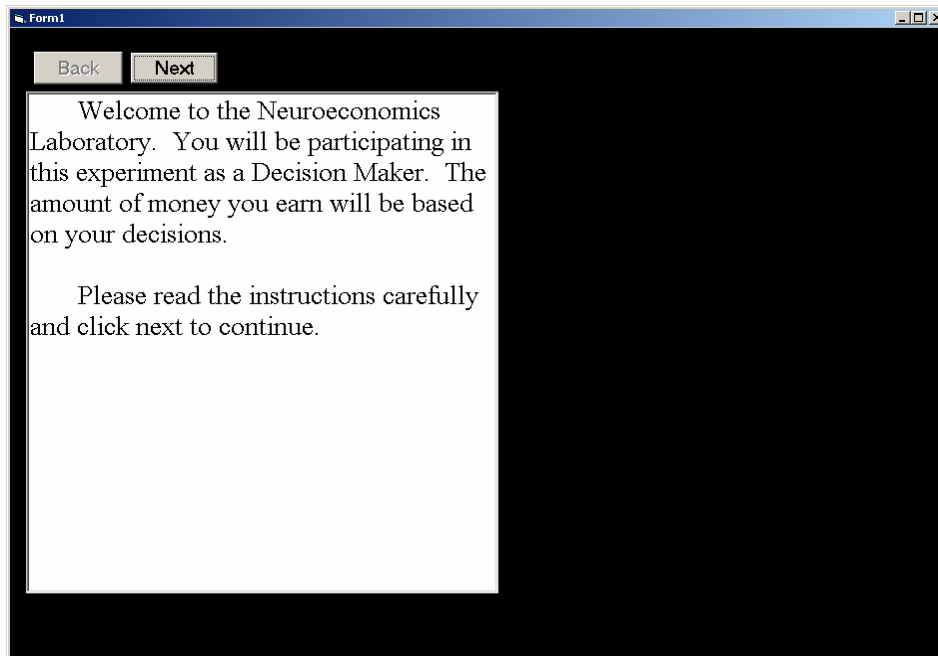


Figure 7.23: Protocol instructions: Welcome screen

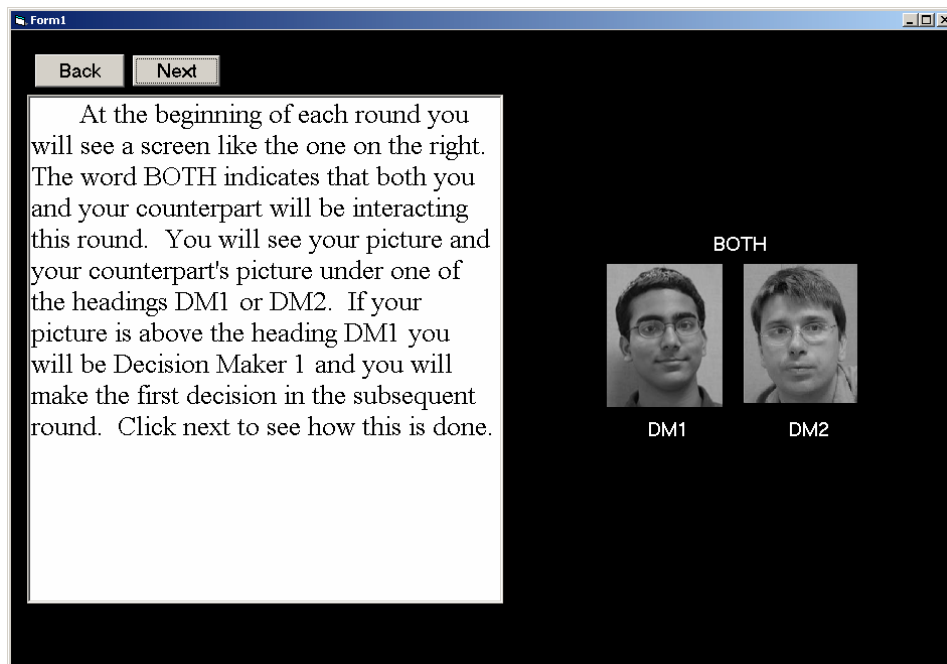


Figure 7.24: Protocol instructions: Introduction screen

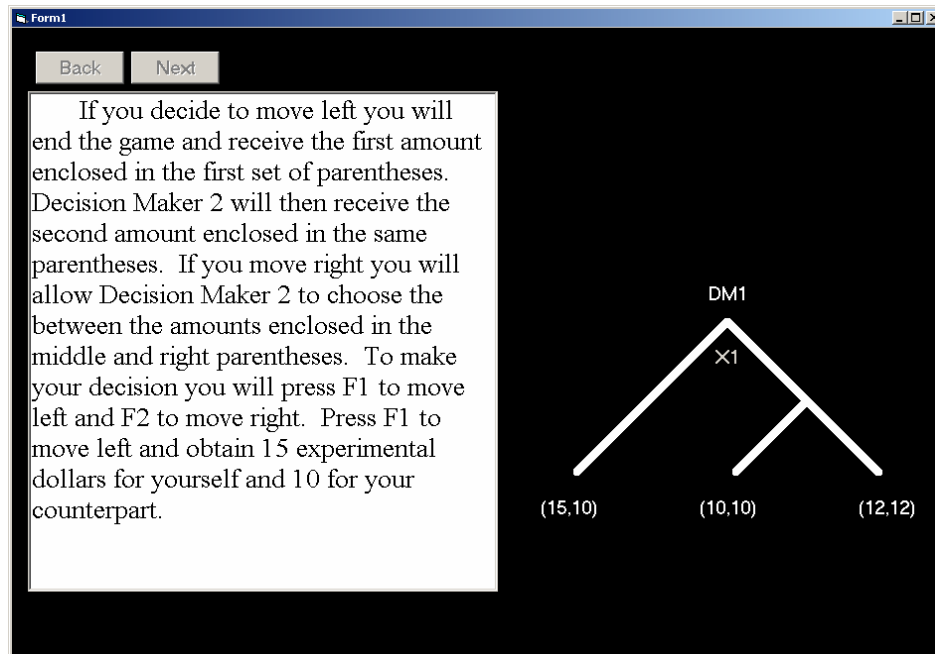


Figure 7.25: Protocol instructions: Game instructions screen

7.4.1.4 Data analysis

The analysis was conducted using Matlab to plot levels of oxygenated and deoxygenated hemoglobin for every channel versus time. Timing data from the protocol was then superimposed onto the plots to divide the plot into intervals representing game duration and the exact time when the player made a decision. Spatial map plots of each channel's average hemoglobin levels over the period of activation as compared to baseline were also generated to identify which areas under observation showed the largest changes over time.

The extracted hemodynamic parameters were analyzed using mean oxy-hemoglobin (HbO_2), deoxyhemoglobin (Hb), and total hemoglobin (HbT) and the corresponding standard deviation for each channel for each period of activation. The

maximum value attained during a period and the time taken to achieve the maximum value for every channel during the period of stimulation was also calculated. The data was also analyzed using a standard student T-test to further reveal the degree of hemodynamic changes produced by different decisions and also between a period of rest and a period of activation. Spatial hemodynamic profiles were used to reveal regions of the brain that were differentially activated by the experimental task. This was achieved by simultaneously comparing hemodynamic data obtained from different channels of the NIRS instrument across different decision types.

The data was analyzed using modified Beer Lambert's law for the calculation of hemoglobin concentrations. Tomographic images were reconstructed using inverse reconstruction techniques. The temporal traces were corrected for motion artifacts by examination of all the measured channels for large data aberrations or noise. Such artifacts created by motion are filtered out and suppressed during data processing. Further the data is high pass filtered to remove slow drift components and low pass filtered to remove noise caused by physiological components such as heart rate. These components are separately recorded as auxiliary inputs. The results are then analyzed for temporal and spatial evolution corresponding to the presented stimulus. The data is compared to the type of stimulus presented and the degree of activation it produces indicated by changes in the hemoglobin levels.

Plots of oxygenated and deoxygenated hemoglobin were constructed for every channel versus time. Timing data from the protocol was then superimposed onto the

plots to divide the temporal plot into several intervals, representing which game was played and the exact time when the player made a decision.

Spatial maps of each channel's average oxygenated hemoglobin levels over the entire period of activation were compared to the baseline readings to identify which areas of the prefrontal under observation showed the largest changes in oxy-hemoglobin over time. Baseline indicates readings taken when the subject is in resting state (awake, eyes open but no stimulation). Activation indicates readings taken when the subject is making decisions during a neuroeconomic protocols. The additional knowledge provided by the NIRS study as compared to previously conducted neuroeconomic studies using fMRI will be temporally relating a decision type to the hemodynamic response in an event related design as opposed to the block average examination of the tasks to the activation they produce in various areas of the brain.

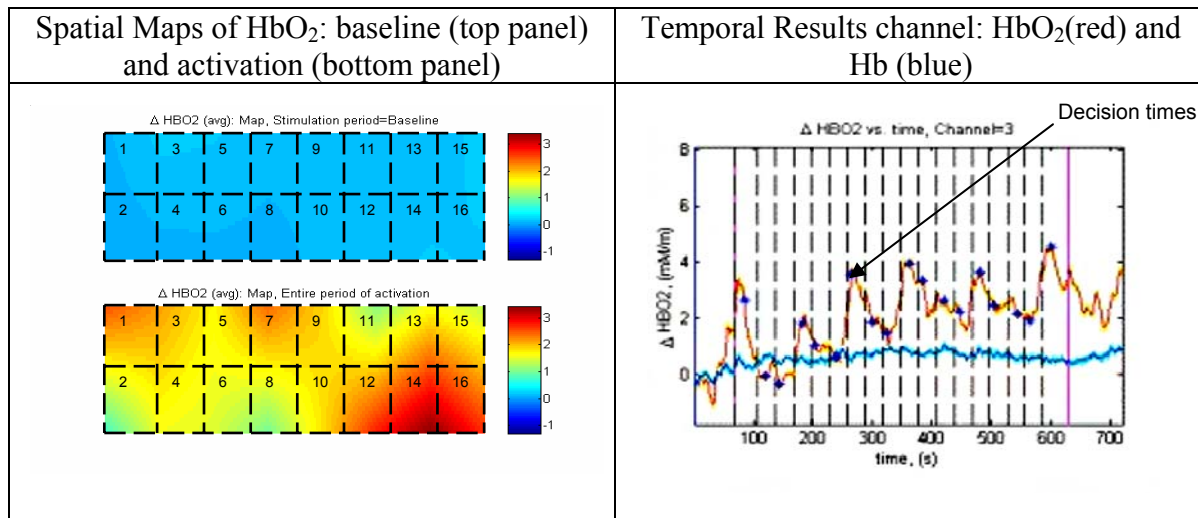
7.4.2 Results

Representative the temporal readings the region of interest and a spatial distribution of increase in HbO₂ from the study are shown in Table 7.9. Previously published results show that the prefrontal region is more active when subjects play a human counterpart than when they play a computer counterpart following a fixed (and known) probabilistic strategy. This suggests that cooperation requires an active convergence zone, possibly in prefrontal cortex, that binds joint attention to mutual gains with the inhibition of immediate reward gratification to allow cooperative decisions. This result was corroborated in the experiments conducted

The goal of the study was to correlate the hemodynamic response to the task presented and also the behavior of the subject. To elaborate, some of the neuroeconomic tasks were single decision maker tasks and the subject did not play an active role as a decision maker as described in the protocol. Such games showed little or no change in the oxygenated hemoglobin level. Other games/decisions involved the subject and the counterpart for the decision-making. Timing data from the protocol was then superimposed onto the NIR plots to correlate the NIR data with the intervals during which each game was played. The data was analyzed to correlate the behavior exhibited during the trust and punish games to hemoglobin level differences produced during a block of game play. Temporally the data was analyzed to relate degree of activation to the type of decision made i.e. whether the subject made a cooperative/trust decision versus a non-cooperative/punish decision. The data results show distinct task related hemodynamic responses.

If the subject made a cooperative decision then a larger change (increase) in oxyhemoglobin levels was observed when compared to decisions where subjects made a non-cooperative decision. To reiterate, the temporal results prove the hypothesis stated above that cooperation requires an active convergence zone and binds joint attention to mutual gains with the inhibition of immediate reward gratification to allow cooperative decisions. Therefore cooperative/trust decisions show larger hemodynamic responses than non-cooperative/trust decisions. Also the hemodynamic response is distinct when the subject is actively involved in the game and not surpassed in the decision by the other player.

Table 7.9: Spatial and temporal results of a neuroeconomic task

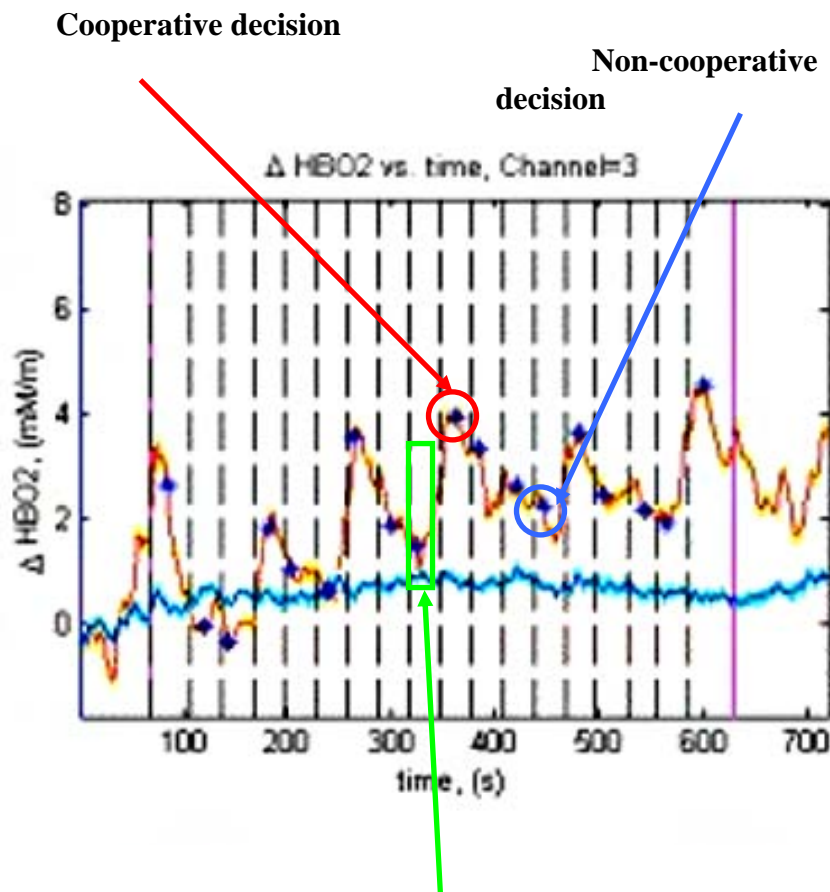


The graphs shown in Figure 7.26 and Table 7.9 (right panel) represent the following observations:

- *Oxygenated hemoglobin [HbO₂] (Red line plot)*: Rise in oxygenated hemoglobin is used as an indicator of increased blood and oxygen supply to the region and thus reveals activation of the region under stimuli when compared to the resting stage.
- *Deoxygenated hemoglobin [Hb] (Blue line plot)*: It is relatively unchanged during experiment
- *Two Markers (Pink vertical lines)*: The two pink markers are placed at the start of the stimulation period (beginning of the game rounds) and at the end of stimulation period (end of all game rounds). The period before the first marker indicates the baseline/resting period, which is used as a reference (period of zero activation). All levels in the stimulation period are relative to the levels measured during this period and thus show only changes with respect to the baseline.

Timing data from the protocol was then superimposed onto the NIR plots to correlate the NIR plots with the intervals during which each game was played.

- *Time period of each game (Dashed black lines):* The dashed black lines are used to break the plot into individual periods, during which the games were played, thus indicating the exact changes of oxy-hemoglobin within the period of a given game.
- *Exact time when the player made a decision (Blue stars):* Blue stars indicate the exact oxygenated hemoglobin level at the time when the subject made the decision.



Single decision maker game: Subject not involved in decision

Figure 7.26: Temporal evolution of the hemodynamic response measure by NIRS

7.4.3 Discussion

Data was analyzed to reveal activation in regions of interest as compared to baseline as well as control tasks. The goal of the research study was to correlate the hemodynamic response evoked by the task presented and also the behavior of the subject. To elaborate, some of the neuroeconomic tasks were single decisions and the subject did not play an active role as a decision maker while in other games/decisions involved the subject as well as the counterpart for the decision-making. The data was analyzed to correlate the total cooperation scores during the trust and punish games to hemoglobin level differences produced during a block of game play. Temporally the data was compared within a subject to look for specific hemodynamic patterns that relate to whether the subject made a cooperative/trust decision versus a non-cooperative/punish decision. Since all the decisions were financially motivated, the evolution of the hemodynamic responses to the games was expected to reveal the areas of activation produced by financial decisions and also the behavior of the person during the trial.

In conclusion, this study demonstrated that the prefrontal cortex is activated by neuroeconomic tasks causing an increase in the regional cerebral oxygenated hemoglobin level while little effect was seen on the trend of deoxygenated hemoglobin levels. Analyzing the spatial data revealed that neuroeconomic games caused an increase in activation concentrated primarily in the inferior prefrontal cortex. Additional analysis of the temporal profile of the cerebral activation evoked by the stimulus protocol revealed that cooperative decisions (where both players gained financially

from a decision) created the larger hemodynamic changes as compared to non-cooperative (punish/selfish decisions where one player gained more than his counterpart). The least activation (indicated by negligible hemodynamic changes from baseline levels) was observed in one person decisions where the second player had no part in the game.

7.4.4 Conclusions

Cooperation between individuals requires the ability to infer each other's mental states from shared expectations over mutual gains and cooperative choices that realize these gains. From evidence that the ability for mental state attribution involves the use of prefrontal cortex, we hypothesized that this area is involved in integrating theory-of-mind processing with cooperative actions. The results presented are from study data from a functional NIRS experiment designed that tested this hypothesis. Subjects played standard two-person "trust and reciprocity" games with human counterparts for cash rewards. Behavioral data shows that subjects consistently attempted cooperation with their human counterpart. The NIRS measurements were made over the prefrontal cortex, which was identified as a region of interest based on previously reported fMRI studies with the same protocol. The data shown represents the hemoglobin concentration analyzed spatially and temporally for a subject exhibiting high cooperation behavior (inferred from the decisions made during the trust game).

7.5 Chapter summary

The chapter presents the different protocols and results that were obtained using near infrared spectroscopy for psychological based tasks. Results of analyzing the data with the developed models are also shown to establish the validity of the models. In addition, invasive multimodality data using NIRS and laser speckle imaging was used to further validate the single and multicompartement models and their versatility in describing vascular and oxygen transport dynamics.

CHAPTER 8

SUMMARY AND FUTURE WORK

This dissertation contained both theoretical and experimental components and goals. Theoretically, the research goal was to develop physiologically relevant models using multimodality data that determined cerebral metabolic rate and blood flow during stimulus driven cerebral activation. The critical part and emphasis of this goal are the words, “physiologically relevant”, as many models exist in literature that are empirical or highly simplified due to the complexity of including underlying phenomena that give rise to functional imaging contrast. Specifically three key issues were addressed in this work: (1) Determination of the blood flow, blood volume and vascular compliance as well as oxygen transport relationship; (2) Prediction of the hidden variables that determine the neural and metabolic correlates of cerebral activation by external stimuli; and (3) Calculation of system parameters that describe the physiological and anatomical properties of the brain not revealed by composite hemodynamic measurements.

The theoretical goal of this dissertation was motivated by the experimental results obtained. Experimentally, the research attempts to demonstrate the viability of noninvasive NIRS to predict cerebrovascular and metabolic changes using complex psychological protocols such as verbal fluency protocol and neuroeconomic tasks. In order to describe the underlying physiological phenomena, rigorous and physiologically realistic models are required to determine direct measures of neural activity based on

readings obtained using NIRS. The efficacy of the models was also validated using previously published multimodality data. The models were also tested in a controlled laboratory set-up using a compliant vascular phantom.

8.1 Theoretical development

Pursuant to the theoretical goals, this dissertation contributes three new neurovascular models described below.

8.1.1 Single compartment Windkessel model

Previous research contains a basic flow-volume inductive model. This dissertation makes the following contributions:

- a. Set up of a Pseudo-Bayesian framework to include multimodality measurements to reduce uncertainty in the values and interdependence of parameters that define the neurophysiological processes that underlie the measured cerebral hemodynamic response
- b. Extension of the inductive flow-volume model to define hemodynamic changes during long duration stimulus which increases the versatility of the Windkessel model (e.g. psychological experiments such as verbal fluency task)
- c. Development of two new models (namely oxygen extraction and mitochondrial activity models) to define oxygen transport and consumption that determine metabolic activity at the tissue and mitochondrial level during activation using the single compartment flow-volume dynamics.

- d. Development of novel tomographic maps of blood flow and metabolic rate to define the spatial extent of cerebral activation and predict BOLD measurements from noninvasive NIRS hemodynamic data.

8.1.2 Inductive multi-compartment Windkessel model

This model is novel and has not been previously explored in literature. The model makes the following contributions

- a. Development of a new model to define flow and volume changes in a capillary compliance model. This model makes it possible to segment the measured spatially averaged hemodynamic data into changes in the arterial, capillary and venous compartments to define the individual contribution and temporal evolution of cerebral blood volume and flow in each vascular compartment. This helps to quantify compartmentalized hemodynamics based on a realistic representation of cerebrovascular structures thus helping to define their physiological role and contribution to measured cerebral hemodynamics
- b. Development of a new model to define oxy- and deoxy-hemoglobin changes using capillary oxygen transport phenomena. An inductive three compartment capillary oxygen extraction model is developed to provide a description of the underlying biophysical mechanisms using temporal basis functions for the oxygen extraction. Oxygen extraction is assumed to result from the capillary compartment alone which has the highest contribution to tissue oxygenation with negligible contributions from the arteriolar and venous compartments. This

model provides a physiologically relevant description of metabolic activity and can be exploited in the diagnosis and treatment of diseases such as Alzheimer's which cause aberrational changes in localized cerebral metabolism.

- c. Studies of cerebral metabolism have suggested that oxygen consumption originates at the cellular level (in the mitochondria) and follows a path of oxygen transport from the blood vessels to the parenchymal tissue to the mitochondrial structures where it is consumed to support increased energy demand created by activation. A new mitochondrial activity model is developed in this research to define the oxygen transport pathway with the temporal basis function at the cellular level. The model helps to accurately determine parameters that define the underlying metabolic process; a direct result of activation which provides a true measure of brain function from the cumulative hemodynamic measurements obtained using current imaging techniques.

8.1.3 Deductive neurovascular model

Previous research contains a single compartment neurovascular flow-volume model that describes the neural and hemodynamic model relevant to fMRI measurements. The model was developed for fMRI studies to predict the BOLD signal. This research specifically makes the following contributions:

- a. Inclusion of intermediate states such as blood flow and volume to reduce uncertainty in the values and interdependence of parameters that define the measured cerebral hemodynamic response.

- b. Development of an explicit neurovascular multicompartment model to describe the measured cerebral hemodynamic response in the context of compliance. The model provides a direct relationship between input stimulus (described by a simple step function that depends on experimental timing) and the evoked hemodynamic response. It provides the missing link between neural response and the measured hemodynamic response. This biophysical neurovascular model is extensively explored in the context of vessel compliance and stimulus duration. Note the reduction in the number of model parameters as compared to inductive models. This manifests as computational efficiency and removes interdependencies of parameter definitions that hinder accurate and unique solutions to the system.

8.2 Experimental development

Experimental contributions are made through *in vivo* noninvasive human studies using NIRS and development of a realistic compliant vascular phantom to model the flow-volume characteristics.

8.2.1 Compliant vascular phantom

A vascular model set up to mimic the physiology described by the single compartment Windkessel model. The goal of the experiments was to,

- a. Develop a compliant vasculature to describe the single Windkessel model and test the validity of the assumptions in a controlled setup.

- b. Data acquisition for modeling vessels using pressure, compliance, peripheral resistance, flow and volume

8.2.2 Experimental protocols and results

The development of near infrared spectroscopy (NIRS) as a viable brain imaging technique has previously centered on measuring hemodynamic values that are associated with the performance of perceptual or motor tasks. This research is novel in that far less research has attempted to validate NIRS as a viable means of measuring neurological correlates of cognitive activity which is the basis for the choice of protocols in this research. Data from *in vivo* human experiments is used to validate the developed models. The protocols used to acquire temporal and spatial measurements of cerebral blood volume and oxygenations were: Categorical learning, Verbal fluency, Neuroeconomic and Physical exercise tasks.

8.3 Future work

The work of this dissertation lends itself to the potential for long term future research in several aspects. These can be classified into theoretical and experimental developments.

8.3.1 Future theoretical development

The theoretical models developed can be extended to include the following

- a. An explicit model of the effect of vaso-reactive signaling molecules could be included to describe the response to measured neuronal stimulation
- b. Further development of models to include anomalous biomechanical effects from conditions such as aneurysms and hematomas to extend the use of the such modeling procedures to the early detection of disease
- c. Extension of the physiological models to include a behavioral model using psychological experiments thus allowing the prediction of behavior patterns and their implications using hemodynamic data. (e.g.: The neuroeconomic data collected in this research can be fit into actor-critic model)

8.3.2 Future experimental development

The following experiments can be conducted to further explore cerebral activation:

- a. A potential variation on the phantom could include doing multiple, periodic pulses to model repeated stimuli with tubes of varying compliance in series
- b. Furthermore, physiologically realistic structures could be made by placing several tubes together using y-connections to model the complicated capillary bed. Further work is also required to completely characterize the vessels and to compare their dynamic properties (such as pulse velocity and spatial flow profiles) with those of a natural artery.
- c. Finally, the vascular phantom could be significantly modified to model oxygen transport dynamics.

- d. In vivo experiments that use noninvasive EEG/MEG or invasive readings using electrodes to record electrical signals in addition to hemodynamic data
- e. Further exploration of event related protocols using NIRS
- f. Experiments to record hemodynamic changes applied to diagnosis and treatment monitoring of disease

APPENDIX A

RESEARCH PUBLICATIONS

Publications that resulted from this research

Journal Publications

1. Monica Allen, Jeffery Allen, Kambiz Alavi, “Study of cerebral blood volume and blood flow using integral equation theory”, *Libertas Mathematica*, vol. XXVI, p. 109-117, 2006
2. Huppert, T.J.*, Allen, M.S*, and Boas, D.A. “The feasibility of inferring flow, volume, and cerebral metabolism from measurements by fMRI or diffuse optical imaging” - in preparation, *Proceedings of the National Academy of Sciences* (*equal contribution)
3. Huppert, T.J., Allen, M.S, and Boas, D.A. “A multi-compartment vascular model for inferring baseline and functional changes in cerebral oxygen metabolism and arterial dilation” - accepted, *Journal of cerebral blood flow and metabolism*

Conference Proceedings

1. Huppert, TJ, Allen, M.S, and Boas, DA. “Inferring baseline and functional blood flow, volume and cerebral metabolism from measurements of blood oxygenation”, ISMRM Conference Talk [6431 04], May 2007

2. Huppert, TJ, Allen, M.S, and Boas, DA. “Inferring baseline and functional blood flow, volume and cerebral metabolism from measurements of blood oxygenation”, SPIE Conference Talk [6431 04], January 2007
3. Huppert, TJ, Allen, M.S, and Boas, DA. “Estimating CMRO₂ with multimodality imaging using a multi-compartment vascular model”, Human Brain Mapping, Florence, Italy, Conference Talk, 2006.
4. Huppert, TJ, Allen, M.S, and Boas, DA. “Estimating CMRO₂ with multimodality imaging using a multi-compartment vascular model” Optical Society of America, Ft. Lauderdale, FL , Conference Talk, 2006.
5. Allen, M.S, Huppert, TJ, and Boas, DA. “Estimating CMRO₂ with multimodality imaging using a multi-compartment vascular model”.,SPIE Conference Talk, [6081 27], January 2006
6. Monica S. Allen, Jeffery W. Allen, Shweta Mikkilineni, and Hanli Liu, “Trends in cerebral oxygenation during mental and physical exercises measured using near-infrared spectroscopy (NIRS) – potential for early detection of Alzheimer’s disease”, Proc. SPIE Vol. 5693, p. 396-405, January, 2005 .

REFERENCES

- [1] D. G. Nair, "About being BOLD," *Brain Res Brain Res Rev*, vol. 50, pp. 229-43, Dec 15 2005.
- [2] R. B. Buxton and L. R. Frank, "A model for the coupling between cerebral blood flow and oxygen metabolism during neural stimulation," *J Cereb Blood Flow Metab*, vol. 17, pp. 64-72, Jan 1997.
- [3] R. B. Buxton, E. C. Wong, and L. R. Frank, "Dynamics of blood flow and oxygenation changes during brain activation: the balloon model," *Magn Reson Med*, vol. 39, pp. 855-64, 1998.
- [4] J. B. Mandeville, J. J. Marota, C. Ayata, M. A. Moskowitz, R. M. Weisskoff, and B. R. Rosen, "MRI measurement of the temporal evolution of relative CMRO(2) during rat forepaw stimulation," *Magn Reson Med*, vol. 42, pp. 944-51, Nov 1999.
- [5] J. B. Mandeville, J. J. Marota, C. Ayata, G. Zaharchuk, M. A. Moskowitz, B. R. Rosen, and R. M. Weisskoff, "Evidence of a cerebrovascular postarteriole windkessel with delayed compliance," *J Cereb Blood Flow Metab*, vol. 19, pp. 679-89., 1999.
- [6] R. B. Buxton, K. Uludag, D. J. Dubowitz, and T. T. Liu, "Modeling the hemodynamic response to brain activation," *Neuroimage*, vol. 23 Suppl 1, pp. S220-33, 2004.
- [7] Y. Zheng, D. Johnston, J. Berwick, D. Chen, S. Billings, and J. Mayhew, "A three-compartment model of the hemodynamic response and oxygen delivery to brain," *Neuroimage*, vol. 28, pp. 925-39, Dec 2005.
- [8] H. Girouard and C. Iadecola, "Neurovascular coupling in the normal brain and in hypertension, stroke, and Alzheimer disease," *J Appl Physiol*, vol. 100, pp. 328-35, Jan 2006.
- [9] J.B.Pochon, R.Levy, P.Fossati, S.Lehericzy, J.B.Poline, B.Pillon, D. L. Bihan, and B.Dubois, "The neural system that bridges reward and cognition in humans : an fMRI study," *Proceedings of the National Academy of Sciences*, vol. 99, pp. 5669-5674, April 16, 2002.

- [10] B. Knutson, A. Westdorp, E. Kaiser, and D. Hommer, "fMRI Visualization of Brain Activity during a Monetary Incentive Delay Task," *Neuroimage*, vol. 12, pp. 20-27, 2000.
- [11] B. Knutson, C. M. Adams, G. W. Fong, and D. Hommer, "Anticipation of Increasing Monetary Reward Selectively Recruits Nucleus Accumbens," *The Journal of Neuroscience*, vol. 21, pp. 1-5, 2001.
- [12] B. Knutson, G. W. fong, S. M. Benett, C. M. Adams, and D. Hommer, "A region of mesial prefrontal cortex tracks monetarily rewarding outcomes: characterization with rapid event-related fMRI," *Neuroimage*, vol. 18, pp. 263-272, October 14, 2002.
- [13] K. McCabe and V. Smith, "Intentionality detection and 'mindreading': Why does game form matter?," *Proceedings of the National Academy of Sciences*, vol. 97, p. 4404, November 4, 2000.
- [14] K. McCabe and V. Smith, "A comparison of naive and sophisticated subject behavior with game theoretic predictions," *Proceedings of the National Academy of Sciences*, vol. 97, p. 3777, 2000.
- [15] M. S. Allen, J. W. Allen, S. Mikkilineni, and H. Liu, "Trends in cerebral oxygenation during mental and physical exercises measured using near-infrared spectroscopy (NIRS) - potential for early detection of Alzheimer's disease (submitted)," *Journal of Biomedical Optics*, January 2005.
- [16] M. L. Kringelbach and E. T. Rolls, "The functional neuroanatomy of the human orbitofrontal cortex: evidence from neuroimaging and neuropsychology," *Progress in Neurobiology*, vol. 72, pp. 341-372, 2004.
- [17] D. L. Johnson, J. S. Wiebe, S. M. Gold, N. C. Andreasen, R. D. Hichwa, G. L. Watkins, and P. L. L. Boles, "Cerebral blood flow and personality: a positron emission tomography study," *American Journal of Psychiatry*, vol. 156, pp. 252-257, February, 1999.
- [18] M. A. Franceschini, S. Fantini, V. Toronov, M. E. Filiaci, and E. Gratton, "Cerebral Hemodynamics Measured by Near-Infrared Spectroscopy at Rest and During Motor Activation," *Optical Society of America*, pp. 73 - 80, 2000.
- [19] M. A. Franceschini, V. Toronov, M. E. Filiaci, E. Gratton, and S. Fantini, "On-line optical imaging of the human brain with 160 - ms temporal resolution," *Optical Society of America*, vol. 6, pp. 49 - 57, 31 January 2000.

- [20] M. A. Franceschini and D. A. Boas, "Noninvasive measurement of neuronal activity with near - infrared optical imaging," *NeuroImage*, vol. 21, pp. 372 - 386, 2004.
- [21] B. Chance, E. Anday, S. Nioka, S. Zhou, L. Hong, K. Worden, C. Li, T. Murray, Y. Ovetsky, D. Pidikiti, and R. Thomas, "A novel method for fast imaging of brain function, non-invasively, with light," *Optics Express*, vol. 2, pp. 411-423, 1998.
- [22] H. Liu, Y. Song, K. L. Worden, X. Jiang, A. Constantinescu, and R. P. Mason, "Noninvasive Investigation of Blood Oxygenation Dynamics of Tumors by Near Infrared Spectroscopy," *Applied Optics*, vol. 39, pp. 5231-5243, 2000.
- [23] H. Liu, Y. Gu, J. G. Kim, and R. P. Mason, "Near infrared spectroscopy and imaging of tumor vascular oxygenation," *Imaging in Biological Research, Part B*, pp. 349-378, 2004.
- [24] A. Duncan, J. H. Meek, M. Clemence, C.E.Elwell, P. Fallon, L.Tyszczuk, M.Cope, and D. Delpy, "Measurement of cranial optical path length as a function of age using phase resolved near infrared spectroscopy," *Pediatric Research*, vol. 39, pp. 889-894.
- [25] S. Gopinath, C. S. Robertson, R. G. Grossman, and B. Chance, "Near-infrared spectroscopic localization of intracranial hematomas," *Journal of Neurosurgery*, vol. 79, pp. 43-47, 1993.
- [26] C. Cheung, J. P. Culver, K. Takahashi, J. H. Greenberg, and A. G. Yodh, "In vivo cerebrovascular measurement combining diffuse near-infrared absorption and correlation spectroscopies," *Phys. Med. Biol*, vol. 46, pp. 2053-2065, 2001.
- [27] G. Zhang, A. Katz, R. R. Alfano, A. D. Kofinas, P. G. Stubblefield, W. Rosenfeld, D. Beyer, D. Maulik, and M. R. Stankovic, "Brain perfusion monitoring with frequency-domain and continuous-wave near-infrared spectroscopy: a cross-correlation study in newborn piglets," *Phys. Med. Biol*, vol. 45, pp. 3143-3158, 2000.
- [28] M. Fabiani, G. Gratton, and P. M. Corballis, "Noninvasive near infrared optical imaging of human brain function with subsecond temporal resolution," *Journal of Biomedical Optics*, vol. 1, pp. 387-398, 1996.
- [29] R. Wenzel, H. Obrig, J. Ruben, K. Villringer, A. Thiel, J. Bernarding, U. Dirnagl, and A. Villringer, "Cerebral blood oxygenation changes induced by visual stimulation in humans," *Journal of Biomedical Optics*, vol. 1, pp. 399-404, 1996.

- [30] D. A. Boas, T. Gaudette, G. Strangman, X. Cheng, J. J. A. Marota, and J. B. Mandeville, "The accuracy of near infrared spectroscopy and imaging during focal changes in cerebral hemodynamics," *NeuroImage*, vol. 13, pp. 76-90, 2001.
- [31] D. A. Boas, G. Jaszewski, G. Strangman, J. P. Culver, and R. Poldrack, "Modeling of the Hemodynamic Response Function for Event Related Motor and Visual Stimuli as Measured by Near Infrared Spectroscopy," *OSA Biomedical Topical Meetings, Technical Digest*, vol. MC5-1, Miami Beach, FL, April 7-10, 2002.
- [32] J. C. Hebden, M. C. Hillman, A. Gibson, N. Everdell, R. M. Yusof, D. T. Delpy, S. R. Arridge, T. Austin, and J. H. Meek, "Time resolved optical imaging of the newborn infant brain: initial clinical results," *OSA Technical Digest*, in *OSA Technical Digest*, Miami, FL, 2002, pp. 587-589.
- [33] A. Villringer, J. Planck, C. Hock, L. Schleinkofer, and U. Dirnagl, "Near infrared spectroscopy (NIRS): a new tool to study hemodynamic changes during activation of brain function in human adults," *Neuroscience Letters*, vol. 154, pp. 101 - 104, 1993.
- [34] H. L. Gallagher and C. D. Frith, "Functional imaging of 'theory of mind'," *TRENDS in Cognitive Sciences*, vol. 7, pp. 77-83, 2003.
- [35] J. N. Wood and J. Grafman, "Human prefrontal cortex: processing and representational perspectives," *Nature Reviews - Neuroscience*, vol. 4, pp. 139-147, February 2003.
- [36] S. R. Arridge and J. C. Hebden, "Optical imaging in medicine: II. Modeling and reconstruction," *Phys. Med. Biol*, vol. 42, pp. 841-853, 1997.
- [37] M. S. Patterson, B. Chance, and B. C. Wilson, "Time resolved reflectance and transmittance for the non - invasive measurement of tissue optical properties," *Applied Optics*, vol. 28, pp. 2331 - 2336, 15 June 1989.
- [38] E. M. Sevick, B. Chance, J. Leigh, S. Nioka, and M. Maris, "Quantization of time- and frequency-resolved optical spectra for the determination of tissue oxygenation," *Annals of Biochemistry*, vol. 195, pp. 330-351, 1991.
- [39] K. D. Paulsen and H. Jiang, "Spatially varying optical property reconstruction using a finite element diffusion equation approximation," *Med. Phys.*, vol. 22, pp. 691-701, 1995.

- [40] S. R. Arridge and M. Schweiger, "Photon measurement density functions. Part II: Finite-element-method calculation," *Applied Optics*, vol. 34, pp. 8026-8037, 1995.
- [41] A. H. Hielscher, A. D. Klose, and K. M. Hanson, "Gradient-Based Iterative Reconstruction Scheme for Time-Resolved Optical Tomography," *IEEE Transaction on Medical Imaging*, vol. 18, pp. 262-271, 1999.
- [42] Y. Q. Yao, Y. Wang, Y. L. Pei, W. W. Zhu, and R. L. Barbour, "Frequency-domain optical imaging of absorption and scattering distributions by Born iterative method," *Journal of the Optical Society of America A*, vol. 14, pp. 325-342, 1997.
- [43] S. R. Arridge, "Photon-measurement density functions. Part I: Analytical forms," *Applied Optics*, vol. 34, pp. 7395-7409, 1995.
- [44] K. D. Paulsen and H. Jiang, "Enhanced frequency domain optical image reconstruction in tissues through total variation minimization," *Applied Optics*, vol. 35, pp. 3447-3458, 1996.
- [45] H. Jiang, K. D. Paulsen, and U. L. Sterberg, "Optical image reconstruction using DC data: Simulations and experiments," *Phys. Med. Biol*, vol. 41, pp. 1483-1498, 1996.
- [46] J. C. Schotland, "Continuous-wave diffusion imaging," *Journal of the Optical Society of America*, vol. 14, pp. 275-279, 1997.
- [47] H. Hielscher, R. E. Alcouffe, and R. L. Barbour, "Comparison of finite-difference transport and diffusion calculations for photon migration in homogeneous and heterogeneous tissue," *Phys. Med. Biol*, vol. 43, pp. 1285-1302, 1998.
- [48] R. L. Barbour, H. L. Graber, J. W. Chang, S. L. S. Barbour, P. C. Koo, and R. Aronson, "MRI-guided optical tomography: Prospects and computation for a new imaging method," *IEEE Trans. Comput. Sci. Eng*, vol. 2, pp. 63-67, 1995.
- [49] R. B. Buxton, K. Uludag, D. J. Dubowitz, and T. T. Liu, "Modeling the hemodynamic response to brain activation," *Neuroimage* vol. 23 pp. S220-233, 2004.
- [50] M. A. Mintun, B. N. Lundstrom, A. Z. Snyder, A. G. Vlassenko, G. L. Shulman, and M. E. Raichle, "Blood flow and oxygen delivery to human brain during functional activity: theoretical modeling and experimental data," *Proceedings of the National Academy of Sciences* vol. 98, pp. 6859-6864, 2001.

- [51] D. G. Nair, "About being BOLD," *Brain Research Reviews*, vol. 50, pp. 229-243, 2005.
- [52] S. P. Robinson, F. A. Howe, L. M. Rodrigues, M. Stubbs, and J. R. Griffiths, "Magnetic resonance imaging techniques for monitoring changes in tumor oxygenation and blood flow," *Semin. Radiat. Oncol.*, vol. 8, pp. 198-207, 1998.
- [53] R. B. Buxton and L. R. Frank, "A model for the coupling between cerebral blood flow and oxygen metabolism during neuronal stimulation," *Journal Cerebral Blood flow and Metabolism*, vol. 17, pp. 64-72, 1997.
- [54] M. S. Olufsen, C. C. Peskin, Y. Kim, E. M. Pedersen, and A. Nadim, "Numerical simulation and experimental validation of blood flow in arteries with structured-tree outflow conditions," *Annals of biomedical Engineering*, vol. 28, pp. 1281-1299, 2000.
- [55] M. Johns, C. A. Giller, and H. Liu, "Computational and in vivo investigation of optical reflectance from human brain to assist neurosurgery," *Journal of Biomedical Optics*, vol. 3, pp. 437-445, 1998.
- [56] R. B. Buxton, E. C. Wong, and L. R. Frank, "Dynamics of blood flow and oxygenation changes during brain activation: the balloon model," *Magnetic Resonance Med.*, vol. 39, pp. 855-864, 1998.
- [57] D. A. Boas, G. Strangman, J. P. Culver, R. D. Hoge, G. Jaszewski, R. A. Poldrack, B. R. Rosen, and J. B. Mandeville, "Can the cerebral metabolic rate of oxygen be estimated with near-infrared spectroscopy?," *Phys Med Biol*, vol. 48, pp. 2405-18, Aug 7 2003.
- [58] B. Grubb, J. M. Colacino, and K. Schmidt-Nielsen, "Cerebral blood flow in birds: effect of hypoxia," *Am. Journal Physiol. Heart Circ Physiol.* vol. 234, pp. H230-H234, 1978.
- [59] J. B. Mandeville, J. J. Marota, C. Ayata, G. Zaharchuk, M. A. Moskowitz, B. R. Rosen, and R. M. Weisskoff, "Evidence of a cerebrovascular postarteriole windkessel with delayed compliance," *J Cereb Blood Flow Metab*, vol. 19, 1999.
- [60] R. D. Hoge, M. A. Franceschini, R. J. M. Covolan, T. J. Huppert, J. B. Mandeville, and D. A. Boas, "Simultaneous recording of task-induced changes in blood oxygenation, volume, and flow using diffuse optical imaging and arterial spin-labeling MRI," *NeuroImage* vol. 25, pp. 701-707, 2005.

- [61] R. B. Buxton, E. C. Wong, and L. R. Frank, "Dynamics of blood flow and oxygenation changes during brain activation: the balloon model," *Magnetic Resonance in Medicine*, vol. 39, pp. 855-864, 1998.
- [62] J. R. Petrella, C. DeCarli, M. Dagli, C. B. Grandin, J.H.Duyn, J. A. Frank, E.A.Hoffman, and W.H.Theodore, "Age-related vasodilatory response to acetazolamide challenge in healthy adults: a dynamic contrast-enhanced MR study," *American Journal of Neuroradiology*, vol. 19, pp. 39-44, 1998.
- [63] S. G. Imbesi, K. Knox, and C. W. Kerber, "Aneurysm flow dynamics: alterations of slipstream flow for neuroendovascular treatment with liquid embolic agents," *American Journal of Neuroradiology*, vol. 24, pp. 2044-2049, 2003.
- [64] E. B. Hanlon, I. Itzkan, R. R. Dasari, M. S. Feld, R. J. Ferrante, A. C. McKee, D. Lathi, and N. W. Kowall, "Near-infrared fluorescence spectroscopy detects Alzheimer's disease in vitro," *Photochem Photobiol* vol. 70, pp. 236-242, 1999.
- [65] K. Matsuo, T. Kato, M. Fukuda, and N. Kato, "Alteration of hemoglobin oxygenation in the frontal region in elderly depressed patients as measured by near-infrared spectroscopy," *Journal of Neuropsychiatry and Clinical Neuroscience*, vol. 12, pp. 465-471, 2000.
- [66] A. J. Fallgatter and W. K. Strik, "Reduced frontal functional asymmetry in schizophrenia during a cued continuous performance test assessed with near-infrared spectroscopy," *Schizophrenia Bulletin*, vol. 26, pp. 913-919.
- [67] H. Saitou, H. Yanagi, S. Hara, S. Tsuchiya, and S. Tomura, "Cerebral blood volume and oxygenation among poststroke hemiplegic patients: effects of 13 rehabilitation tasks measured by near-infrared spectroscopy," *Arch Phys Med Rehabil*, vol. 81, pp. 1348-1356, 2000.
- [68] T. J. Huppert, M. S. Allen, H. Benav, A. Devor, P. Jones, A. Dale, and B. D.A., "A multi-compartment vascular model for inferring arteriole dilation and cerebral metabolic changes during functional activation," *In Cerebral Blood Flow Metabolism*, vol. accepted, 2006.
- [69] D. W. Marquardt, "An Algorithm for Least-Squares Estimation of Nonlinear Parameters," *Journal of the Society for Industrial and Applied Mathematics*, vol. 11, pp. 431-441, 1963.
- [70] A. Mechelli, R. Turner, C. Price, and K. Friston, "Nonlinear responses in fMRI: The Balloon model, Volterra kernels and other hemodynamics," *NeuroImage*, vol. 12, pp. 466-477, 2000.

- [71] Y. Zheng, J. Martindale, D. Johnston, M. Jones, J. Berwick, and J. Mayhew, "A model of the hemodynamic response and oxygen delivery to brain," *Neuroimage*, vol. 16, pp. 617-37, Jul 2002.
- [72] Y. Kong, Y. Zheng, D. Johnston, J. Martindale, M. Jones, S. Billings, and J. Mayhew, "A Model of the Dynamic Relationship between Blood Flow and Volume Changes During Brain Activation," *Journal of Cerebral Blood Flow and Metabolism*, vol. 24, pp. 1382-1392, 2004.
- [73] O. P. Habler and K. F. Messmer, "The physiology of oxygen transport," *Transfus Sci*, vol. 18, pp. 425-35, Sep 1997.
- [74] P. Herman, H. K. Trubel, and F. Hyder, "A multiparametric assessment of oxygen efflux from the brain," *J Cereb Blood Flow Metab*, vol. 26, pp. 79-91, Jan 2006.
- [75] E. Vovenko, "Distribution of oxygen tension on the surface of arterioles, capillaries and venules of brain cortex and in tissue in normoxia: an experimental study on rats," *Pflugers Arch*, vol. 437, pp. 617-23, Mar 1999.
- [76] J. Berwick, P. Redgrave, M. Jones, N. Hewson-Stoate, J. Martindale, D. Johnston, and J. E. Mayhew, "Integration of neural responses originating from different regions of the cortical somatosensory map," *Brain Res*, vol. 1030, pp. 284-93, Dec 31 2004.
- [77] J. W. Severinghaus, "Simple, accurate equations for human blood O₂ dissociation computations," *J Appl Physiol*, vol. 46, pp. 599-602, Mar 1979.
- [78] J. B. Mandeville and J. J. Marota, "Evidence of a cerebrovascular postarteriole windkessel with delayed compliance," *Journal Cerebral Blood flow and Metabolism*, vol. 19, pp. 679-689, 1999.
- [79] A. Devor, I. Ulbert, A. K. Dunn, S. N. Narayanan, S. R. Jones, M. L. Andermann, D. A. Boas, and A. M. Dale, "Coupling of the cortical hemodynamic response to cortical and thalamic neuronal activity," *Proc Natl Acad Sci U S A*, vol. 102, pp. 3822-7, Mar 8 2005.
- [80] A. K. Dunn, A. Devor, A. M. Dale, and D. A. Boas, "Spatial extent of oxygen metabolism and hemodynamic changes during functional activation of the rat somatosensory cortex," *Neuroimage*, vol. 27, pp. 279-90, Aug 15 2005.
- [81] S. A. Sheth, M. Nemoto, M. W. Guiou, M. A. Walker, and A. W. Toga, "Spatiotemporal evolution of functional hemodynamic changes and their relationship to neuronal activity," *J Cereb Blood Flow Metab*, vol. 25, pp. 830-41, Jul 2005.

- [82] I. Vanzetta, R. Hildesheim, and A. Grinvald, "Compartment-resolved imaging of activity-dependent dynamics of cortical blood volume and oximetry," *J Neurosci*, vol. 25, pp. 2233-44, Mar 2 2005.
- [83] L. Kocsis, P. Herman, and A. Eke, "Mathematical model for the estimation of hemodynamic and oxygenation variables by tissue spectroscopy," *J Theor Biol*, Jan 10 2006.
- [84] M. Sharan and A. S. Popel, "A compartmental model for oxygen transport in brain microcirculation in the presence of blood substitutes," *J. Theor. Biol.*, vol. 216, pp. 479-500, 2002.
- [85] Y. Zheng, D. Johnston, J. Berwick, D. Chen, S. Billings, and J. Mayhew, "A three-compartment model of the hemodynamic response and oxygen delivery to brain," *Neuroimage* vol. 28, pp. 925-939, 2005.
- [86] A. L. Brody, S. Saxena, P. Stoessel, L. A. Gillies, L. A. Fairbanks, S. Alborzian, M. E. Phelps, S.-C. Huang, H.-M. Wu, M. L. Ho, M. K. Ho, S. C. Au, K. Maidment, and L. R. Baxter, Jr., "Regional Brain Metabolic Changes in Patients With Major Depression Treated With Either Paroxetine or Interpersonal Therapy: Preliminary Findings." vol. 58, 2001, pp. 631-640.
- [87] A. Drzezga, N. Lautenschlager, H. Siebner, M. Riemenschneider, F. Willoch, S. Minoshima, M. Schwaiger, and A. Kurz, "Cerebral metabolic changes accompanying conversion of mild cognitive impairment into Alzheimer's disease: a PET follow-up study.," *European Journal of Nuclear medicine and molecular imaging*, vol. 30, pp. 1104-1113, 2003.
- [88] S. Saxena, A. L. Brody, K. M. Maidment, J. J. Dunkin, M. Colgan, S. Alborzian, M. E. Phelps, and L. R. B. Jr., "Localized Orbitofrontal and Subcortical Metabolic Changes and Predictors of Response to Paroxetine Treatment in Obsessive-Compulsive Disorder," *Neuropsychopharmacology* vol. 21, pp. 683-693, 1999.
- [89] A. Bechara, A. R. Damasio, H. Damasio, and S. Anderson, "Insensitivity to future consequences following damage to human prefrontal cortex," *Cognition*, vol. 50, pp. 7-12, 1994.
- [90] J. Riera, E. Aubert, K. Iwata, R. Kawashima, X. Wan, and T. Ozaki, "Fusing EEG and fMRI based on a bottom-up model: inferring activation and effective connectivity in neural masses," *Philos Trans R Soc Lond B Biol Sci*, vol. 360, pp. 1025-41, May 29 2005.
- [91] E. W. Washburn, "The Dynamics of Capillary Flow," *Physics Review Letters*, vol. 12, pp. 273-283, 1921.

- [92] K. J. Friston, W. D. Penny, and O. David, "Modelling brain responses," in *International Review of Neurobiology, Neuroimaging, Part A*, M. F. Glabus, Ed.: Elsevier, 2005.
- [93] T. Q. Duong and S. G. Kim, "In vivo MR measurements of regional arterial and venous blood volume fractions in intact rat brain," *Magn Reson Med*, vol. 43, pp. 393-402, Mar 2000.
- [94] A. Kienle and M. S. Patterson, "Improved solutions of the steady-state and the time-resolved diffusion equations for reflectance from a semi-infinite turbid medium," *Journal of the Optical Society of America A*, vol. 14, pp. 246-250, 1997.
- [95] M. A. Mintun, B. N. Lundstrom, A. Z. Snyder, A. G. Vlassenko, G. L. Shulman, and M. E. Raichle, "Blood flow and oxygen delivery to human brain during functional activity: theoretical modeling and experimental data," *Proc Natl Acad Sci U S A*, vol. 98, pp. 6859-64, Jun 5 2001.
- [96] A. G. Tsai, P. C. Johnson, and M. Intaglietta, "Oxygen gradients in the microcirculation," *Physiol Rev*, vol. 83, pp. 933-63, Jul 2003.
- [97] G. K. Aguirre, E. Zarahn, and M. D'Esposito, "The variability of human, BOLD hemodynamic responses," *Neuroimage*, vol. 8, pp. 360-9, Nov 1998.
- [98] V. L. Marcar and T. Loenneker, "The BOLD response: a new look at an old riddle," *Neuroreport*, vol. 15, pp. 1997-2000, Sep 15 2004.
- [99] K. Irikura, K. I. Maynard, and M. A. Moskowitz, "Importance of nitric oxide synthase inhibition to the attenuated vascular responses induced by topical 1-nitro-arginine during vibrissal stimulation," *Journal Cerebral Blood flow and Metabolism*, vol. 14, pp. 45-48, 1994.
- [100] J. Mayhew, D. Hu, Y. Zheng, S. Askew, Y. Hou, J. Berwick, P.J.Coffey, and N. Brown, "An evaluation of linear models analysis techniques for processing images of microcirculation activity," *Neuroimage*, vol. 7, pp. 49-71, 1998.
- [101] C. Iadecola, "Regulation of the cerebral microcirculation during neural activity: is nitric oxide the missing link?," *Trends in Neurosciences*, vol. 16, pp. 206-214, 1993.
- [102] M. E. Raichle, "Behind the scenes of functional brain imaging: A historical and physiological perspective " *Proc Natl Acad Sci*, vol. 95, pp. 765-772, 1998.

- [103] A. Mechelli, C. Price, and K. Friston, "Nonlinear coupling between evoked rCBF and BOLD signals: A simulation study of hemodynamic responses," *NeuroImage*, vol. 14, pp. 862-872, 2001.
- [104] J. Allen, "A Simulation Tool Suite for the Modeling and Optimization of Multiple Quantum Well Structures," in *Electrical Engineering* Arlington: University of Texas at Arlington, 2002.
- [105] L. F. Shampine and M. W. Reichelt, "The MATLAB ODE Suite," *SIAM Journal of Scientific Computing*, vol. 18, pp. 1-22, January 1997.
- [106] W. H. Press, S. A. Teukolsky, W. T. Vetterling, and B. P. Flannery, *Numerical Recipes in C: The Art of Scientific Computing*, Second ed. New York: Cambridge University Press, 1992.
- [107] J. R. Dormand and P. J. Prince, "High Order Embedded Runge-Kutta Formulae," *Journal of Computational and Applied Mathematics*, vol. 7, pp. 203-211, 1981.
- [108] Mathworks, "MATLAB® The Language of Technical Computing," 2: F-O ed Natick, MA: The Mathworks, 2004.
- [109] D. Houcque, "Applications of MATLAB: Ordinary Differential Equations (ODE)," Robert R. McCormick School of Engineering and Applied Science - Northwestern University, Evanston.
- [110] J. R. Dormand and P. J. Prince, "A Family of Imbedded Runge-Kutta Formulae," *Journal of Computational and Applied Mathematics*, vol. 6, pp. 19-27, 1980.
- [111] J. R. Dormand, *Numerical Methods for Differential Equations*: CRC Press, 1996.
- [112] G. Grabner, R. Kittinger, and A. Kecskeméthy, "An Integrated Runge-Kutta and polynomial root finding method for reliable event-driven multibody simulation," in *IFAC Workshop on Lagrangian and Hamiltonian Methods for Nonlinear Control*, Seville, 2003, pp. 1-6.
- [113] R. Buxton, E. Wong, and L. Frank, "Dynamics of blood flow and oxygenation changes during brain activation: the balloon model," *Magnetic Resonance in Medicine*, vol. 39, pp. 855-864, 1998.
- [114] J. B. Mandeville, J. J. Marota, C. Ayata, M. A. Moskowitz, R. M. Weisskoff, and B. R. Rosen, "MRI measurement of the temporal evolution of relative

- CMRO₂ during rat forepaw stimulation," *Magn Reson Med* vol. 42, pp. 944-951, 1999.
- [115] T. Durduran, G. Yu, M. G. Burnett, J. A. Detre, J. H. Greenberg, J. Wang, C. Zhou, and A. G. Yodh, "Diffuse optical measurement of blood flow, blood oxygenation, and metabolism in a human brain during sensorimotor cortex activation," *Opt Lett*, vol. 29, pp. 1766-8, Aug 1 2004.
- [116] R. D. Hoge, M. A. Franceschini, R. J. Covolan, T. Huppert, J. B. Mandeville, and D. A. Boas, "Simultaneous recording of task-induced changes in blood oxygenation, volume, and flow using diffuse optical imaging and arterial spin-labeling MRI," *Neuroimage*, vol. 25, pp. 701-7, Apr 15 2005.
- [117] H. C. Lou, L. Edvinsson, and E. T. MacKenzie, "The concept of coupling blood flow to brain function: Revision required?." vol. 22, 1987, pp. 289-297.
- [118] T. Fellin and G. Carmignoto, "Neurone-to-astrocyte signalling in the brain represents a distinct multifunctional unit." vol. 559, 2004, pp. 3-15.
- [119] W. W. Nichols and M. F. O'Rourke, *McDonald's Blood Flow in Arteries*. London, 1990.
- [120] R. D. Walker, R. E. Smith, S. B. Sherriff, and R. F. M. Wood, "Latex vessels with customized compliance for use in arterial flow models," *Physiological measurement*, vol. 20, pp. 277-286, 1999.
- [121] R. G. Linford and R. W. Ryan, "Pulsatile flow in rigid tubes," *Journal of Physiology*, vol. 20, pp. 1078-1082, 1965.
- [122] P. A. J. Bascom , R. S. C. Cobbold, H. F. Routh, and K. W. Johnston, "On the Doppler signal from a steady flow asymmetrical stenosis model: effects of turbulence," *Ultrasound Medical Biology*, vol. 19, pp. 197-210, 1993.
- [123] D. W. Holdsworth, D. W. Rickey, M. Drangova, D. J. M. Miller, and A. Fenster, "Computer-controlled positive displacement pump for physiological flow simulation," *Medical Biology Engineering*, vol. 29, pp. 565-570, 1991.
- [124] R. D. Walker, "Haemodynamic modelling of the femoral arterial circulation," University of Sheffield, 1998.
- [125] S. Einav, A. Sternberg, and Z. Millo, "Hemodynamic aspects of obliterative processes in peripheral blood vessels-rigid and soft narrowing," *Journal of Biomechanical Engineering*, vol. 114, pp. 263-274, 1992.

- [126] O. Frank, "Die Grundform des arteriellen Pulses," *Zeitung für Biologie*, vol. 37 pp. 483-586, 1899.
- [127] R. F. Wilson, "Critical Care Manual," F. A. Davis Company, Philadelphia 1992
- [128] D. R. Kerner, "Solving Windkessel Models with MLAB "<http://www.civilized.com/mlabexamples>," 2006.
- [129] A. Noordergraaf, *Circulatory System Dynamics* vol. 1. New York: Academic Press Inc., 1978.
- [130] "<http://www.keithley.com/products/dataacqmodules/?mn=KUSB-31>."
- [131] K. McDermott, S. E. Peterson, J. M. Watson, and J. G. Ojemann, "A procedure for identifying preferentially activated by attention to semantic and phonological relations using functional magnetic resonance imaging," *Neuropsychologia*, vol. 41, pp. 293-303, 2003.
- [132] T. Yoshiura, F. Mihara, A. Tanaka, K. Ogomori, Y. Ohyagi, T. Taniwaki, T. Yamada, T. Yamasaki, A. Ichimiya, N. Kinukawa, Y. Kuwabara, and H. Honda, "High b value diffusion - weighted imaging is more sensitive to white matter degeneration in Alzheimer's disease," *NeuroImage*, vol. 20, pp. 413 - 419, 2003.
- [133] B. J. Cummings, A. J. L. Mason, R. C. Kim, P. C.-Y. Sheu, and A. J. Anderson, "Optimization of techniques for the maximal detection and quantification of Alzheimer's - related neuropathology with digital imaging," *Neurobiology of Aging*, vol. 23, pp. 161 - 170, 2002.
- [134] G. Chetelat and J.-C. Baron, "Early diagnosis of Alzheimer's disease: contribution of structural neuroimaging," *NeuroImage*, vol. 18, pp. 525 - 541, 2003.
- [135] B. A. Ardekani, S. J. Choi, G.-A. H.-. Zadeh, B. Porjesz, J. L. Tanabe, K. O. Lim, R. Bilder, J. A. Helpert, and H. Begleiter, "Functional magnetic resonance imaging of brain activity in the visual oddball task," *Cognitive Brain Research*, vol. 14, pp. 347 - 356, 2002.
- [136] C. Hock, K. Villringer, F. M.-. Spahn, R. Wenzel, H. Heekeren, S. S.-. Hofer, M. Hofmann, S. Minoshima, M. Schwaiger, U. Dirnagl, and A. Villringer, "Decrease in parietal cerebral hemoglobin oxygenation during performance of a verbal fluency task in patients with Alzheimer's disease monitored by means of near - infrared spectroscopy (NIRS) - correlation with simultaneous rCBF - PET measurements," *Brain Research*, vol. 755, pp. 293 - 303, 1997.

- [137] F. Q. Gao, S. E. Black, F. S. Leibovitch, D. J. Callen, C. P. Rockel, and J. P. Szalai, "Linear width of the medial temporal lobe can discriminate Alzheimer's disease from normal aging: the Sunnybrook Dementia Study," *Neurobiology of Aging*, vol. 25, pp. 441 - 448, 2004.
- [138] Y. Ouchi, E. Yoshikawa, M. Futatsubashi, H. Okada, T. Torizuka, and M. Kaneko, "Activation in the premotor cortex during mental calculation in patients with Alzheimer's disease: relevance of reduction in posterior cingulate metabolism," *NeuroImage*, vol. 22, pp. 155-163, May 2004.
- [139] F. Remy, F. Mirrashed, B. Campbell, and W. Richter, "Mental calculation impairment in Alzheimer's disease: a functional magnetic resonance imaging study," *Neuroscience Letters*, vol. 358, pp. 25 - 28, 2004.
- [140] M. Ogawa, H. Fukuyama, Y. Ouchi, H. Yamauchi, and J. Kimura, "Altered energy metabolism in Alzheimer's disease," *Journal of the Neurological Sciences*, vol. 139, pp. 78 - 82, 1996.
- [141] L. Palleschi, F. Vetta, E. D. Gennaro, G. Idone, G. Sottosanti, W. Gianni, and V. Marigliano, "Effect of Aerobic Training on the cognitive performance of elderly patients with senile dementia of Alzheimer type," *Archives of Gerontology and Geriatrics Supplement*, vol. 5, pp. 47 - 50, 1996.
- [142] G. W. Faris and M. Banks, "Potential for optical imaging in the 1 - 1.3 micron range using an upconverting time gate," *SPIE*, vol. 2389, pp. 35 - 39, 1995.
- [143] A. K. Dunn, A. Devor, H. Bolay, M. L. Andermann, M. A. Moskowitz, A. M. Dale, and D. A. Boas, "Simultaneous imaging of total cerebral hemoglobin concentration, oxygenation, and blood flow during functional activation," *Opt Lett*, vol. 28, pp. 28-30, Jan 1 2003.
- [144] A. Devor, A. K. Dunn, M. L. Andermann, I. Ulbert, D. A. Boas, and A. M. Dale, "Coupling of total hemoglobin concentration, oxygenation, and neural activity in rat somatosensory cortex," *Neuron*, vol. 39, pp. 353-9, Jul 17 2003.
- [145] M. Kohl, U. Lindauer, G. Roysl, M. Kuhl, L. Gold, A. Villringer, and U. Dirnagl, "Physical model for the spectroscopic analysis of cortical intrinsic optical signals," *Phys Med Biol*, vol. 45, pp. 3749-64, Dec 2000.
- [146] J. D. Briers, "Laser Doppler, speckle and related techniques for blood perfusion mapping and imaging," *Physiol Meas*, vol. 22, pp. R35-66, Nov 2001.
- [147] C. K. Carter and R. Kohn, "Markov Chain Monte Carlo in Conditionally Gaussian State Space Models," *Biometrika*, vol. 83, pp. 589-601, 1996.

- [148] J. L. Devore, "Simple Linear Regression and Correlation". Probability and Statistics for Engineering and the Sciences," 4th Edition ed Belmont, CA USA: Wadsworth Inc, 1995, pp. 474-522.
- [149] R. Adolphs, "Cognitive neuroscience of human social behaviour," *Nature Reviews - Neuroscience*, vol. 4, pp. 165-178, March 2003.
- [150] C. Fong and K. McCabe, "Are decisions under risk malleable?," *Proceedings of the National Academy of Sciences*, vol. 96, p. 10927, 1999.
- [151] C. Camerer, G. Loewenstein, and D. Prelec, "Neuroeconomics:How neuroscience can inform economics," 2004.
- [152] A. Bechara, D. Tranel, and H. Damasio, "Characterization of the decision-making deficit of patients with ventromedial prefrontal cortex lesions," *Brain*, vol. 123, pp. 2189-2202, 2000.
- [153] W. Schultz, "Multiple reward signals in the brain," *Nature Reviews - Neuroscience*, vol. 1, pp. 199-207, December 2000 2000.
- [154] D. Houser, K. McCabe, and V. Smith, "Cultural group selection, co evolutionary processes and large-scale cooperation (by Joseph Henrich)," *Journal of Economic Behavior & Organization*, vol. 53, p. 85, January 2004.
- [155] P. R. Montague and G. S. Berns, "Neural Economics and the biological substrates of valuation," *Neuron*, vol. 36, pp. 265-284, October 10, 2002.
- [156] K. Smith, J. Dickhaut, K. McCabe, and J. V. Pardo, "Neuronal substrates for choice under ambiguity, risk, gains and losses," *Management Science*, vol. 48, pp. 711-718, June 2002.
- [157] K. McCabe, D. Houser, L. Ryan, V. Smith, and T. Truward, "A functional imaging study of cooperation in two-person reciprocal exchange," *Proceedings of the National Academy of Sciences*, vol. 98, pp. 11832-11835, September 25, 2001.
- [158] K. McCabe and S. J. Rassenti, "Game theory and reciprocity in some extensive form of experimental games," *Proceedings of the National Academy of Sciences*, vol. 93, p. 13421, November 12, 1996.

BIOGRAPHICAL INFORMATION

Monica Allen received her BSEE from the Maharashtra Institute of Technology in 1999 and MSEE from the University of Texas at Arlington in 2002. Monica has previously worked for the telecommunication industry as a Systems engineer. After a short academic break, Monica returned to the University of Texas at Arlington in 2003 to complete her PhD where she primarily worked in the research areas of theoretical and experimental biomedical imaging. Apart from her main thrust in optical imaging, Monica has also conducted research projects in quantum mechanics and nonlinear optics and where she is also published in the field. Monica is a member and former officer of the IEEE and Engineering honor society, Tau Beta Pi. She is also affiliated to the Electrical Engineering honor society, Eta Kappa Nu and the Society of Women engineers. After graduation, Monica intends to pursue a career as a research scientist that spans her two fields of interest namely optics and medical imaging. Monica intends to eventually return to academia.